Quantification of the BOLD Response via Blood Gas Modulations

By Paula.L Croal, BSc. (Hons) MSc.

Thesis submitted to The University of Nottingham for the degree of Doctor of Philosophy

May 2014

ABSTRACT

This thesis investigates the mechanisms which underlie the blood oxygenation level dependent (BOLD) functional magnetic resonance imaging (fMRI) signal. Detailed understanding of the BOLD signal will allow fMRI to make the transition from a qualitative to quantitative neuroimaging technique, increasing its clinical potential. It is possible to further investigate the vascular, neuronal and physical processes which combine to give a resulting BOLD signal by using respiratory challenges to alter blood levels of carbon dioxide and oxygen.

Isocapnic hyperoxia was found to have no significant effect on vascular responses at 7 Tesla (T). No significant change was found in resting-state cerebral blood flow (CBF), resting-state cerebral blood volume (CBV) and task evoked CBF. This suggests that the convention that oxygen has a vasoconstrictive effect on blood vessels reported in prior studies was based on an effect associated with a drop in carbon dioxide accompanying the increase in oxygenation. The effect of isocapnic hyperoxia on neuronal oscillations was assessed with magnetoencephalography (MEG). Whilst a significant reduction in oscillatory power is reported in the occipital lobe in response to hyperoxia, the change is significantly smaller than the global reduction in oscillatory power that has been previously measured with hypercapnia. Together these findings suggest that hyperoxia is an ideal tool for calibrated BOLD fMRI, although further research is required to quantify the association between neuronal oscillations and the cerebral metabolic rate of oxygen ($CMRO_2$).

With no significant effect on vasculature, isocapnic hyperoxia is a useful tool for investigating the relationship between the change in blood oxygenation and the change in transverse signal (ΔR_2^*). This relationship plays a key role in calibrated BOLD fMRI and has previously been determined by numerical and analytical simulations or experimental measures which have been confounded by a change in cerebral blood volume. The relationship between the fractional change in blood oxygenation and ΔR_2^* was found to be sub-linear across 1.5, 3 and 7 T, although a linear dependence was found to be a reasonable approximation.

Differences between these results and previous results which suggest a supralinear relationship at 1.5 and 3 T and a linear relationship at 7 T, are attributed to the relative contribution of intravascular and extravascular signals and their dependence on both field strength, blood oxygenation and choice of echo times.

Hypercapnia is a potent vasodilator and is a popular and useful research tool when investigating cerebral metabolism and cerebrovascular reactivity. Due to the effect of hypercapnia on transit time, it is likely that arterial spin labelling (ASL) measures of CBF made at a single post-label label delay time (TI) will be prone to errors. A comparison of single and multiphase ASL is made at 7 T, with a modified Look-locker EPI sequence presented. The modified sequence allows simultaneous measurement of CBF and transit time, whilst increasing the available BOLD signal. Whilst the hypercapnia-induced change in CBF was found to be significantly higher with multiphase ASL, the change in BOLD signal was equivalent between single and multi-phase ASL. This could have important implications for hypercapnia calibrated BOLD fMRI, where the choice of ASL sequence may affect the estimated change in $CMRO_2$. Furthermore, by increasing the sensitivity to perfusion and BOLD, this provides a framework for future cerebral haemodynamic studies in health and disease where simultaneous measurements are required.

Contents

<u>**Glossary**</u>

ASL	Arterial Spin Labelling
BBB	Blood-brain barrier
BOLD	Blood Oxygenation Level Dependent
BS	Background Suppression
CASL	Continuous Arterial Spin Labelling
CBF	Cerebral Blood Flow
CBV	Cerebral Blood Volume
EEG	Electroencephalography
EPI	Echo Planar Imaging
TE	Echo Time
FA	Flip Angle
FAIR	Flow-sensitive Alternating Inversion Recovery
$F_{ET}CO_2$	Fractional end-tidal concentration of CO_2
$F_{ET}O_2$	Fractional end-tidal concentration of O_2
$FiCO_2$	Inspired level of carbon dioxide
FID	Free Induction Decay
FiO_2	Inspired level of oxygen
fMRI	Functional Magnetic Resonance Imaging
FOV	Field of View
GE	Gradient Echo
GM	Grey Matter
Hypercapnia	Increased level of CO_2 in the blood
Hyperoxia	Increased level of O_2 in the blood

Hypocapnia	Decreased level of O_2 in the blood
IR	Inversion Recovery
LL	Look Locker
MEG	Magnetoencephalography
MPRAGE	Magnetisation Prepared Rapid Gradient Echo
MRI	Magnetic Resonance Imaging
NMR	Nuclear Magnetic Resonance
Normocapnia	Normal levels of CO_2 in the blood
Normoxia	Normal levels of O_2 in the blood
PASL	Pulsed Arterial Spin Labelling
PCASL	Pseudo-continuous Arterial Spin Labelling
$P_{ET}CO_2$	End-tidal partial pressure of CO_2
$P_{ET}O_2$	End-tidal partial pressure of O_2
R_1	Longitudinal Relaxation Rate
R_2	Transverse Relaxation Rate
RF	Radio Frequency
SE	Spin Echo
SENSE	Sensitivity Encoding
SNR	Signal to Noise Ratio
SQUID	Superconducting Quantum Interference Device
T_1	Longitudinal Relaxation Time
T_2	Transverse Relaxation Time
TE	Echo Time
TI	Post-Label Delay
TR	Repetition Time
V_E	Minute Ventilation

1 Introduction

Functional MRI (fMRI) images the physiological response of the brain in response to activation. It arose from the discovery that the magnetic properties of blood are dependent on its oxygenation level [1-5]. Over the past twenty years, this blood oxygenation level dependent (BOLD) response has been an area of active research, providing an invaluable tool in the fields of psychology and neuroscience. The use of the BOLD response within a clinical setting is currently limited by the fact it is an indirect measure of neural activity which is dependent on baseline physiology (such as cerebral blood flow (CBF), cerebral blood volume (CBV) [6] and blood oxygenation (Y)) which varies between subjects, particularly on ageing and patient groups. The work presented in this thesis investigates the physiological processes that give rise to the BOLD response, with the aim of increasing the validity of future fMRI research.

Calibration of the BOLD response using functional MRI (fMRI) can provide a fractional change in the cerebral metabolic rate of oxygen consumption ($CMRO_2$) [7, 8]. $CMRO_2$ as measured with calibrated BOLD fMRI, minimises the vascular contribution to the BOLD signal and is therefore more closely linked to neuronal activity than the BOLD response. The two main methods of calibration rely on respiratory challenges. The original method used hypercapnia to modulate CBF [7] and this was adapted for a hyperoxic stimulus which directly modulated oxygenation [8]. Both techniques assume these stimuli do not modulate neuronal activity. More recently combined methods have been proposed where both CBF and oxygenation are modulated using hyperoxia and hypercapnia to estimate absolute $CMRO_2$ [9, 10]. This thesis aims to improve the quantitative nature of calibrated BOLD by assessing the assumptions made in the calibrated BOLD model. The experimental data provide a novel insight into the most appropriate stimulus choice, parameter estimation and imaging acquisition for calibrated BOLD.

1.1 <u>Thesis Outline</u>

This thesis describes how the modulation of oxygen (O_2) and carbon dioxide (CO_2) can be used to investigate the cerebral haemodynamics which underlie the blood oxygenation level dependent (BOLD) response. The experimental findings presented in Chapters 4-6 are from work carried out in The Sir Peter Mansfield Magnetic Resonance Centre, Department of Physics and Astronomy at The University of Nottingham between September 2010 and February 2014.

Chapter 2 introduces the basic principles which underlie NMR and how they are applied in MRI to enable image acquisition. The imaging sequences are introduced along with the MRI hardware required to implement them. Only healthy volunteers were scanned for the work presented in this thesis, however there are still ethical and safety considerations to be made and these are discussed.

Chapter 3 provides an overview of neuro-anatomy and physiology. The BOLD contrast is introduced along with current limitations of interpreting BOLD fMRI data. BOLD fMRI, arterial spin labelling (ASL), Phase-Contrast Magnetic Resonance Angiography (PC-MRA) and magnetoencephalography (MEG) are used in this thesis to assess the different physiological components of the BOLD response. Chapter 3 introduces these techniques, describing the background theory and their implementation.

Chapter 4 describes how modulation of blood gas levels of O_2 can be used to calibrate the BOLD response to estimate the rate of cerebral O_2 metabolism ($CMRO_2$). The effect of isocapnic hyperoxia on resting state physiology is measured in order to assess the assumptions currently made in hyperoxia calibrated BOLD fMRI. Chapter 4 then presents findings on the effect of isocapnic hyperoxia on evoked responses to functional activation, assessing the role of O_2 in functional hyperaemia.

Chapter 5 presents the experimental findings from a cross-field study at 1.5, 3 and 7 Tesla. A novel method for assessing the relationship between transverse relaxation rate (R_2^*) and fractional oxygenation ($1-Y_v$) is introduced. It is proposed

that when intravascular and extravascular signal contributions are accounted for, this relationship is sub-linear. This finding is contrary to prior belief that the relationship is supralinear at 1.5 and 3 T and tends towards a linear relationship at 7 T. The implications of this finding for calibrated BOLD fMRI are discussed.

Chapter 6 introduces a modified pulse sequence termed Look-Locker Double Acquisition with Background Suppression (LL_DABS) to allow more accurate measurements of simultaneous BOLD and cerebral blood flow (CBF) under situations of increased flow, such as hypercapnia, where transit time changes must be considered. The current challenges faced when measuring the effects of hypercapnia on cerebral physiology are assessed and direct comparison made between two alternative arterial spin labelling (ASL) readout schemes with a view to improving the validity of future research.

Chapter 7 summarises the experimental work and introduces future research directions.

2   Magnetic Resonance Theory

2.1   Outline

This chapter introduces the basic principles which underlie nuclear magnetic resonance (NMR). The behaviour of a single proton in the presence of a static magnetic field is discussed and then expanded to an ensemble of protons. These principles are used in magnetic resonance imaging (MRI), and a brief introduction of how the MR signal is spatially encoded to produce an image is provided, including an overview of scanner hardware and relevant pulse sequences.

2.2   Nuclear Magnetic Resonance

2.2.1   Quantum mechanical description

Spin angular momentum is a quantum mechanical property of a nucleus, taking the vector quantity $\mathbf{J}$ with cartesian components $[\hbar I_x\, \hbar I_y\, \hbar I_z]$. The magnitude of $\mathbf{J}$ is described by Equation 2-1:

$$|\mathbf{J}| = \hbar\sqrt{I(I+1)}\, , \qquad\qquad\qquad \text{2-1}$$

where $\hbar$ is Plank's constant divided by 2π and I represents the spin quantum number. I can take either integer, half-integer values, or zero (a non-zero value is required for a nucleus to exhibit MR properties). A particle with quantum spin number I, can take $2I+1$ states when placed in an external magnetic field, B, as determined by m_I, where $m_I = -I, (-I+1), \dots I$. The quantum number m_I determines the discrete orientation of the spin angular momentum, such that if the magnetic field is parallel to the z-axis, J_z can be described by:

$$J_z = m_I \hbar\, . \qquad\qquad\qquad\qquad \text{2-2}$$

The primary nucleus of interest in magnetic resonance imaging (which will be the focus of this thesis) is hydrogen (^{1}H), due to its high natural abundance in the human body. For ^{1}H, the single proton in the nucleus deems that I = ½, thus

4

there are two distinct spin states of m_I; $+ 1/2$ (spin up) and $- 1/2$ (spin down) and spin angular momentum $J_z = \pm \frac{1}{2}\hbar$. These discrete values describe two distinct spin states; for spins parallel to B_0 ($m_I = + \frac{1}{2}$), and anti-parallel to B_0 ($m_I = - \frac{1}{2}$), where B_0 is the magnitude of the magnetic field in the z-direction,

$$\mathbf{B} = B_0\mathbf{z} \qquad \qquad \textbf{2-3}$$

Classically, each individual hydrogen nucleus can be viewed as a rotating charged sphere (henceforth referred to as a "spin"), thus it possesses a magnetic moment ($\mathbf{\mu}$) in addition to spin angular momentum. The gyromagnetic ratio ($\gamma = 42.57$ MHz/T for ^{1}H) [11] is a nucleus-specific proportionality constant relating the two properties such that

$$\mathbf{\mu} = \gamma \mathbf{J} \qquad \qquad \textbf{2-4}$$

Using Equation 2-2, the z-component of $\mathbf{\mu}$ can be written as

$$\mu_z = \gamma \hbar m_I \qquad \qquad \textbf{2-5}$$

The nucleus will acquire energy (E) in the presence of an external magnetic field, B_0, given by $E = -\mu_z B_0$. Substituting for μ_z gives $E = -\gamma \hbar m_I B_0$. It can be seen that each spin state will have a different energy level, with the parallel spin-state (spin up or $+\frac{1}{2}$) orientation having the lowest energy.

The energy associated with a spin state is proportional to the applied magnetic field, B_0. Therefore, in the absence of an external magnetic field, there is no splitting of energy levels. The separation of energy levels in a magnetic field is known as Zeeman splitting [11] (Figure 2-1), where for the ^{1}H nucleus energy difference it is defined as:

$$\Delta E = \gamma \hbar B \ . \qquad \qquad \textbf{2-6}$$
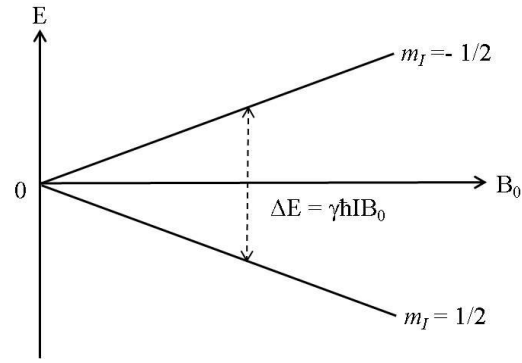
Figure 2-1) Schematic of Zeeman splitting for ^{1}H. The difference in energy level (ΔE) is the product of the gyromagnetic ratio (γ), $\hbar$ (Planck's constant divided by 2π) and the external magnetic field (B_0). In the absence of a magnetic field, the energy levels of both states are equal.

In NMR, by applying an oscillating magnetic field B_1 in the xy-plane, a transition can be made between spin states (i.e. low-energy parallel state to high energy anti-parallel state). The required oscillatory frequency (v_0) is determined by

$$v_0 = \frac{\gamma B_0}{2\pi} \qquad\qquad \textbf{2-7}$$

which is typically written in terms of angular frequency, ω_0, where $\omega_0 = 2\pi v_0$ and

$$\omega_0 = \gamma B_0 \,. \qquad\qquad \textbf{2-8}$$

This is termed the Larmor frequency which for hydrogen is 63.8 MHz at 1.5 T, 127.6 MHz at 3 T and 297.7 MHz at 7 T.

Thus far, only a single proton has been considered. In a sample of 2 x 2 x 3 mm (a typical MRI voxel), there will be on the order of 8.0 x 10^{20} protons per voxel (where a single volume of spins can be called a spin isochromat). The Boltzmann distribution, as described by Equation 2-9, determines how populated each energy state is at thermal equilibrium. Assuming each spin is non-interacting, N^+ and N^- denote the number of nuclei in the parallel spin state ($m_I = +\frac{1}{2}$) and anti-parallel spin state ($m_I = -\frac{1}{2}$) respectively, k is Boltzmann's constant (1.38 x10^{-23} Joules/Kelvin) and T is the temperature in Kelvin [12].

$$\frac{N^-}{N^+} = e^{-\Delta E / kT}$$

2-9

In the high temperature limit $\Delta E << kT$, Equation 2-9 can be expanded using the first two terms of the Taylor series and substituting Equation 2-7 gives

$$\frac{N^-}{N^+} \approx 1 - \frac{\gamma \hbar B_0}{kT} \quad .$$

2-10

The total number of spins (N) can be taken as the sum of N^+ and N^-, (where the difference between states is so small such that $N^+ \approx N^-$) so that the population difference, *n,* can be written as

$$n = \frac{N^+ \gamma \hbar B_0}{kT} = \frac{N \gamma \hbar B_0}{2kT} \quad .$$

2-11

It can be seen from Equation 2-11 that the energy difference between states and the population difference is dependent on B_0, therefore the signal to noise ratio is improved with increasing field strength. Similarly, using Equation 2-11 to derive the magnitude of the net magnetisation (**M**) indicates the signal dependence on field strength.

$$|\mathbf{M}| = n\mu$$

2-12

where, $\mu = \frac{\gamma \hbar}{2}$, such that

$$|\mathbf{M}| = \frac{N(\gamma \hbar)^2 B_o}{4kT}$$

2-13

In the absence of an external magnetic field, the spins will be randomly oriented and therefore $\mathbf{M}_0$ will be zero (Figure 2-2A). However, in the presence of an external magnetic field, spins are aligned either parallel or anti-parallel to B_0. Slightly more spins occupy the low-energy parallel state, so that $\mathbf{M}_0$ is non-zero (Figure 2-2B).
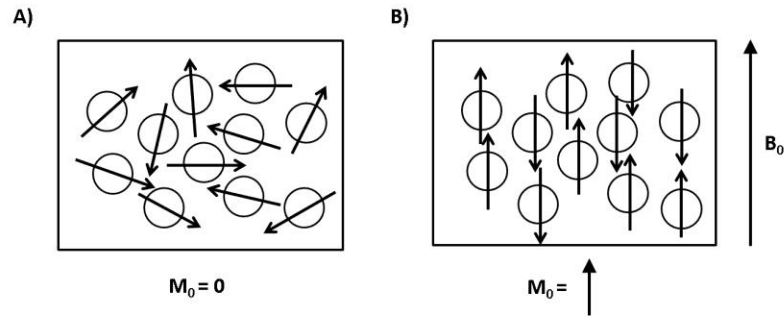
Figure 2-2) A) In the absence of an external magnetic field (B$_0$), spins are randomly oriented such that the net magnetisation (M) is zero. B) In the presence of B$_0$, spins are positioned either parallel or anti-parallel to the field. Slightly more spins are in the parallel state such that M$_0$ >0.

2.2.2 Classical description

A magnetic moment placed in a magnetic field, B$_0$ will experience a torque and so the spin angular momentum vector *J* will begin to precess about B$_0$ at a constant angle with respect to B$_0$, as given by Equation 2-14.

$$\frac{d\mathbf{J}}{dt} = \boldsymbol{\mu} \times \mathbf{B} ,$$

2-14

where $\mathbf{B} = B_0 \mathbf{z}$

2-15

This can be written in terms of magnetic moment (Equation 2-4) and assuming that the magnetic field is parallel to the z-axis (Equation 2-15), the precession can be described along the x, y and z components (Equations 2-17-2-19, Figure 2-3).

$$\frac{d\boldsymbol{\mu}}{dt} = \gamma \boldsymbol{\mu} \times \mathbf{B}$$

2-16

$$\frac{d\mu_z}{dt} = 0 ,$$

2-17

$$\frac{d\mu_x}{dt} = \gamma \mu_y B_z ,$$

2-18

$$\frac{d\mu_y}{dt} = \gamma \mu_x B_z$$

2-19

The frequency of this precession is known as the Larmor frequency (ω_0) (Equation 2-20), corresponding to the resonance frequency defined by quantum theory (Equation 2-8).

$$\omega_0 = \gamma . B_0 \qquad\qquad\qquad \textbf{2-20}$$
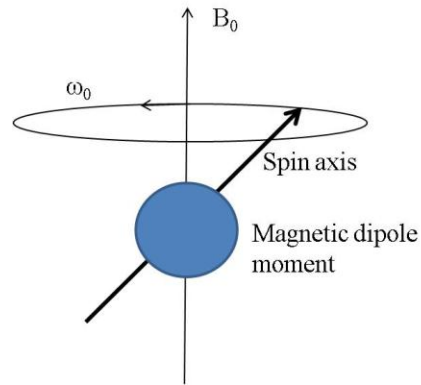
Figure 2-3) Precession of a magnetic dipole when placed in an external magnetic field (B_0). The torque exerted by B_0 in combination with the angular momentum of the magnetic dipole, causes it to precess around B_0 with angular frequency ω_0.

2.2.3 <u>Rotating Frame of Reference and the application of a radiofrequency pulse (B_1)</u>

Before considering how magnetisation is detected, it is useful to simplify the mathematics by introducing the rotating frame of reference. In the rotating frame of reference (with co-ordinates x', y' and z'), it is assumed that the world is rotating about z (i.e. z = z') at frequency ω_r relative to the laboratory frame. For the condition $\omega_r = \omega_0$ spins at the Larmor frequency no longer appear to precess but appear stationary.

With the effective removal of precession, the application of an oscillating magnetic field at the Larmor frequency, B_1 along the x'-axis causes the protons to precess about B_1. This is generally in the radiofrequency range and so this field perturbation is also called a radiofrequency (RF) pulse and is generated by an oscillating current through a transmit coil. The application of B_1 for time t causes

the net magnetisation to move from the z'-plane in to the x'y'-plane by flip angle (FA) θ as defined by

$$\theta = \gamma B_1 t \,.$$ **2-21**

RF pulse types that are regularly used in MR pulse-sequences are an excitation pulse (θ = 90°) and an inversion pulse (θ = 180°). Following an RF pulse of θ = 90°, the net magnetisation vector is zero in the z'-plane and M_0 in the x'y'-plane. Following an RF pulse of θ = 180°, the net magnetisation vector is inverted through the x'y'-plane so that it is now along the negative z'-axis (Figure 2-4). The tipping of the net magnetisation away from the z' (or z) axis in to the x'y' (transverse) plane is essential for NMR signal detection.
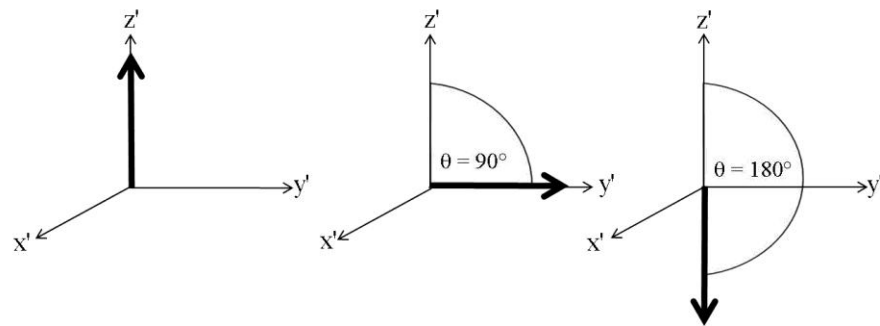

Figure 2-4) After B_1 is applied for time t along the x'-axis, the net magnetisation tips into the x'y'-plane with θ = γB_1t. For θ = 90°, the net magnetisation is tipped fully into the x-y'-plane. C) For θ = 180°, the net magnetisation is inverted to be along the –z' axis.

2.3   Relaxation

At equilibrium, the z-component of magnetisation vector is equal to the equilibrium magnetisation vector ($M_z = M_0$) and $M_{xy} = 0$. During an RF pulse, the longitudinal magnetisation is perturbed due to the transition of spin states, and transverse magnetisation (M_{xy}) is induced via phase coherence. After an RF pulse, the longitudinal and transverse signal components relax back to their equilibrium state, each with different rate constants.

2.3.4 Longitudinal Relaxation

Longitudinal relaxation arises from spins experiencing fluctuating magnetic fields. Each spin has its own magnetic dipole moment and so when an individual spin is precessing at the Larmor frequency, a magnetic field is generated. This generated magnetic field will cause neighbouring nuclei to change spin-state and so gradually restore the equilibrium state where slightly more spins exist in the lower energy spin-state than the higher energy spin-state. The interaction between spins and the surrounding lattice is affected both by the molecule's ability to move through the lattice, described by the correlation time (τ_c) which itself is temperature dependent.

Following an RF pulse, the spin system returns energy to the lattice (surrounding environment) in order to re-establish the Boltzmann distribution of spin states. The time taken for M_z to recover back to the equilibrium value of M_0 is characterised by the time constant T_1 (Figure 2-5). In general, longitudinal recovery can be described as an exponential process, as described by the simplified Bloch Equation:

$$\frac{dM_z}{dt} = \frac{M_0 - M_z}{T_1}$$

2-22

The solution following a 180° inversion pulse such that $M_z = -M_0$ at time $t = 0$ is given by:

$$M_z = M_0(1 - 2e^{-t/T_1})$$

2-23

T_1 varies according to sample properties such as water binding, water content and concentration of macromolecules and so can provide a useful contrast mechanism to distinguish between different tissue types (Table 2-1). T_1 is most commonly measured by an inversion recovery (IR) sequence. After the initial inversion pulse (Figure 2-6) there is a delay or "inversion time" (TI), allowing some signal to recover, before a 90° RF pulse knocks the magnetisation at time TI into the transverse plane. This is then repeated for differing values of TI and the resulting data are fitted to Equation 2-23.
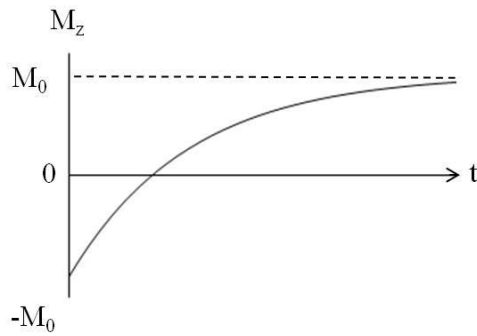
Figure 2-5) Relaxation of the longitudinal magnetisation component M_z back to equilibrium state M_0 following a 180° inversion RF pulse. Recovery is governed by the time constant T_1 (Equation 2-22).

Field Strength (T)	T_1 (ms)		
	Grey Matter	White Matter	Venous Blood
1.5	1197 [13]	646 [13]	1429 [14]
3.0	1607 [13]	838 [13]	1667[14]
7.0	1939 [13]	1126[13]	1905[14]

Table 2-1) Example longitudinal relaxation times (T_1) in milliseconds, for tissue and blood at 1.5, 3 and 7 T.
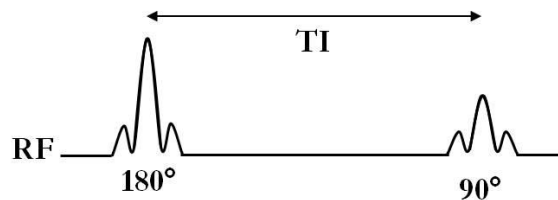
Figure 2-6) Basic pulse diagram for an inversion recovery (IR) sequence. The delay between the 180° RF pulse and 90° RF pulse is characterised by the inversion time (TI).

2.3.5 Transverse Relaxation

Following an RF excitation pulse, all spins are initially in phase, precessing at approximately the same frequency, ω_0. However, the transverse signal component decays as the spin system loses phase coherence. If all spins were to precess at the Larmor frequency, then M_{xy} would precess coherently about the z-axis, appearing to be static in the rotating frame. However, each spin experiences a slightly different magnetic field causing a range of precession frequencies. In the rotating frame, spins which rotate at a frequency above or below the Larmor frequency will cause the spin isochromats to fan out, until they are normally distributed and $M_{xy} = 0$ (Figure 2-7).
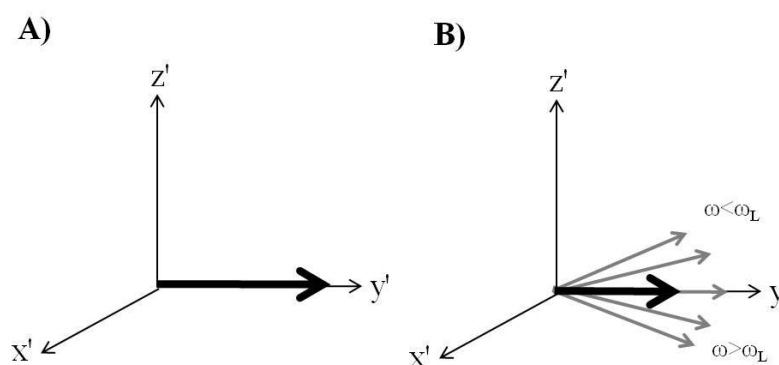
Figure 2-7) A) Transverse magnetisation in the x'y'-plane (rotating frame of reference) immediately following a 90° RF pulse. B) M_{xy} reduces over time via T_2 or T_2^* relaxation, caused by loss of phase coherence due to individual spins precessing at frequencies other than the Larmor frequency (ω_L).

During the recovery of M_{xy} to equilibrium state (where $M_{xy} = 0$), energy is transferred between spins but does not exchange with the energy of the lattice. The exponential decay of the transverse component of magnetisation is governed by the time constant T_2 (or T_2^*) (Figure 2-8). The transition of spin states which induce T_1 effects will contribute to the loss of phase coherence and thus T_1 contributes to T_2 relaxation. Transverse relaxation can be described by the following simplified Bloch Equation as given by:

$$\frac{dM_{xy}}{dt} = -\frac{M_{xy}}{T_2} \; ,$$

2-24

Equation 2-25 gives the solution:

$$M_{xy} = M_0 e^{-t/T_2} \; .$$

2-25
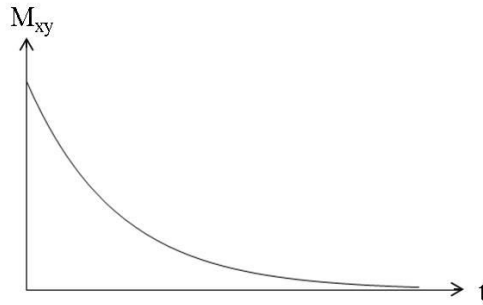
**Figure 2-8) Relaxation of the transverse magnetisation component M_{xy} to equilibrium following an RF pulse. Recovery is governed by the relaxation time constant T_2 (Equation 2-24).**

As well as the irreversible time variant processes (T_2), transverse decay can also be caused by invariant changes (T_2') in the local magnetic field, which cause irreversible and reversible transverse decay. The combination of these effects is described by the rate constant, T_2^*, where

$$\frac{1}{T_2^*} = \frac{1}{T_2} + \frac{1}{T_2'}$$

2-26

In order to measure T_2, it is necessary to rephase the static T_2' effects. T_2' effects can be refocused using a spin-echo sequence [15] which uses a 180° refocusing pulse (applied at time TE/2 after the initial RF pulse) to refocus the magnetisation vector (Figure 2-9). Phase accumulation is now reversed so that spins precessing at a frequency greater than the Larmor frequency now have a negative net phase. Assuming that they continue to precess at the same frequency, dephased spins are rephased by an equal amount, such that at time TE an echo of the original signal can be measured. By repeating a SE sequence across a range of TE values, T_2 can be measured.
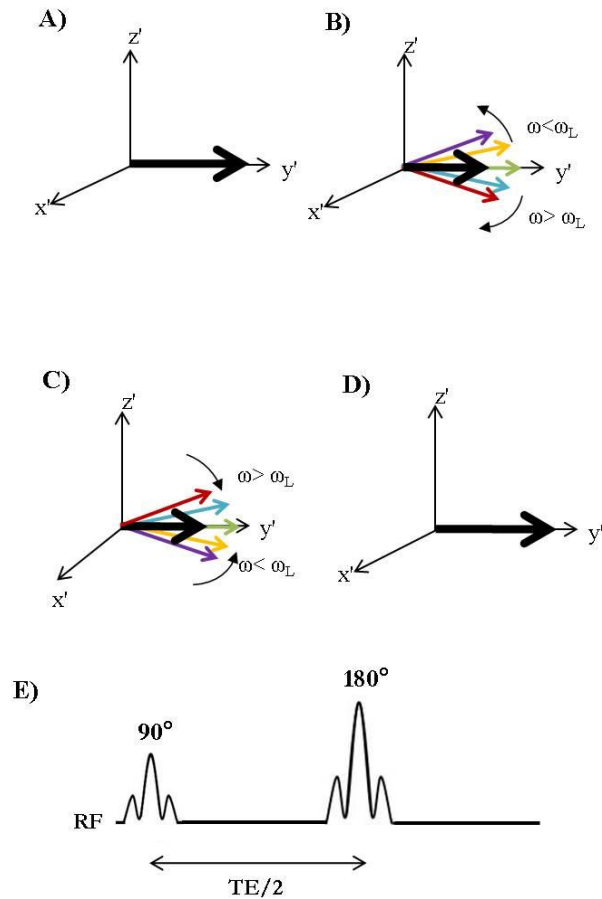
**Figure 2-9) Transverse magnetisation in the x'y'-plane immediately following a 180° RF pulse B) M_{xy} reduces over time via T_2 relaxation, caused by loss of phase coherence over time due to individual spins precessing at frequencies other than the Larmor frequency (ω_L). C) At time TE/2, a 180° refocusing pulse is applied along the y'-axis so that phase accumulation is reversed. D) At time TE, an echo of the original signal is formed on the y'-axis. E) Basic pulse sequence diagram for a spin echo sequence; a 180° RF pulse is applied at time TE/2.**

Diffusion effects become more problematic at high field strengths as T_2 decreases and so the relative contribution of diffusion effects increases, meaning a spin echo repeated at different echo times is not the optimal method to measure T_2. An alternative approach to a spin-echo sequence is a Carr-Purcell-Meiboom-Gill (CPMG) sequence [16, 17]. By applying a series of 180° refocusing pulses (with TE defined as the time between each refocusing pulse and increasing incrementally), the available time for diffusion effects to accumulate is minimised.

15

This results in a more accurate T_2 value, which can be made in a single experiment, provided the pulses are short.

The separate effects of these three relaxation time constants and their role in signal contrast will be discussed in more detail in Chapter 5. Literature values of T_2 and T_2^* across field strength are shown in Table 2-2. The measurement of T_2^* is introduced in section 2.4.12 and the quantification and modelling of T_2^* considered further in Chapter 5.

Field Strength (T)	Grey Matter		White Matter		Venous Blood	
	T_2 (ms)	T_2^* (ms)	T_2 (ms)	T_2^* (ms)	T_2 (ms)	T_2^* (ms)
1.5	83.5 [18]	84.0 [14]	80.0 [18]	66.2 [14]	128.0 [19]	40.0 [20]
3.0	72.0 [18]	66.0 [14]	71.0 [18]	53.2 [14]	31.1 [21]	14.3 [20]
7.0	46.5 [18]	33.2 [14]	47.0 [18]	26.8 [14]	13.1 [22]	4.3 [20]

Table 2-2) Example T_2 and T_2^* relaxation times in milliseconds, across different field strengths.

2.3.6 Free Induction Decay

After an RF pulse is applied with carrier frequency ω_0, the resulting signal in the transverse plane will induce a current in the receiver coil (Faraday's electromagnetic induction law) which oscillates at the Larmor frequency. This signal decays with a transverse time constant back to equilibrium, according to the Bloch Equations (Equation 2-24). The signal difference between the Larmor and carrier frequencies is known as the free induction decay (FID) and is the basic form of all MR signals arising from a single RF pulse (Figure 2-10). The magnitude of the FID depends on the flip angle and the magnitude of M_0 which is dependent on the strength of the applied magnetic field, B_0 and the proton density.
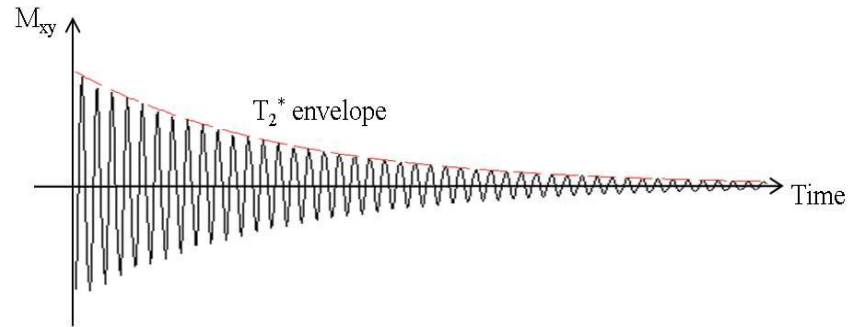
Figure 2-10) Schematic of the free induction decay of magnetisation following an RF pulse. The signal decays exponentially as described by time constant T_2^*, taking ~ $5T_2^*$ to decay to zero.

2.4 Magnetic Resonance Imaging

This section extends the basic principles of NMR to the field of MRI and will outline the theory behind the imaging techniques used in this thesis. So far, the theory of using an RF excitation pulse to generate a signal has been introduced. Here this is extended to explain how the signal is spatially encoded to produce an image.

2.4.7 Magnetic Field Gradients

Magnetic field gradients (G) are used to produce linearly varying fields along the axis in which they are applied (Equation 2-27, where i refers to either the x, y or z axis).

$$G_i = \frac{dB_z}{di} \qquad \text{2-27}$$

Applying a gradient G will lead to a spatial variation in the Larmor frequency such that frequency is described as a function of position r by

$$\omega(r) = \gamma(B_0 + Gr) \qquad \text{2-28}$$

In the absence of a gradient, all spins will precess with the same frequency and phase and so it is not generally possible to determine if/how the signal varies across image voxels. By applying magnetic field gradients along the x, y and z axes,

17

it is possible to gain 3D spatial information in order to reconstruct an image from the MR signal [23]. Arrangement of surface coils can be used to encode additional spatial information; however such parallel acquisition techniques are beyond the scope of this thesis.

MR signals can be represented as either a function of frequency or time. Signal oscillations are recorded over time, which represent many different frequencies, each different frequency corresponding to a different spatial location. Frequency and time hold a reciprocal relationship, such that a Fourier transform (FT) can translate MR signal from the frequency domain to the time domain.

2.4.8 Slice Selection

To excite an image slice, rather than the entire sample, a magnetic field gradient is applied along the z-axis (G_z) so that the Larmor frequency now varies with z. The RF pulse used has a narrow frequency bandwidth so that only a limited range of frequencies ($\Delta\omega$) are excited. From Figure 2-11 it can be seen that an RF pulse of bandwidth $\Delta\omega$ selects a slice of width Δz, perpendicular to the z-axis, where

$$\Delta\omega = \gamma G \Delta z \qquad\qquad \textbf{2-29}$$
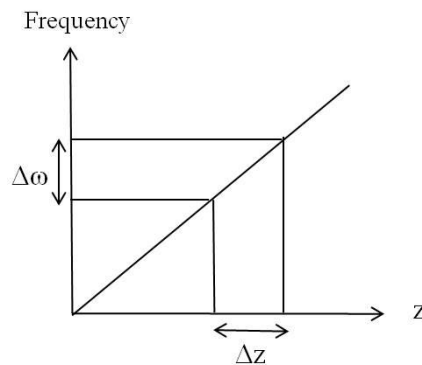
Figure 2-11) Applying an RF pulse of finite duration along the z-axis excites a narrow range of frequencies Δω corresponding to a slice width Δz.

An RF pulse of a single carrier frequency is convolved with a sinc function ($\sin(x)/x$), such that the FT of the product is a boxcar (Figure 2-12) with non-zero values across a bandwidth $\Delta\omega$. However, the RF pulse is of a finite length and so the sinc function must be truncated, meaning the boxcar is less well-defined but

18

remains a sufficient approximation. Slice thickness is defined by the amplitude of the gradient, G or, the RF bandwidth $\Delta\omega_0$. Multi-slice acquisition is achieved by applying sequential RF pulses of bandwidth $\Delta\omega$ with different carrier frequencies, ω_0.
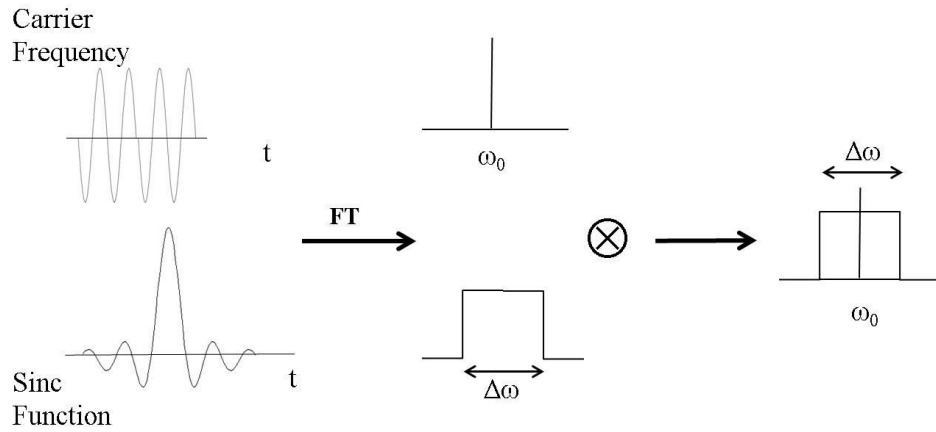
Figure 2-12) Convolution of the Fourier Transformed (FT) RF pulse with a truncated sinc function (with defined carrier frequency, ω_0 to excite a narrow width of frequencies $\Delta\omega$) will produce a boxcar of non-zero values and when in the presence of a linear gradient will produce a square slice profile.

2.4.9 k-space

k-space is a two or three dimensional array of spatial frequencies. The frequency array arises from the combined effects of magnetic field gradients (along their respective axis) which have accumulated between the initial excitation pulse and the readout pulse. If the readout occurs at time t', k-space coordinates from a two-dimensional array can be defined as:

$$k_x(t') = \int_0^{t'} \gamma G_x(t)dt \,.$$
2-30

From Equation 2-30 it can be seen that the location of a data point within k-space is determined by the gradient strength and duration. By applying a combination of gradients along the x axes, k-space can be traversed and a series of data points

19

sampled. An object at a particular position in a gradient will produce a signal which varies sinusoidally in k space at a frequency which depends on its position. The k_x coordinates represent spatial frequencies (typically measured in mm^{-1}) i.e. the rate at which signal phase will change as a function of position. A similar approach can be taken in the other two spatial dimensions.

The centre of k-space stores low spatial-frequency information such as overall shape and image contrast. High frequency information is stored on the edge of k-space, encoding information such as edges. This highlights the need for an image to be reconstructed from as much of k-space as possible in order to increase the image spatial resolution. In the simplest of image acquisitions, one line of k-space is acquired following an RF pulse in each repetition time (TR), however there are many different methods to fill k-space. The main pulse sequence used in this thesis is Echo-Planar Imaging (EPI) technique, more details of this method are provided in section 2.4.12.

The matrix size and sampling of k-space will determine the field of view (FOV) and spatial resolution of the image. FOV is the inverse of Δk, in both x (frequency encoding) and y (phase encoding) directions. The spatial resolution is the inverse of the maximum spatial frequency, such that for a standard symmetric array, spatial resolution = FOV/matrix size.

2.4.10 Frequency encoding

To gain spatial specificity beyond the slice/volume of spins which have been excited, it is necessary to use frequency encoding (FE) gradients. These are applied after the slice-select gradient. Applying the gradient along the x-axis (G_x), so that G_x varies with x, further spatial localisation is gained by separating out the signal frequencies.

2.4.11 Phase encoding

With a third magnetic field gradient, applied along the y-axis, spatial localisation can be extended across 3 dimensions. After the application of G_y, the phase varies linearly along the y-axis. By applying G_y for a short period of time after slice

selection but prior to the readout gradient each line of k-space has a different phase/frequency combination. Whilst the work in this thesis uses 2D MRI techniques, it is worth noting that in 3D imaging, phase encoding is applied along a third dimension in relation to the frequency and phase encoding directions used in 2D imaging.

SENSE

Parallel imaging uses array receive coils to allow the acquisition of fewer lines of k-space in order to reduce acquisition time, which in the case of echo planar imaging (EPI, see Section 2.4.12) reduces image artefacts. If the distance between each line of k-space is increased but the maximum value held constant (resolution unaltered). Reducing the number of acquired lines decreases k_y resulting in reduced FOV and image aliasing (see section 2.4.13), where the image is folded over such that signal is no longer encoded to spatially distinct k-space coordinates.

Sensitivity Encoding (SENSE) is a common method of parallel imaging [24] which is implemented on Philips platforms. By using a receive coil with multiple receive elements (8/32/32 channels at 1.5/3/7 T respectively), the ambiguous spatial encoding can be resolved using the unique signal sensitivity profile of each coil. A reference scan is acquired prior to the main imaging sequence, so that the sensitivity for each separate receive element can be mapped. The amount that k-space has been reduced by is defined as the SENSE factor and this is limited by the number of receive elements and their geometry.

2.4.12 <u>Imaging Sequences</u>

<u>Gradient Echo</u>

In a basic gradient echo (GE) sequence, only one line of k-space is acquired from each RF pulse. Each repeat has a different k_y encoding and so in this way k-space can gradually be acquired (Figure 2-13). The transverse magnetisation must recover between each RF excitation and so the basic GE sequence is time-consuming.

k-space is acquired by initial application of a negative frequency encoding gradient (G_x) and phase encoding gradient (G_y) for time T, which dephases spins (Figure 2-14). Subsequently, a positive G_x is applied for time 2T, which acts to first re-phase the spins, creating an "echo". As the switch in gradient polarity does not move the spins into another plane, the same static (T_2) and time-variant (T_2') field changes are experienced and so GE is sensitive to both effects and so T_2^*.
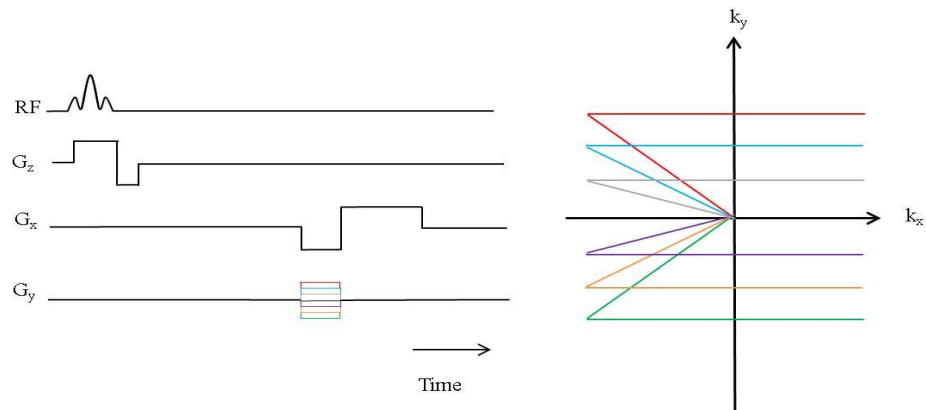
Figure 2-13) Pulse sequence diagram and k-space trajectory for standard 2D gradient echo (GE). In each TR a single line of k-space is acquired.
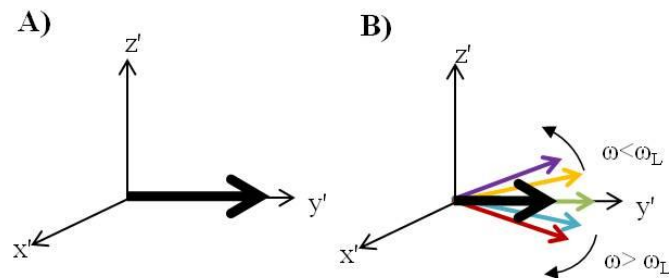
Figure 2-14) Schematic of net magnetisation in basic Gradient Echo (GE) sequences. A) Net magnetisation is moved into the transverse plane by the excitation pulse. B) Net magnetisation in the transverse plane decreases as spins dephase. Reversing the polarity of the frequency encoding gradient rephases the spins magnetisation in the transverse plane is restored at the centre of the second frequency encoding gradient. And net

Echo Planar imaging

Echo Planar Imaging (EPI) is a technique developed at The University of Nottingham by Mansfield et al [25]. By acquiring multiple lines of k-space in a single TR, EPI rapidly reduces the acquisition time of an image. With increased temporal resolution it is possible to image dynamic processes such as the cerebral haemodynamic response function (HRF) in functional MRI (fMRI) which is on the order of seconds (See Chapter 3).
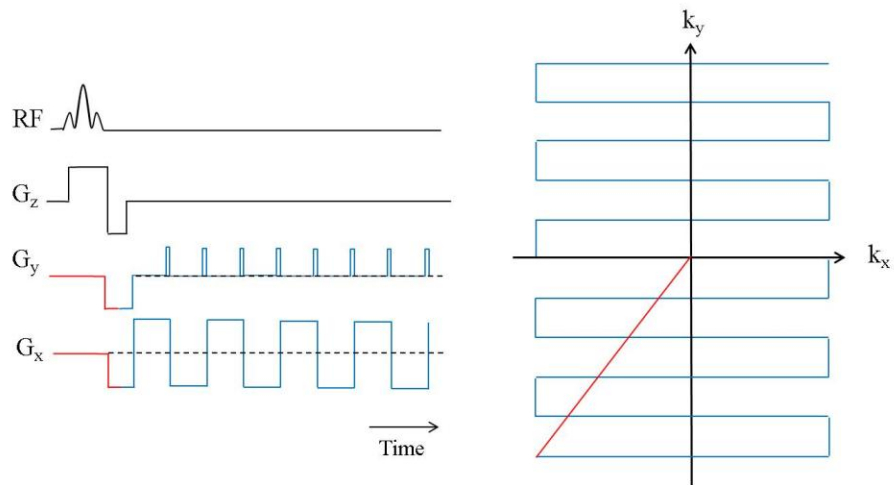

Figure 2-15) Pulse sequence diagram and k-space trajectory for 2D echo planar imaging (EPI).

Figure 2-15 shows the basic pulse sequence and k-space trajectory in 2D-EPI. By rapidly switching the frequency encoding gradient (G_x), each alternating line of k-space is traversed in an opposing direction. The read-out moves between lines by a small step in k_y after each line is acquired. Alternate lines of k-space must be time-reversed prior to Fourier transformation to correct for opposing acquisition directions. EPI can be either single shot (full acquisition of k-space in a single TR), or segmented, where a sub-set of lines of k-space are acquired in each shot.

Double echo (DE) EPI can be implemented whereby a second set of gradients are applied after the first EPI train, at a later TE (Figure 2-16A). This allows k-space to be sampled a second time without the need for a second excitation pulse [26]. Multi-echo EPI can be achieved by increasing the number of gradient repeats even further. This can only be done if there is sufficient signal, but T_2^* is the

limiting factor. As this scheme acquires k-space at subsequently later echo times, it can be used to map T_2^* [27].
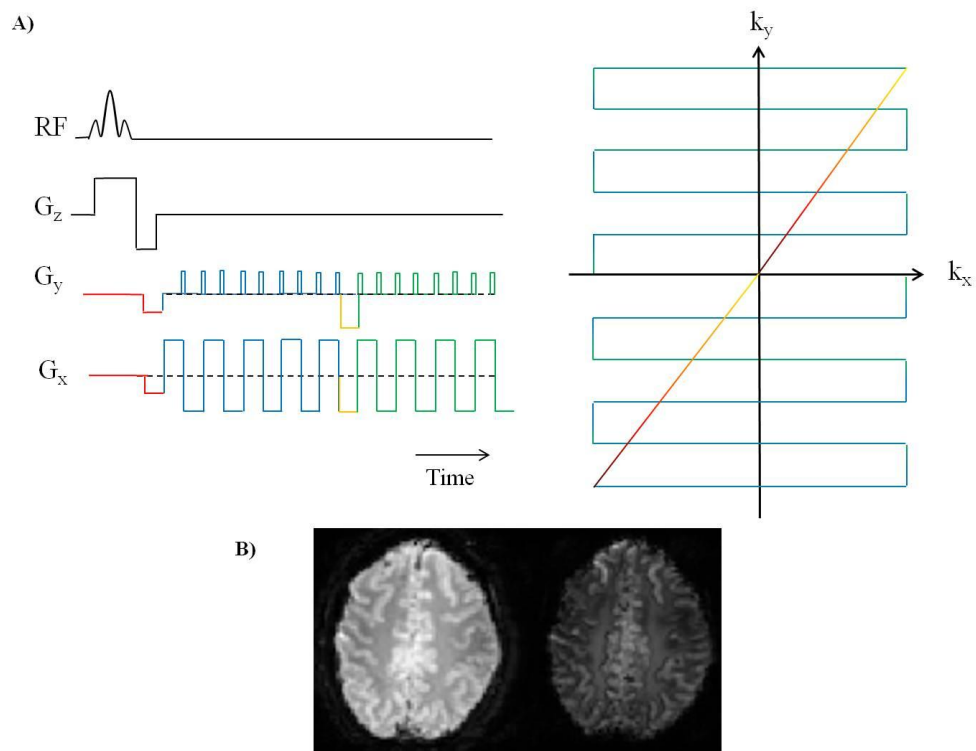
Figure 2-16) A) Pulse sequence and k-space trajectory for double echo EPI. By applying a second set of refocusing gradients at a later TE, k-space can be sampled a second time within the same TE. B) Example Double Echo 2D-EPI images at 7 T (TE$_1$/ TE$_2$/TR = 16/46.9/3000 ms, 2x2x3 mm^3, FOV = 192x192x15 mm, SENSE 2.5)

<u>MPRAGE</u>

Magnetisation Prepared Rapid Gradient Echo (MPRAGE) is a T_1-weighted pulse sequence commonly used for anatomical images in neuroscience. This pulse sequence usually has a short TR and so an initial 180° inversion pulse is applied to control T_1-weighting prior to the excitation RF pulse (Figure 2-17), with contrast dependent on the time between the inversion, the centre of k-space and the readout pulses. MPRAGE is a rapid acquisition method, developed from Turbo Fast Low Angle Shot (TurboFLASH) and so has a short TR which may not allow sufficient time for all transverse magnetisation to decay. To overcome this

problem, RF or gradient spoilers (or both) can be applied before each subsequent excitation pulse. The longitudinal magnetisation is preserved by using small flip angles of typically less than 8°.
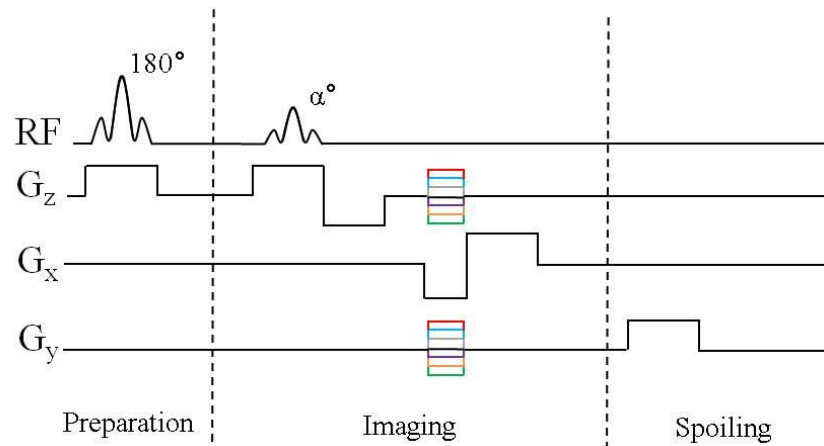
Figure 2-17) Pulse sequence diagram for anatomical imaging sequence Magnetisation Prepared Rapid Gradient Echo (MPRAGE). During the preparation step, an inversion pulse is applied to control T_1-weighting. In the spoiling step, remaining transverse magnetisation is dephased prior to the next RF pulse. Multiple imaging and spoiling steps can be performed for a single preparation step.

2.4.13 <u>Image Artefacts</u>

Image artefacts can be a regular occurrence attributable to many different factors such as operator error, parameter choice or the presence of metallic objects. This section will focus on the main types of artefacts which are common in MRI.

The Nyquist ghost (or N/2) is a common artefact in EPI, whereby a ghost image is overlaid on top of the actual image, but shifted in the phase encoding direction by half of the FOV (N/2). It is caused because the alternating direction of k-space trajectory may have systematic errors in the centre of k-space. If k-space lines are acquired slightly off centre, they cannot be perfectly reversed prior to the Fourier Transform.

Aliasing or signal wrap-around is caused when regions outside of the FOV are excited so that the receive coil also detects these unencoded signals. If any

detected frequencies exceed the maximum frequency (f_{max}, determined by the Nyquist theorem) by Δf, then the signal will be encoded in k-space at a location $f_{max} - \Delta f$. This results in the signal being wrapped to the opposite side of the image. To minimise the occurrence of aliasing, the FOV can be increased to cover a larger region, however this can reduce the achievable spatial resolution and increase scan time. Depending on the region of interest, surface coils (with higher SNR) help to minimise aliasing as the signal outside the FOV is much lower than with a volume coil. Finally, the signal outside the FOV can be saturated using outer volume suppression techniques in which RF pulses such as rest-slabs are used to suppress signal.

The bandwidth (BW) per pixel relates to the range of frequencies encoded and detected and the frequency of k-space sampling. It is directly related to SNR, which increases as BW decreases. A small bandwidth increases image distortion, described by Equation 2-31 where Δx is the spatial shift in signal encoding and x is the voxel size. This is most problematic in EPI, where the bandwidth is small, particularly in the phase encoding direction.

$$\Delta x = \frac{\Delta \omega}{BW_{per\,pixel}}$$

2-31

An artefact is often seen at boundaries between air and tissue due to the different magnetic susceptibilities (χ). Magnetic susceptibility is a constant which describes how magnetised a material will become in the presence of an external magnetic field. At a susceptibility boundary, there will be a change in local magnetic field which will cause image distortion due to phase changes (and so incorrect sampling of k-space). The presence of a metallic object will create an extreme susceptibility boundary and create a more extreme distortion, albeit far less common due to safety precautions in place.

An image can be distorted at fat-water boundaries due to their different resonant frequencies [28]. The change of frequency is incorrectly attributed to a change in spatial location and so the fat signal is shifted in the frequency encoding direction. In brain imaging, the fat in the scalp can be problematic unless the signal from the fat is suppressed. Suppression is achieved by an inversion or suppression pulse

prior to image acquisition. Commonly employed techniques rely on the selective excitation of fat spins and/or different T_1 times. At higher field strength, SPIR (Spectral Presaturation with Inversion Recovery) is a popular technique which uses a 90° RF pulse to selectively excite fat-bound protons which have a different resonant peak to water protons. As the signal from fat recovers through the null point, the standard MR sequence is collected. Whilst SPIR is advantageous because it does not cause inherent T_1-weighting, it requires good B_0 homogeneity so that the frequency ranges of fat and water are distinct and so a smaller FOV is preferable. SPAIR (Spectral Adiabatic Inversion Recovery) is an adaptation of SPIR which uses a 180° adiabatic to selectively excite the fat-bound protons which reduces the sensitivity to B_1 inhomogeneities. STIR (Short Inversion-time Inversion Recovery) is based on different T_1 times, using a 180° inversion pulse to invert the spins of both fat-bound and water protons. The acquisition sequence is started as the fat signal crosses the null point. Whilst subsequent tissue contrast will be altered, it does not depend on chemical shifts and so is insensitive to B_0 inhomogeneities, therefore it is suitable for lower field strengths and/or larger FOV's. For spin-echo based sequences, slice-selective gradient reversal (SSGR) can be used [29], where the polarity of the 180° refocusing pulse is reversed so that no echo is formed from the fat signal (where displacement of the fat signal relative to water is proportional to bandwidth). It is better suited to high field, where the chemical shift between fat and water are increased and can be combined with SPIR for improved results [30].

2.4.14 Hardware

The majority of MRI scanners use superconducting magnets as they generate larger magnetic fields than permanent magnets. Large currents are sent through magnet coils, and since they are maintained superconductive by liquid helium, the current flows indefinitely. A cryostat and cryocoolers maintain the required low temperature and also prevent boil-off. This thesis presents data collected on 1.5, 3.0 and 7.0 Tesla Philips Achieva whole body MR scanners (Best, Netherlands). Each of these scanners utilises a horizontal bore magnet (schematic shown in Figure 2-18) , which is shielded by an iron box to minimise the extent of the

fringe field and prevent passers-by from experiencing increased magnetic fields and the associated safety risks (see section 2.4.15). A bed can be moved in/out of the cylindrical bore so that the volume of interest can be placed in the magnet iso-centre.
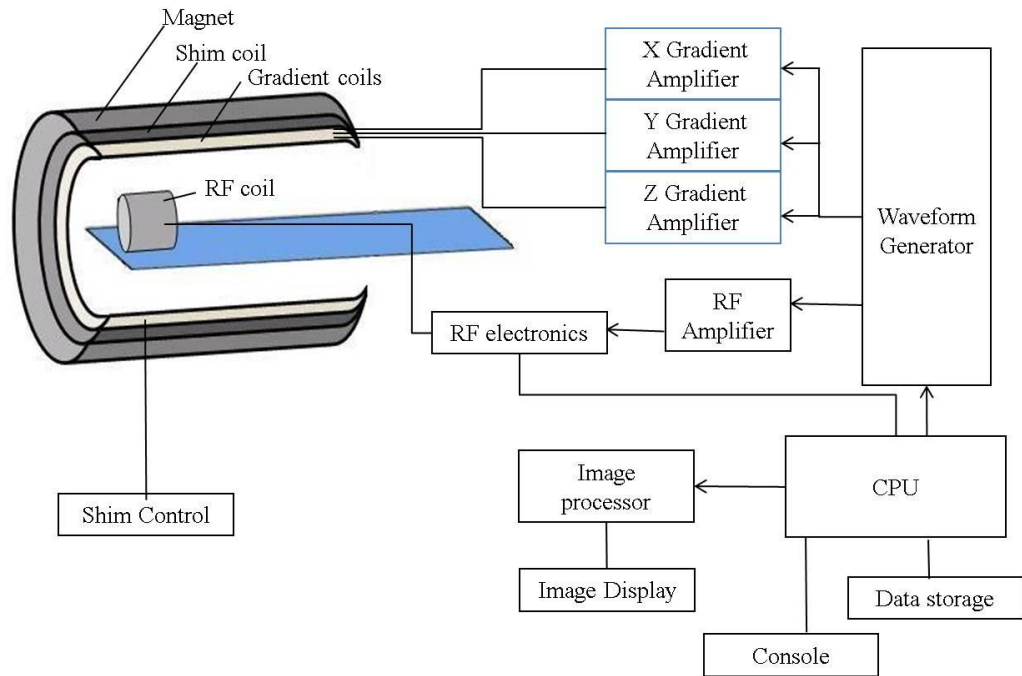
Figure 2-18) A schematic outline of an MRI system.

Gradient coils are used to induce a linear variation in the magnetic field along the x, y and/or z-axis (as described in section 2.4.7). To allow rapid data collection for EPI, the gradient must be able to switch at a high rate. Gradient coils are defined by their maximum amplitude (induced field strength) and slew rate (maximum switching rate). The rapid switching can increase the temperature by resistive heating, and so gradient coils are typically water-cooled.

In order to image over a large volume, the magnetic field (static B_0) must be spatially homogenous. The method of detecting and correcting any inhomogeneities is called shimming. Both passive and active shimming techniques are used. Passive shimming is done using ferromagnetic blocks which are inserted into the magnet bore after installation and aim to minimise the residual between expected and observed magnetic field [31]. Active shimming passes current through shim coils (Figure 2-18) to correct for any field inhomogeneities. For first

order shimming, pencil beam excitations are made at 2 echo times along the x, y and z axes. The phase difference between the two echo times is proportional to B_0 inhomogeneity and ΔTE. Thus the field offset can be calculated and distortions corrected for. For second order shimming, excitations are also made along the z^2, zx, zy, xy and x^2, y^2 axes). FASTMAP [32] is an active technique which can be automatically implemented by the scanner. The magnetic field is sampled and corrected, in around 3-4 iterations, taking approximately 20 seconds. Although FASTMAP offers a rapid robust shimming technique, image-based shimming methods have been shown to be preferable at 7 T [33] and have been employed in the ultra-high field work presented in this thesis. At the start of each scan session, a B_0 map is taken prior to the main scan which is used to strip the skull and create a brain mask. Shim coils are used to eliminate field inhomogeneities from inside the mask [33].

A radiofrequency (RF) transmit coil generates the field perturbation (B_1) required to excite spins and tip the longitudinal magnetisation into the transverse plane (Section 2.2.3). In the 1.5 and 3.0 T Philips Achieva systems, a body transmit coil is situated at the innermost layer of the scanner bore. In the 7.0 T system, a head volume transmit coil is used. Whilst surface coils exist, volume coils transmit and receive homogenous signal over a relatively large volume and so only volume coils are used in the scope of this thesis.

For MRI of the brain, RF receive coils (which detect MR signal) are usually situated close to the subject's head, as coil sensitivity reduces with distance. The receive coil generally has multiple receive elements which reduces scan acquisition time if they can be used with acceleration methods such as SENSE (Section 2.4.12). The receive coil is gated off during RF transmission as the excitation pulse from the transmit coil is on the order of kilovolts, whilst the received signal is on the order of millivolts.

Since the detected signal does not provide information on whether the change in phase is positive or negative (i.e. whether precession is clockwise or anticlockwise) relative to the rotating frame, a quadrature detection coil solves this problem by detecting two signals 90° out of phase (one real, one imaginary).

The scanner console is used to set up the scan sequence parameters and enter subject identification details etc. The console calculates the required waveforms and RF pulses and sends these to the waveform generator as a digital signal (Figure 2-18). The digital signal is converted to analogue, amplified and sent to the relevant coil. After being received, the signal is converted back to digital and reconstructed to an image by the image processor. The console is also responsible for monitoring safety aspects such as the gradient temperature and specific absorption rate (SAR) see section 2.4.15.

2.4.15 <u>Safety Considerations</u>

Static magnetic fields can pose a number of safety risks. Firstly, magnetic objects will be attracted towards the scanner bore with significant force. Projectiles pose a serious risk of both injuring people and damaging the scanner and care should be taken not to take any magnetic objects within the magnet hall, this includes chairs, the patient trolley and standard fire extinguishers (extinguishers in the near vicinity of the scanner are non-magnetic). Subjects must fill in a safety screening questionnaire prior to entering the scanner control room and those who have contraindications such as pacemakers (which may malfunction in the presence of magnetic fields), aneurysm clips or dental implants will not be allowed beyond the 5 gauss line (0.5 mT). All persons who are to be in close vicinity to the scanner must remove any magnetic items from themselves (e.g. coins or bank cards in a pocket). Safety screening also minimises any potential risk of thermal burns, by identifying any metallic objects which may interact with the RF field (see below).

RF radiation has the potential to cause thermal burns. Tissue which is not well perfused is of greater risk as increased heat is dissipated via blood flow. This deposition of power is known as the specific absorption rate (SAR), measured in watts/kilogram and is dependent on such things as pulse sequences, body mass and coil configuration. This rate is monitored so that core body temperature does not increase by more than 1°C (International Commission on Non-ionising Radiation Protection guidelines, 2004).

RF radiation can also cause thermal burns via the heating of electrical conductors, which absorb heat until they are dangerously hot. This risk is minimised by ensuring that the subject does not have any metallic objects on their person and a full screening to ensure they have no metallic implants. This risk extends to tattoos, where the metallic dye in older tattoos may lead to heating effects and risk burning. When objects which pose a potential risk are present in the magnet bore, e.g. the vector cardiogram (VCG) box and leads, insulating padding is used to minimise direct contact with skin. Thermal burns may also be induced by circulating currents through body parts such as crossed arms and feet, so patients are instructed not to do this.

Subjects may suffer temporary discomfort whilst moving through the static field, including dizziness, sickness, headaches and a metallic taste in the mouth. Care is taken to move the scanner bed in/out of the magnet at a slow rate to minimise these effects induced by crossing a number of magnetic fields in quick succession. Similarly, staff should take care when changing coils or other such maintenance to avoid these effects.

In case of emergency, a scanner can be quenched, whereby the helium is dispersed, resulting in a loss of superconductivity. A build-up of heat induces resistance in the magnet coil and the magnetic field is ramped down. This presents a safety risk to anybody in the vicinity as if the helium is inadvertently allowed to enter the room, oxygen levels may be reduced and so an oxygen depletion alarm is installed in the scanner control room. It is likely that a scanner will be damaged if quenched, and it will take significant time to ramp back up to the required magnetic field, therefore it is only performed if someone is in immediate danger. Risks associated with the handling of the super-cooling liquefied gases (cryogens) are minimised by all users receiving appropriate training as well as the wearing the appropriate protective clothing such as a mask and gloves.

There is a considerable amount of acoustic noise associated with MRI due to the rapid switching of magnetic gradient coils. All subjects must wear sufficient ear protection to limit acoustic exposure and maintain patient comfort. At 1.5 and 3.0 T, this protection comprises of earplugs and headphones. At 7 T (where there is

less space within the head coil), earplugs and foam padding are used. Rapid switching of gradients may cause peripheral nerve stimulation (PNS) where subjects may feel a twitching sensation, particularly in their extremities, due to induced currents along nerves. Staff should be aware of this issue and effort should be taken to minimise these effects when deciding on a scan protocol. For safety, a maximum slew rate is set. For the scope of this thesis, slew rates used were 160, 200 and 166 mT/m/s at 1.5, 3.0 and 7.0 T respectively. Rapid switching of gradient sets can induce mild heating of tissue via increased absorption of energy.

Whilst in the scanner, subjects should always have access to the emergency alarm, which is to be tested prior to each scan. If a patient raises the alarm and needs to be removed from the scanner as a matter of emergency, the scanner bed may be undocked and removed from the magnet hall where they can then be transferred to the patient trolley. In the event that emergency services are required in the scanner hall, a member of staff must wait at the entrance in order to ensure no magnetic items are to be brought near the scanner. A coded door prevents unauthorised access to the scanner control room.

In the case of an adverse effect whilst scanning, staff must document it on the scanning record, which is to be completed for each scan and also provides details on staff exposure to high magnetic field strength. Staff exposure is limited so as not to exceed the International Electrotechnical (IEC) guidelines.

2.4.16 Ethics

All human studies require prior approval from an ethics boards to ensure approval guidelines are in place. The University of Nottingham has its own ethics committee which oversees such protocols, and all research presented in this thesis was carried out with full ethical approval.

All volunteers gave informed written consent prior to taking part in the studies. The consent forms require the volunteer to advise the experimenter on which course of action to take should an abnormal finding occur. In such a case, the

image(s) is sent for review by a radiologist, with the subjects informed of the results only if prior consent is granted.

3 Functional neuroimaging methods

3.1 Outline

The primary goal of functional neuroimaging is to develop more detailed knowledge of the workings of the brain. By understanding normal brain function, neurological dysfunction can be better interpreted, improving diagnosis and treatment outcomes. The first real insight into the link between brain structure, function and behaviour came from cortical lesion studies. However, the advent of neuroimaging technology allowed brain function to be investigated relatively non-invasively. This chapter provides a basic introduction to cerebral vasculature and physiology, before introducing a range of widely used functional neuroimaging techniques. Focus will be given to the MR techniques used in this thesis; blood oxygen level dependent (BOLD) fMRI, arterial spin labelling (ASL), phase-contrast MRI (PC-MRI) and magnetoencephalography (MEG). Attention is paid to how the physiological and biophysical processes which accompany brain activity can be measured. This lays the groundwork for the experimental work in Chapters 4-6 in which such responses are evaluated and quantified.

3.2 Cerebral vasculature

The human brain is a complex structure, accounting for only 2 % of body weight, yet consuming around 20 % of oxygen intake and 15 % of blood flow. Its structure is comprised of grey matter (cell bodies), white matter (cell fibres), cerebrospinal fluid (CSF) and blood vessels. The brain surface, or cortex, is highly folded; increasing the surface area and enabling higher cognitive function. The folds (gyri) and accompanying grooves (sulci) are useful in identifying landmarks in the brain. Brain regions can be fundamentally separated into the cerebrum (with left and right hemispheres), cerebellum and brainstem. The cerebrum is further divided into the frontal, parietal, temporal and occipital lobes; each with a

core set of functions. Sub-cortical structures are generally responsible for relatively autonomous functions; such as homeostasis, hormone production, circadian rhythm. However, as the quantification of the haemodynamic response is a central theme of this thesis, it is the cerebral vasculature which will be discussed in more detail.
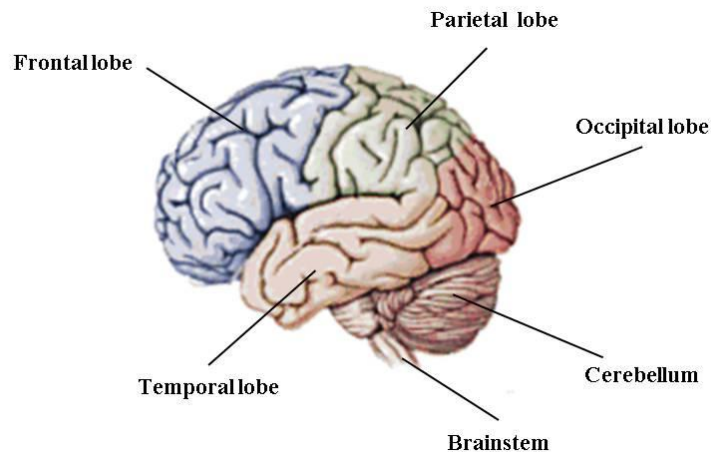
Figure 3-1) Schematic representation of the basic structures of the human brain (shown for a single hemisphere) adapted from [34]. Sub-cortical regions are found beneath the cortical lobes.

The vascular network consists of macrovasculature (arteries and veins) and microvasculature (arterioles, venules and capillaries). Figure 3-2 is a schematic of a capilliary network, taking oxygenated blood (red) from a high pressure artery to the tissue, to deliver the required oxygen and nutrients, and removing waste products via deoxygenated blood (blue) in the low-pressure venous system. Capillaries therefore carry a mixture of oxygenated and deoxygenated blood depending on their position in the vascular network (where normal oxygenation levels are ~95-98 % for arteries, reducing to ~60-80 % for veins). Cerebral capillaries differ from those found in the rest of the body, with their endothelial lining constructed to increase the number of tight junctions. This restricts the passage of molecules from the general circulation into the brain, allowing small useful molecules in, whilst preventing larger harmful molecules and bacteria, from entering [35]. Essential nutrients such as glucose and amino acids have specified pathways, whilst oxygen (O_2) and carbon dioxide (CO_2) can freely diffuse [36].
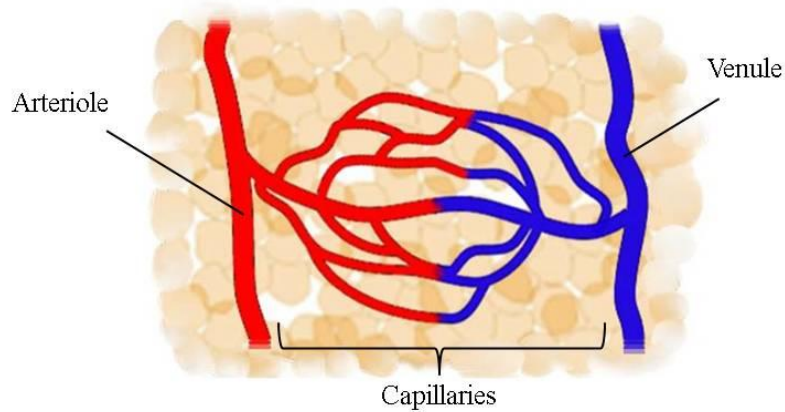
Figure 3-2) Schematic of a cerebral capillary network. Oxygenated blood (shown in red) moves from the arterial side across the capillaries where oxygen and nutrients are delivered to tissue. Deoxygenated blood (blue) and waste products are taken away from the tissue via the venous system.

Approximately 80 % of the arterial network supplying the brain branches from the common carotid artery. It ascends within the neck before bifurcating at the carotid body (approximate to the C3 vertebra) to give rise to the left and right interior and exterior carotid arteries (ICA, ECA respectively). The ICA supply intracranial regions, whilst the ECA supply the face and neck [37]. The ICA divides into the anterior common arteries and the middle cerebral arteries, the ACA from the left and right ICA are joined via the anterior communicating artery. The remaining arterial blood supply is from the left and right vertebral arteries (VA), stemming from the subclavian artery. The VA fuse to form the basilar artery (at approximately the pons level) which splits into the left and right posterior cerebral artery (PCA) and posterior communicating arteries. Figure 3-3 shows schematically how these vessels are linked together, forming the Circle of Willis. The Circle of Willis provides collateral circulation, ensuring adequate blood supply in the event of vascular blockage or degradation.
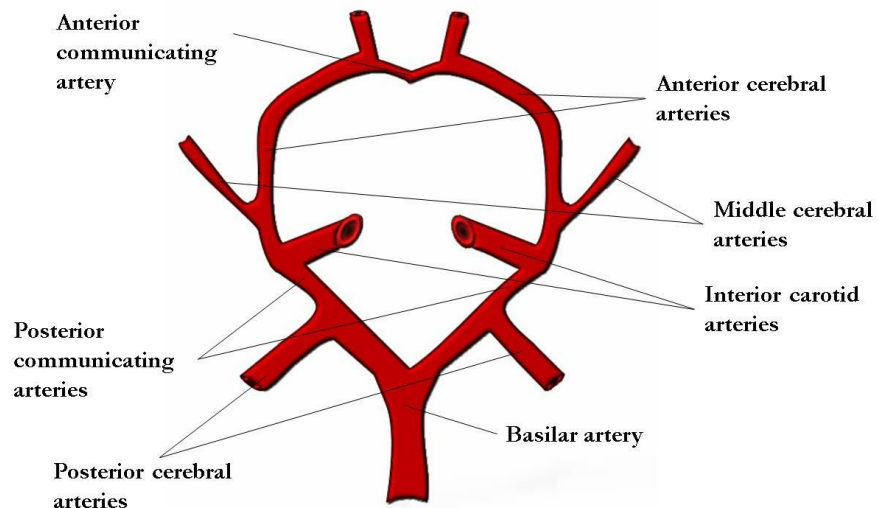
Figure 3-3) Schematic[*] of the main arteries forming the Circle of Willis, a key part of the cerebral arterial network, creating collaterals which ensure adequate blood supply to the brain in case of arterial stenosis or blockage. [*] Not to scale

The venous system can be divided into the deep and superficial vascular systems. Pial veins drain the outermost regions of the brain, feeding into the superior cerebral veins (draining the superior cortical regions) and eventually feeding into the superior sagittal sinus. Deeper cortical veins drain the sub-cortical regions into the lateral, straight and sigmoid sinuses [37]. Both systems drain into the internal jugular vein which descends in the neck. Veins in the head and neck differ to those throughout the rest of the human body in that they do not require valves due to their downwards draining nature which is in this case assisted by gravity.

3.3   Functional MRI

The notion that neural activity is accompanied by a regional increase in cerebral blood flow (CBF) was first introduced in the late nineteenth century [38]. With the development of positron emission tomography (PET) in the 1970's came a quantitative method of measuring regional blood flow and O_2 [39, 40]. MRI was primarily a structural technique until the widespread uptake of EPI, which allowed "snapshots" of biological processes [41]. A dynamic technique coupled with the discovery that the oxygenation level of blood acts as an intrinsic contrast agent in

MRI (the BOLD signal) [42] led to the development of functional MRI (fMRI). The advent of fMRI expanded the use of MRI to assess physiological changes associated with neuronal activity.

The BOLD response (described in detail in Section 3.3.1) relies on the spatial and temporal relationship between neuronal activity and CBF, a relationship better known as neurovascular coupling [43]. Neurovascular coupling is a complex process, and the BOLD signal is actually determined by the dynamic interplay of cerebral metabolic rate of oxygen ($CMRO_2$), cerebral blood volume (CBV), CBF and neuronal activity.

Figure 3-4 provides a schematic indication of how the BOLD response arises from the interaction of these physiological mechanisms. Shortly after the BOLD response was identified, multiple research groups observed an increase in BOLD signal in response to both visual activation [44-46] and a motor task [47]. This identified a potential role of the BOLD response in mapping functional brain activity.
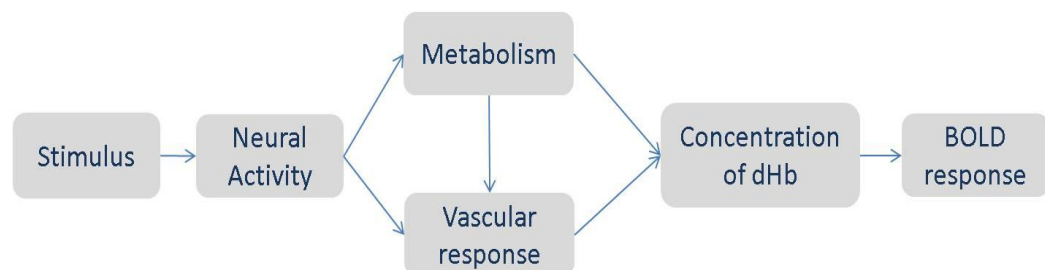

Figure 3-4) A schematic overview of the competing physiological mechanisms contributing to the BOLD response following a stimulus.. The positive BOLD response is robust and is used regularly to infer neuronal activity.

3.3.1 The BOLD response

Blood is the transport medium providing nutrients to tissue via the vascular network. Around 45 % of human blood is red blood cells (RBC), the remainder made up of plasma (a straw-coloured liquid), white blood cells and platelets.

Although it is water-bound protons which are crucial for MR signal generation, the RBC play a fundamental role in fMRI. Their biconcave disc shape is optimised to transport oxygen (O_2) from the lungs to the rest of the body and return carbon dioxide (CO_2) for excretion from the lungs to the atmosphere. There are 5×10^{12} RBC per litre of blood, each cell containing 280 million haemoglobin (Hb) molecules. Hb is made up of four polypeptide chains, each attached to an iron-containing haem group which reversibly combines with an O_2 molecule, such that each haemoglobin molecule can carry up to four O_2 molecules. In the oxygenated state, Hb is referred to as oxyhaemoglobin (HbO_2) and deoxyhaemoglobin (dHb) in the fully or partially deoxygenated state. Approximately 95-98% of Hb in arterial blood is in the HbO_2 form, whilst in the veins this is reduced to around 60%. This is generally described as the blood oxygenation (Y).

$$Y = \frac{HbO_2}{HbO_2 + dHb}$$

3-1

A crucial factor in the BOLD signal is that dHb and HbO_2 have different magnetic susceptibilities ($\Delta\chi$). Whilst HbO_2 is weakly diamagnetic ($\Delta\chi_{HbO2} = -0.26 \times 10^{-7}$), dHb is paramagnetic ($\Delta\chi_{dHb} = +1.57 \times 10^{-7}$), both with respect to water [48]. It follows that when blood is deoxygenated, the magnetic field will be perturbed as the water-bound protons in both the blood and surrounding tissue will experience increased dephasing. This forms the basis of the intrinsic T_2^* contrast mechanism known as the blood oxygenation level dependent (BOLD) response. However, there are some counter-intuitive physiological changes which underlie the BOLD response.

Ogawa et al. [1] discovered it was possible to measure the effect of a change in blood oxygenation on the MR signal of blood and surrounding tissue, with T_2^* increasing with increasing oxygenation. It was shown that the BOLD signal

increased in response to functional activation [44-47], suggesting that neuronal activity leads to a counter-intuitive increase in oxygenation.

Given a task, neural tissue becomes more active and so energy demand increases. Adenosine triphosphate (ATP) is an energy source for many processes within the brain and body, in particular re-establishing ionic gradients across cellular membranes following action potentials. ATP synthesis occurs in the mitochondria, and is necessary to allow repeated action potentials and thus neural activity. O_2 (in addition to glucose) is an essential substrate for ATP synthesis and so ATP metabolism is tightly coupled to O_2 metabolism in the healthy brain [49]. Studies show that measurements of $CMRO_2$ correlate with measurements of ATP synthesis [50, 51] which in turn is equal to ATP metabolism, a relationship unique to the brain [52]. Aerobic ATP synthesis is much more efficient than anaerobic (glucose-based) synthesis and so O_2 consumption is assumed to be more closely linked to neuronal activity than glucose consumption (this assumption will be discussed further in Chapter 4).

In order to meet this increased demand for O_2, a corresponding increase in cerebral blood flow (CBF) is observed, termed functional hyperaemia. The increase in CBF has been found to surpass the increase in $CMRO_2$ by as much as 50% [53, 54]. Multiple theories have been proposed as to why the relative increase in CBF is so large. The oxygen limitation model [55] proposes that only a small amount of O_2 delivered to the tissue is extracted from the blood and that by increasing CBF the amount of O_2 extracted (oxygen extraction fraction, OEF) actually decreases due to a decreased capillary transit time. Within this model, a large increase in CBF is required to support a small increase in $CMRO_2$ [56]. Following activation, the sudden influx of oxygenated blood causes the BOLD signal to increase. Figure 3-5 shows a typical BOLD response where a positive overshoot can be observed around 6 seconds after activation. The increased CBF is accompanied by an increase in the cerebral blood volume (CBV) as the two are interrelated. An increase in CBV increases the fractional volume of both arterial and venous blood within a voxel (and so also reduces the fraction occupied by tissue and CSF). Increasing the blood fraction means that more dHb is present and so field perturbations will be increased, attenuating the BOLD signal. This

actually counteracts the effect of increased oxygenation observed on activation. Although these physiological changes are well reported, their causative mechanisms are not yet fully understood. Whilst the BOLD response is associated with the venous and deoxygenated capilliarial networks, it is thought that it is the arterial dilation that drives an increase in CBV and CBF [57-60] rather than venous dilation [55]. CBV transients are thought to explain the post-stimulus undershoot (PSU) in signal which is often seen following the positive overshoot of the BOLD signal (Figure 3-5).
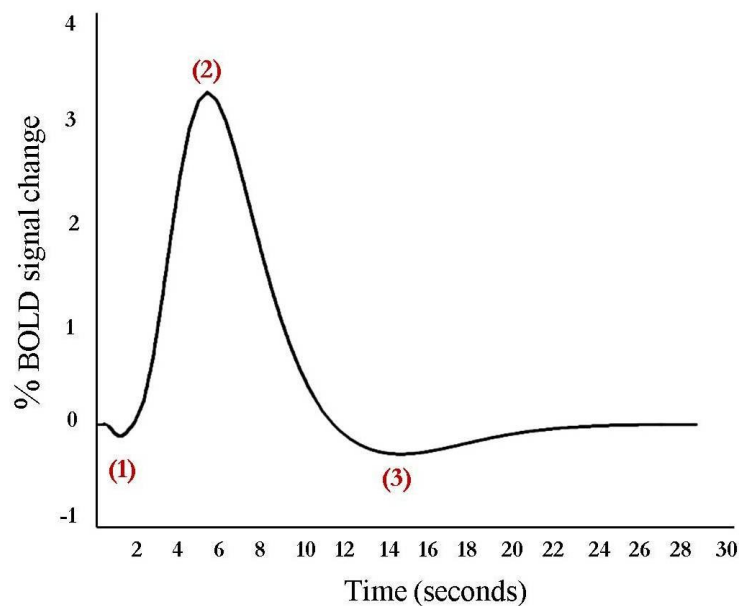
Figure 3-5) Schematic of the BOLD timecourse. An initial dip (1) below baseline has been reported within 2 seconds of stimulus presentation, followed by a positive overshoot (2) at around 6 seconds. The BOLD signal is slow to recover to baseline, a post-stimulus undershoot (3) is observed, returning to baseline at around 25-60 seconds after stimulus presentation.

There are three main mechanisms proposed to explain the origin of the PSU. Firstly, a decoupling between cerebral blood flow (CBF) and cerebral blood volume (CBV) as proposed by the balloon model [61] and Windkessel model [62] whereby CBV remains elevated once CBF and blood oxygenation has returned to baseline. Secondly, a decoupling between haemodynamics and metabolism [63, 64], where elevated $CMRO_2$ (but normalised CBF and CBV) leads to a reduction

41

in deoxyhaemoglobin (dHb) concentration. Finally, a decrease in post-stimulus CBF has been observed [54, 65, 66] but it has been argued that this may be an artefactual contribution from the BOLD response [67]. It is likely that more than one mechanism contributes to the PSU and there is a need to elucidate the relative contribution of each mechanism.

There have been some reports of a temporal lag between the increase in $CMRO_2$ and corresponding increase in CBF and CBV. This is thought to give rise to the "initial dip" [68], a drop in BOLD signal which occurs shortly after the stimulus (Figure 3-5) and is thought to reflect a drop in HbO_2. There has been much of research interest in the initial dip as it is thought to have increased spatial localisation to the site of neuronal activity than the positive BOLD response [69]. In this short period, it may be possible to characterise $CMRO_2$ changes without confounding effects of CBF and CBV. However, the initial dip is elusive, so much so that its existence has been debated [70-72]. Whilst the initial dip has been observed with optical imaging techniques in animals and humans [E.g. 68, 73, 74], it has proven difficult to reliably and repeatedly extend to humans at the field strengths using MRI.

3.3.2 <u>fMRI data analysis</u>

fMRI experiments take the form of either a block design (stimuli repeated continuously over a longer time period) or event-related paradigm (a single short stimulus) as shown in Figure 3-6. To increase the signal to noise ratio (SNR), stimuli are presented multiple times with rest periods between which allow the haemodynamic response to recover to baseline. If stimuli are presented very close together, with a short rest period, the BOLD response will plateau.
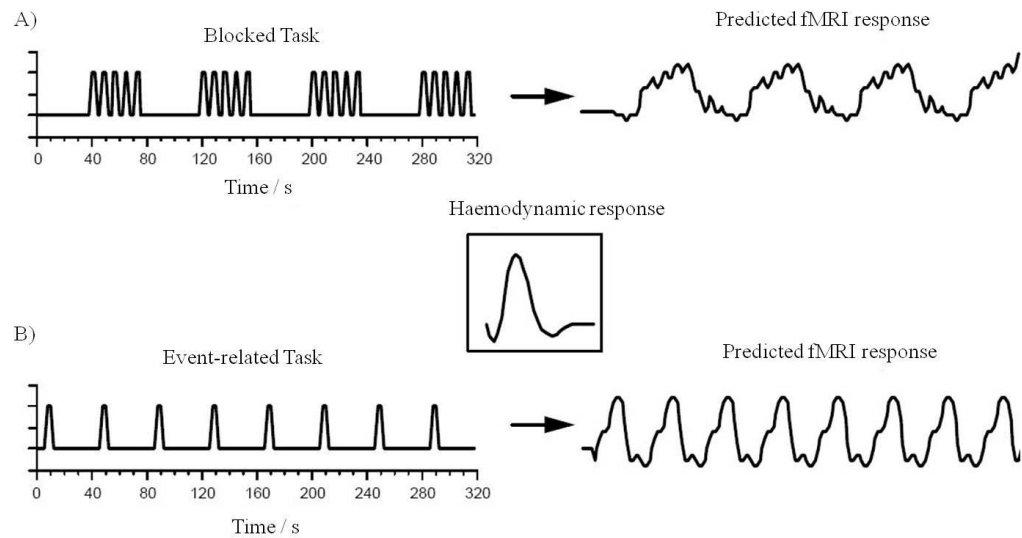
Figure 3-6) A) In a block design paradigm a stimulus is presented continuously for a period of time, which is then alternated with a rest period. B) An event-related paradigm consists of presentation of a single short stimulus followed by a rest period.

Analysis of fMRI data areimproved by a series of pre-processing steps, which will be briefly described here and later outlined in more detail when used in the experimental work in this thesis. Here, pre-processing is described within the context of the FMRIB Software Library (FSL, Oxford, UK), although the underlying theory is similar across platforms. Due to the fine spatial resolution used in functional MRI, even subject motion of a few millimetres or rotation of a few degrees can result in the same voxel corresponding to a different spatial location across image volumes/dynamics. This change in signal intensity can be larger than the BOLD effect and so be very problematic in analysis of functional data. In this thesis, motion correction ensures that the spatial location of voxels is consistent across dynamics and any movement artefacts that have occurred are minimised or removed. Here, motion correction is implemented using MCFLIRT (FMRIB, Oxford, UK), this software compares the similarities between a "reference" image (here chosen to be the first dynamic) and subsequent images [75]. Using a cost function, 6 rigid-body parameters are minimised (translation in and rotation about x, y and z directions), and a corrective translation matrix is created. This translation matrix is then applied to each subsequent dynamic (here

double echo fMRI data are collected, and the corrective translation matrix also applied to the data set acquired at the second echo time) using tri-linear interpolation.

Spatial smoothing uses a Gaussian smoothing kernel to average the signal from neighbouring voxels. Spatial smoothing improves the signal-to-noise ratio (SNR) but at the cost of reducing the image spatial resolution. The FWHM of the kernel must not be too large so as to prevent image blurring; typically 1.5-2 times the voxel size is used.

Temporal filtering reduces noise (thus increasing SNR) without removing the effect of interest. A high-pass filter is used to remove low frequency drift such as system noise (magnetic field drift over time), physiological noise (pulsatile effects) or thermal noise. If respiratory and cardiac data are recorded during acquisition, physiological noise can be further reduced by retrospectively correcting using RETROICOR software [76]. A low-order Fourier series is used to model the additive contributions from the respiratory and cardiac noise. This can then be subtracted from the fMRI timecourse.

In order to produce a statistical map of the BOLD response, each voxel's signal time course is compared to a model of the expected signal. Analysis tools commonly employ a univariate General Linear Model (GLM) to assess the fit between the model and observed data. To obtain a good model, the model design is convolved with a canonical haemodynamic response function (HRF) to mimic the delayed physiological response of the brain (Figure 3-6).

$$\mathbf{Y} = \mathbf{X}.\beta + \varepsilon \qquad\qquad\qquad 3\text{-}2$$

Univariate GLM analysis can be explained with a simple matrix equation (Equation 3-2), where $\mathbf{Y}$ represents the observed data in a single voxel across time, $\mathbf{X}$ represents the design matrix which should explain the observed data, β is a parameter estimation which defines the contribution of $\mathbf{X}$ to $\mathbf{Y}$ and is estimated to minimise ε, the error term representing the difference between $\mathbf{Y}$ and $\mathbf{X}.\beta$. The

result of GLM analysis is a statistical parametric map (SPM) of voxels, showing which effects of interest in the design matrix correlate significantly with the observed data in each voxel.

The voxel signals which significantly correlate with the modelled data are assigned a t-statistic (the β parameter estimate divided by residual error), which can be converted to a Gaussian Z-statistic which can then be converted to an uncorrected p-value. t, Z and p-values all reflect how significantly the voxel of interest is related to the model design. The p-value is uncorrected if the time-course of each voxel is independently analysed. However in fMRI data, as there are a large number of voxels analysed, it follows that here will be a large number of false-positives. If $p < 0.01$, then 1 voxel in every 100 activated voxels will not reflect a true correlation. The risk of a false-positive occurring within a group of inferences is described by the family-wise (Type I) error rate (FWE). To minimise FWE, it is necessary to correct for multiple comparisons such as with Bonferroni correction, where the p-value required for statistical significance is reduced in proportion to the number of statistical tests performed. However, whilst controlling for FWE, Bonferroni correction increases the likelihood of failing to detect activation (Type II error). Gaussian Random Field Theory is typically applied as the spatial correlation across voxels defies the assumptions made in a Bonferroni correction [77]. The risk of a false-positives result is further reduced by applying cluster-size thresholding, as clusters of activated voxels are more likely to reflect true brain activity. A newer alternative control is the false discovery rate (FDR), which assesses the proportion of false positives. Unlike FWE, the number of false-positives estimated by FDR scales with the number of positive results.

3.4 Imaging cerebral perfusion and blood flow

In order to maintain a steady rate of metabolism and tissue function, all cells require a consistent supply of O_2 and nutrients. This is maintained via the process of perfusion; the delivery of oxygenated blood to the tissue capillary network (quantified in units of ml/100g/min). After arriving at the tissue, O_2 and nutrients exchange from the blood to tissue (using both active and passive mechanisms,

dependent on the substrate in question), and waste products are removed from the tissue. Inadequate perfusion will induce such problems as cellular acidosis (via accumulation of lactic acid) and ischaemia, causing potentially irreversible cerebral and cardiovascular damage. Accurate and rapid perfusion quantification can help diagnose abnormal tissue function with the potential to improve patient treatment and outcome. Furthermore, as outlined in Section 3.3.1, cerebral blood flow is assumed to be one of the driving forces behind the BOLD response and so accurate quantification of perfusion plays a key role in understanding the physiological changes which underpin neuronal activation.

Non-MR imaging methods of perfusion measurement exist, and a brief introduction will be given before introducing the MR methods used in this thesis in more detail. As introduced in Chapter 1, PET is an imaging technique which uses a radiopharmaceutical tracer (E.g. ^{15}O, ^{11}C, ^{18}F) to provide 3D images of both function (perfusion, oxygen and glucose metabolism, depending on tracer choice) albeit with limited spatial resolution. As the tracer decays, a positron is emitted which will eventually collide with an electron, causing a pair of gamma rays. A ring of sensors around the head are used to detect the gamma ray origin. As the concentration of tracer varies throughout the body, a 3D image is built up. For perfusion imaging with PET, $H_2^{15}O$ is often used (and generally considered to be the gold-standard clinical perfusion measurement [78]) however quantification requires the arterial concentration of $H_2^{15}O$ to be known which requires invasive continuous arterial sampling [79]. Furthermore, radiopharmaceuticals must be manufactured on-site due to their short half-life, which makes the imaging technique expensive.

Single-photon emission computed tomography (SPECT) works in a similar manner to PET, however the signal from a gamma-emitting tracer (E.g. ^{99m}Tc or ^{123}I) is measured. By using a series of gamma cameras to measure single gamma rays, 2D images are acquired, which can be reconstructed to gain a 3D image. SPECT is a more cost-effective imaging method, and offers the clinical advantage that it can be implemented at the bedside [80]. However, the spatial resolution is limited by scattered photons, and so it may be more beneficial as an additional complementary technique to PET or MRI.

Whilst the nuclear methods described above are widely used in clinical settings, they are disadvantaged by the need for an ionising radioactive tracer, which necessitates limiting patient exposure to repeated scans to prevent potential tissue damage. MR methods offer a non-invasive, non-ionising means of perfusion quantification with relatively high spatial and temporal resolution. This section will provide a basic overview of Arterial Spin Labelling (ASL) theory and models, focusing on the ASL schemes used in this thesis. MR methods of perfusion imaging can be separated by the choice of an endogenous or exogenous tracer. Dynamic susceptibility contrast (DSC) [81, 82] uses an injection of an exogenous tracer such as gadolinium chelate (Gd-DTPA). By measuring the transverse relaxation of the injected bolus at a given location, this provides measurements of CBF, total CBV and mean transit time (MTT) of blood through the tissue. DSC is a relatively rapid technique with increased SNR in comparison to ASL, however, it generally provides relative rather than absolute measures of perfusion, and the contrast agent poses a risk to patient groups with compromised kidney function [83]. Furthermore, the invasive nature of DSC means that it is not easily repeated, which compromises the temporal resolution. Arterial Spin Labelling (ASL) is a non-invasive MR method which uses an endogenous tracer of magnetically labelled water protons. The remainder of this section will focus solely on ASL as a measurement of cerebral perfusion.

3.4.3 Basic Principles of ASL

In ASL, the longitudinal magnetisation of arterial water protons with respect to tissue is varied so that blood water is "labelled" and acts as an endogenous contrast agent. Typically, an RF inversion pulse is used to invert the net magnetisation of inflowing blood to a selected labelling plane (Figure 3-7). Following the labelling scheme (see Section 3.4.4 for details on the different ASL schemes), an image is acquired after a post-label delay (TI), which provides time for the blood to reach and perfuse the tissue. The ASL perfusion-weighted signal obtained is dependent on the perfusion rate (as protons in arterial blood exchange with those in tissue), but is also dependent on T_1 decay. A second control image is then acquired, where blood is not labelled, subtracting the signal of the labelled

image (M_{label}) from the control image ($M_{control}$) provides a difference image where the change in signal is dependent on perfusion [84]. The control image also corrects for magnetisation transfer (MT) effects.

When labelling the water-bound protons proximal to the imaging slice, the RF inversion pulse is off-resonance with respect to the imaging slice. However, both water-bound and macromolecule-bound protons will exist in the labelling plane, with the frequency band of macromolecule-bound protons being much broader. Therefore an off-resonance RF pulse is likely to label both pools of protons and the magnetisation transferred (MT) between them via spin-spin interactions and water diffusion. Such MT effects are compensated by acquiring a control image (see Section 3.4.4).
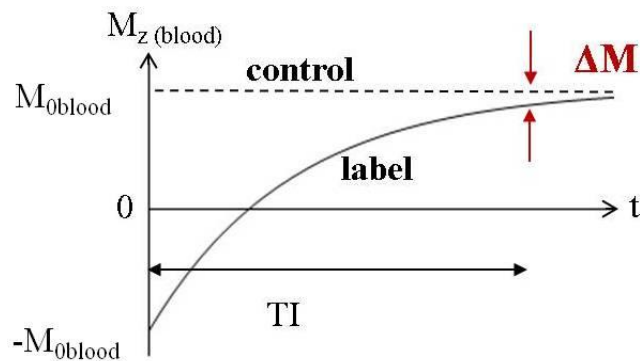
Figure 3-7) Schematic representation of how ASL manipulates longitudinal magnetisation of blood ($M_{Z\ (blood)}$). In the labelled condition, a 180° RF pulse inverts the blood magnetisation (M_{0blood}). The tissue magnetisation difference between the control and label condition (ΔM) is measured at one or more post-label delays (TI), allowing time for blood to perfuse the tissue and is thus proportional to perfusion.
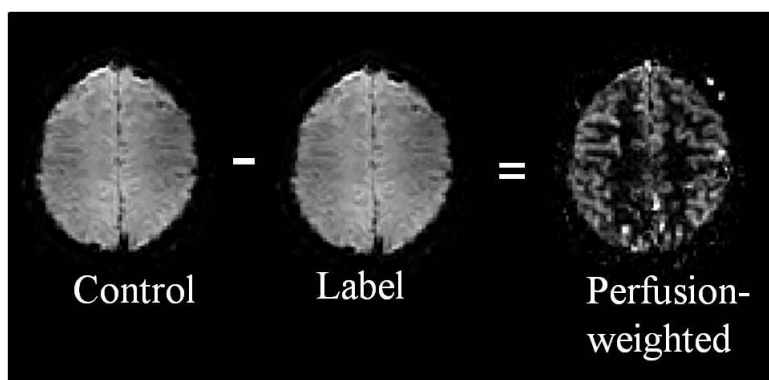
Figure 3-8) Subtraction of the label image from the control image provides a perfusion-weighted difference image. This dataset shows a representative image at a post-label delay (TI) of 1400ms.

The signal change between label and control images is in the region of 1-2 % (dependent on field strength) and so multiple averages of perfusion-weighted images are needed in order to improve the contrast to noise ratio (CNR). Furthermore, the fluctuations in signal from static tissue signal (e.g. due to subject motion or physiological noise) will increase the noise considerably and reduce the CNR of ASL images. The use of pre- and post-saturation pulses (applied immediately before and after the labelling scheme) ensure that the tissue signal is equivalent for the label and control condition at the start of each image acquisition [85] and also allows the use of a shorter TR. Background suppression, by the application of one or more global inversion pulses prior to image acquisition minimises physiological noise contributions in the tissue signal [86] (Figure 3-9). The timing of the background suppression pulses must be optimised according to the post-label delay and T_1 of the tissue of interest so that the ASL readout is performed close to the time when the tissue signal has just crossed the null-point [87].
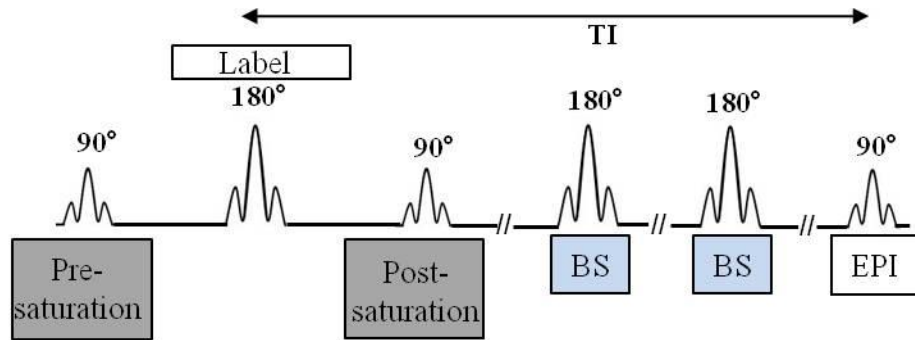
Figure 3-9) Schematic of an ASL pulse sequence. Pre- and post-saturation pulses are applied immediately before and after the RF labelling pulse for both label and control images to ensure static tissue is equivalent. Background suppression (BS) pulses are applied using one or more global inversion RF pulses in order to ensure the tissue signal is close to null at the readout time, TI.

In ASL, the labelling and readout schemes can be selected independently of each other, with many different SE or GE based image acquisition schemes routinely used. 2D GE-EPI is used as the acquisition scheme for all data presented in this thesis, and provides the advantages of allowing rapid image acquisition of multiple slices before the label decays, as well as simultaneous BOLD weighted image acquisition. ASL has low sensitivity so a short echo time (TE) should be used in order to maximise the measured signal change. Longer TEs become sensitive to T_2^* changes, which can lead to BOLD contributions in the ASL signal which can result in underestimation of perfusion [88], a factor discussed in Chapter 4.

3.4.4 Labelling Sequences:

There are three main labelling schemes used in ASL: Pulsed ASL (PASL) [89], Continuous ASL (CASL) [90] and pseudo-Continuous ASL (pCASL) [91]. The ASL measurements presented in this thesis use only the PASL scheme, however a brief overview of each scheme is given below.

Pulsed ASL (PASL) scheme

PASL creates a slab of labelled blood using a single short duration adiabatic RF pulse (10-20 ms) [85, 89, 92, 93]. The term PASL encompasses a range of pulse

sequences. Figure 3-10 describes the most basic pulse sequence used in PASL, and the three main schemes (FAIR, EPISTAR and PICORE) are summarised below and shown in Figure 3-11.
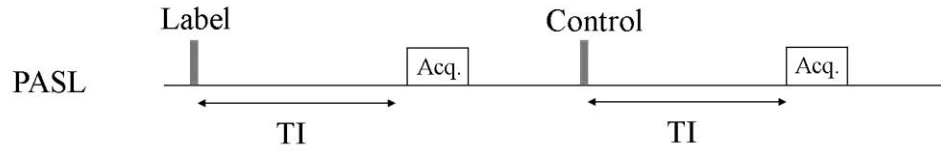
Figure 3-10) Schematic of a pulsed ASL (PASL) pulse sequence. Image acquisition (Acq.) is separated from the label/control scheme by a post-label delay (TI).

FAIR (Flow Alternating Inversion Recovery) [93] uses a non-selective (NS) inversion pulse (label) and a slice-selective (SS) inversion pulse (control). In the label image, all spins in the volume covered by the RF transmit coil are inverted, however, in the control image, the slice selective gradient inverts blood only in the imaging plane (Figure 3-11C). The perfusion weighted signal for FAIR is then calculated as $\Delta M = M_{control\,(SS)} - M_{label\,(NS)}$. In the FAIR scheme, blood is inverted both proximal and distal to the imaging plane, removing any assumptions about the direction of flow.

EPISTAR (Echo-Planar MR Imaging and Signal Targeting with Alternating RF) [89] uses a slice-selective 180° inversion pulse (adiabatic inversion pulse with nominal RF power of a 360° pulse) to invert a thick slab of arterial spins proximal to the imaging plane (Figure 3-11A). To control for MT effects, the control condition consists of two consecutive slice-selective 180° inversion pulses. The perfusion-weighted signal for EPISTAR is therefore defined as $\Delta M = M_{control} - M_{label}$.

PICORE (Proximal Inversion Controlling for Off-Resonance Effects) [85] is a variation of EPISTAR which uses the same labelling sequence but for the control image the slice selective-gradient is removed resulting in an inversion pulse off-resonance (Figure 3-11B). By doing this, MT effects are matched. However, since

PICORE uses different gradient waveforms in the label and control conditions, PICORE is more susceptible to eddy current effects.
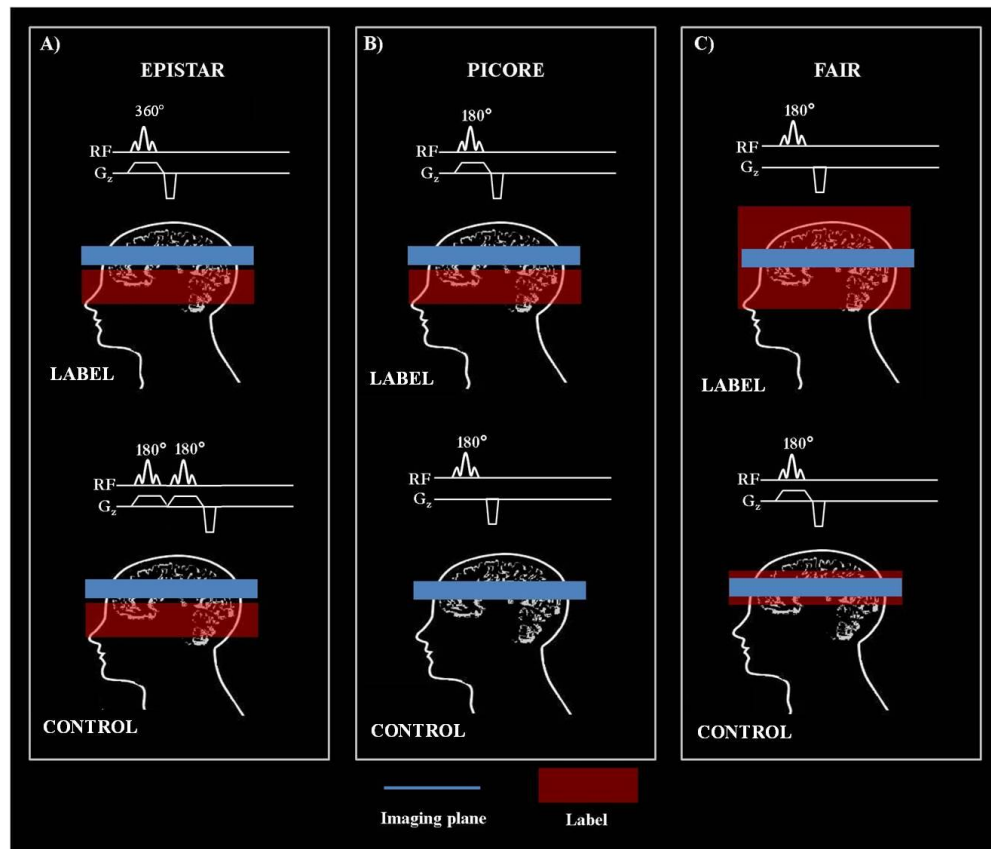
Figure 3-11) Schematic of different PASL labelling schemes with label and control conditions shown. The imaging plane is shown in blue and the labelling plane in red.

Continuous ASL (CASL) scheme

CASL involves labelling over a long period of time in a given labelling plane in the neck. This causes the longitudinal magnetisation of protons in arterial blood to undergo flow driven adiabatic inversion via a field gradient applied simultaneous to a continuous low power RF pulse (Figure 3-12) [84, 90]. Approximate RF amplitude is 3.5 µT for a gradient strength of 1 mT/m [91], applied for ~1.5 s. A label and control image are acquired, with the frequency of the RF inversion pulse inverted for the control image so that the labelling plane is now moved distal to the imaging plane [94]. Whilst CASL offers benefits such as increased perfusion signal [84], the extended length of the RF pulse results in higher SAR than PASL

– limiting its use at ultra-high field strengths. MT effects can be limited by the use of separate labelling and imaging coils, so that only the spins in a selected upstream artery are saturated. However, this requires specialised hardware.
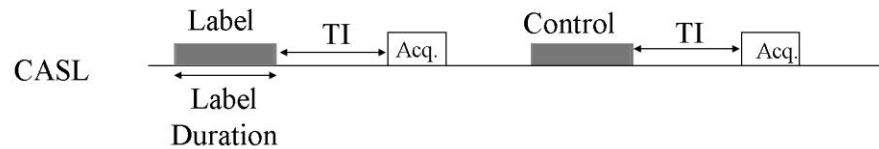

Figure 3-12) Schematic of a continuous ASL (CASL) pulse sequence. Image acquisition (Acq.) is separated from the label/control scheme by a post-label delay (TI).

Pseudo-Continuous ASL (pCASL)

pCASL is an extension of CASL and offers the combined benefits of both PASL and CASL [87]. By using a train of short low flip-angle RF pulses (typically 1500 RF pulses of flip angle 18, each lasting 0.5 ms and repeated every 1 ms [95, 96]), a continuous flow-driven adiabatic inversion label can be produced, thus increasing labelling efficiency whilst maintaining a comparatively lower SAR and removing the need for a specialised labelling coil (Figure 3-13). The control image is acquired for the same train of pulses but with 180° phase shifts between pulses, such that the average B_1 is zero. Despite these advantages, pCASL is susceptible to errors in quantification due to changes in eddy currents and B_0 inhomogeneity particular of ultra-high field. Although pCASL has lower SAR than CASL, it is still significantly higher than in PASL, which remains problematic (limiting the SNR per unit time) at ultra-high field strength [94].
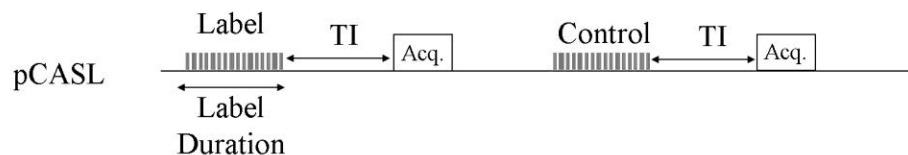

Figure 3-13) Schematic of a pseudo-continuous ASL (pCASL) pulse sequence. Image acquisition (Acq.) is separated from the label/control scheme by a post-label delay (TI).

3.4.5 Quantifying perfusion from ASL data

As previously described, perfusion is the delivery of nutrients to tissue via the blood. Therefore, when quantifying perfusion, it can be broken down into tissue and blood signal. In the simplest of cases, a single compartment model is used, modelling the signal from either the blood or tissue perspective. Here the tissue-based model will be introduced. The more complex two compartment approach considers signal contribution from both compartments and how the exchange across time as the tissue is perfused with labelled blood.

Single compartment model

Detre et al. [90] combined the Bloch equation for longitudinal relaxation with a single well-mixed compartment model in order to quantify the perfusion-weighted difference image. The change in tissue signal (M) can be described by Equation 3-3, where M_0 is the fully relaxed signal, f is regional perfusion, M_b is the blood signal and λ is the blood:brain partition coefficient (typically set to 0.98 ml/g [97]). The λ term accounts for the lower concentration of water (and consequently magnetisation) in tissue relative to blood.

$$\frac{dM(t)}{dt} = \frac{M_0 - M}{T_1} + fM_b - \frac{fM}{\lambda} \qquad \textbf{3-3}$$

The positive term fM_b denotes fresh blood flowing into the imaging slice and the negative term fM/λ denotes blood flowing out of the slice. M_0 (the tissue equilibrium magnetisation) can be obtained from the signal recovery curve fitted to the Bloch equation for longitudinal relaxation or taken from a separate M_0 calibration image which has been acquired at an equivalent TE. Assuming that the T_1 of tissue (T_{1t}) is equal to that of blood (T_{1b}), for FAIR, the signal following a slice-selective (SS) inversion pulse will recover according to the apparent T_1 (T_{1app}) (Equation 3-4),

$$\frac{1}{T_{1app}} = \frac{1}{T_1} + \frac{f}{\lambda},$$

3-4

with the magnetisation (M_{SS}) at time t can be described by:

$$M_{SS}(t) = M_0\left(1 - 2e^{-t(\frac{1}{T_1}+\frac{f}{\lambda})}\right).$$

3-5

Following a non-selective inversion pulse, the magnetisation recovers as:

$$M_{NS}(t) = M_0\left(1 - 2e^{\frac{-t}{T_1}}\right).$$

3-6

The measured signal difference between the non-selective (M_{NS}) and slice-selective (M_{SS}) signal is then given by

$$M_{SS}(t) - M_{NS}(t) = 2M_0 e^{\frac{-t}{T_1}}\left(1 - e^{\frac{-ft}{\lambda}}\right),$$

3-7

Assuming full inversion efficiency, Equation 3-7 can be modified to Equation 3-8 for ft/λ much less than 1 such that the last term can be ignored..

$$M_{SS}(t) - M_{NS}(t) = 2\frac{f}{\lambda}M_0 t e^{\frac{-t}{T_1}}.$$

3-8

A schematic of the perfusion-weighted signal difference according to the single compartment model is shown in Figure 3-14.
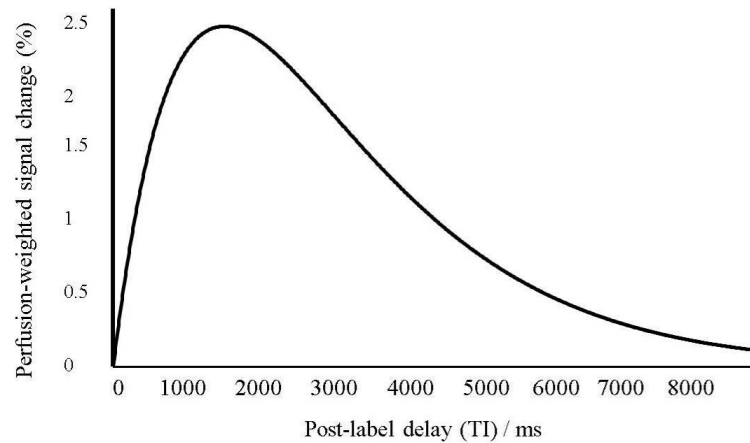
Figure 3-14) Schematic of perfusion-weighted signal as a function of post-label delay (TI).

The assumption that labelled blood will arrive instantly at the tissue (i.e. fast exchange) is over-simplistic. The above model can be extended to take account of the blood arrival time (time taken for blood to reach the tissue). The general kinetic model [98] is a popular model which relaxes the assumption of instantaneous blood exchange and encompasses the dynamic behaviour of blood by considering the delivery and clearance of labelled blood in addition to the magnetisation relaxation.

Blood and tissue model

Perfusion quantification can be made more physiologically plausible by increasing the number of compartments in the model. By modelling both blood and tissue, the effect of blood transit time can be more easily accounted for. Francis et al. [99] assume a multi-compartment vascular model (Figure 3-15); the arterial component outside the imaging slice (compartment 1), the intravoxel arteriolar component (compartment 2) and the exchange site between the capillary bed and tissue (compartment 3). The absolute signal is modelled within each compartment at regular time intervals (~200 µs), and the weighted sum of the difference signal (SS minus NS) between compartments 2 and 3 gives rise to the perfusion signal. A brief overview of the signal model and associated parameters for each compartment is given below as this model is used in experimental work presented in Chapters 4 and 6.
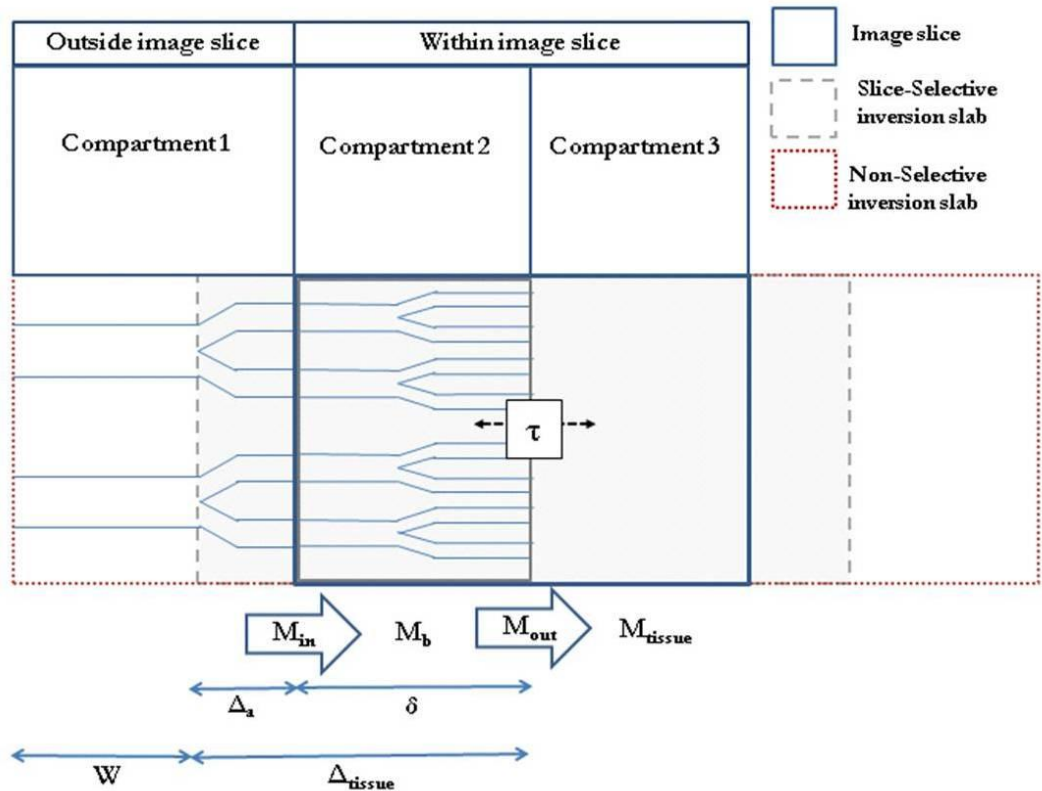
Figure 3-15) A) Schematic of the multi-compartment model developed by Francis et al. [99].

From Figure 3-15 it can be seen that the selective inversion slab is wider than the imaging slab to allow 100% inversion over the imaging plane. This leads to an arterial transit time (Δa), the time for the labelled blood to reach the arteriolar part of the voxel. Labelled blood remains in the arterial compartment for time δ, before perfusing the tissue. W represents the bolus duration for the NS case, i.e. the additional time taken for the labelled blood to enter the imaging slice in the non-selective condition. Assuming a square inversion profile and constant blood velocity across the vessel cross-section (i.e. "plug flow"), the following conditions hold true for the selective condition. $M(0)$ refers to the magnetisation flowing into the voxel and M_{b0} describes the initial magnetisation of the blood signal.

If $t < \Delta a$ $\qquad\qquad\qquad\qquad M(0) = - M_{b0},$ $\qquad\qquad\qquad$ **3-9**

if $\Delta a < t < W + \Delta a$ $\qquad\qquad\qquad M(0) = -M_{b0},$ $\qquad\qquad\qquad$ **3-10**

where + M_{b0} is the resultant signal for the non-selective condition

If $t > W + \triangle a$ $\qquad\qquad\qquad M(0) = +M_{b0}.$ **3-11**

The behaviour of M_b at time t in compartment 2 (the intravoxel arteriolar component) can be described by Equation 3-12. F is the normalised arterial blood flow per unit volume of voxel, and M_{in} and M_{out} reflect the magnetisation flowing into and out of the compartment respectively.

$$\frac{dM_b(t)}{d(t)} = \frac{M_{b0} - M_b(t)}{T_{1b}} + FM_{in}(t) - FM_{out}(t)$$ **3-12**

Where M_{out} is calculated in small (200 µs) iterative steps and takes account for the arteriolar blood being exposed to successive RF pulses with each additional readout. By modelling M_b it is possible to estimate F and δ from which aCBV can be quantified. This is used in Section Effect of isocapnic hyperoxia on aCBV 4.4.2.

Compartment 3 is where the capillary blood magnetisation exchanges with the magnetisation of the extravascular component. The change in M_{label} across time is described by Equation 3-13, the solution to which describes the signal recovery between each RF pulse (Equation 3-14), where f is the voxel perfusion rate and T_{1app} has the same definition as in the general kinetic model for single-TI measurements (Equation 3-4). Figure 3-16 shows the cerebral blood flow and volume weighted signal as a function of post-label delay.

$$\frac{dM_{label}(t)}{d(t)} = \frac{M_{label0} - M_{label}(t)}{T_{1t}} + f\frac{M_{out}(t)}{\lambda} - fM_{label}(t)$$ **3-13**

$$M_{label}(t) = M_{label0}\left(1 - e^{\frac{-t}{T_{1app}}} + \frac{fe^{\frac{-t}{T_{1b}}}}{\lambda\left(\frac{1}{T_{1b}} - \frac{1}{T_{1app}}\right)} - \frac{fe^{\frac{-t}{T_{1app}}}}{\lambda\left(\frac{1}{T_{1b}} - \frac{1}{T_{1app}}\right)}\right)$$ **3-14**

$$+ M_{out}(t)\left(\frac{fe^{\frac{-t}{T_{1app}}}}{\lambda\left(\frac{1}{T_{1b}} - \frac{1}{T_{1app}}\right)} - \frac{fe^{\frac{-t}{T_{1b}}}}{\lambda\left(\frac{1}{T_{1b}} - \frac{1}{T_{1app}}\right)}\right) + M_{label0}e^{\frac{-t}{T_{1app}}}$$
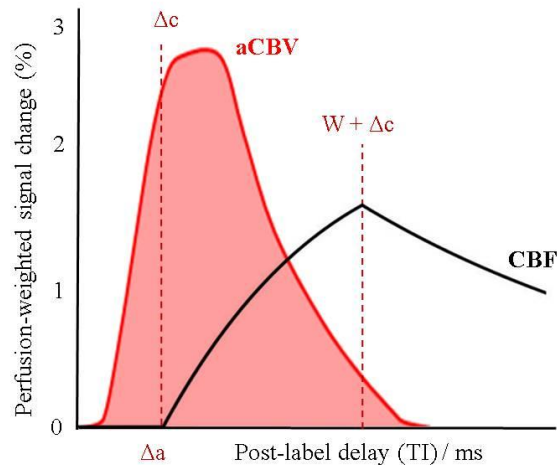
Figure 3-16) Schematic of perfusion-weighted signal as a function of post-label delay. Here the effect of transit time is accounted for, according to the multi-compartment kinetic model of Francis et al. [99]. Labelled blood arrives at the tissue within the imaging plane at time ($\Delta c = \Delta a + \delta$) and after time δ begins to exchange with the tissue.

Tissue perfusion is typically the main focus of ASL sequences. The measured ASL signal will contain a contribution from both aCBV and CBF (Figure 3-16). Bipolar gradients can be applied to provide 'vascular crushing' to eliminate arteriolar and arterial blood signal.

3.4.6 Readout sequences

Single TI

Early ASL experiments perform one image acquisition after a single post-label delay (TI). An acquisition at a single TI is easy to implement, however, taking a single TI measurement is likely to introduce errors as the blood arrival time (time taken for the labelled blood to reach the tissue) is unknown and cannot be taken into account in the fit. This is especially true when studying a dynamic process such as the response to a functional task or gas challenge. In single TI sequences, it is either necessary to assume a value for the arrival time; selecting a TI which is long enough to ensure that the labelled blood has arrived, but short enough to ensure that sufficient signal remains, or to repeat the experiment across a range of

59

TIs to estimate arrival time. The suitability of single-TI acquisitions will be discussed in more detail in Chapter 6, with particular emphasis on hypercapnia measurements.

Multiple TI

The accuracy of perfusion measurements can be increased by acquiring images at multiple post-label delays (TI, separated by time interval TA) across the perfusion-weighted signal recovery curve. By combining Look-Locker (LL) sampling with FAIR labelling and EPI readout schemes (LL FAIR ASL or multiphase ASL), perfusion and transit time (which may vary across brain regions, activation state and individual subjects) can be measured with high temporal resolution [99]. A single inversion pulse is followed by a series of low angle flip-angles from which the longitudinal magnetisation recovery can be followed.

It is important that the effect of multiple RF pulses on the magnetisation of arteriolar blood is taken into account, else perfusion will be underestimated. The stepwise multi-compartment kinetic model of Francis et al. [99], refined earlier LL-FAIR methods [100, 101] by modelling the expected arteriolar signal suppression prior to its exchange with tissue magnetisation.

In LL-FAIR ASL, the flip angle of the readout pulses in this scheme is kept low (typically 35°) to maximise the tissue signal. By alternatively minimising tissue signal and maximising arterial blood signal, LL-FAIR ASL in combination with a 2 compartment vascular kinetic model can also provide a measure of arterial CBV (aCBV) [102]. Rapid application of an increased flip angle (~45°) suppresses signal from the tissue exchange compartment (minimising sensitivity to perfusion), while the inflow of blood refreshes the signal of the arterial non-exchange compartment. The use of a short TI and ΔTI result in the blood being rapidly refreshed so that the inflowing signal remains high. aCBV is thought to drive the hyperaemic response and so an accurate non-invasive aCBV measurement technique offers a useful investigative technique for investigating brain function as well as a potentially useful clinical tool [E.g. 103, 104-106]
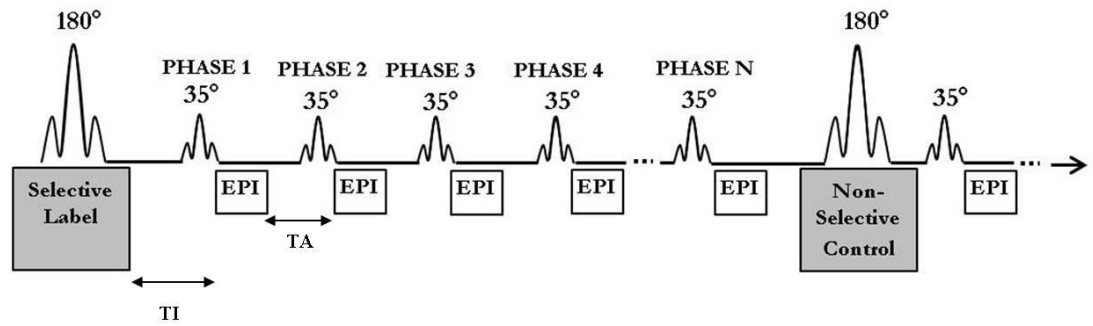
Figure 3-17) Schematic of the LL-EPI FAIR ASL scheme. A 180° inversion pulse is used in both the label and control conditions, both are followed by multiple EPI readouts which occur after a smaller RF pulse is applied (typically 35°). The first EPI readout occurs after time TI, with subsequent spacing described by time TA.

3.4.7 Phase Contrast Magnetic Resonance Angiography

Rather than measuring tissue perfusion, blood flow in vessels can be assessed using MR angiography (MRA). There are two types of MRA; Time of Flight (TOF) and Phase Contrast MRA (PC-MRA), both of which rely on the ability to visualise moving blood, generally, without the use of exogenous contrast agents [107]. Unenhanced MRA gives images of only blood flowing through the vessel and not the vessel itself [108].

In TOF, signal from stationary spins in the vessel and surrounding tissue is saturated, while the signal from moving spins in the inflowing blood is unsaturated. As blood flows into the imaging slice it brings with it unsaturated spins which receive RF excitation for the first time and so enhance vasculature contrast [109]. Signal enhancement in TOF is based on inflow effects, and the induced changes depend on longitudinal or T_1 relaxation as for ASL [108].

The alternative scheme is PC-MRA which uses the phase shift of transverse magnetisation to estimate blood flow; contrast relies on the motion of spins with respect to linear gradients. PC-MRA thus provides a T_1-independent method of measuring blood velocity. Here, the phase shift is induced by moving spins experiencing a change of phase relative to stationary spins as they flow along the

61

magnetic field gradient [108]. For a linear field gradient, the phase shift is proportional to velocity [110]. Two datasets are acquired; the first image has equal phase modulation for both stationary and moving spins, but the second image is flow-sensitive, using a gradient of equal strength but opposite polarity to produce a flow encoding phase-shift (Figure 3-18) [108]. Subtraction of the bipolar datasets suppresses any shifts in phase caused by parameters other than velocity [111], with the remaining phase difference Φ used in a voxel-wise calculation of velocities [108, 112].

The strength of the bipolar gradient determines the velocity encoding (VENC) where $VENC = \pi/(\gamma\Delta M_1)$, where M_1 is the product of bipolar gradient strength and duration squared $(M_1 = GT^2)$ [113]. It follows that slower velocities need a stronger gradient to achieve the same phase shift as faster velocities with a weaker gradient. The correct choice of VENC ensures that the maximal phase shift is induced in flowing spins in order to produce hyper-intense vessels in the resulting magnitude images. The VENC value must be set close to the maximum velocity of the flowing blood. If the blood velocity exceeds the VENC value then aliasing will occur and an abrupt change in signal intensity will be seen where there is a loss of signal in high flow regions [108].

The data acquired using PC-MRA can be used to produce both magnitude and phase images. Magnitude images give the signal intensity of each voxel (with arteries and veins hyper-intense) but lacks information on flow velocity and direction. Phase map images allow quantification of both flow velocity and flow direction, with the signal intensity depicting the phase difference Φ, while the sign of Φ depicts flow direction (brighter or darker than the grey static tissue, dependent on direction). PC-MRA is described in detail in Chapter 4 where it is used to measure the effect of isocapnic hyperoxia on blood flow in the internal carotid arteries (ICA).
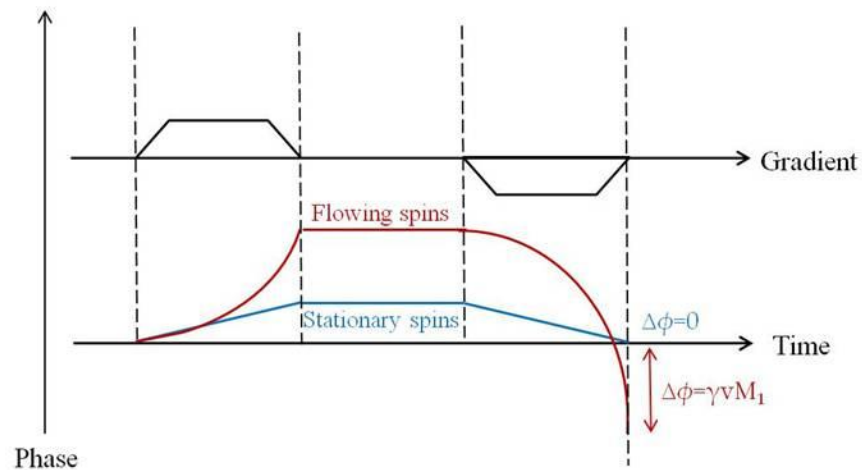
Figure 3-18) After the RF pulse, spins are in phase, with both stationary and flowing spins experiencing equal phase shift at the start of the first bipolar gradient. After the second bipolar gradient, the stationary spins are rephased ($\Delta\phi=0$) but the moving spins have acquired additional phase, where $\Delta\phi=\gamma vM_1$, where v is the veolcity and M_1 is the product of the bipolar gradient strenth and duration squared. PC-MRA is only sensitive to spins within and flowing perpendicular to the imaging slice. Adapted from [114].

PC-MRA can be used to measure the velocity of blood in any blood vessel which is perpendicular to the imaging slice. Both 2D and 3D PC-MRA sequences exist [115]. 2D PC-MRA has a shorter acquisition time whilst still remaining flow sensitive and so can provide a relatively quick snapshot of blood vessels in the head and neck, from which single imaging slices can be selected for 3D PC-MRA, ensuring that they are placed perpendicular to vessels of interest. 3D PC-MRA offers superior spatial resolution and SNR, however uses longer acquisition times, pulsatile flow variation over the cardiac cycle is more likely to be problematic and may cause phase encoding artefacts [116]. Synchronising data acquisition with the cardiac cycle, as with prospective cardiac gating, eliminates motion associated with the systolic phase of the cardiac cycle by collecting only over the diastolic phase (

Figure 3-19). The R-peak of the ECG/VCG waveform (as used here) or alternatively the systolic peak of the PPU waveform act as a trigger to start data acquisition. Data are collected over a pre-determined number of points (phases) across the cardiac cycle, after which the acquisition is paused until the end of the R-R interval to compensate for any physiological variation in the length of the cardiac cycle [110].
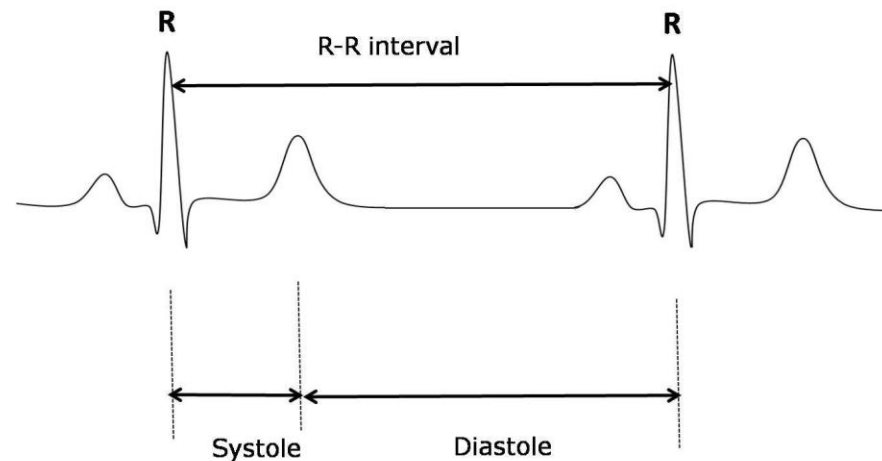
Figure 3-19) With ECG/VCG gating, the R-peak (point with greatest signal amplitude) is used to trigger the sequence, since the R-R interval is the time between two sequential R-peaks and is determined by the patient heart rate, the TR is heart rate dependent. Data are acquired after the systolic period to minimise phase misshaping due to pulsatile flow and cardiac motion. Adapted from [109].

3.5   Measurements of electrophysiology

Despite the high spatial resolution of fMRI, it has relatively low temporal resolution (on the order of seconds) and remains an indirect measure of brain activity. There are a range of electrophysiological techniques, from invasive techniques such as single unit recordings and electocorticography to non-invasive techniques such as electroencephalography (EEG) and magnetoencephalography (MEG). Electrophysiological recordings directly target neuronal activity, however the spatial resolution of non-invasive techniques is limited (as discussed below). Single-unit recordings have high temporal and spatial resolution, and

64

contributions have been invaluable in characterising electrical activity within the brain and establishing basic neuronal behaviour [117]. From a clinical perspective, ECoG aids pre-surgical planning and surgical resectioning, whilst offering good spatial resolution. However, these methods are very invasive. Non-invasive methods offer a simple repeatable method in which both the healthy and diseased brain can be studied. The remainder of this section will outline the theory and methodology of such non-invasive measures, focusing on MEG as this is used in Chapter 4 to assess the impact of isocapnic hyperoxia on neuronal oscillations.

Neuronal signal is transmitted between neurons across synapses. The synapse is the extracellular space between the axon terminal of one neuron and the dendritic fibres of one or more others. Upon receiving a signal, a post-synaptic potential (PSP) travels down the dendritic fibre to the axon hillock, where an action potential may be initiated, continuing the transmission process. An excitatory PSP is a temporary wave of depolarisation, with the flow of current creating both local electrical and magnetic fields. In magnetoencephalography (MEG), it is generally the PSPs of the pyramidal cells that are of interest.

A measurable magnetic field can be produced from the summed synchronised activity of large groups of similarly oriented pyramidal cells. This allows the group of neurons to be approximated as a single current dipole (Figure 3-20), which is a reasonable approximation [118]. The summed intracellular current flow is known as the primary or impressed current. The extracellular current flow which is established by the repolarisation of the neuronal membrane is not measured in MEG and together with signal from the skull and scalp is known as the secondary or volume current. It is not practical to consider the current flow established by an action potential along a neuronal axon as the transmission is too fast and this activity is more asynchronous across cells.

Magnetoencephalography (MEG) measures this neuromagnetic flux non-invasively and thus provides a direct non-invasive measure of functional brain activity. Electroencephalography (EEG) offers an affordable alternative electrophysiological measure and can provide a convenient method of translating some MR findings to a clinical setting. EEG detects electric potentials via scalp

electrodes rather than magnetic fields and as such, it is the volume current measured with EEG. Whilst both MEG and EEG have relatively high temporal resolutions, in comparison to fMRI, the spatial resolution is limited.
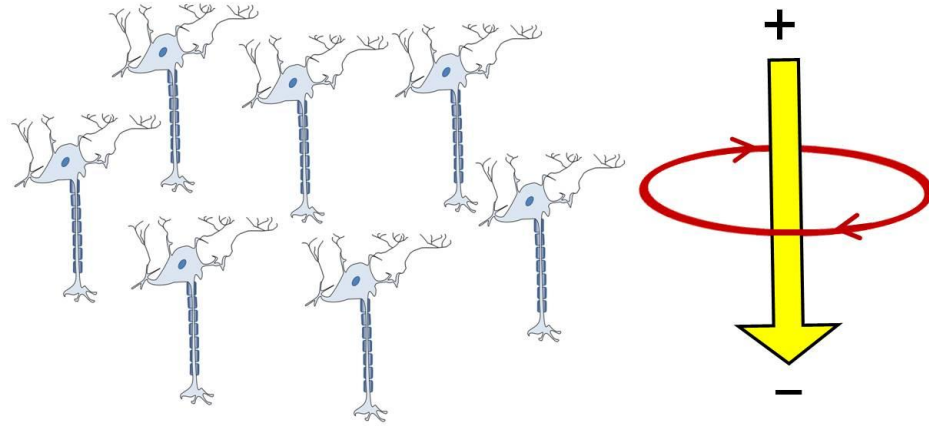
Figure 3-20) Synchronised postsynaptic potentials (and the corresponding wave of depolarisation) along dendritic fibres are the main source of primary current which induces the neuromagnetic field measured by MEG. Current flow along an individual dendrite is extremely small and so large synchronous groups are modelled as a single current dipole, with a current source and a current sink.

In EEG, it is necessary to translate the voltage distribution measured on the scalp to a spatial distribution of dipoles inside the brain. In MEG, it is necessary to link the magnetic distribution measured outside the head to the current distribution inside the head. Unfortunately, there are multiple dipole configurations that will give rise to the same surface measurement. This is called the inverse problem and is ill-posed with no unique solution, requiring complex algorithms in order to solve it. The advantage of MEG over EEG is that the signal source localisation is more straightforward as neuromagnetic fields are not distorted by the skull or scalp. However, EEG is inexpensive, portable and readily available making it a popular clinical technique for a range of neurological conditions to include non-convulsive seizures, brain injury and psychiatric disorders [119-121]. Whilst MEG is more expensive, systems tend to include around ten times more sensors than with EEG.

MEG relies on a head model, which is fundamentally spherical (number of spheres and positioning varies across models) and is thus insensitive to dipoles which are positioned radial to the scalp (i.e. pointed directly towards or away from the scalp), whilst EEG is sensitive to both radial and tangential sources.

The approximate dipole moment from the summed activity of 10^6 pyramidal neurons is on the order of 25 nAm [122]. The use of extremely sensitive signal detectors is crucial for measuring such small signal changes. Multiple Superconducting Quantum Interference Devices (SQUIDS) are situated within the super-cooled dewar helmet so that they will cover a spherical section over the head about 2-3 cm apart. Each SQUID simultaneously measures the magnetic field at a specific spatial location. The fluctuations in neuromagnetic field are relatively weak in comparison to the Earth's magnetic field and magnetic field disturbance caused by objects such as computers and cars. For this reason, the MEG system is placed within a magnetically shielded room, which blocks most external magnetic fields. In addition, to distinguish between neuromagnetic fields induced by neuronal activity and residual external magnetic fields, the gradient of the magnetic field is measured by gradiometers. First-order gradiometers consists of two coils (a pickup and a compensation coil), placed in series but wired in opposing directions [123]. The gradient of background magnetic fields will be near constant and so the signal from the pickup coil and compensation coil will cancel out. In contrast, the neuromagnetic field will show a steeper gradient (as the signal extends only a few centimetres beyond the head) and so produces a net change which it transmits to the SQUID via a flux transformer.

As introduced above, the acquired data must be converted from sensor space to source space i.e. from scalp to brain. There are many methods to do this; in this thesis, a scalar beamformer [124] is used to spatially filter the data. The source localised signal for a dipole at location y and orientation θ (y_θ) can be defined by Equation 3-15, where $\mathbf{b}(t)$ is the time course of measured signal summed across each channel and $\mathbf{W}_\theta^{\mathrm{T}}$ is a transposed matrix of channel weights, which is derived from the lead field vector and the covariance data of measured data.

$$y_\theta(t) = \mathbf{W}_\theta^{T}.\mathbf{b}(t) \hspace{4cm} \textbf{3-15}$$

The lead field vector is simply the solution to the forward problem for an instantaneous unit dipole at a defined location and orientation. By comparing the sensor signal with the expected signal from the lead field vector, the signal to noise ratio can be maximised and the optimal dipole position identified.

The scalar beamformer (Equation 3-15) is repeated across time such that a time course summed across weighted channels can be acquired. This time course can be separated into frequency bands using a band pass filter. Whilst frequency band definitions are subject to subtle differences in definition, they can be generally categorised as delta (<4 Hz), theta (4-8Hz), alpha (8-13 Hz), beta (13-30 Hz) and gamma (30-100 Hz) [122]. Further methods are provided in Chapter 4.

3.6 <u>Summary</u>

Having introduced the basic principles underlying BOLD fMRI, ASL, PC-MRA and MEG, Chapters 4-6 will implement these techniques to assess the physiological and physical impact of modulating O_2 and CO_2. By using multiple techniques to measure different response to such respiratory challenges, it is possible to gain a more quantitative insight in to the BOLD response.

4 The effect of hyperoxia on neurophysiology

4.1 Introduction

This chapter describes the effect of hyperoxia, (raising the inspired fraction of oxygen (FiO_2) above normal physiological levels (0.21)), on physiology and neuronal activity. Hyperoxic modulation is often used in the calibration of the BOLD signal [8] under the assumption that increased oxygenation has no significant impact on neurophysiology or neuronal activity. The first aim of this chapter is to provide an experimental measure of these effects, to assess the validity of hyperoxia calibrated BOLD. The second aim is to use the isocapnic hyperoxia to investigate the effect of hyperoxia in functional hyperaemia.

This chapter reviews the published effects of hyperoxia and discusses the possibility that some findings on the response to hyperoxia may be confounded by fluctuations in carbon dioxide (CO_2). First, the hyperoxia calibrated BOLD model will be outlined to provide an understanding of the motivation behind the experimental work. Three experiments will then be presented to assess the effect of hyperoxia on the following baseline measures: (i) mean blood flow (MBF), (ii) arterial cerebral blood volume (aCBV) and (iii) neuronal oscillations. Secondly, the regulatory mechanisms in functional hyperaemia will be discussed. Experimental work will assess the impact of hyperoxia on task-evoked cerebral blood flow changes (CBF).

4.2 Hyperoxia calibrated BOLD

Calibrated functional magnetic resonance imaging (fMRI) provides a non-invasive method to quantify the fractional change in cerebral metabolic rate of oxygen ($CMRO_2$) consumption which gives rise to the BOLD signal change during an fMRI experiment [7, 66, 125-128]. $CMRO_2$ is thought to be more closely coupled to neuronal activity than the BOLD signal and therefore provides a means of

quantification, which is crucial in order for a method to be established as a reliable clinical technique.

In the original quantitative calibrated fMRI model of Davis et al. [7], the effect of hypercapnia on CBF was used to normalise the BOLD signal in order to remove vascular contributions which did not directly reflect neuronal activity. Whilst a well-established and popular research technique, hypercapnia-based BOLD calibration is likely compromised by the known reduction in electrophysiological activity that accompanies hypercapnic stimuli, which may impact the measured value of $CMRO_2$ [129-133]. It is worth noting, that such a reduction in $CMRO_2$ has been contested [134].

Hyperoxia has been proposed as an alternative means of BOLD signal calibration [8, 135], providing the advantages of a more precise estimate of $CMRO_2$ and a more tolerable stimulus which can be applied for longer periods. Hyperoxia increases arterial oxygen content (mostly through an increase in O_2 dissolved in blood plasma), thus increasing venous oxygen saturation, and hence decreasing the concentration of *dHb* in capillaries and veins [136]. *dHb* is paramagnetic and so a reduction in *dHb* will increase the transverse relaxation time (T_2^*) of blood in vessels (intravascular component) and the surrounding tissue (extravascular component) causing a global increase in the BOLD signal [42, 137].

The original hyperoxia model [8] is simply an adaptation of the hypercapnia calibration model [7], however, rather than a vasodilatory stimulus modulating CBF, with hyperoxia it is venous oxygenation that is modulated. The hyperoxia model originates from the same expression for BOLD signal change (Equation 4-1) as used in the hypercapnia model [138],

$$\frac{\Delta BOLD}{BOLD_0} = -TE\Delta R_2^* \; , \qquad\qquad \textbf{4-1}$$

and uses the expression for R_2^* defined by [139] (Equation 4-2):

$$R_2^* = A\left(CBV[dHb]_v^\beta\right) \; , \qquad\qquad \textbf{4-2}$$

where $[dHb]_v$ is the venous concentration of deoxyhaemoglobin, A is a proportionality constant (incorporating field strength and susceptibility shift) and β is a constant which expresses the power relationship between oxygenation and R_2^*. β is generally assumed to be ~1.5 at 1.5 T, reducing to ~ 1.3 at 3 T and 1 at 7 T (see Chapter 5 for a further discussion).

Equation 4-2 can be substituted into Equation 4-1 for the stimulus and rest conditions (where the subscript 0 denotes the rest condition) to give Equation 4-3. M is the calibration parameter identical to that in Davis et al. [7].

$$\frac{\Delta BOLD}{BOLD_0} = \underbrace{TE.A.CBV_0.[dHb]_{v0}^{\beta}}_{M}\left(1 - \left(\frac{CBV}{CBV_0}\right)\left(\frac{[dHb]_v}{[dHb]_{v0}}\right)^{\beta}\right) \qquad \textbf{4-3}$$

Equation 4-3 can be written in terms of CBF by means of Grubb's constant, α [140]:

$$\frac{\Delta BOLD}{BOLD_0} = M\left(1 - \left(\frac{CBF}{CBF_0}\right)^{\alpha}\left(\frac{[dHb]_v}{[dHb]_{v0}}\right)^{\beta}\right) \qquad \textbf{4-4}$$

Under the assumption that a hyperoxic stimulus has no significant effect on CBF CBV or OEF, Equation 4-4 simplifies to:

$$\frac{\Delta BOLD}{BOLD_0} = M\left(1 - \left(\frac{[dHb]_{v0}}{[dHb]_v}\right)^{-\beta}\right). \qquad \textbf{4-5}$$

After calculation of the calibration parameter M from a hyperoxia challenge Equation 4-6 can be used to calculate the relative change in $CMRO_2$ from an activation task such as a finger tap, in which BOLD and CBF are measured.

$$\frac{\Delta BOLD}{BOLD_0} = M\left(1 - \left(\frac{CBF}{CBF_o}\right)^{\alpha-\beta}\left(\frac{CMRO_2}{CMRO_{2|0}}\right)^{\beta}\right) \qquad \textbf{4-6}$$

As with the hypercapnia calibration model, hyperoxia calibration also relies on the assumption that the stimulus is isometabolic i.e. $CMRO_2$ does not change. To date,

there remains some doubt as to the effect of the hyperoxia stimulus on tissue blood flow and neuronal activity (Section 4.4), and any such changes would complicate or undermine the use of hyperoxia-based BOLD calibration. More recently, a combined method of hyperoxia-hypercapnia BOLD calibration has been proposed [10, 141], with the potential to offer a clinically viable alternative to PET for quantification of baseline rather than relative $CMRO_2$. However, this method will combine the potential pitfalls associated with the separate delivery of hyperoxia and hypercapnia, and so even greater emphasis must be placed on the accuracy of these separate calibration methods.

Sections 4.7-4.8 of this chapter assess the physiological assumptions made in the above model; whether CBF and CBV remain constant under hyperoxia, and if hyperoxia is an isometabolic stimulus. This experimental work focuses only on the effects of isocapnic hyperoxia, in order to remove the potentially confounding effects of CO_2 fluctuations. Therefore it is first necessary to understand how isocapnic hyperoxia is established and administered.

4.3 The RespirAct^{TM}

Previous studies have attempted to control arterial gases, however most methods are complex leading to potential errors. A closed-loop system to target end-tidal values by adjusting inspired gas concentrations on a breath-by-breath basis is ideal [142-144]. However this method requires sophisticated and relatively expensive software. This 'end-tidal forcing' technique relies on respiratory frequency and tidal volume and may lead to the need for conflicting actions [145]. Many clinical studies [146, 147] use a self-regulating breathing system which allows maintenance of isocapnia and iso-oxia without requiring complex feedback [145]. However, these simple circuits are unable to target end-tidal partial pressures of CO_2 and O_2 ($P_{ET}CO_2$, $P_{ET}O_2$) precisely or independently of each other. Additionally, the effects observed with a simple breathing mask are unpredictable and difficult to reproduce. For hypercapnic sequences, a popular and easy to implement method is breath-holding [148-150], but breath-holding can be complicated by the variability of an individual's breathing, such as how long each breath lasts and how controlled their exhalation is (so that $P_{ET}O_2$ and $P_{ET}CO_2$ can be measured).

However, recent work suggests that the effects of such inter-subject differences can be minimised by monitoring $P_{ET}CO_2$ via a nasal cannula and using this trace as a regressor [151].

Paced breath-holding can be combined with visual feedback to induce controlled hypoventilation or hyperventilation in order to target a specific $P_{ET}O_2$ or $P_{ET}CO_2$ [152], but this requires training and is difficult to implement in an MRI scanner as it requires a metronome to pace breathing.

The RespirAct™ (Thornhill Research Inc., Toronto, Canada) is a feed-forward low gas-flow system which is used with a sequential gas delivery (SGD) circuit (Figure 4-1). It uses a blend of source gases; 100 % O_2, medical air and two blends of O_2, CO_2 and N_2 gas (each containing a minimum of 10 % O_2 for safety purposes) to precisely target $P_{ET}CO_2$ and $P_{ET}O_2$ independently of each other following the approach developed by [145]. SGD circuits provide sequential flow of "fresh" gas and "neutral" gas. The neutral gas is drawn from a reservoir of previously expired gas and so does not alter CO_2 levels [153]. The aim of the RespirAct™ system is to independently control $P_{ET}CO_2$ and $P_{ET}O_2$, allowing the user to both target and clamp end-tidal gases at a steady value.
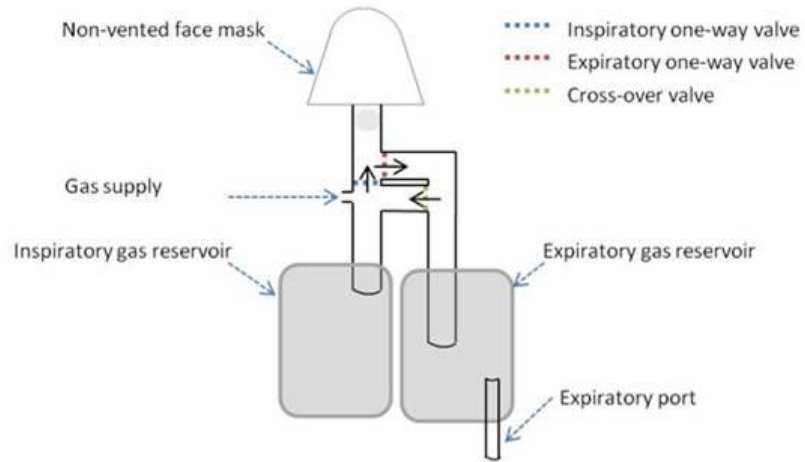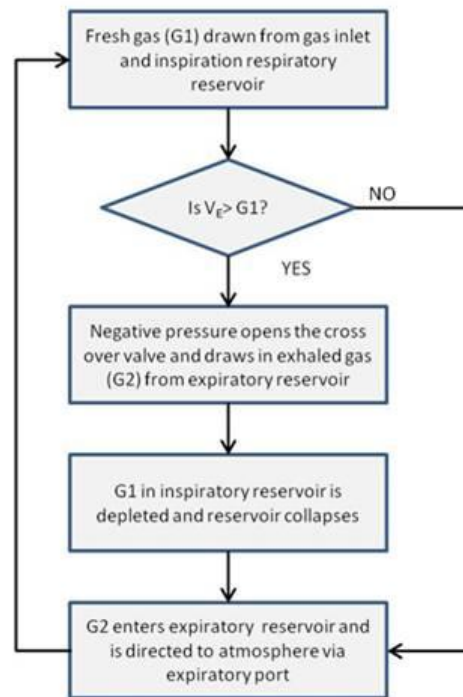
Figure 4-1) A) Sequential gas delivery (SGD) circuit based on [145]. **B)** Flowchart depicts inspiration and expiration through a sequential gas delivery circuit. G1 and G2 refer to fresh and exhaled gas respectively, V_E refers to minute ventilation.

4.3.1 Basic principles

Using the RespirAct^{TM}, $P_{ET}O_2$ and $P_{ET}CO_2$ can be prospectively calculated in spontaneously breathing subjects using four rules, derived from basic physiological principles outlined in Slessarev et al. (2007).

Rule 1: If the flow of newly inspired gas is less than or equal to alveolar ventilation, then this flow rate determines alveolar ventilation.

If the flow of newly inspired gas entering the fresh gas inlet decreases below minute ventilation (volume of air expired from lungs in one minute), the negative pressure will cause the crossover valve in the bypass conduit to open so that the subject "rebreathes" their previously expired gas. Initially, the previously expired gas will fill only anatomical dead space (as the lung is near full of freshly inspired gas) and so the fractional end-tidal concentration of CO_2 (representing the alveolar concentration of CO_2, $F_{ET}CO_2$) will not change. The RespirAct^{TM} relies on the opening of the crossover valve to remove the physiological dependence of alveolar ventilation on minute ventilation. It is vital that the fresh gas and previously expired gas flow in sequence, hence the RespirAct^{TM} system is used with a SGD circuit.

Rule 2: A component of a gas mixture can be assumed neutral with respect to alveolar ventilation if the concentration equals that in the mixed alveolar gas.

If the flow of newly inspired gas is less than or equal to alveolar ventilation, the alveolar gas filling the anatomical dead space is previously expired gas. During rebreathing, it simply re-enters the anatomical dead space and so will not affect the alveolar fractional concentration of CO_2 and O_2 (FACO$_2$, FAO2). The gas concentrations between anatomical dead space and alveolar mixed gas are equal and only an increase in lung volume will be observed. CO_2 and O_2 can be treated as independent components of alveolar gas in terms of neutrality, such that inhalation of previously expired gas can be neutral with respect to CO_2 only, whilst still altering $F_{ET}O_2$.

Rule 3: The fractional end-tidal concentrations of O_2 and CO_2 ($F_{ET}O_2$, $F_{ET}CO_2$) are independent of minute ventilation if the flow of newly inspired gas is less than or equal to alveolar ventilation.

If there is an increase in respiratory frequency, there will be a corresponding decrease in the fraction of newly inspired gas obtained with each breath. Nevertheless, minute ventilation cannot exceed alveolar ventilation and so is constrained by the flow of newly inspired gas. Similarly, if tidal volume increases then $F_{ET}O_2$ will increase and $F_{ET}CO_2$ will decrease. If the flow of newly inspired gas does not meet the rate of alveolar ventilation, gas will be drawn from the expiratory reservoir, thus filling the anatomical dead space with neutral gas with respect to alveolar ventilation. This will have no impact on either $F_{ET}CO_2$ or $F_{ET}O_2$

Rule 4: The flow of newly inspired gas can be divided into a "neutral gas" and a "fresh gas" which constitutes alveolar ventilation.

The flow of newly inspired gas can be divided into two virtual components, one with CO_2 which determines alveolar ventilation and one which is CO_2 neutral which has zero impact on CO_2 exchange. This simple concept allows $F_{ET}CO_2$ and $F_{ET}O_2$ to be independently targeted and maintained. Assuming that the flow of newly inspired gas remains constant, when alveolar ventilation exceeds the flow of newly inspired gas it is susceptible to changes in CO_2 concentrations which can be used to manipulate alveolar ventilation independently of minute ventilation. Under the same assumption, the manipulation of O_2 concentrations in newly inspired gas will alter alveolar ventilation for O_2 and so $P_{ET}O_2$.

4.3.2 Limitations of RespirAct™

Slessarev et al. [145] allow only for the distribution of gas to anatomical dead space (mouth, trachea etc.) and to well-perfused alveoli. Yet inspired air will be distributed both to anatomical dead space and alveolar dead space (regions of alveoli which do not partake in gas exchange), the sum of which is deemed the physiological dead space. In healthy people, anatomical dead space is roughly equivalent to physiological dead space as alveoli are very well perfused, however

in patients with lung disease, the alveolar dead space may be significantly increased [154-156]. This highlights the need for healthy subjects who have no prior history of lung disease.

While the RespirAct^{TM} can independently control end tidal gas concentrations it is still constrained by physiological limitations. Traditionally, transitions between end tidal gas concentrations should be as rapid as possible (square-wave) and reproducible. However, control over end tidal values will be sacrificed at transition periods due to the need for a sudden change in flow to reach the new targeted value. For example, in a transition from baseline $P_{ET}O_2$ to moderate hyperoxia, the RespirAct^{TM} will deliver a sudden burst of gas of pure O_2 in order to rapidly raise $P_{ET}O_2$. This means that there is no CO_2 delivered for a short period of time (compared to the standard 0.03%) and this change immediately reduces the control the system has over $P_{ET}CO_2$. With hyperoxia, achieving the target gradually rather than with a square-wave step provides much tighter control over end tidal O_2 and CO_2 as it minimises the change in flow rates and so prevents a "burst" of gas upon transition. Although this ramped approach increases the sequence length, accuracy and patient comfort are improved. Further, this method allows the assessment of sinusoidal transitions, such as has been used for cerebrovascular reactivity maps [157].

The subject may not continue to rebreathe if the flow of freshly inspired gas exceeds their minute ventilation. In this case, a proportion of the fresh gas will overflow into the expiratory reservoir meaning that this gas is no longer neutral and there will be a change in alveolar ventilation. The software will assume that all fresh gas was inspired and future inhaled gas concentrations will be incorrectly calculated on this assumption. Again, this specific limitation can be overridden by programming a slow gradual transition which minimises any changes in flow such that the subject can maintain their minute ventilation.

4.4 The effect of hyperoxia on the resting-state brain

Hyperoxia is a popular tool in both clinical treatment and research as it is readily available, portable and cost-effective. Normobaric hyperoxia (1 ATA) has been proposed as a treatment for cerebral ischemia [158-160], traumatic brain injury [161-163] and cluster headaches [164]. With regards to research, hyperoxia is a well established non-invasive exogenous (originating outside the body) contrast in MRI [136, 165, 166]. It is not only used to provide a method of calibrating the blood oxygenation level dependent (BOLD) effect [8], but also to study venous blood oxygenation and venous blood volume [135, 167-169].

The following studies were approved by the University of Nottingham Medical School Ethics Committee. MR scanning was performed using a 7 T Philips Achieva system with head volume transmit and 32 channel SENSE receive coil with foam padding used to reduce head motion. MEG recordings were made using a 275-channel axial gradiometer CTF MEG system (MISL, Port Coquitlam, BC, Canada)

4.4.1 Effect of isocapnic hyperoxia on mean blood flow brain

A hyperoxia-induced decrease in CBF was first noted by Kety and Schmidt [170] using a nitrous washout technique, now deemed the Kety-Schmidt method. Despite shortcomings, such as the assumption that the jugular venous blood is fully representative of cerebral blood and that cerebral blood can be fully saturated with nitrous oxide within 15 minutes [171], this method paved the way for many future methods and studies into CBF measurements. Many recent studies agree with the findings, and again suggest that normobaric hyperoxia decreases CBF [152, 165, 172], concluding that hyperoxia has vasoconstrictive properties.

However, it is worth noting that previous studies may have been confounded by associated arterial hypocapnia. Hyperoxia increases minute ventilation (leading to hyperventilation) and reduces arterial CO_2 ($PaCO_2$) via the Haldane effect (a reduction in CO_2 carrying capacity of oxyhaemoglobin (HbO_2) during hyperoxia) [173, 174]. Since the vasculature is very sensitive to changes in blood levels of CO_2 [175], a relatively low level of concomitant hypocapnia may significantly decrease blood flow. Therefore to properly characterise the effect of hyperoxia it is important to control or monitor any confounding changes in the level of CO_2. For this reason, the work presented herein uses isocapnic hyperoxia as a stimulus, where CO_2 is maintained constant throughout (see Section 4.3).

An additional complication when characterising the hyperoxia-CBF relationship is that the technique of Arterial Spin Labelling (ASL), which is frequently used to measure cerebral blood flow (CBF) and can also be used to measure aCBV, is dependent on the tissue and blood longitudinal relaxation times (T_1). On hyperoxia, dissolved plasma oxygen shortens the T_1 of blood [176, 177] and tissue [178] which would lead to an under-estimation of CBF/aCBV on hyperoxia if not properly accounted for when modelling the data.

The following experiment was designed to provide a T_1-independent measure of baseline blood flow on hyperoxia to test the assumption made in hyperoxia calibrated BOLD that hyperoxia has no significant effect on CBF [8].

4.4.1.1. Experiment protocol

Six subjects (aged 24-28 years, 4 female) participated and gave prior informed written consent. Prior to the MRI measurements, each subject sat upright on the scanner bed while baseline metabolic values were estimated and targeted. The subject then lay supine in the scanner connected to the RespirAct circuit, with medical air administered until the respiratory challenge commenced. The respiratory challenge consisted of 1 minute of normoxic baseline (subject-specific $P_{ET}O_2$ and $P_{ET}CO_2$), followed by 5 minutes of isocapnic hyperoxia ($P_{ET}O_2 = 500$mmHg, equivalent to $F_iO_2 = 0.6$, subject's resting $P_{ET}CO_2$), and then 5 minutes of normoxic baseline. This was then followed by 2 cycles of 2 minutes of

hypercapnia (subject's resting $P_{ET}O_2$, $P_{ET}CO_2$ = baseline + 8mmHg), separated by 2 minutes of baseline, followed by 1 minute of baseline (

Figure 4-2 4-2). The total duration of the respiratory challenge was 20 minutes, including transitions between the blood gas levels. All hyperoxia transitions consisted of a graded increase/decrease in target $P_{ET}O_2$ (between subject specific baseline and 500mmHg across 1 minute). This graded change minimises discrepancies between targeted and actual $P_{ET}O_2$, allowing a steady-state to be reached near instantaneously.
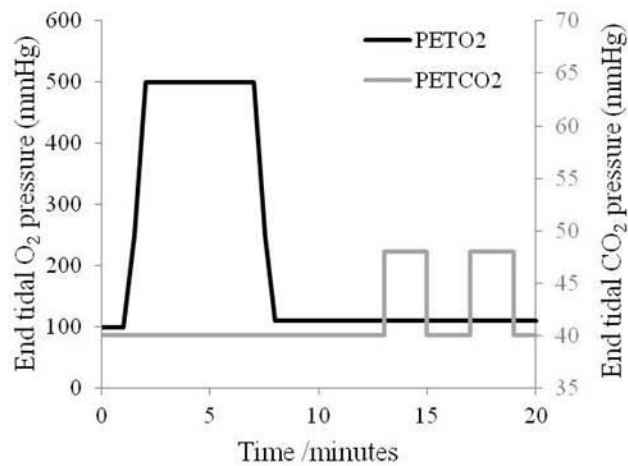
Figure 4-2) Targeted respiratory paradigm: isocapnic hyperoxia ($P_{ET}O_2$ = 500 mmHg) followed by 2 cycles of iso-oxic hypercapnia (subject specific baseline $P_{ET}CO_2$ + 8 mmHg). The one minute transitions can be seen for hyperoxia. Requested end tidal pressure of O_2 is traced in black and CO_2 in grey.

Mean blood flow (MBF) was measured in the left and right internal carotid arteries (ICA). The ICAs are the main supply of oxygenated blood to the brain (Chapter 3). Furthermore, the left and right vessels are approximately parallel, allowing blood flow to be measured within a single phase-contrast acquisition. To allow vessel visualisation, 2 slices of sagittal and coronal 2D PC-MRA data were acquired with the imaging parameters TR/TE = 14/7.6 ms, flip angle (FA) = 20°, slice thickness 30 mm, FOV = 230 x 230 mm^2, SENSE acceleration factor 2, v_{ENC}

= 30 cm/s. The scan duration was 47 s for 4 averages. Blood flow was then measured using a vectorcardiogram (VCG) gated, 2D PC-MRA acquisition on a 6 mm axial slice perpendicular to the targeted ICA. Imaging parameters were TR/TE = 15/6.5 ms, FA = 25°, FOV = 280 x 77 mm^2, 0.75 x 0.75 x 6 mm^3 reconstructed, SENSE acceleration factor 4, v_{ENC} = 100 cm/s, and 0 cm/s. The scan duration was 1 min 25 s for 2 averages. The measurement plane was positioned through the C1 segment of the spinal cord, where the left and right ICA were approximately parallel (Figure 4-3). PC-MRA data were collected throughout the 20 minute respiratory challenge, resulting in a minimum of 16 and maximum of 25 phases across the cardiac cycle. The number of PC-MRA repeats was determined by the subject's heart rate, resulting in a range of 2-4 repeats across the group. The repeated data acquisition allowed the variance of the flow measurement to be assessed and so the minimum detectable change (MDC) observable with PC-MRA at 7 T to be quantified.
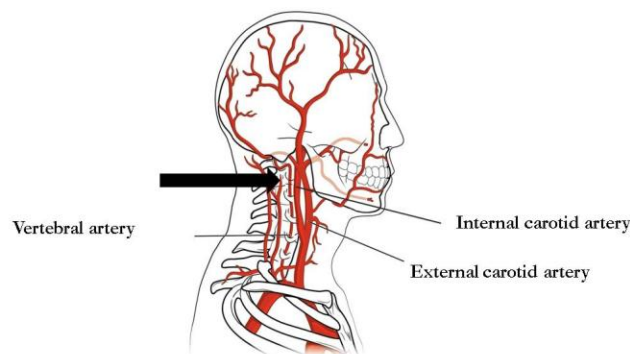
Figure 4-3) Schematic drawing of the main arteries which supply the brain, modified from [179]. The C1 cervical vertebrae is highlighted to depict placement of the imaging slice. The angle of the imaging plane was dependent on the vessel orientation to ensure it was perpendicular to the left and right internal carotid arteries.

4.4.1.2.   Data Analysis

PC-MRA flow data were analyzed using QFlow software (Philips, Best, Netherlands). Regions of interest (ROIs) were drawn manually around the lumen of the carotid arteries on each phase contrast modulus image (Figure 4-4C), and

contour detection software was used to improve the ROI accuracy. These automated ROIs were then manually checked against the phase images (Figure 4-4D). The mean signal intensity in the ROIs reflected the flow velocity for each cardiac phase in cm/s. The cross-sectional area of each vessel lumen was calculated ($\pm$ 0.1 mm^2) and multiplied by the mean velocity, to compute, for each cardiac phase, the carotid artery flux in ml/min. The flux data were then averaged across left and right ICAs, and repeated measurements, to give an average carotid artery flux waveform at normoxia, hyperoxia and hypercapnia. The data within a waveform were then averaged across all phases of the cardiac cycle to provide a single estimate of mean blood flow (MBF) at normoxia, hyperoxia and hypercapnia. The variance between repeated measures of MBF under normoxia was assessed, and the minimum detectable change (MDC) calculated from the standard error in mean (SEM) using a 95 % confidence level, calculated according to $MDC = 1.96 \, x \, \sqrt{2} \, x \, SEM$. Statistical tests were performed using SPSS 16, Chicago, IL, USA.
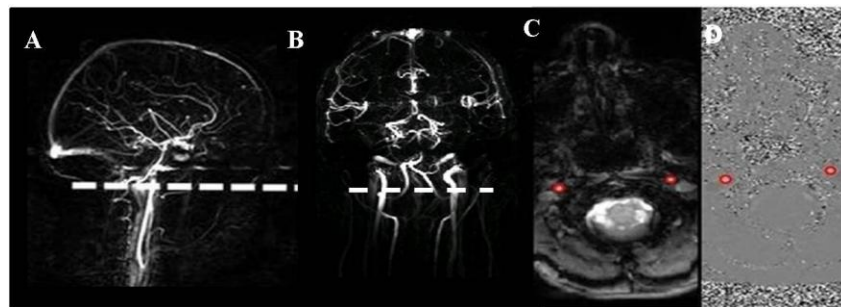
Figure 4-4) Localisation of the 2D PC-MRA imaging slice (dashed white line) perpendicular to left and right internal carotid arteries was based on the A) 2D sagittal phase-contrast angiogram and B) 2D coronal phase-contrast angiogram. C) 2D PC-MRA modulus and D) phase images, where cross-section of internal carotid arteries are highlighted in red.

4.4.1.3. <u>Results</u>

One of the six subjects was excluded due to the tortuous configuration of their ICAs, preventing the imaging slice being placed perpendicular to both left and right ICA simultaneously. The mean hyperoxic step was 460 $\pm$ 13 mmHg, with a

baseline of 111 ± 7 mmHg (mean ± SEM across subjects), while $P_{ET}CO_2$ varied by less than 1 mmHg. The average hypercapnic step was 4.2 ± 0.5 mmHg, while $P_{ET}O_2$ varied by less than 1 mmHg.

Hyperoxia did not cause a significant change in mean blood flow from normoxia (paired t-test, power = 0.8, p = 0.80), as shown in Figure 4-5 and Table 4-1. A 95 % confidence interval of -3.2 to +3.3 % was observed, suggesting that less than 5 % of results would show the 4 % reduction in blood flow reported in previous literature for a comparable increase in FiO_2 of 0.6 [165]. The minimum detectable change for p = 0.05 was assessed from repeated measures of normoxic MBF and found to be 3.6 %, again, this is less than the previously reported reduction. As expected, an increase in MBF occurred during hypercapnia compared to normoxia, with MBF being found to increase by 6.8 ± 1.5 % per mmHg of CO_2 (power = 0.8, p = 0.03).
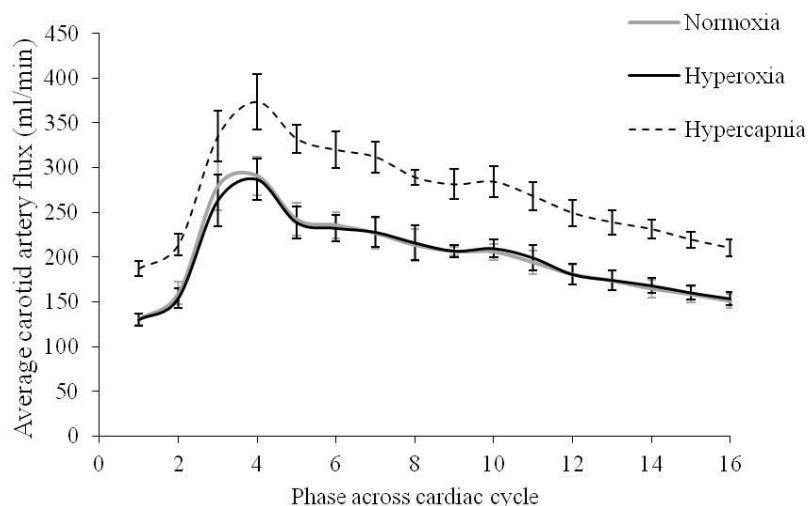
Figure 4-5) The effect of normoxia (grey solid line), hyperoxia (black solid line) and hypercapnia (black dashed line) on the mean average carotid artery flux waveform averaged across subjects. Error bars indicate the standard error of mean.

	MBF (ml/min)
Normoxia	201 ± 11
Hyperoxia	201 ± 12
Hypercapnia	$272 \pm 14^{*}$

Table 4-1) Effect of isocapnic hyperoxia, iso-oxic hypercapnia and normoxia (mean $\pm$ SEM) on mean blood flow (MBF), averaged across left and right ICA and all subjects. * denotes statistical significance from normoxia (p<0.05).

4.4.1.4. <u>Discussion</u>

A phase contrast based MR blood flow measure was used to ensure insensitivity to any changes in the T_1 relaxation time of the blood or tissue on hyperoxia. The phase contrast sequence monitors the (velocity induced) phase shift of the blood signal in the lumen of vessels across the cardiac cycle to estimate MBF, as such it is independent of changes in absolute phase of the blood due to hyperoxia. Here, MBF sensitivity to hyperoxia was measured in the internal carotid arteries to give maximum sensitivity to global changes in CBF. Whilst measurement in the internal carotid arteries neglects the posterior contribution to global CBF, it has been shown that the anterior circulation provides up to 82 % of cortical flow [180, 181], with both systems reacting equally to external stimuli [182].

The PC-MRA blood flow results presented here support the findings of a recent ASL study [183] which found no significant change in grey matter CBF in response to isocapnic hyperoxia. However, the ASL study did not correct for a change in T_1 blood relaxation time on hyperoxia which would lead to an underestimation of CBF on hyperoxia, potentially masking an actual increase in CBF. Previously reported reductions in CBF [184] may be attributed to accompanying hypocapnia since the $P_{ET}CO_2$ level was not controlled.

4.4.2 Effect of isocapnic hyperoxia on aCBV

As a change in cerebral blood volume (CBV) is thought to drive both CBF and the BOLD response [57, 102], this is an important determinant factor when investigating flow-metabolism coupling. Whilst the effect of hyperoxia on CBV is still under debate [152, 185], it is generally assumed to have no significant effect on CBV at low-levels and hyperoxia has been used to measure CBV [168, 169] .

The following experiment assesses the effect of isocapnic hyperoxia on aCBV to test the assumption made in hyperoxia calibrated BOLD that CBV is constant under hyperoxia [8].

4.4.2.1.   Experiment protocol

Seven subjects (age 24-48 years, 3 female) participated and gave prior informed written consent. Prior to MRI measurement, the subject sat upright on the scanner bed connected to the RespirAct circuit while baseline metabolic values were estimated and targeted. This experiment comprised 1 minute of baseline followed by 2 minutes of isocapnic hyperoxia ($P_{ET}O_2$ = 500 mmHg, subject's resting $P_{ET}CO_2$) and 1 minute of baseline (Figure 4-6). $P_{ET}CO_2$ was maintained at subject specific resting levels throughout. The duration of the respiratory challenge was 6 minutes, including transitions.
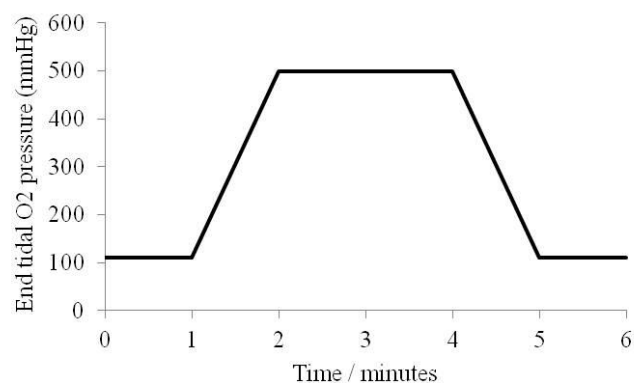

Figure 4-6) Targeted respiratory paradigm: isocapnic hyperoxia ($P_{ET}O_2$ = 500 mmHg), $P_{ET}CO_2$ targeted at subject-specific baseline throughout.

Flow-sensitive alternating inversion recovery (FAIR) Arterial Spin Labelling (ASL) was combined with a Look-Locker (LL) sampling scheme to map aCBV using a two compartment vascular kinetic model (Chapter 3) [99, 102]. The acquisition parameters were: initial inversion delay (TI) = 150 ms, readout spacing (TA) = 100 ms, TR = 3000ms, FA = 45°, SENSE factor 2 and 21 readout phases per TR. Images were acquired with a GE-EPI readout; single axial slice of 3 mm thickness, TE = 16ms, in-plane resolution of 2 x 2 mm, FOV = 192 x 192 mm. In addition, at normoxia, a base magnetisation image was acquired and a series of inversion recovery EPI images (10 inversion times, 100 - 2600 ms) which were fitted for T_1.

A grey matter (GM) mask was then formed by thresholding the T_1 map at $1.7 \leq T_1 \leq 2.3$ s. aCBV-weighted difference images were formed by subtraction of the label from control images (Figure 4-7A). The average aCBV difference signal within the GM mask for each LL-readout was then estimated, for both the normoxia and hyperoxia periods. These signal curves were normalised to the base magnetisation blood signal from the middle cerebral artery, and the resulting normalised aCBV signal curves at normoxia and hyperoxia fitted for GM aCBV and $\Delta_{arterial}$ using the model described in [102].

Fitting the signal for aCBV required an estimate of T_{1blood} on normoxia and hyperoxia. The measurement of T_{1blood} at normoxia and hyperoxia *in vivo* in humans at 7 T is difficult due to its fast flow rate and the limited coverage of the head transmit coil, therefore the T_1 of arterial blood ($F_iO_2 = 0.2$) is assumed to be 2200 ms at 7 T (T_{1blood} normoxia) [186, 187]. To estimate T_{1blood} on hyperoxia at 7 T we can first use the T_1 of arterial blood at 7 T together with the value at 1.5 T of 1205 ms [176] to calculate the exponent in the expression of Rooney et al. [188] relating T_1 to field strength (B_0), giving $T_1 = 839(B_0)^{0.39}$. Using this expression, we can then extrapolate the value of $T_{1blood} = 979$ ms at $F_iO_2 = 1$ measured at 1.5 T [176] to 1792 ms at 7 T. These 7 T values of T_{1blood} at $F_iO_2 = 0.2$ and 1, can then be exponentially interpolated [165] to estimate the T_{1blood} at 7 T for $F_iO_2 = 0.6$ of 1986 ms (T_{1blood} hyperoxia).

Significant effects of hyperoxia on mean aCBV and arterial transit time were assessed across subjects using a non-parametric Wilcoxon Signed Rank test.

4.4.2.2.   Results

The mean hyperoxic step ($\pm$ SEM) was 486 $\pm$ 12 mmHg, with a baseline of 119 $\pm$ 1 mmHg averaged across subjects, while $P_{ET}CO_2$ varied by less than 2 mmHg. Figure 4-7A shows the aCBV-weighted LL-FAIR ASL data in a representative subject, from which the mean GM aCBV was measured to be 1.2 $\pm$ 0.4 % during normoxia and 1.1 $\pm$ 0.3 % during hyperoxia (Table 4-2). This reduction was not significant (power = 0.8, p = 0.64, paired t-test), with a 95 % confidence interval of -0.21 to +0.31%. There was no significant change in mean arterial transit time, Δ_a which was found to be 318 $\pm$ 7 ms during normoxia and 309 $\pm$ 4 ms on hyperoxia (power = 0,8, p = 0.68, paired t-test), with a 95 % confidence interval of -69 to +95 ms.
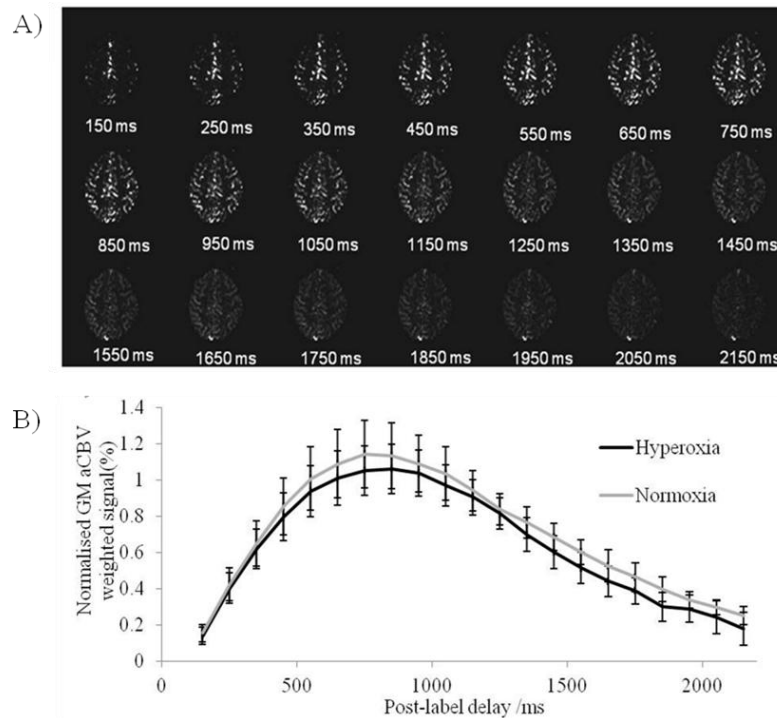
Figure 4-7) A) Example perfusion weighted LL-FAIR aCBV data. The effective post label delay is given in milliseconds. B) GM aCBV weighted normalised LL ASL signal curves at normoxia (grey solid line) and hyperoxia (black solid line). Data averaged across subjects. Error bars indicate the standard error of mean (SEM).

	GM aCBV (%)	$\Delta_{arterial}$ (ms)
Normoxia	1.2 ± 0.4	0.32 ± 0.07
Hyperoxia	1.1 ± 0.3	0.31 ± 0.04

Table 4-2) Effect of hyperoxia on mean arterial cerebral blood volume (aCBV) and arterial transit time ($\Delta_{arterial}$), averaged across cortical grey matter in all subjects.

4.4.2.3. Discussion

aCBV reflects vasoconstriction of the arterioles which controls blood flow through the capillaries and hence tissue perfusion. The aCBV compartment is known to be more responsive to activation compared to the venous blood volume [102]. Using intravenous perflurocarbon in anesthetised rats, Lee et al. showed that the relative increase in aCBV in response to a hypercapnic challenge was 5.3 times larger than the relative increase in venous CBV (vCBV) [189]. Using electrical forepaw stimulation in anesthetised rats, Kim et al [59] investigated regional responses using ASL. No significant differences were observed between aCBV and total CBV, suggesting a negligible change in vCBV in response to functional activation.

Here, aCBV was measured using LL-FAIR ASL which is a multiphase readout ASL sequence. This had a relatively high flip angle and small readout spacing, allowing aCBV and arterial transit time to be fitted simultaneously. It is important to assess both measures since a change in aCBV is often also accompanied by a change in transit time. Therefore if a constant transit time is assumed at a single inversion time, changes in aCBV may be masked. Further, the reduction in T_{1blood} that occurs on hyperoxia can cause an apparent change in the ASL aCBV-weighted signal in the absence of any true change in aCBV. This was accounted for by assuming a reduction in T_{1blood} on hyperoxia (from 2200 ms at normoxia to 1986 ms at hyperoxia) when fitting the aCBV data.

To investigate the potential effect of neglecting such a reduction in T_{1blood} on the fitted value of aCBV, the aCBV weighted signal was simulated using the LL-FAIR

ASL sequence timings used in this experiment [102]. Additional simulation parameters are given in Table 4-3. Simulating aCBV weighted LL-FAIR ASL data (100 iterations, SNR = 100:1) with T_{1blood} of 1986 ms (shortened by ~ 10 % at 7 T on hyperoxia) and fitting the data assuming T_{1blood} of 2200 ms (as for normoxia) led to an underestimation of aCBV by 10 ± 0.3 % (error in fitted mean ± SEM across iterations), while $\Delta_{arterial}$ remained largely unaffected (underestimated by 0.6 ± 0.5 %).

Parameter	Value
Blood volume, aCBV (%) (assumed using a bulk flow rate F of 180 ml/100g and exchange time, Δ, of 400 ms) (model described in [57, 102].	1.2
Longitudinal relaxation time of tissue, $T_{1tissue}$ (ms) ([188]	2200
Arterial transit time, $\Delta_{arterial}$ (ms)	100
Bolus duration, W (ms)	1200
Equilibrium magnetisation, M_0	1
Simulated T_{1blood} (ms) at 7 T for FiO2 (%) = 0.2, 0.4, 0.6, 0.8, 1.0 (Extrapolated from [188] and (Bulte et al. 2007b))	2200, 2144 2090, 2037, 1986

Table 4-3) Parameters used to simulate aCBV data, as described in (Brookes et al. 2007).

It has also been shown that CBF changes would be underestimated if the effect of hyperoxygenation on T_{1blood} was ignored [190] and another study has shown no change in CBF when correcting for the arterial blood T_1 decrease [190, 191]. The aCBV signal is derived solely from the arterial blood compartment due to the suppression of the tissue signal by the rapid sequence (every 100ms) of high flip angle (45°) pulses in the LL sequence, and therefore it is insensitive to any changes in tissue T_1 which in any case are likely to be small in the brain. Although this simulation was carried out for aCBV-weighted ASL data, these results highlight the more general importance of accounting for any change in T_{1blood}

when fitting ASL signal curves for both aCBV and CBF quantification on hyperoxia.

No significant change in aCBV was found on hyperoxia, in agreement with the MBF results of Section 4.4.1. The results presented in Section 4.4 have important implications for calibrated BOLD measurements using hyperoxia [8, 135, 192], and the more recent combined O_2 and CO_2 calibrated BOLD methods [10, 141]. The results imply that isocapnic hyperoxia based methods of BOLD calibration need not be corrected for changes in baseline CBF or CBV [8]. Hyperoxia can also be used to investigate vascular function and structure, as highlighted by its recent use in venous CBV estimations [169] and vessel size imaging [193], techniques for which the lack of any change in blood flow on hyperoxia is important.

4.4.3 Effect of isocapnic hyperoxia on CMRO$_2$

The effect of hyperoxia on neuronal activity has previously been studied using electrophysiology. Using electroencephalography (EEG) to assess the effect of 35% O_2 on cognitive performance and brain activity, a reduction in beta and gamma power, increase in delta power and reduction in alpha power was observed [194]. However, others [195-197] found no significant effect of a change in blood oxygenation level on electrophysiology signals. Unfortunately, to date, these studies have either employed scalp level electric field measures with limited spatial resolution, or very focal invasive electrode recordings (rat whisker studies [195]). Section 4.4.3 presents data collected with magnetoencephalography which provides a non-invasive method of spatially resolving the electrophysiological effects of hyperoxia across cortical grey matter.

4.4.3.1.   Experiment protocol

Nine subjects (23-30 years, 4 female) participated and gave prior informed written consent. Prior to the MEG measurements, subjects sat upright on the scanner bed connect to the RespirAct circuit, whilst baseline metabolic values were estimated and targeted. The respiratory paradigm involved 1 minute of baseline followed by

2 cycles of 5 minutes of isocapnic hyperoxia ($P_{ET}O_2 =$ 500mmHg, subject's resting $P_{ET}CO_2$) separated by 5 minutes of baseline with a final 1 minute of baseline (Figure 4-8). The duration of the respiratory challenge was 21 minutes, including transitions.
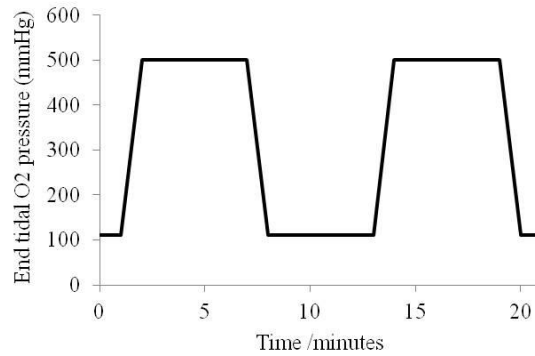
Figure 4-8) Targeted respiratory paradigm: 2 cycles of isocapnic hyperoxia ($P_{ET}O_2$=500 mmHg), $P_{ET}CO_2$ targeted at subject-specific baseline throughout.

MEG data were acquired using a 275-channel CTF MEG system (MISL, Port Coquitlam, BC, Canada), at a rate of 600 Hz, with a 150 Hz anti-aliasing hardware filter and with synthetic third order gradiometer interference suppression. Subjects were instructed to lie supine on the MEG bed and to fixate their eyes on a dot presented on a screen located around 40 cm in front of them. For head localisation, three electromagnetic coils were placed on the head (nasion, left preauricular and right preauricular), the position of these coils on the subject's head were measured using a 3D digitiser (Polhemus isotrack). These coils were energised to locate the position of the subject's head within the MEG helmet. An MPRAGE structural scan was acquired using a Philips Achieva 3 T MR scanner. Imaging acquisition parameters were TI/TE/TR = 960/3.9/8.3 ms, FOV = 256 x 256 x 160 mm, 1 mm^3 isotropic resolution, FA = 8°, SENSE acceleration factor = 3. The locations of the fiducial markers and MEG sensors with respect to the brain anatomy were determined by matching the digitised head surface to the head surface extracted from the structural MRI.

MEG data were processed using the method previously described to study the effect of hypercapnia on electrophysiological signals [130]. First 4 dimensional/volumetric maps of the timecourse of the change in electrical oscillatory amplitude for the theta (4 – 8 Hz), alpha (8 – 13 Hz), beta (13 – 30 Hz) and low gamma (30 – 50 Hz) bands, were derived using the beamformer approach on a 5 mm grid [198-204] spanning the whole brain. For all voxels and frequency bands, the difference in the mean amplitude envelope between the hyperoxia and normoxia time windows (discarding transition periods) was computed and normalised by the normoxic value. Statistical significance in the difference between normoxia and hyperoxia was assessed using a Monte Carlo technique [205-207] in which 50 'fake' pseudo-T statistical images were calculated with active and control windows randomly switched. Voxels were conservatively identified as having statistically significant changes if they fell in the upper 5th percentile of T-values computed in the randomised images.

Regions of interest were probed further in finer frequency bands using local beamformer estimates of neural oscillatory amplitude; the 17 frequency bands used were: 1 – 4 Hz, 2 – 6 Hz, 4 – 8 Hz, 6 – 10 Hz, 8 – 13 Hz, 10 – 15 Hz, 13 – 20 Hz, 15 – 25 Hz, 20 – 30 Hz, 25 – 35 Hz, 30 – 40 Hz, 35 – 45 Hz, 40 – 50 Hz, 45 – 55 Hz, 50 – 60 Hz, 55 – 65 Hz and 60 – 80 Hz. Since no prominent areas of oscillatory amplitude change were observed on the initial beamformer images, we chose to probe three brain locations in which changes had been previously observed for hypercapnia; the occipital lobe (MNI [-8 -80 -6] mm), the right motor cortex (MNI [34 -24 54] mm) [130] and the medial frontal cortex (MNI [-2 36 32] mm), an area associated with cognitive processing in working memory [207]. Hilbert envelopes for each frequency band were averaged across periods of hyperoxia and normoxia, and the resulting spectra averaged across subjects. Significant differences between hyperoxia and normoxia were tested using a non-parametric Wilcoxon Signed Rank test with Bonferroni correction for multiple comparisons.

4.4.3.2.   <u>Results</u>

The mean hyperoxic step was 471 ± 13 mmHg, with a baseline of 116 ± 3 mmHg averaged across subjects, while $P_{ET}CO_2$ varied by less than 1 mmHg. There was no significant change in breathing rate (Pearson correlation, $p = 0.49$) or alpha band oscillatory amplitude (Pearson correlation, $p = 0.23$) across time, suggesting subjects' alertness did not diminish with task duration.

Hypercapnia data has been previously published by Hall et al. [130], and uses the same experimental paradigm (subjects focused on a fixation cross throughout). Figure 4-9A depicts group averaged maps of neural oscillatory amplitude in response to hyperoxia in the alpha, beta and gamma frequency bands and the equivalent hypercapnia images (in response to $\Delta P_{ET}CO_2 = 6.7 \pm 0.7$ mmHg) [130] are also shown (Figure 4-9B).
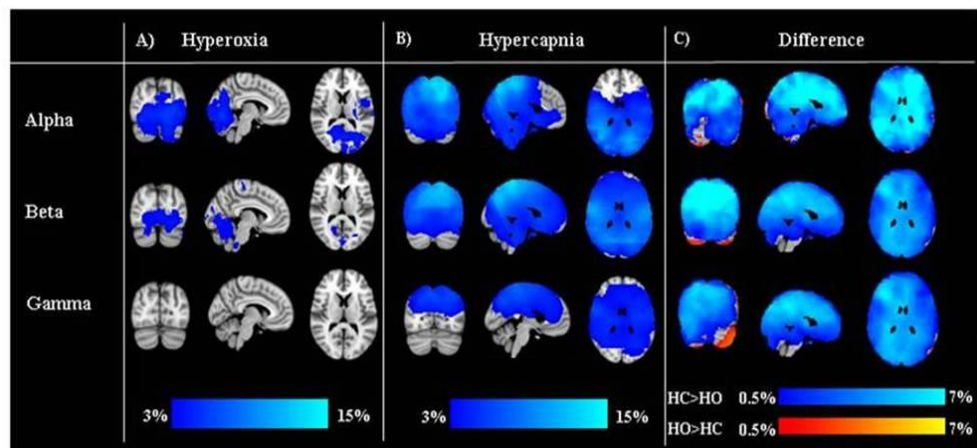
Figure 4-9) Group maps of the reduction in neural oscillatory amplitude in response to hyperoxia in the alpha (8-13 Hz), beta (13-30 Hz) and gamma (30-50 Hz) bands, (3-15 %). B) This is contrasted with a previously reported hypercapnic stimulus (3-15 %) [130] which produced a robust global desynchronisation, evident across all subjects, (3-15%). C) The regions where a hypercapnia induced change is greater than a hyperoxia induced change are shown in dark/light blue (0.5-7 %). Regions where a hyperoxia induced change is greater are shown in red/yellow (0.5-7 %).

Whereas hypercapnia elicited large scale, robust changes in MEG measured oscillatory amplitude, the equivalent changes observed using hyperoxia involve small focal areas of amplitude reduction, predominantly in occipital brain areas. Figure 4-9C shows the difference in oscillatory response between hypercapnia and hyperoxia, with a positive difference on hypercapnia shown in blue and hyperoxia in red. It should be noted that regions in red are predominantly in the cerebellum, spatial locations where the SNR of MEG is limited. Maps of change in the theta band (not shown) showed no robust changes for either hyperoxia or hypercapnia.

Figure 4-10A-C show the spectral changes in neural oscillatory amplitude elicited by hyperoxia and hypercapnia [130] in three selected brain regions. Figure 4-10D-F show the corresponding changes in amplitude across the alpha, beta and gamma band. As seen in Figure 4-9A, the most pronounced change occurred in the occipital lobe (MNI [-8 -80 -6] mm) across the alpha band (8-13 Hz) where a reduction of 0.5 ± 0.06 nAm was observed under hyperoxia.

These figures allow the change in neuronal oscillations in response to isocapnic hyperoxia to be contrasted with previous results from an iso-oxic hypercapnic stimulus. Previously reported hypercapnia data [130] produced a robust global desynchronisation, evident across all subjects. In the hyperoxic case, changes are smaller in magnitude and spatial extent, and are less robust across subjects.
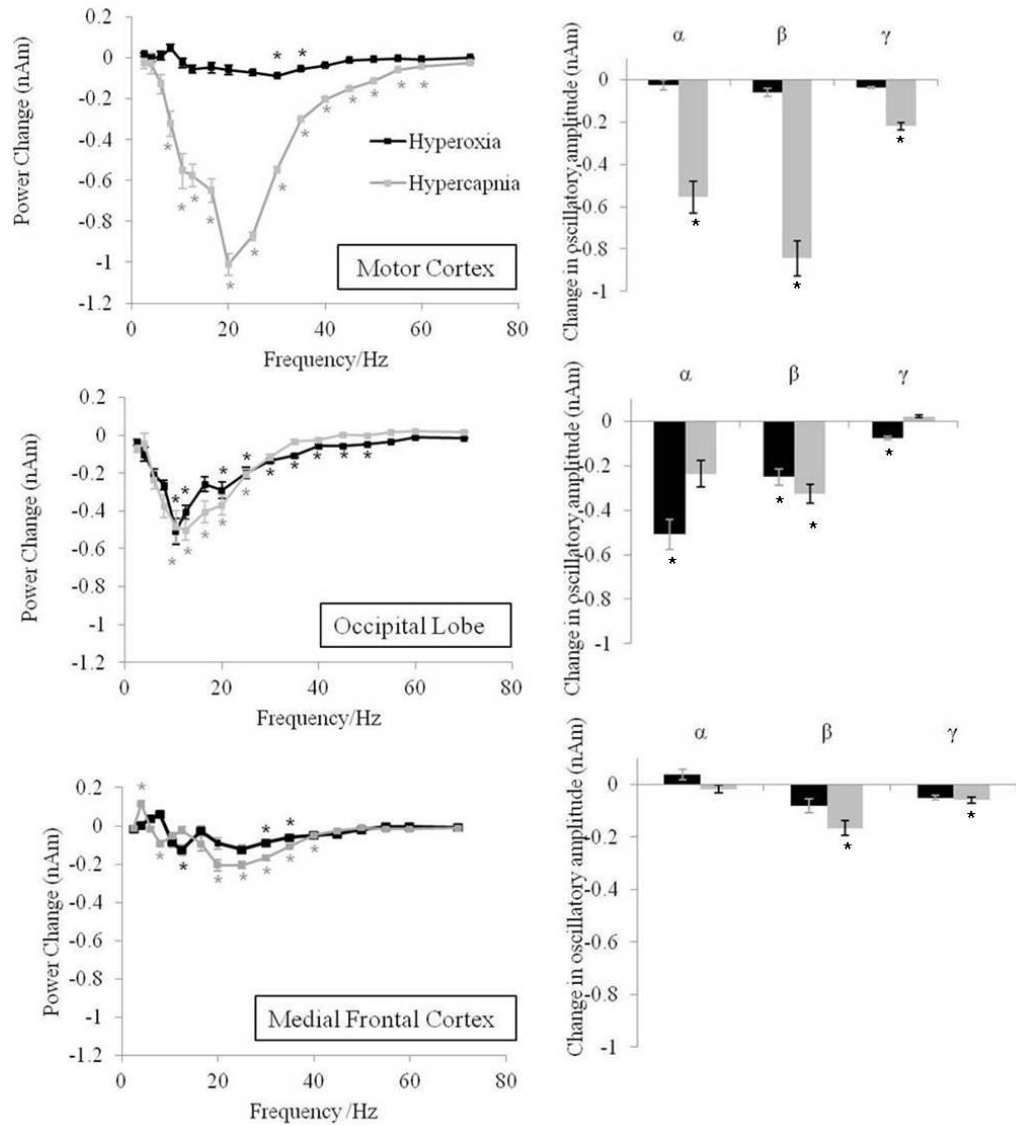
Figure 4-10) The reduction in neural oscillatory power (mean ± SEM) was interrogated across A) the motor cortex, B) the occipital lobe and C) the medial frontal cortex (F) in response to hyperoxia (black) and hypercapnia (grey) (Hall et al. 2011). D-F) This power change is further compared in the same regions across the alpha, beta and gamma band. * denotes where p < 0.05 (Wilcoxon Signed Rank test).

4.4.3.3.　　**Discussion**

The results from this study show that hyperoxia produces a small focal change in spontaneous MEG signals. This is in contrast to previous findings of a global effect of greater amplitude on hypercapnia [130, 133]. Both of these findings could significantly impact on the fundamental assumptions regarding the isometabolic nature of hyperoxia and hypercapnia for calibrated BOLD, albeit to different extents. Although there is no causal link between neuronal oscillations and changes in $CMRO_2$, it is believed that MEG signals are generated by synchronised, post-synaptic current flow in the dendrites of pyramidal neurons, and theoretical evidence [208] suggests that the majority of energy use in the brain is involved with similar post synaptic events. This suggests, albeit indirectly, that a change in the MEG signal is associated with energy demand. This has been supported by invasive studies in animals [209] and humans [210, 211], as well as non-invasive studies using MEG [124, 212-215] which suggest a relationship between task driven modulations of neural oscillations and the BOLD response. Furthermore recent evidence [216] shows that hypercapnia induces measurable, spatially-dependent changes in $CMRO_2$ which are in good agreement with the electrophysiological oscillatory changes previously reported [130]. Therefore it seems unlikely that the observed changes in neural oscillations observed can occur without concomitant changes in cerebral energetics.

The significant reduction in amplitude of low frequency neural oscillations in the occipital lobe in response to hyperoxia is consistent with the reduction in alpha power in previous EEG recordings [194] and may reflect an increase in vigilance with supplementary O_2 [217]. Confounding effects due to patient discomfort and somatosensory activation are minimised, as hyperoxia is difficult to distinguish from medical air, as highlighted by its use in placebo-controlled trials [217-219]. The proposed role of hyperoxia on altered vigilance, task performance and cerebral metabolism needs further investigation, with particular emphasis on the dynamic relationship between these factors.

As discussed, it is likely that the altered neural oscillatory processes induced by both hyperoxia and hypercapnia [130] will indeed impact on the assumption of

96

iso-metabolism made in BOLD calibration. However, the finding that isocapnic hyperoxia induces neural oscillatory changes that are smaller in magnitude, smaller in spatial extent and less robust across subjects compared to iso-oxic hypercapnia implies that isocapnic hyperoxia is a more appropriate stimulus than hypercapnia for calibrating the BOLD response [8]. This said, the small focal effect of hyperoxia on neural signals in the occipital lobe remains significant, suggesting that further investigation is required in order to determine if the observed change may lead to an under/overestimation of $CMRO_2$ in these areas. The significant but differential effects of hyperoxia and hypercapnia on neural oscillatory processes may be of even greater importance to the more recent combined calibrated BOLD models [10, 141]. Further investigation would allow quantification of separate hyperoxia and hypercapnia $CMRO_2$ error terms.

4.5 Effect of isocapnic hyperoxia on functional hyperaemia

The coupling of blood flow and neuronal activity is fundamental to the interpretation of haemodynamic responses. The cardinal study by Roy and Sherrington gave rise to the idea that increased neuronal activity coincides with an increase in local CBF [38] and gave rise to an entire research field. This evoked response is known as functional hyperaemia, and the mechanisms which govern it have been an area of great research interest for over 100 years. The mechanisms behind the coupling between neuronal activity and vascular changes are still poorly understood. Whilst a brief overview will be given here, the available physiological and biochemical data far surpasses the scope of this thesis. Here, the role of functional hyperaemia is considered within the context of oxygen delivery. This section first introduces the key proposed mechanisms and later presents results which address fundamental question, is the evoked CBF increase caused by decreased O_2 concentration?

At rest, the majority of baseline energy required for ATP turnover is from oxidation of glucose via the TCA cycle [220]. With the reported mismatch of $CMRO_2$ and CBF increases in response to functional activation it was proposed that $CMRO_2$ and CBF uncouple [53, 221]. However, Buxton and Frank [61]

97

proposed that rather than uncoupling, the much larger CBF increase is necessary to ensure the adequate delivery of O_2. During activation, the coupling of CBF and $CMRO_2$ is non-linear. The Oxygen Limitation Model (OLM) assumes that tissue pO_2 is so low such that capillary pO_2 determines the diffusion gradient and increased perfusion acts to increase delivery of oxygen to the tissue.

The key assumption that tissue pO_2 is close to zero (that $CMRO_2$ cannot increase without a rise in CBF) has been challenged by experimental evidence. Whilst capillary pO_2 has been found to be 40-50 mmHg [222], tissue O_2 remains ~ 20-30 mmHg [223-226]. Further research into the maintenance of tissue pO_2 [225] proposed that the increase in CBF maintains pO_2 in distal regions with low levels of pO_2 and increases pO_2 in regions with high levels of pO_2. In essence, the hyperaemic response serves as an evolutionary safety mechanism to prevent dangerously low pO_2 levels during transient activation-induced periods of hypoxia.

It is not clear whether the depletion of O_2 directly triggers the hyperaemic response. Mintun et al [227], assessed the effects of mild hypoxia [$F_iO_2 = 0.12$] on the evoked local CBF in response to a visual activation task using ^{15}O PET and. results showed that the evoked response under visual activation was equivalent between normoxia and hypoxia. They concluded that the increase in CBF observed in response to functional activation is not driven by the need to match local O_2 concentration to $CMRO_2$. Paradoxical findings have been presented from the Akita Laboratory, Japan, where they have investigated the effect of supplementary O_2 on evoked responses[228, 229]. It was demonstrated in anesthetised rats that the magnitude of the evoked local CBF (lCBF) response (due to hind paw electrical stimulation of 5Hz frequency) increased by 64-68% under 100% O_2 inhalation as measured with laser Doppler flowmetry (LDF).[228, 229]. They reported a similar effect in the human visual cortex [230], assessing amplitude and temporal dynamics of the BOLD response. On visual activation the hyperoxic BOLD response was 13% higher than normoxic conditions, which was supported by a reduced rise time (from 5.3 to 5.1 s), but this was not significant (p = 0.06). Under 100% O_2, the hyperoxic BOLD response at rest was found to be approximately 1.1% higher than under normoxia. Whilst the authors

propose the BOLD results support an increase in evoked CBF on hyperoxia, a lack of direct perfusion measurement limits the interpretation of the results.

Roy and Sherrington hypothesised that neuronal activity is coupled to the evoked blood flow response via vasodilative by-products of metabolism [38]. It is plausible that other non-oxidative metabolic products regulate CBF. These could include (but are not limited to) adenosine [231, 232], nitric oxide [233] or arachidonic acid and associated derivatives [234-236]. However the involvement of these neurotransmitters could also play a feed-forward signalling role, whereby increase glutamatergic signalling results in vasodilation before $CMRO_2$ is necessarily required [237]. It has been proposed that a post-synaptic increase in calcium ion ($Ca2^+$) plays a significant role in modulating the arachidonic acid pathways in astrocytes [238]. However, controversy exists over the temporal mismatch between Ca^{2+} dynamics, functional hyperaemia and the role of astrocytes (a non-neuronal cell which can detect synaptic activity [239]) in neurovascular coupling [237, 238, 240]. The inability to distinguish between common pathways held by feedback and feed-forward signalling further complicates this issue [238].

Previous research into the effects of O_2 on functional hyperaemia have observed a concomitant change in baseline CBF [227-229]. The results in section 4.4.1 have confirmed that it is unlikely that O_2 is an active vasoconstrictor, suggesting that observed changes in CBF on hyperoxia [152, 165, 172] reflect CO_2 fluctuations. It is likely that an alteration in baseline state will impact on O_2 extraction and alter the functional response.

The aim of the present study is to assess the effect of isocapnic hyperoxia on evoked CBF, where baseline CBF remains constant across conditions. Following the same principles as Matsuura et al. [229], it is hypothesised that if O_2 concentration serves as a trigger for functional hyperaemia, the evoked CBF response will be reduced under hyperoxia.

4.5.3.1. Experimental protocol

The study was approved by the University of Nottingham Medical School Ethics Committee, twelve subjects (age 24-48 years, 4 female) participated and gave prior informed written consent. MR scanning was performed using a Philips Achieva 7 T system with head volume transmit and 32 channel SENSE receive coil with foam padding used to reduce head motion.

Prior to the MRI measurement, the subject sat upright on the scanner bed while baseline metabolic values were estimated and targeted. The hyperoxic challenge in this experiment involved 7 minutes of baseline, 7 minutes of isocapnic hyperoxia ($P_{ET}O_2$ = 500 mmHg, subject's resting $P_{ET}CO_2$), presented in a pseudo-random order, followed by a final minute of baseline normoxia.

An initial functional localiser scan (GE-EPI, SENSE factor 2, TE/TR=25/3000ms, 2x2x3mm^3 resolution, FOV=192x192x45mm^3) was acquired to identify slices comprising the motor cortex via IViewBOLD (Philips, Best, Netherlands). During the localiser, subjects were required to perform a 5 minute bilateral finger-tap task (30 s rest, 30 s tap). At rest, a small white fixation cross on a black background was projected on a screen at the end of the magnet bore, with the active condition cued by a large red "TAP" on a black background. Subjects wore prism glasses throughout in order to view the screen.

The main functional task consisted of a bilateral finger-tap (30 s tap, 30 s rest) repeated throughout the respiratory challenge (Figure 4-11). A LL-FAIR (multiphase) ASL scheme (selective and non-selective imaging volumes of 45 and 250 mm respectively) with in-plane saturation was used to measure CBF. Acquisition parameters were FA = 35°, TI/TA/TR=200/300/3000 ms and 8 readout phases per TR. Vascular crushing was applied using a bipolar gradient of 10 ms duration with v_{ENC} = 50 mms^{-1}. Images were acquired using a GE-EPI readout; 5 contiguous slices per TR, 2x2x3 mm^3, FOV = 192x192x45 mm^3, TE = 25 ms (minimum due to applying vascular crushing), SENSE factor 2. A 90° pulse was applied to the final phase to increase the BOLD weighting. This allowed the simultaneous measure of CBF and BOLD on normoxia and hyperoxia in

response to a functional challenge (Figure 4-11B and C). Inversion recovery (IR) data were acquired across 10 inversion times (100-2500ms) for T_1 mapping, from which to create a GM mask defined as those voxels with $1.7 \leq T_1 \leq 2.3$ s.
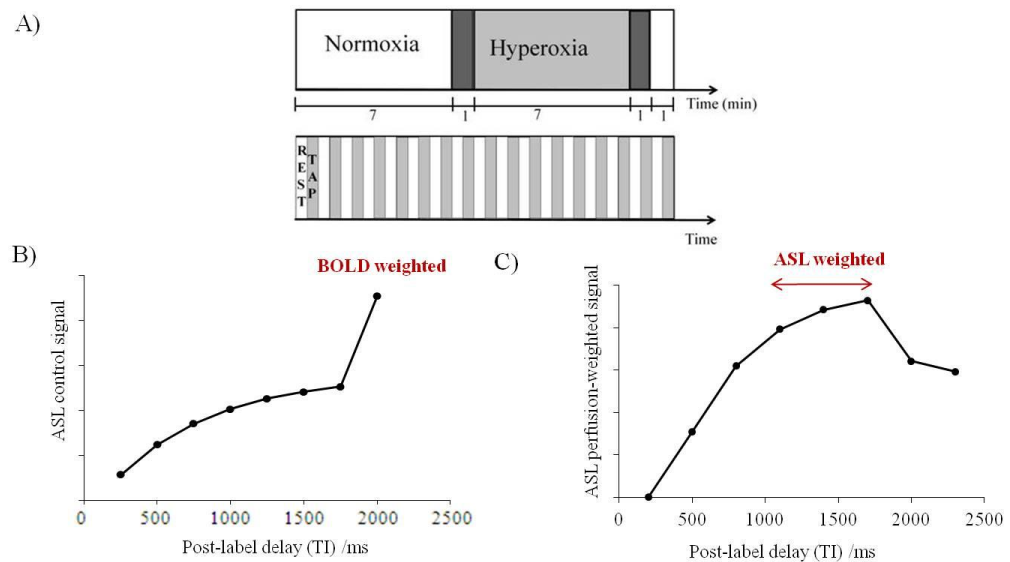
Figure 4-11) A) Schematic of the respiratory and functional paradigm. The normoxic (white) and hyperoxic (light grey) stimuli both lasted for 7 minutes, with 1 minute transition periods to and following hyperoxia (dark grey). Stimuli were presented in a pseudo-random order, with one minute baseline period presented at the end or start of the sequence depending on whether normoxia was presented first or second respectively. The subject was required to perform a bilateral finger-tap of 30 s rest/tap cycles throughout the respiratory challenge. B) Schematic of Look-Locker-EPI ASL (LL-EPI ASL) control signal (TI/TA = 200/300 ms, 8 readouts) as a function of post-label delay (TI). A 90° RF pulse applied at the final TI increases the BOLD weighting. The perfusion-weighted difference signal is shown in C), phases 4-6 (TIs 1100 ms - 1700 ms) provide maximal perfusion weighting and are used in the GLM analysis.

4.5.3.2. Data Analysis

Label and control images were subtracted to produce perfusion weighted difference image for each readout phase, with an effective temporal resolution of 6 seconds. Perfusion weighted images were visually inspected for motion artefacts (most easily identified by "ringing" of extremely high or low signal intensity in these difference images) and 1 subject with severe motion artefacts were discarded. To increase the contrast-to-noise ratio, the perfusion-weighted (PW) difference images from phases 4-6 were averaged to form a single PW image on which GLM analysis could be performed. Phases 4-6 (TI's 1100 ms – 1700 ms) were selected as they represent time points where there should be a large PW signal difference between rest and activation. Data were smoothed with a 5 mm FWHM Gaussian kernel and a temporal filter with 120 s cut-off was applied (twice the length of a single rest/activation trial). Maps of statistical significance of the CBF response to the motor task were formed using GLM analysis in FEAT (FSL, FMRIB). The resulting activation maps were converted to binary masks (where $Z > 2.3$ and $p < 0.05$) in MATLAB. The CBF ROI was used for both CBF and BOLD analysis. Close agreement is observed between the perfusion and BOLD activation maps, shown for an example subject in Figure 4-12. However, CBF activation is limited to the primary motor cortex, rather than additional supplementary motor area activation.
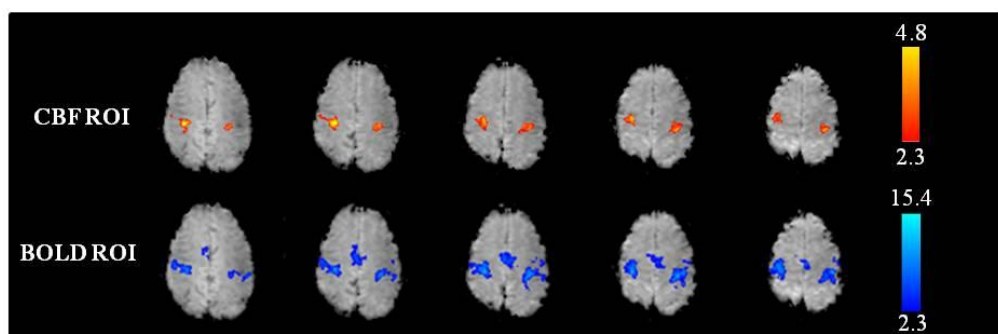
Figure 4-12) Motor cortex activation maps from GLM analysis for a representative subject. The CBF response (red) shows a smaller spatial extent than the BOLD response (blue), there is close agreement between the two ROIs.

The motor ROI identified from the GLM analysis was multiplied by the GM mask to ensure that it included only GM voxels within the motor cortex, to prevent confounds from white matter voxels (where perfusion values are expected to be lower). To assess baseline perfusion, a baseline GM mask was created by subtracting the motor GM ROI from the full GM mask (Figure 4-13). LL-FAIR datasets (for the motor ROI), were divided into active and rest conditions at both normoxia (NO) and hyperoxia (HO). The GM ROI and baseline GM ROI were interrogated for all conditions. Data across transition periods was discarded. Data were averaged within an ROI to obtain a perfusion-weighted signal time-course across the 8 readout phases for each of the four conditions (NO-rest, NO-tap, HO-rest, HO-tap). Normoxic M_0 was estimated from the T_1 map according to the equation $S(t) = M_0(A - e^{(-t/B)})$ using a least squares fit and accounting for the successive flip angles. The change in T_2^* induced by motor activation and hyperoxia in the 'Motor ROI' was calculated from phase 8 of the LL-control BOLD, and this modulation was used to scale M_0 for hyperoxia and activation [67]. The timecourses were normalised by the respective M_0 values and using the kinetic model of Francis et al. [99], the normalised time courses were fitted for CBF, transit time ($\angle_a$) and exchange time (δ), where tissue arrival time, $\angle_{tissue}$, can be estimated from $\angle_a + \delta$. The T_1 of blood was assumed to be 2.2 s at NO [186, 187] and 2.0 s at HO [7,8], whilst the T_1 of grey matter (GM) was assumed to be constant at 2.0 ms.
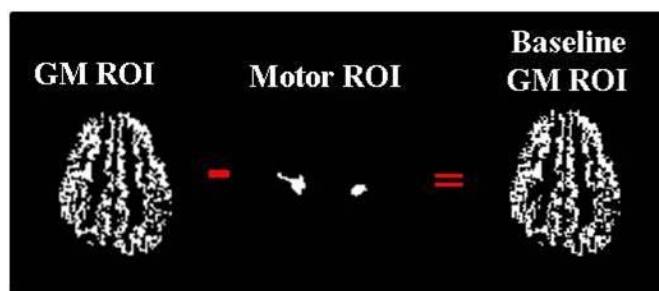
Figure 4-13) A 'baseline grey matter (GM) mask' was created on an individual subject basis by subtracting the 'motor ROI' from the 'GM ROI'.

The 90° flip angle used for the last readout phase provided sufficient sensitivity to assess BOLD weighting in the label and control data. The average BOLD signal was measured within the CBF motor ROI for normoxic and hyperoxic periods

(with transitions discarded) for tap and rest conditions. The percentage BOLD signal change was measured between the tap and rest conditions for normoxia and hyperoxia. Statistical significance of changes was assessed with a non-parametric Wilcoxon Signed Rank test (SPSS 16, Chicago, IL, USA).

4.5.3.3. <u>Results</u>

On hyperoxia $P_{ET}O_2$ increased by 359 ± 14 mmHg (mean ± SEM across 11 subjects) from a baseline of 118 ± 5 mmHg. $P_{ET}CO_2$ varied by less than 1.5 mmHg. Figure 4-14A shows example CBF weighted images overlaid with a CBF statistical activation map to finger tapping, all subjects showed robust activation of the motor cortex in response to the task. Example perfusion time courses from the motor ROI are shown for each condition in Figure 4-14B.
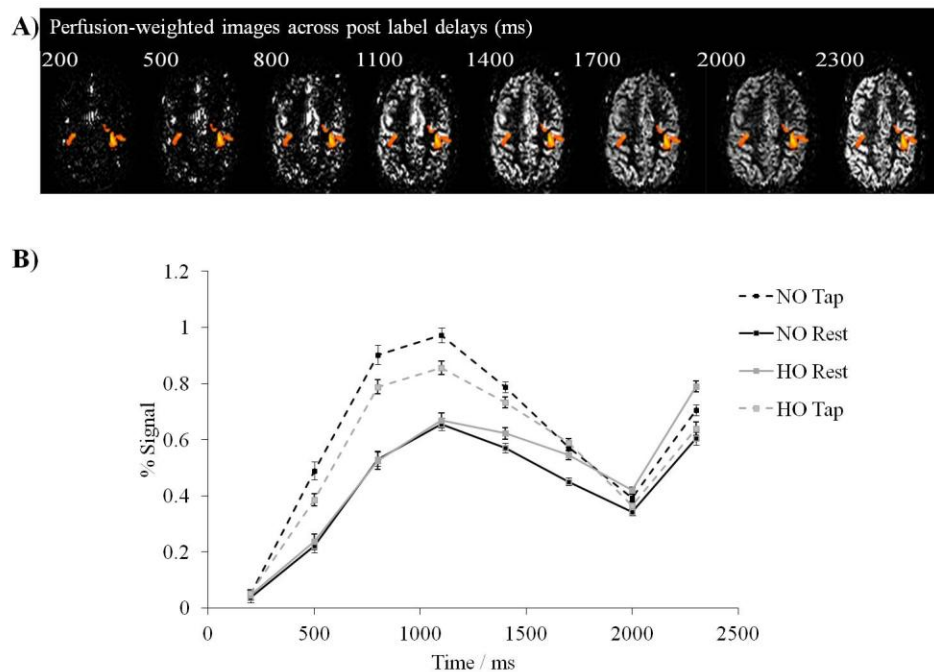
Figure 4-14) A) Example CBF-weighted images for each label delay (in ms) overlaid with active regions defining the motor ROI as produced in FEAT (FSL, FMRIB). B) LL-EPI FAIR timecourses across the 8 readout phases for normoxia (NO, grey) and hyperoxia (HO, black) from the 'Motor ROI'. The rest condition is depicted by a solid line and the tap condition by a broken line.

Table 4-4 shows the absolute and relative CBF and Δ_{tissue} in the 'Motor ROI' for normoxic and hyperoxic conditions. Hyperoxia had no significant effect on CBF or Δ_{tissue} at rest (Figure 4-15) or under motor activation (Figure 4-16). For both normoxia and isocapnic hyperoxia a significant increase in CBF and reduction in Δ_{tissue} in response to the motor task was seen ($p < 0.05$, Wilcoxon Signed Rank test).

		CBF (ml/min/100g)	Tissue Arrival Time (ms)
Normoxia	**Rest**	64.4 ± 5.6	581.5 ± 105
	Tap	101.0 ± 11.6	417.8 ± 64.5
	Evoked response (%)	64.0 ± 11.1	-23.5 ± 5.8
Hyperoxia	**Rest**	54.9 ± 5.2	566.7 ± 78.5
	Tap	82.0 ± 8.9	453.1 ± 72.2
	Evoked response (%)	55.5 ± 15.7	-17.8 ± 6.9

Table 4-4) Absolute CBF (ml/min/100g), tissue arrival time (Δ_{tissue}, ms) from the 'Motor ROI' for the tap and rest condition, and CBF evoked responses to the fingertap (% change) under both normoxia and isocapnic hyperoxia.

In the 'Baseline GM ROI', resting state perfusion was found to be 57 ± 5 ml/min/100g under normoxia, and 54 ± 5 ml/min/100g under hyperoxia (Figure 4-15Bii). Tissue arrival time was found to be 441± 36 ms under normoxia and 423 ± 47 ms under hyperoxia (Figure 4-15Bi). There were no significant differences in baseline GM CBF or Δ_{tissue} between normoxia and hyperoxia.

The resting BOLD signal increased by 2.1 ± 0.4% going from normoxia to hyperoxia ($p < 0.001$). The BOLD response to the motor task was found to be 10 ± 7 % higher under hyperoxia (Figure 4-16B), however the increase was not significant ($p = 0.25$, Wilcoxon Signed Rank Test).
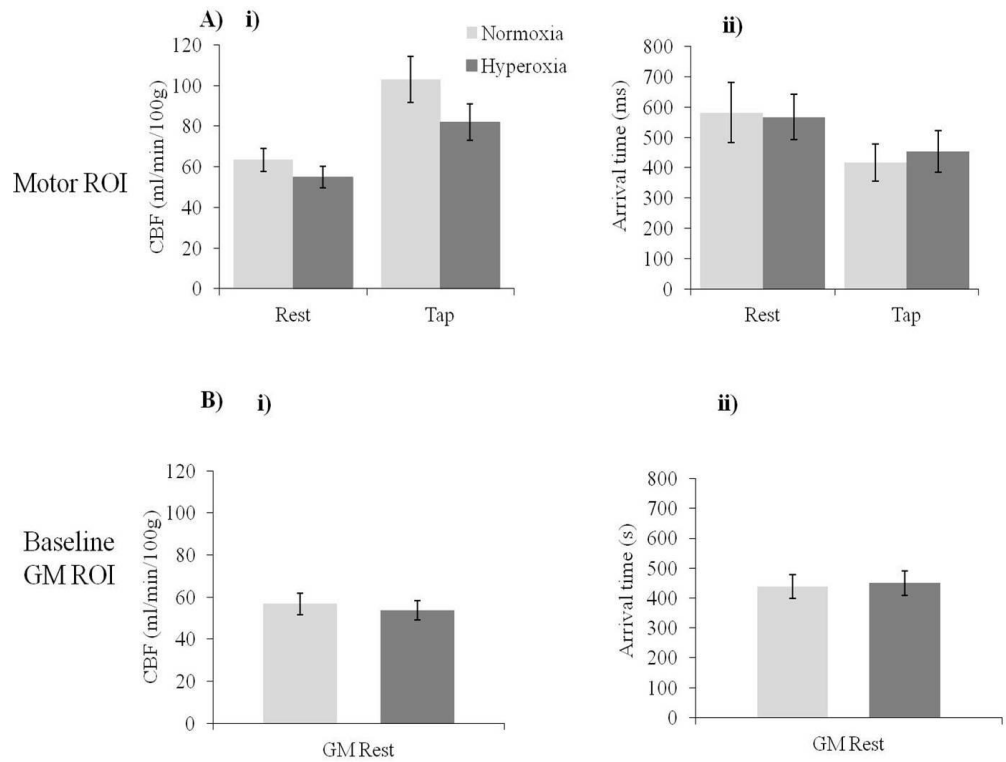
Figure 4-15) Absolute measurements for rest and tap conditions under normoxia (pale grey) and isocapnic hyperoxia (dark grey) from the 'Motor ROI'. A) i) CBF from the motor ROI and ii) Absolute tissue arrival time (Δ_{tissue}). B) i) Measurements for the 'Baseline GM ROI', i) CBF and ii) Resting-state Δ_{tissue}. Hyperoxic results did not differ significantly from normoxic results in either condition or ROI (Wilcoxon Signed Rank test).
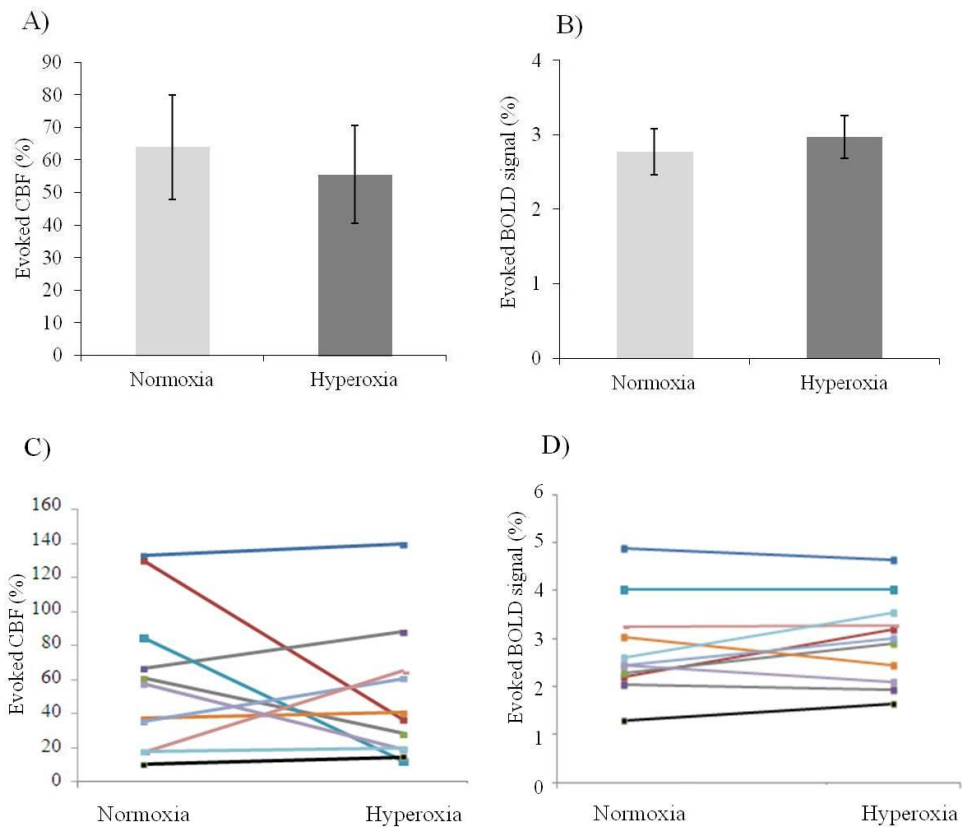
Figure 4-16) Percentage change in A) CBF and B) BOLD signal in the 'Motor ROI' in response to motor activation during normoxia (blue) and hyperoxia (red) averaged across subjects. Individual changes are shown for C) CBF and D) BOLD signal.

4.5.3.4.   Discussion

Here, the role of O_2 in modulating the hyperaemic response was investigated using an isocapnic hyperoxic stimulus. If the hyperaemic response is triggered by the depletion of O_2, the delivery of supplementary O_2 would be expected to modulate this. Previous research in both animals [228, 229, 241] and humans [230] has found a paradoxical increase in local CBF in response to functional activation under hyperoxia. The results presented show no significant change in task-evoked CBF or BOLD signal under hyperoxia, with a trend for CBF change to be reduced. They support the notion that functional hyperaemia is not triggered by a reduction in O_2. From these findings, it was concluded that the evoked response

was independent of metabolic demand but that O_2 may interact with the pathways which regulate changes in local CBF.

This study differs from previous research in that baseline CBF was not allowed to significantly fluctuate under O_2 modulation (in agreement with PC-MRA measurements of mean blood flow under isocapnic hyperoxia presented in Section 4.4.1). Under hypoxia, a global increase in CBF has been reported [227], whilst under hyperoxia, a reduction has been reported [228-230, 241]. When modulating O_2, it may not be sufficient to normalise the evoked response by the stimulus-specific baseline as it is possible that OEF will be augmented. This was highlighted in the recent study of Tajima et al. [241] who used the Hyder model [242] to explain the increased evoked local CBF response. The Hyder model amends the OLM [61], allowing O_2 diffusivity (D) to vary with O_2 tension and CBF. It relates OEF to O_2 diffusivity (D) and CBF, according to Equation 4-7 and in turn relates CBF to $CMRO_2$ (Equation 4-8).

$$OEF = 1 - e^{-D/CBF} \qquad\qquad \textbf{4-7}$$

$$CMRO_2 = CBF.Ca.(1 - e^{-D/CBF}) \qquad\qquad \textbf{4-8}$$

Here diffusivity is considered proportional to both CBF and capillary blood volume [242]. Tajima et al. [241] report a constriction of capillaries, as such assuming reduced O_2 diffusivity under hyperoxia. Under this assumption, a larger CBF increase would be needed to support an equivalent $CMRO_2$ change under normoxic functional activation. However, the experimental results in this chapter (here using ASL to assess CBF, in Section 4.4.1 using PC-MRA to assess MBF and Section 4.4.2 using ASL to assess aCBV) have demonstrated that isocapnic hyperoxia does not have vasoconstrictive properties. It is perhaps more likely that the reduction measured in response to 100% O_2 reflects the vasoconstrictive properties of induced hypocapnia.

Over recent years, there has been a shift away from the original idea that CBF and $CMRO_2$ are modulated by a single process. The present results provide support against the theory of "oxygen limitation". Buxton has instead proposed a dichotomous interpretation of $CBF/CMRO_2$ coupling; independent

haemodynamic and metabolic responses working in parallel [243]. This raises the fundamental question of which aspects of neural activity drive changes in perfusion and which drive metabolism. This question remains unanswered, leaving a potential for future research.

The effect of hyperoxia on the BOLD response was smaller than might be expected. A previous study by this research group reported an increase in baseline BOLD signal of 6.7 ± 0.8 % (B0 = 7 T, TE = 25 ms) in response to an equivalent increase in $P_{ET}O_2$ [244]. In contrast, the observed change is more line with results observed in response to 100 % O_2, where a change of 1.1 % has been observed in humans [230] and 1.7 % in anesthetised rats [245]. Similarly, an evoked change in BOLD signal of less than 3 % in response to a motor task was observed for both normoxia and hyperoxia conditions, which whilst significant, was less than the expected value closer to 5 % at 7 T. The differences may have arisen from the use of a different functional paradigm (where 2 x three minute blocks of hyperoxia were used in [244]) or ROI definition (the intersection between CBF and BOLD ROI's were used to form a 'combined ROI' in [244]).

The reduced BOLD sensitivity to isocapnic hyperoxia could perhaps be explained by the use of a combined ASL/BOLD measurement. Here BOLD is assessed by increasing the flip angle of the final readout phase of the LL readout from 35° to 90° to yield BOLD weighting. However, the baseline BOLD signal is limited by the recovery time between readout phases (TA). In Chapter 6, a modified LL-EPI FAIR sequence will be presented, which increases the recovery time before the final readout phase in order to increase BOLD sensitivity whilst obtaining good CBF and transit time sensitivity.

Whilst ASL depends on longitudinal relaxation, the detrimental contribution of a change in T_2^* on activation, particularly at ultra-high field, has been highlighted in the literature [67, 88, 246, 247]. The observed increase in BOLD signal in response to hyperoxia and motor activation reflects a change in T_2^*, therefore, here, the contribution of T_2^* to the ASL signal was accounted for when estimating M_0 [67]. Failure to account for an increase in M_0 (due to increased T_2^*) would likely lead to an overestimation of perfusion on activation. At normoxia, failure to

109

account for a change in T_2^* increased the measured task-evoked CBF under both normoxia and hyperoxia (both relative to baseline normoxia for the 'motor ROI') (Figure 4-17). However these changes were not significant (p = 0.08 and 0.43 respectively, Wilcoxon Signed Rank test). Future work could also extend the T_2^* correction to account for the gradient in oxygenation (and so T_2^*) between the venous and arterial sides of the capillary network [88]. By incorporating a more dynamic measure of T_2^*, this would increase the sensitivity to detecting changes in perfusion between rest and activation.
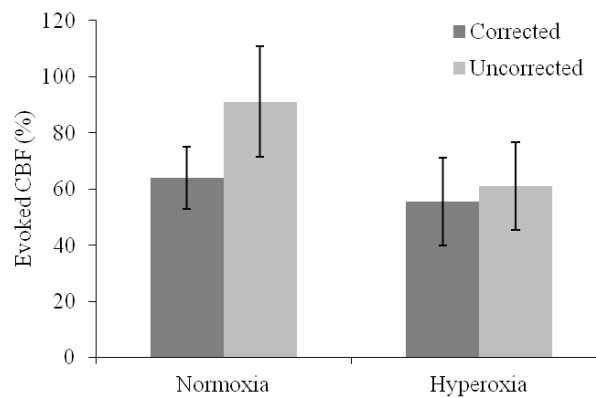
Figure 4-17) Failure to correct for a change in T_2^* (pale grey) led to an increase in the task evoked CBF under both normoxia and hyperoxia when compared to the corrected measure of CBF (dark grey). These change were not significant (Wilcoxon Signed Rank Test). Data areaveraged across subjects (± SEM).

Owing to the complex biochemical pathways under investigation, much of the research to-date has been performed in-vitro or using *in-vivo* animal models. This study has used isocapnic hyperoxia in awake volunteers to remove some of the confounds of earlier work, such as fluctuating CO_2, baseline CBF or neuronal activity. As such, these results support the theory that a change in O_2 concentration is not responsible for the evoked CBF response. Whilst researchers have discussed the relative merits of the metabolic and neurogenic hypotheses, given the breadth of research to date and the lack of definitive answers, it is likely to be an interaction of biochemical pathways.

4.6   <u>Conclusion</u>

The results presented in this chapter have investigated the effect of isocapnic hyperoxia on neurophysiology both at rest and under activation. It was shown using PC-MRA and LL-EPI FAIR ASL that isocapnic hyperoxia does not have a vasoconstrictive effect on mean blood flow in the ICA or arterial CBV, supporting the use of isocapnic hyperoxia as a stimulus in calibrated BOLD. Isocapnic hyperoxia was found to have a significant impact on neuronal oscillations in the occipital lobe, most likely attributed to a change in subject vigilance under hyperoxia. However, the measured changes are smaller than previous changes observed under hypercapnia [130]. These results suggest that hyperoxia is a more reliable stimulus than hypercapnia for calibrated BOLD. After establishing that isocapnic hyperoxia did not have significant vasoconstrictive effects, the role of oxygen in functional hyperaemia was assessed using LL-EPI FAIR ASL. Whilst previous studies have reported in an increased evoked CBF response under 100 % O_2 [228, 229, 241], here no significant change in evoked CBF was found between normoxia and isocapnic hyperoxia. These findings suggest that the task-evoked CBF increase is not caused by a decreased O_2 concentration.

5 Dependence of R_2^* on oxygenation across field strength

5.1 Outline

Chapter 3 introduced the physiological and biophysical origins of the BOLD signal. This chapter further investigates the biophysical dependence of the apparent transverse relaxation (R_2^*) on fractional oxygenation changes. In simple terms, $R_2^* = A.CBV[dHb]^\beta$ [7], where A is a constant, CBV is cerebral blood volume and β is the power law relating concentration of deoxyhaemoglobin (dHb) to R_2^*. β has traditionally been predicted from simulations and models [139, 248, 249] and more recently, experimental measures have been published [9, 250-252]. However, while theoretical values do not fully account for intravascular signal contributions, experimental values to date are subject to concomitant changes in CBV, both of which will bias results.

This chapter first introduces the basic theory underlying models of R_2^* and then discusses theoretical and experimental values of β in the literature. Finally a novel method of experimentally measuring β, without confounding changes in CBV, will be presented and evaluated.

5.2 Introduction

The transverse signal relaxation rate (R_2^*, where $R_2^* = 1/T_2^*$), from which the BOLD signal arises from a change in this parameter, has both intravascular (IV) and extravascular (EV) signal contributions. Whilst the EV signal has been well characterised by numerical simulations [139, 248] and analytical models [249], the IV component was initially neglected, due to the limited space occupied by blood vessels. Intravascular R_2^* ($R_{2\ IV}^*$) is more commonly measured through *in-vitro* experiments [20, 253].

5.2.1 **Extravascular Signal**

Extravascular R_2^* ($R_2^*{}_{EV}$) depends on the spatial distribution of deoxyhaemoglobin (dHb) within blood vessels in a given voxel, the diffusion of water protons through the resulting field gradients surrounding blood vessels, as well as the underlying R_2^*. $R_2^*{}_{EV}$ has been extensively modelled [E.g. 139, 248, 249, 254, 255], and whilst some models considered blood vessels as spherical perturbers [254, 256], the idea of a blood vessel as an infinite cylinder is more physiologically plausible [E.g. 139, 248, 249].

Figure 5-1 shows the basic concept of the infinite cylinder model, where it generally assumes a voxel contains a series of randomly oriented vessels which each contain dHb and occupy a volume fraction f.
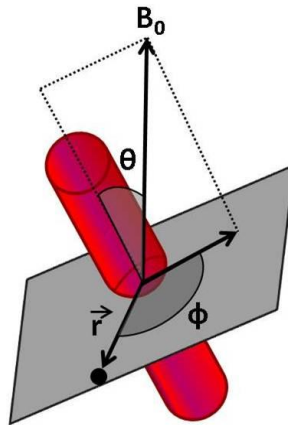
Figure 5-1) The concept of modelling a blood vessel as a magnetised infinite cylinder embedded in a medium where their susceptibilities differ underlies many BOLD models which assume a voxel containing a series of randomly oriented vessels [E.g. 139, 248, 249]. The cylinder (with radius r_b) is oriented at angle θ from the applied B_0 field and the proton position defined by vector $\vec{r}$, which is at an angle ϕ to the component of B_0 in the normal plane.

If a blood vessel exists in a tissue medium with a magnetic susceptibility difference of $\Delta\chi$ between blood and medium, then the vessel magnetic field will

be perturbed around the vessel. This perturbation will lead to a dephasing of protons and so a decay of signal. Ogawa et al. [248] and Weisskoff et al [48] showed that the nuclear processional frequency of spins ($\Delta\omega$) in an inhomogenous field can be characterised by Equation 5-1. It can be seen that the $\Delta\omega$ depends on the susceptibility difference ($\Delta\chi$) induced by a change in oxygenation ($1-Y_v$) and/or magnetic field strength (B_0), where Y_v is the venous oxygenation fraction which is inversely proportional to the concentration of dHb in the blood.

$$\Delta\omega = \gamma.\frac{4}{3}.\pi.\Delta\chi.(1-Y).B_0 \qquad\qquad \textbf{5-1}$$

For a given vessel, the field gradient is proportional to the vessel radius and so the spin dephasing regime is dependent on the vessel size. If the diffusion path length (L_D) is of the order of field perturbations, spins can sample all possible field values during the echo time (TE) and so experience diffusive dephasing (motional narrowing) (Figure 5-2A). If L_D is smaller than the field perturbation (comparable to vessel radius), then static dephasing occurs (Figure 5-2B) where on average a near constant field is experienced by each spin leading to a near constant rate of dephasing between different spins and a linear relationship between R_2' and intravascular frequency offset. The effects of diffusive dephasing are time-dependent as the spin diffuses, various different field offsets are experienced and so dynamic averaging must be used, leading to a quadratic relationship between R2' and echo time [248], i.e. as the echo time increases, spins experience a larger range of field perturbations. The static and diffusive terms in R_2^* are described by Equations 5-2 and 5-3 respectively [257],

$$R_2^*{}_{LV} = k_1(\Delta\omega)b_{LV}f + k_2, \qquad\qquad \textbf{5-2}$$

$$R_2^*{}_{SV} = k_1(\Delta\omega)^2 b_{SV}f + k_2, \qquad\qquad \textbf{5-3}$$

where k_1 and k_2 are constants, $\Delta\omega$ is the frequency offset between the surface of the blood vessel and tissue space, and b_{LV} and b_{SV} are the blood volumes for large and small vessel respectively.
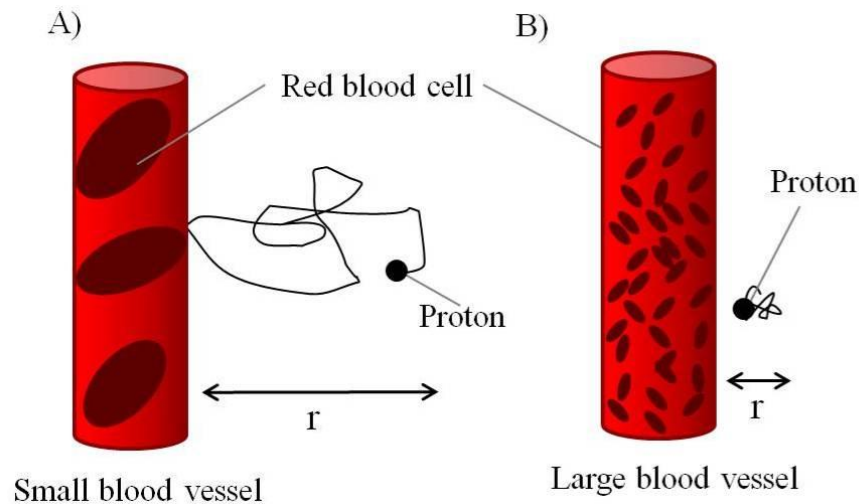
Figure 5-2) Static and diffusive (motional narrowing) averaging is dependent on the length of the diffusion pathway relative to the vessel radius (r) and hence the extent of field gradient . Figure adapted from [257].

5.2.2 Intravascular Signal

R_2^* within a blood vessel ($R_{2\,IV}^*$) can arise from either erythrocyte-plasma proton exchange or from diffusion of protons through field gradients local to erythrocytic membranes. It has been demonstrated in bovine blood that the diffusive effects are predominant [258]. The erythrocyte dimensions are very small in comparison to the diffusion pathway and so it is possible to average the intravascular dephasing effects dynamically, and thus it follows that there will be a quadratic dependence of $R_{2\,IV}^*$ on frequency shift.

In-vitro measures of human blood have achieved a large range of oxygenation values by bubbling 100% O_2 through heparinised blood samples, and shown that whilst there is a quadratic dependence of $R_{2\,IV}^*$ on fractional oxygenation, a linear approximation can be made across the limited range of oxygenation of 0.6-0.8 expected from a functional response [20, 259]. *In-vivo* measurements of blood oxygenation are difficult to obtain, due to the long echo times required and effects of pulsatile flow. The TRUST technique [260] provides a measure of global venous oxygenation taken from the sagittal sinus. A CPMG T_2 measurement is used in combination with ASL labelling to identify the venous blood and quantify

oxygenation from the estimated T_2. However there are difficulties associated with isolating a pure blood voxel.

It may be naive to neglect the IV signal contribution, as the field gradients established around each deoxygenated erythrocyte are much larger than extravascular gradients. This is due to the close proximity of the erythrocyte which houses the dHb to the protons in the plasma [261]. A greater field gradient results in an increased phase change and a larger change in IV signal between rest and activation in comparison to EV signal. It has been shown that at low field strengths, the intravascular transverse decay constant ($T_{2\ IV}^*$) is over an order of magnitude larger than the extravascular T_2^* ($T_{2\ EV}^*$) and so intravascular signal dominates despite occupying only a small voxel fraction [139, 248]. The IV signal component has been shown to account for 53-100% of the BOLD response at 1.5 T and 23-60% at 3 T [262-264]. At high field however, the IV component is significantly reduced in comparison to the EV component [262, 265] due to the very short T_2^* of blood [66], shown to be 4.3 ms at 7 T (*in-vitro* measure) [20].

In fMRI, it is the change in BOLD signal between rest and activation which is generally of interest. This change in signal is dependent on field strength, where vascular contribution to ΔR_2^* decreases with increased field strength. This leads to a change in the IV:EV signal ratio with field strength, such that at 7 T, the signal will be dominated by extravascular signal from the microvasculature. As both the IV and EV compartments will exhibit a degree of diffusive dephasing, both compartments (and the ratio between them) will also depend on TE, the time available for spins to dephase and phase offsets to accumulate. Shorter TE's will increase the IV weighting as the signal will not yet have fully decayed. However, at longer TE's (such as those used in a standard fMRI experiment), at 7 T there will be little signal arising from the IV compartment.

5.2.3 $\underline{\Delta R_2^*\ \text{dependence on fractional oxygenation}}$

The calibration of the BOLD fMRI signal was introduced in detail in Chapter 4 and the physiological assumptions assessed. It is also necessary to assess the

biophysical parameter that is included in calibrated BOLD models [7, 8]; the power law β which relates ΔR_2^* to fractional venous oxygenation $(1-Y_v)$. It is widely accepted that $\beta = 1.5$ at 1.5 T and decreases with field strength, so that β ~1 at 7 T. These values were initially taken from the aforementioned Monte Carlo simulations [139, 248] and analytical models, which were based on the EV signal contribution (discussed below).

In the EV compartment, β is determined by the interplay of static and diffusive dephasing regimes, so that $1<\beta<2$. As B_0 increases, the vessel size limit where the transition is made from one regime to the other reduces, such that at high field strength, the limit where static dephasing occurs is reduced [254] and the majority of vessels are in the static regime such that β tends to 1 [139, 248, 249]. The limit where static dephasing occurs will also depend on echo time, TE, as this determines the length of the diffusive pathway. This is the basis for the assumed values of β in calibrated BOLD models as described above.

5.2.4 <u>Simulating signal perturbation</u>

The initial value of β of 1.5 as used in the original Davis model [7] was based on Monte Carlo simulations by Boxerman et al [139] which investigated the relationship between tissue parameters, imaging parameters and susceptibility contrast. Their work expanded previous simulations of spherical perturbers [256] to magnetised cylinders. By including a network of magnetised cylinders, the model was more physiologically plausible than previous work based on a single cylinder [248] or four nearest neighbours [254].

For an echo time of 60 ms, (assumed typical of clinical applications at 1.5 T), a proton takes 50 random steps (in the $\bar{x}$, $\bar{y}$ and $\bar{z}$ directions) per $\Delta TE = 10ms$ (with standard deviation $A = \sqrt{(2DTE)}$, where D is the diffusion coefficient (for cerebral cortex $D = 1 \times 10^{-5} cm^{-2}s^{-1}$ [266, 267]). At each proton position, the field perturbation of B_z is calculated by summing the intravascular and extravascular perturbations by each cylinder (assuming non-interacting fields). After repeating until t = TE, the phase accumulated by the nth proton (ϕ_n) is calculated according

to $\Delta\phi_n(t) = \gamma.\Delta B_z.\Delta t$ and the resulting signal from Equation 5-4 as outlined in [256],

$$S(t) = \frac{1}{N}\sum_{n=1}^{N} e^{i\phi_n(t)} \ .$$ 5-4

The signal can then be converted to R_2^* using Equation 5-5 as in [248],

$$R_2^* = \frac{-\ln S(TE)}{TE} \ .$$ 5-5

By repeating simulations across a range of vascular concentrations of Gadolinium DTPA (Gd-DTPA), the concentration dependence of R_2^* was established (Figure 5-3). For the frequency shift induced by 0-1mM Gd-DTPA which approximates the BOLD contrast due to 60 % oxygenation at 1.5 T, the relationship is close to quadratic (power = 2.0), remaining supralinear (power > 1.0) for 1- mM Gd-DTPA (equivalent to BOLD contrast due to 60 % oxygenation at 3 T).
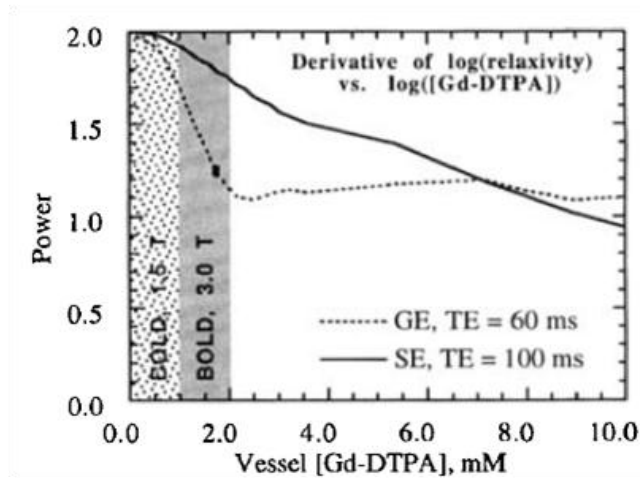
Figure 5-3) Derivative of log (relaxivity, R_2^*) versus log([Gd-DTPA]) provides the power relationship between concentration of Gd-DTPA and ΔR_2^* (dashed line). Reproduced from Boxerman et al. [139]

The notion that β tends to 1 at higher field strength is in good agreement with the analytical expression for ΔR_2^* by Yablonskiy et al [249]. This model is also based on a network of randomly oriented magnetic cylinders, which is then applied to the specific case of a blood vessel network.

118

The relationship between ΔR_2^* and $\Delta\omega$ is limited to the static dephasing regime (where the signal decay time is much smaller than the time taken for a proton to diffuse a distance equivalent to the blood vessel (τ_D)) and so ΔR_2^* estimations are accurate only for medium-large vessel networks (due to increased τ_D) and/or high field strengths (where the signal decay time is shorter). Thus it is predicted that at 1.5 T for small vessel networks only the upper limit of ΔR_2^* would be accurately estimated. Nonetheless, it is now known that large vessels dominate at lower field strength and so the static dephasing model may be more applicable at lower field strength than originally thought. However, as previously mentioned, failing to include the IV contribution in signal decay will have larger impact at lower field strengths [263, 268].

There have been attempts to experimentally test the models on which the assumed values of β are based, each taking a slightly different approach. By repeating a motor task at 1.5, 3 and 7 T, Van der Zwaag et al. [250] used the change in field strength to modulate $\Delta\omega$, finding a linear dependence of ΔR_2^* on field strength. Similarly, the use of hypercapnia to measure BOLD cerebrovascular reactivity (CVR) at 3 and 7 T found a linear dependence on field strength [251]. Most recently, a combined hyperoxic and hypercapnic stimulus was used to directly measure the voxelwise dependence of R_2^* on deoxyhaemoglobin concentration at 3 T [9]. Crucially, the validity of these studies in estimating β is limited by the concomitant changes in CBV, with an increase being observed either due to a hyperaemic response to a motor task [250] or due to vasodilation in response to hypercapnia [9, 251]. The role of CBV as a physiological parameter of the BOLD response was introduced in Section 3.3.1 and Equations 5-2-5-3 suggest the linear dependence of ΔR_2^* on CBV. To accurately determine β as a true biophysical parameter, it is thus necessary to relate $\Delta\omega$ to ΔR_2^* without any accompanying physiological changes. Rossi et al [252] tackled this problem by using 100% O_2 to modulate ΔR_2^*. However, as discussed in Chapter 4, it is thought that CBV will be altered by the vasoconstrictive effects of induced hypocapnia which accompany inhalation of 100% O_2.

By use of a dynamic isocapnic hyperoxic stimulus, this study presents a novel way of measuring the relationship between R_2^* and oxygenation without a change in CBV. Performing this experiment at 1.5, 3 and 7 T, we are able to investigate how this relationship changes across field strength.

5.3 Experiment protocol

This study was approved by The University of Nottingham ethics committee and subjects gave prior informed written consent. Six subjects (24-27 years, 3 female) were scanned at three field strengths (1.5, 3.0 and 7.0 Tesla Philips Achieva systems). The MRI systems were equipped with 8/32/32 channel receive coils respectively.

5.3.1 Respiratory paradigm

A feed-forward, low gas flow system (RespirAct™, Thornhill Research Inc., Toronto, Canada) and a sequential gas delivery (SGD) breathing circuit were used to target end-tidal PCO_2 ($P_{ET}CO_2$) and PO_2 ($P_{ET}O_2$) independently (Chapter 3.4, Slessarev et al., 2007). Prior to MR measurement, the subject lay supine on the scanner bed while baseline metabolic values were estimated and targeted. Whilst in the scanner, the subject received medical air until the respiratory challenge commenced.

Three minutes of baseline normoxia (defined as each subject's resting $P_{ET}O_2$ and $P_{ET}CO_2$) was followed by a 4 minute linear increase in $P_{ET}O_2$ to 500 mmHg (on average 8mmHg targeted increase in $P_{ET}O_2$ with each breath), and a 4 minute linear decrease to baseline, which was maintained for 1 minute, giving a total paradigm duration of 12 minutes (Figure 5-4). $P_{ET}CO_2$ was maintained at a subject specific baseline throughout.
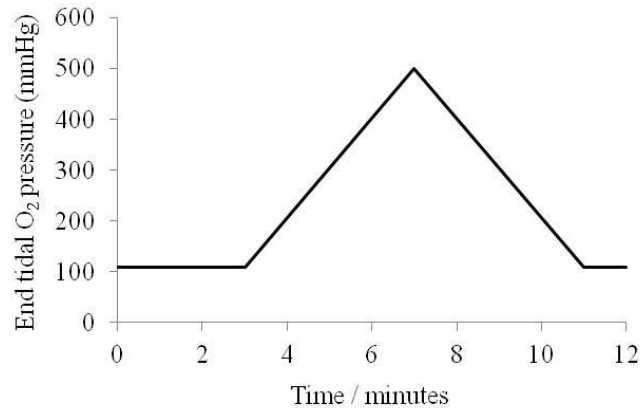
Figure 5-4) Targeted respiratory paradigm: Graded hyperoxia (peak at 500 mmHg O_2). $P_{ET}CO_2$ targeted at subject-specific baseline throughout.

5.3.2 Acquisition

MR Signal was measured dynamics using a double echo gradient echo EPI sequence (SENSE=2.5, FA = 90°, TR=3 s) at two echo times (as shown in Table 5-1) across 240 dynamics. 5 slices were imaged, positioned superior to the ventricles to provide good grey matter coverage. Images consisted of 2x2x3 mm^3 voxels, with a field of view of 212x188x60, 212x184x60 and 192x192x15 mm^3 at 1.5/3/7 T respectively. Inversion recovery EPI (IR-EPI) images were collected (with the same geometry as the DE-EPI data) at 10 post-label delays ranging from 0.1-3 s, from which a grey matter mask was formed. Multi-echo EPI images (TE's ranging from 25-80 ms) were acquired from which to acquire a mask of large vessels.

Field Strength (T)	TE_1 (ms)	TE_2 (ms)
1.5	25	80
3	22	60
7	16	47

Table 5-1) Double echo times (TE_1 and TE_2) for each field strength.

5.3.3 Analysis

Brain masks were created from the first echo time (TE_1) GE-EPI images using the Brain Extraction Tool (BET, FSL) to remove any non-brain tissue from the

image (Figure 5-5A). IR-EPI images were fitted for $M_{0Tissue}$, $T_{1Tissue}$ and inversion flip angle to form $T_{1Tissue}$ maps. These tissue maps were then thresholded to obtain grey matter (GM) masks (Figure 5-5B) Threshold values were 1800-2100 ms for 7 T, 1450-1750 ms for 3 T and 1000-1300 ms for 1.5 T. IR-EPI images were acquired with the same geometry as DE-EPI data and so no further registration was required.

After multiplying the DE-EPI images by both the brain and GM masks (Figure 5-5C), visual inspection showed that it was likely that there was some remaining contribution from CSF and large blood vessels. After applying the GM and brain masks, remaining voxels were sorted in order of signal intensity and the top 3 % were removed in order to remove CSF contribution. To remove large blood vessels the bottom 3 % was removed. This resulted in two GM masks: total GM and masked GM (with CSF and large vessels removed).
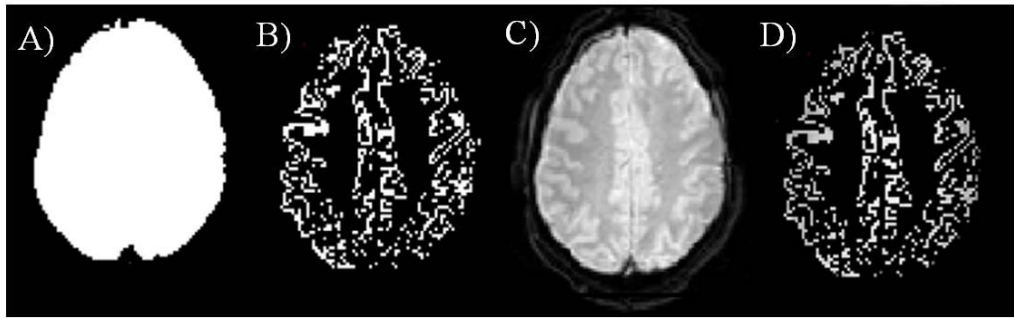
Figure 5-5) Grey-scale Images shown for a representative subject at 3 T. A) Brain mask produced using the Brain Extraction Tool (BET, FSL) applied to the EPI collected at TE_1 (22 ms). B) GM mask produced from thresholding the $T_{1Tissue}$ map obtained from fitting the IR-EPI data from 1450 – 1750 ms. C) EPI collected at TE_1 (22 ms). D) EPI after being multiplied by the masks in (A) and (B).

The simplified Bloch equation for transverse signal decay can be adapted to $S_2 = S_1 e^{-\Delta TE/T_2^*}$ to account for the dual echo acquisition. This can be rearranged to Equation 5-6,

$$R_2^* = \frac{1}{\Delta TE} \ln\left(\frac{S_1}{S_2}\right),$$ **5-6**

where S_1 and S_2 denote the MR signal from TE_1 and TE_2 respectively and $\Delta TE = TE_2 - TE_1$. Using Equation 5-6, R_2^* maps were calculated on a voxel-wise basis for masked GM (i.e. minus CSF and large vessels). This was repeated for each subject at each field strength, using the appropriate ΔTE. Mean baseline R_2^* was taken from the normoxic period and subtracted from each hyperoxic value of R_2^* to obtain ΔR_2^*.

The arterial partial pressure of O_2 can be inferred from $P_{ET}O_2$ and using the method outlined in [8] this can be used to calculate the O_2 saturation of arterial and venous blood (SaO_2 and SvO_2 respectively). O_2 saturation reflects the proportion of heme sites which are bound to O_2 and its relation to the partial pressure of O_2 is described by the O_2 dissociation curve. O_2 dissociation is affected by temperature and pH, but for the general conditions of 310 K and blood pH of 7.4 it can be described by Equation 5-7 [269]:

$$SaO_2 = \frac{1}{\left(\dfrac{23400}{(PaO_2)^3 + 150(PaO_2)} + 1\right)}.$$ **5-7**

After determining PaO_2 and SaO_2, the arterial concentration of O_2 (CaO_2) can be calculated from Equation 5-8,

$$CaO_2 = \left(\phi.[Hb].SaO_2\right) + \left(PaO_2.\varepsilon\right),$$ **5-8**

where ϕ is the O_2 carrying capacity of Hb (1.34 ml_{O2}/g_{Hb} for humans) and ε is the solubility coefficient of O_2 (0.003 $ml_{O2}/(dl_{blood}.mmHg)$). It is assumed that the concentration of Hb is 15 g/dl_{blood} [8]. Unlike PaO_2 and SaO_2, which are unitless values, CaO_2 is measured in ml_{O2}/dl.

Assuming a constant oxygen extraction fraction (OEF), the venous concentration of O_2 (CvO_2) can be calculated from Equation 5-9, where OEF was assumed to equal 0.4. This can be reformulated to correspond to venous O_2, with the partial

pressure of venous O_2 neglected as venous heme sites are unlikely to be saturated, thus no O_2 will be dissolved in venous blood.

$$CvO_2 = CaO_2 - (CaO_2 \mid OEF) \hspace{4cm} \textbf{5-9}$$

Using the calculated CvO_2 the venous O_2 saturation (SvO_2) can be obtained by $CvO_2 = (\phi.[Hb].SvO_2)$. Since it is the venous oxygenation (henceforth termed Y_v) which primarily determines ΔR_2^* (the BOLD contrast), it is this relationship which will be further investigated.

Using the above method each $P_{ET}O_2$ value was converted to Y_v and the $P_{ET}O_2$ trace linearly interpolated so that it was sampled every 3 s, rather than on a breath-by-breath basis, to be in line with the scanner acquisition. Y_v was averaged across the normoxic period to obtain baseline venous oxygenation Y_{v0}.

To enable group averaging of the signal time courses, data bins were created to cover Y_v values across the full theoretical range of 0.6-0.7, in steps of 0.025. R_2^* data were binned and averaged accordingly.

To investigate the effect of field strength on the relationship between ΔR_2^* and (1-Y_v), the data was fit to a a linear 2 parameter least squares fit ($\Delta R_2^* = A(1-Y_v)+C$) to provide the gradient A. To investigate β, the relationship between ΔR_2^* and (1-Y_v), a nonlinear three parameter least squares fit was performed to the power law ($\Delta R_2^* = A.(1-Y_v)^\beta + C$) on an individual subjects basis. β was then averaged across subjects to obtain a mean value for each field strength.

5.4   Results

Three data sets were discarded, due to excessive noise in the R_2^* time course (where the variance in R_2^* masked the change observed in response to hyperoxia), so 6 subjects were analysed at 1.5 T, 4 subjects at 3 T and 5 subjects at 7 T. Out of these, three subjects were scanned at all three field strengths.

	$P_{ET}O_2$ (mmHg)		Interpolated venous Oxygenation (Y_v)	
B_0 (T)	Baseline	Peak	Baseline	Peak
1.5	115.0 ± 3.4	481.8 ± 11.1	0.600 ± 0.001	0.670 ± 0.002
3	108.5 ± 3.1	484.6 ± 9.2	0.600 ± 0.001	0.680 ± 0.001
7	118.6 ± 1.8	490.2 ± 12.6	0.600 ± 0.001	0.670 ± 0.003

Table 5-2) For each field strength (B_0), the baseline and peak $P_{ET}O_2$ values are given with the corresponding venous oxygenation (Y_v) according to the interpolation method outlined in [8].

The average baseline and peak $P_{ET}O_2$ for each field strength are shown in Table 5-1, along with the corresponding interpolated Y_v values. The maximum fluctuation in $P_{ET}CO_2$ was 1.6 % and so was assumed to have minimal influence on R_2^*. There was an inverse correspondence between Y_v and ΔR_2^* as shown for a representative subject at 7 T in Figure 5-6.
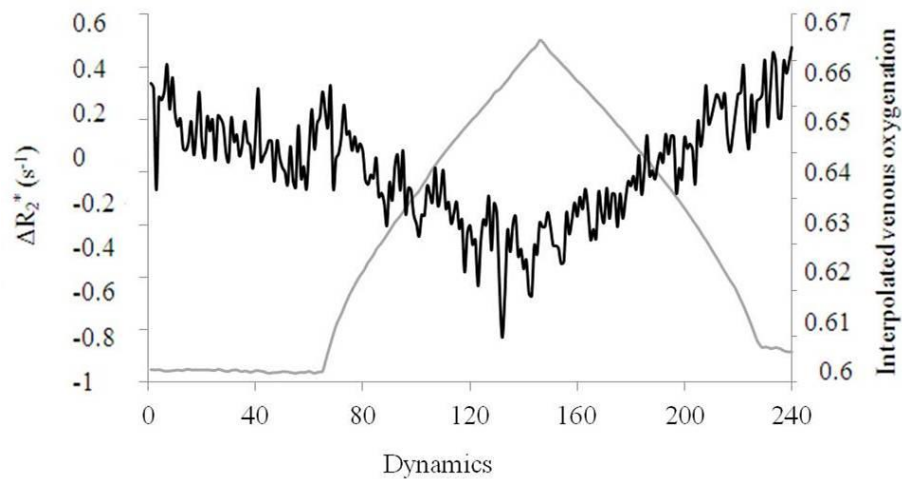
Figure 5-6) Interpolated venous oxygenation (Y_v) time course (solid grey) from a representative subject with the accompanying induced ΔR_2^* (s^{-1}) response at 7 T overlaid (solid black).

As expected, baseline (normoxic) R_2^* increased significantly with field strength as shown in Table 5-3, ($p<0.05$, wilcoxon signed rank test). Figure 5-7 depicts the effect of a change in oxygenation on ΔR_2^* across field strength. The gradient of

$\Delta R_2^* / (1 - Y_v)$ was measured across field strength on an individual subject basis and then averaged (Table 5-3).
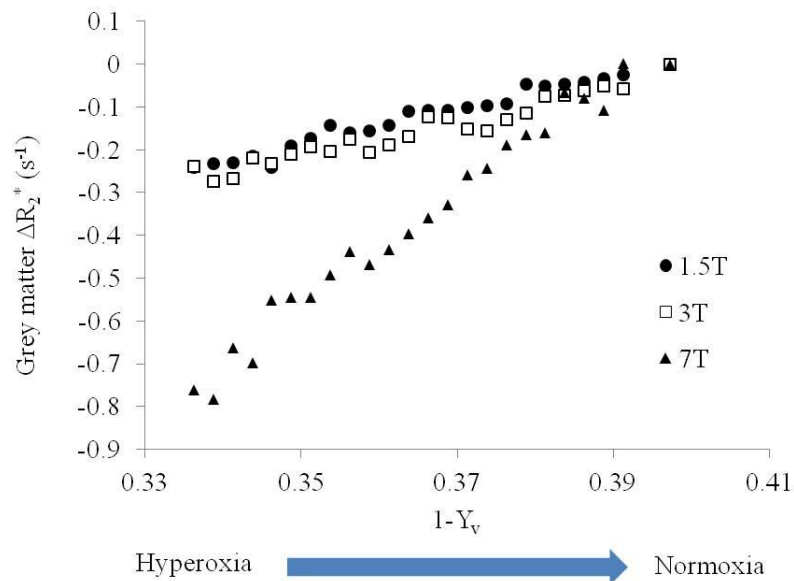
Figure 5-7) The effect of altering venous oxygenation (Y_v) on masked GM ΔR_2^* (s^{-1}) is shown at 1.5 T (black circle), 3 T (white square) and 7 T (black triangle). Data arebinned and averaged across subjects. A nonlinear three parameter least squares fit showed that for masked GM, $\beta < 1$ across all field strengths (Table 5-4). There were no significant differences across field strength (Kruskall-Wallis one-way ANOVA).

Removing large vessels had a significant effect on the gradient at 1.5 T (p <0.02, wilcoxon signed rank test), but not at 3 T or 7 T (Table 5-3). Whilst the gradient at 7 T was significantly steeper than the gradient at 1.5 T or 3 T (p =0.043, Kruskall-Wallis one-way ANOVA), no significant difference was observed between 1.5 T and 3 T.

	B_0 (T)	R_2^* (s^{-1})	$\Delta R_2^*/(1-Y_v)$ (s^{-1})
Total GM	**1.5**	12.8 ± 0.2	4.3 ± 0.5
	3	19.5 ± 1.0	4.0 ± 0.3
	7	33.3 ± 0.7	13.0 ± 2.0
Masked GM	**1.5**	12.7 ± 0.2	4.1 ± 0.4
	3	19.5 ± 0.5	3.9 ± 0.3
	7	33.2 ± 0.7	13.2 ± 2.0

Table 5-3) Baseline R_2^* (s^{-1}) and the $\Delta R_2^*/(1-Y_v)$ gradient (assuming linear model), for total and masked GM (removing large vessels) grey matter (GM) across field strength. Data (mean ± SEM) has been binned and averaged across subjects.

	β		
Subject	**1.5 T**	**3 T**	**7 T**
1	0.4	Excluded	0.3
2	1.0	Excluded	--
3	0.7	0.6	1.3
4	0.5	0.7	0.6
5	0.6	0.9	0.4
6	0.8	0.9	--
7	--	--	0.9
8	--	--	Excluded
Mean (± SEM)	0.7 ± 0.1	0.8 ± 0.1	0.7 ± 0.2

Table 5-4) Measured values of β (mean ± SE) for masked grey matter (GM) across field strength for individual subjects. The dashed line (--) shows that a subject was not scanned at that particular field strength.

Table 5-4 shows the experimental measure of β (from fitting to the power law for masked GM) across subjects, where the average across subjects was <1 at all field strengths. There was no significant difference across field strengths (Kruskall-Wallis one-way ANOVA)

5.5   <u>Discussion</u>

5.5.4   <u>Measuring β across field strength</u>

In this study the dependence of $\Delta R_{2\,GM}^{*}$ on fractional venous oxygenation (1-Y_v) was assessed across three field strengths; 1.5, 3 and 7 T. This was achieved using a graded hyperoxic paradigm which allowed multiple levels of oxygenation to be reached in a single short scan session. The dependence of $\Delta R_{2\,GM}^{*}$ on (1-Y_v) provided a measurement of β; an important parameter for calibration of the BOLD signal to estimate $CMRO_2$. Importantly, the measured values of β presented here are not confounded by a change in CBV, as has been the case in previous studies where CBV has been altered by motor activation [250], the vasodilative effect of hypercapnia [9, 251] or non-isocapnic hyperoxia [252]. The dependence of $\Delta R_{2\,GM}^{*}$ on (1-Y_v), the fitted value of β, was found to be <1 at all field strengths and did not scale with field strength in the manner expected. This section addresses why this may be the case, and whether it may have implications on using values of β which are not experimentally determined.

Equation 5-10 describes the dependence of the frequency shift ($\Delta\omega$) on (1-Y_v) and field strength (B_0),

$$\Delta\omega = k''.\gamma.B_0.\Delta\chi.(1 - Y_v)\,, \qquad\qquad \textbf{5-10}$$

where k" is a constant reflecting vessel geometry, γ is the gyromagnetic ratio and $\Delta\chi$ the change in magnetic susceptibility. It can be seen that $\Delta\omega$ is linearly dependent on B_0, therefore, in simple terms, $\Delta\omega$ will induce a larger change in R_2^{*} at higher field strength and so the $R_2^{*}/(1$-$Y_v)$ is predicted to be steeper. The impact that $\Delta\omega$ has on R_2^{*} is the relationship β.

Baseline (normoxic) R_2^{*} values shown in Figure 5-8 scaled linearly with field strength, in agreement with other cross-field values reported in the literature [250, 252], (Figure 5-8). The variance in R_2^{*} at each field strength is most likely explained by the different acquisition sequences used (single and multi-echo), different methods of ROI selection and different methods of shimming employed in previous studies [250, 252].
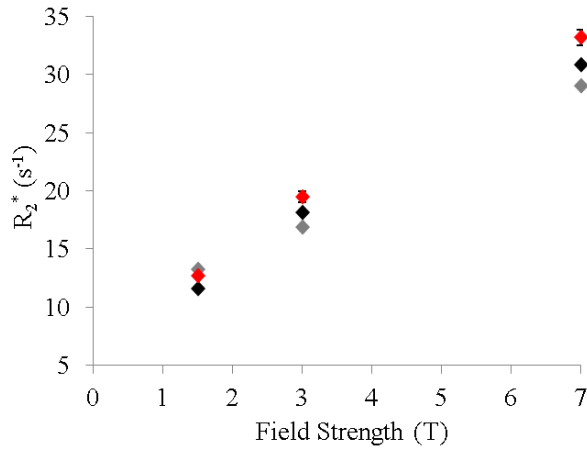
Figure 5-8) Comparison of measured GM tissue R_2^* (s^{-1}) (mean $\pm$ SEM, shown in red) with published GM values ([250] shown in black and [252] in grey).

The gradient of $\Delta R_2^*{}_{GM}/(1\text{-}Y_v)$ scaled with field strength between 7 T and 1.5/3 T did not scale with field strength. However, the gradient at 1.5 T was slightly steeper than 3 T, although this difference was not statistically significant. (Figure 5-7 and Table 5-3). From the measured data, it was possible to use a 3 parameter least squares fit to quantify β. Whilst it has become widely accepted that $\beta = 1.5$ at 1.5 T [7, 139], ~1.3 at 3 T [183, 270, 271] and 1 at 7 T [135, 139, 249], here it has been shown experimentally that β is less than 1 across all field strengths. The results presented here do not agree with the predicted trend for the gradient to scale with B_0 or β to be constrained within a linear and quadratic regime.

The idea of a sub-linear regime for β has previously been proposed [272]. By suggesting the original meaning of β be relaxed so that it also captures the effect of CBV on activation, an optimised $\beta = 0.91$ was suggested for 3 T. It was further argued that the present use of β in the Davis model [7] is an oversimplification and that the use of a single value per B_0 cannot capture the complex dependence of R_2^* on physiological and imaging parameters. This argument is further supported by the modelling work of Martindale et al [273] who used a Monte Carlo simulation of IV and EV BOLD signal sources to develop a look-up table of β values for different values of B_0 and TE. The following section will use these results in combination with IV literature values to investigate the separate

129

contributions of the IV and EV signal to the dependence of ΔR_2^* on a change in fractional oxygenation.

5.5.5 <u>Modelling the intravascular and extravascular signal</u>

To fully understand β and the dependence of ΔR_2^* on a change in fractional oxygenation $(1-Y_v)$, it is necessary to consider both IV and EV signal contributions. However, the assumption that $\beta = 1.5$ at 1.5 T and tends to 1 at 7 T is based on Monte Carlo and analytical models which do not account for the IV signal contribution. Furthermore, using the method presented above and real fMRI experiments, it is not possible to separate fully IV and EV compartments and this must be taken in to account.

Whilst voxels containing large vessels were removed from the region of interest in this study, it is important to note that an average GM voxel is still likely to contain some blood vessels (the cerebral blood volume fraction, f). The GM voxels thus represent a combination of IV and EV signal. Therefore, the β relationship between fractional oxygenation $(1-Y_v)$ and $\Delta R_{2\,EV}^*$ cannot be directly quantified from the given data. Since the BOLD data area combination of both IV and EV signal, a β relationship which reflects two compartments may be more informative for the calibration of the BOLD signal. As outlined in section 5.1.2, the ratio between tissue and blood compartments varies with field strength and echo time and this may explain the unexpected variation in the gradient of $(1-Y_v)$ and GM ΔR_2^* with field strength.

As discussed in Section 5.2.2, the effect of a change in fractional oxygenation on the R_2^* of blood $(R_{2\,IV}^*)$ has been investigated *in-vitro* [20, 253]. Across a large range of susceptibility changes, IV R_2^* has been shown to vary quadratically with Y_v, but this can be viewed as a near-linear relationship across a typical physiological range of 0.6-0.8. Using the *in-vitro* measurements of $R_{2\,Blood}^*$ from [20], the linear relationship between $R_{2\,IV}^*$ and $1-Y_v$ was estimated across the range of oxygenation achieved in this study (0.6-0.7) using a two parameter fit and converted to $\Delta R_{2\,IV}^*$ assuming $Y_0 = 0.6$. Figure 5-9A shows the expected change in $R_{2\,IV}^*$ in response to a graded change in fractional oxygenation.

The value of $\Delta R_2^*{}_{IV}$ can be combined with measured $\Delta R_2^*{}_{GM}$ to simulate the change in $\Delta R_2^*{}_{EV}$ as follows:

Using the simplified solution to the Bloch equation for transverse relaxation, the measured signal can be written in a generalised form S_{voxel}, measured at time TE_X, from the sum of the IV and EV contributions. It is necessary to assume a venous blood volume fraction (f_v) to model the contribution of signals:

$$S_{voxel} = M_0 \left(f_v . e^{-TE_X . R_2^*{}_{IV}} + (1 - f_v) . e^{-TE_X . R_2^*{}_{EV}} \right). \qquad \textbf{5-11}$$

This equation assumes that each compartment exhibits a monoexponential decay and there is no exchange between IV and EV compartments, which is justified in fMRI by the relatively long time water resides in the capillaries (~500ms [274]) in comparison to T_2^* and TE. It is assumed that M_0 is equal between tissue and blood and whilst tissue has a lower water content than blood, the commonly used scaling factor of 0.98 of spin density (where $M_{0tissue} = 0.98 M_{0blood}$) [98] is unlikely to make a significant impact on the model. The ratio of signals collected at TE_1 and TE_2 can be written as:

$$\frac{S_1}{S_2} = \frac{f_v . e^{-TE_1 . R_2^*{}_{IV}} + (1 - f_v) . e^{-TE_1 . R_2^*{}_{EV}}}{f_v . e^{-TE_2 . R_2^*{}_{IV}} + (1 - f_v) . e^{-TE_2 . R_2^*{}_{EV}}} \quad , \qquad \textbf{5-12}$$

For substitution into Equation 5-6. Note this model ignores T1 effects which are likely to be neglibile. $T_{1tissue}$ is shorter than the T_{1blood} which will lead to the IV signal being slightly suppressed relative to tissue for TR = 3s (as used in this study). However, spin density and T_1 effects act in opposite directions and will approximately cancel each other out.

Using the interpolated $R_2^*{}_{IV}$ values from [20] and measured signal $R_2^*{}_{GM}$, Equation 5-12 can be solved for $R_2^*{}_{EV}$ according to Equation 5-6 (Figure 5-9). f_v is assumed to be 3 %; in keeping with a total blood volume fraction of 4.4 % [275], of which 75 % is venous [189]. It can be seen from Figure 5-9 that by removing an assumed IV blood component from the measured GM signal to obtain a pure extravascular R_2^*, results in gradients of $R_2^*/(1-Y_v)$ which increase with field strength as initially expected. From Equation 5-12 it can be seen that when fitting

decay curves described by Equation 5-12 to a single exponent, the apparent R_2^* will depend on the choice of TE, which in turn determines the IV/EV ratio.
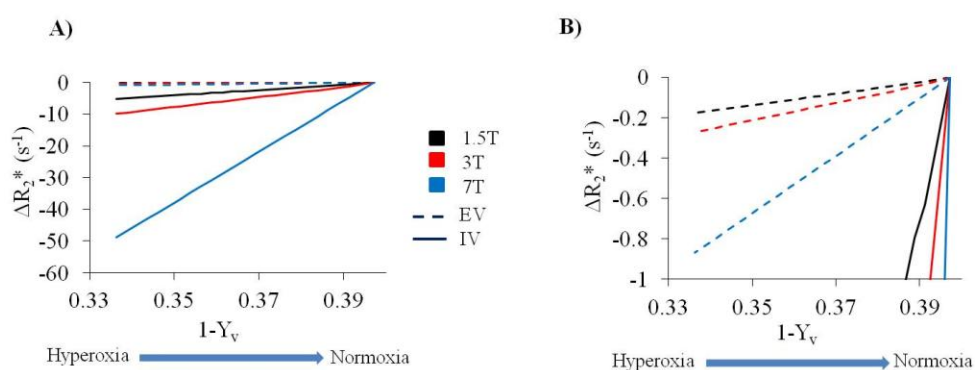
Figure 5-9A) Expected change in R_2^* in the intravascular (solid lines) and extravascular (dashed lines) compartments in response to a graded change in fractional venous oxygenation ($1-Y_v$), for the echo times used in this study (Table 5-1) across field strengths. IV data has been linearly interpolated from [20] across the relevant range of Y_v. EV data has been modelled using Equation 5-12 and the group-averaged GM values and interpolated ΔR_2^* values from [20]. B) The data in (A) is shown magnified across a smaller range of ΔR_2^* (0-1 s^{-1}) in order to better visualise the extravascular component. This EV component should be compared with the $\Delta R_{2\ GM}^*$ shown in Figure 5-7.

This approximate model assumes a linear dependence of $R_{2\ IV}^*$ on ($1-Y_v$) and assumes a linear relationship between $R_{2\ GM}^*$ and ($1-Y_v$), therefore the resulting dependence of estimated $R_{2\ EV}^*$ on ($1-Y_v$) is linear. The short T_2^* of blood means that for the TEs used in this study (Table 5-1), the IV signal is much more sensitive to changes in fractional oxygenation than the EV signal (Figure 5-10), particularly at lower field strengths. In a simple 2 compartment model and these echo times, the EV signal will contribute more at high fractional oxygenation (low $1-Y_v$) than at Y_{v0}.
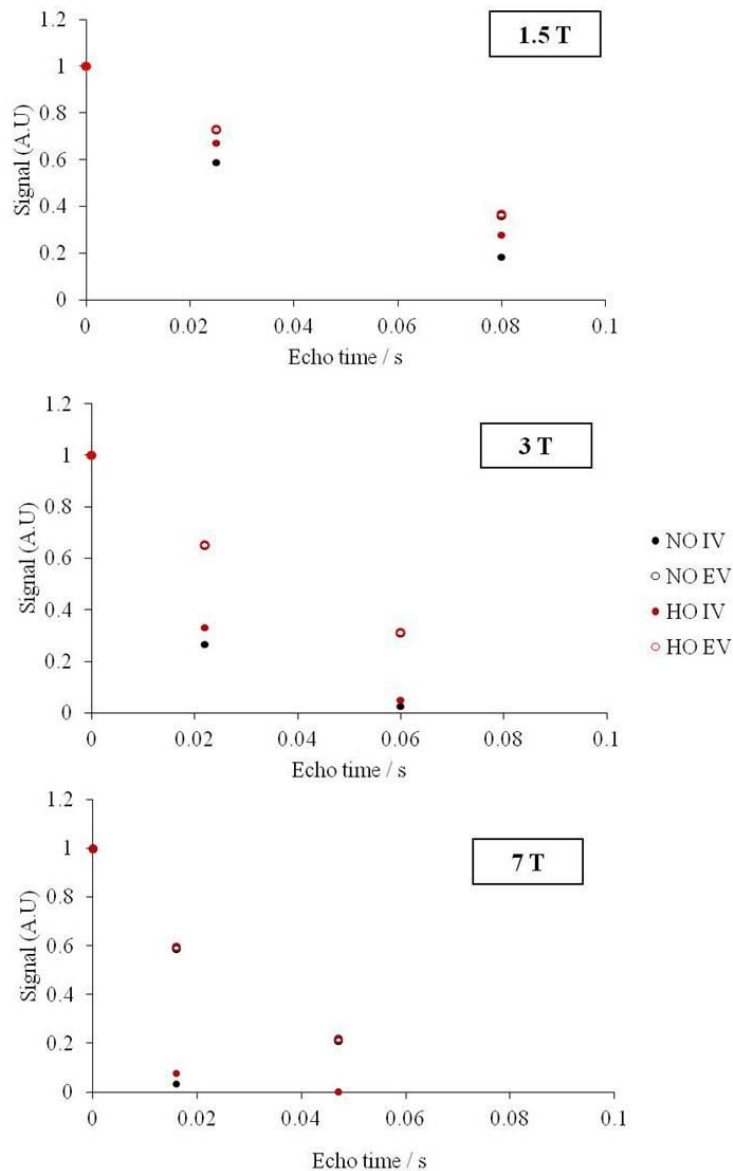
Figure 5-10) Intravascular (IV) and extravascular signal (EV) under normoxia (NO, where 1-Y_v = 0.34) and hyperoxia (HO, where 1-Y_v = 0.39) at each echo time (TE) across field strengths. Data areaveraged across subjects. It can be seen that the signal change in response to hyperoxia is greater for the intravascular compartment for the echo times used in this study (Table 5-1). Normoxia and hyperoxia EV data overlaps on the small scale due to the small difference in signal.

Figure 5-11 demonstrates the estimated dependence of the E signal fraction (using interpolated R_2^* values from [20]) on fractional oxygenation for the echo times used in this study for each TE and field strength. If we now assume a

quadratic dependence of $R_2^*{}_{IV}$ on $(1-Y_v)$ and a linear dependence of $R_2^*{}_{EV}$ on $(1-Y_v)$ for the echo times used in this study, it can be seen that if the total signal becomes increasingly weighted towards the EV contribution as $(1-Y_v)$ increases, then the resulting dependence of $R_2^*{}_{GM}$ on $(1-Y_v)$ could be sub-linear.
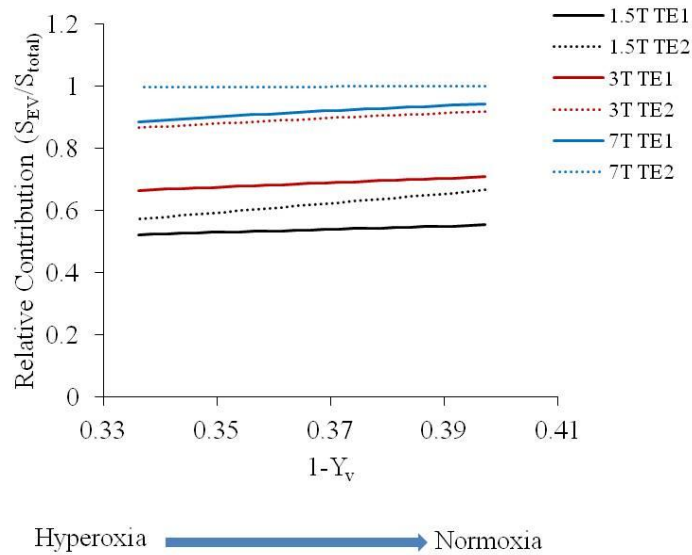
Figure 5-11) Relative extravascular signal contribution (S_{EV}/S_{total}) at each echo time (TE) as a function of fractional oxygenation ($1-Y_v$). Solid lines denote the first echo time (TE1) and broken line the second echo time (TE2).

As discussed in Section 5.2.2, the IV contribution is significantly less at higher field strengths and $T_2^*{}_{IV}$ much shorter, such that for TE_2 of 47 ms at 7 T the intravascular signal is nearly fully attenuated. The IV signal fraction depends on TE, scaling linearly with fractional oxygenation irrespective of vessel size [276]. In order to further investigate the confounding effect of TE on the dependence of IV/EV ratio on fractional oxygenation, it would be useful in future work to increase the number of echoes in order to gain a more accurate measure of R_2^*.

The findings presented in this chapter agree with the notion that β relies on too many experimental factors (notably B_0, IV/EV ratio, TE and CBV) for a single value at each B_0 to be quoted in the calibration of the BOLD response. Nonetheless, for the current experimental protocol a sublinear dependence of $R_2^*{}_{GM}$ on $(1-Y_v)$ was found across all field strengths. It is thought that this can be

attributed to the changing IV/EV signal ratio with changing fractional oxygenation.

5.5.6 <u>Assuming a linear β relationship</u>

Whilst a 3 parameter fit yielded β<1 across all field strengths, a post-hoc test for the coefficient of determination (R^2) showed a linear dependence fitted the data equally well (0.76< r^2 <0.98,   p< 0.05). This suggests that whilst the true dependence of $R_{2\,GM}^{*}$ on (1-Y_v) may be sub-linear at the echo times used in this study, across the limited range of (1-Y_v) = 0.3-0.4, a linear approximation sufficiently describes the observed behaviour. This is demonstrated in Figure 5-12, where it can be seen that while the effect of β has a distinct effect on the shape of the curve across a range of 0-1, when the range is restricted to 0.3-0.4, the curves appear linear. Data shown in Figure 5-12 was simulated according to $x = A(1-Y)^{\beta} + C$.   Constants A and C were arbitrarily set to 4 and -1.5 respectively in order to roughly capture the behaviour of the measured ΔR_{2}^{*} data. Data were simulated for a range of β values (0.5, 1, 1.5, 2) across the full theoretical range of fractional oxygenation (0-1). The region shaded grey shows the induced change in fractional oxygenation in response to 500 mmHg hyperoxia (0.3-0.4).
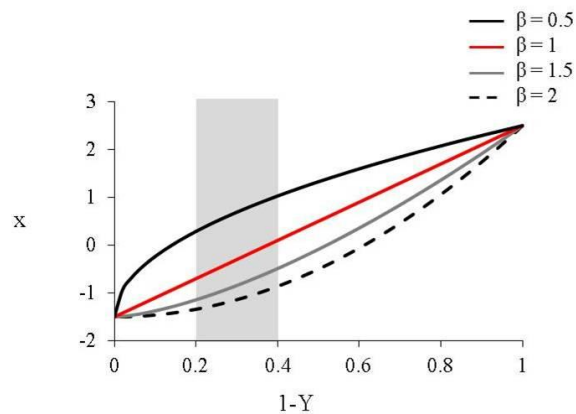
Figure 5-12) Graphical depiction of the effect of β on the model $x = A(1-Y)^{\beta}$. Constants A and C have been arbitrarily set to 4 and -1.5. The shaded grey region reflects the approximate range of fractional oxygenation observed in BOLD fMRI (0.2-0.4).

Thus, for the current experimental parameters, the approximation of β equal to 1 across all field-strengths appears reasonable. This assumption could simplify the calibration of the BOLD signal. In order to fully capture the dynamic relationship oxygenation values close to the maximum and minimum of the full theoretical range must be targeted (0-1). This is not physiologically relevant and would require a hypoxic stimulus, which may then invoke additional vascular responses.

Before extending these findings across all experimental parameters, further work is required to investigate the effect of different echo times across a greater physiological range of blood oxygenation. However, this method provides a framework for doing so and the hyperoxia paradigm offers a means of rapidly achieving a range of Y_v values without altering CBV.

5.6   <u>Conclusion</u>

 This work presents the first experimental measure of β in humans which is not confounded by a change in CBV due to functional activation or modulation of $P_{ET}CO_2$ during a respiratory challenge. Whilst a sub-linear relationship between $\Delta R_{2\,GM}^{*}$ and $(1-Y_v)$ was observed, in agreement with previous simulations which relaxed the interpretation of β to account for a change in β [272], a linear regime is a reasonable approximation. The measured GM signal was combined with in-vitro literature values of $R_{2\,IV}^{*}$, to elucidate a pure extravascular contribution. Whilst the dependence of ΔR_{2}^{*} on $(1-Y_v)$ did not scale with field strength for total GM, when corrected for the IV component this was found to be true. This highlights the need for models of the BOLD signal to take into account both intravascular and extravascular compartments, including how their ratio will depend on TE and oxygenation. As such, the current practice of using a single value of β at each field strength is insufficient at capturing the dependence of ΔR_{2}^{*} on $(1-Y_v)$. However in practice the final results are not strongly dependent on β and a value of $\beta = 1$ could reasonably be used for most studies.

6 Quantification of hypercapnia-induced perfusion changes with arterial spin labelling.

6.1 Introduction

This chapter introduces a modified LL-EPI pulse sequence for multiphase ASL data acquisition (multiple TI data following a single label period), whilst providing high sensitivity to the BOLD signal and applies this method to study the response to hypercapnia. Multiphase ASL provides an ideal method to assess changes on hypercapnia, where assuming a single transit time can cause significant perfusion quantification errors. Experimental results highlight potential issues encountered when quantifying perfusion changes in response to a hypercapnic stimulus, and how these might be minimised. Calibrated BOLD requires simultaneous acquisition of BOLD and CBF, here, a comparison is made between single and multiphase ASL techniques, and the impact that the choice of scheme will have on calibration of the BOLD signal using the Davis model [7]. This chapter provides a framework for future studies where simultaneous measures of CBF, BOLD and CBV will improve our understanding of cerebral haemodynamics in both health and disease. Simultaneous acquisitions cannot be performed unless the sensitivity to all these physiological measures is enhanced.

6.2 Effect of hypercapnia on cerebral haemodynamics

Hypercapnia is an increase in the amount of carbon dioxide (CO_2) in the arterial blood and is a widely used investigative tool in the calibration of the BOLD response, where it is induced by either CO_2 inhalation [7] or breath-holding [277]. This Chapter will focus on moderate hypercapnia induced by raising the inspired fraction of CO_2 (from $FiCO_2 = 0.035$ to ~0.05) and the associated effects on

cerebral haemodynamics. However, it is worth noting that permissive hypercapnia can result from mechanical ventilation in medical conditions such as chronic obstructive pulmonary disease (COPD), obstructive sleep apnea or asthma [278].

Increased arterial CO_2 leads to an increase in hydrogen ions (H^+) in blood due to the production of carbonic acid. This lowers the arterial pH [279-281], which is detected by central and peripheral chemoreceptors and induces a change in both the ventilation and vascular tone [282]. Hypercapnia stimulates ventilation by increasing both the frequency and tidal volume in a bid to clear the excess CO_2 and restore pH.

Hypercapnia is recognised as a potent vasodilator [283], with a reduction in vascular resistance leading to an increase in cerebral blood flow (CBF) [279]. The vasodilation induced by a reduction in pH is thought to be neuroprotective in a bid to prevent an excess of H^+ [284]. The increase in CBF in response to hypercapnia has been well established with different imaging modalities and sequences [E.g. 7, 140, 279, 281, 285-287]. Using the nitrous-washout technique, Kety and Schmidt first reported an increase in global CBF of 8.3 $\pm$ 1.4 %/mmHg CO_2 (mean $\pm$ SEM) [279]. This is in reasonable agreement with a more recent PET study which reports a change of 6 $\pm$ 2.6 %/mmHg, averaged across the frontal, parietal, temporal and occipital lobes [281]. When specifically investigating grey matter (GM) perfusion, the increase is slightly lower, but consistent across the literature, and measured to be an increase of 3-6 %/mmHg with arterial spin labelling [7, 287-289] and 4.8-5.2 %/mmHg with PET [286].

fMRI studies such as calibrated BOLD rely on both CBF and CBV. As introduced in Section 4.2, the coupling between CBF and CBV is often described by Grubb's constant, α where Grubb et al. observed a linear dependence of the change in total cerebral blood volume (CBV) on increasing CO_2 partial pressure ($PaCO_2$) using PET in anaesthetised rhesus monkeys [140]. A non-linear dependence of CBV on CBF was reported, according to the relationship CBV = $0.8.CBF^\alpha$, where α = 0.38 (Grubb's constant). In fMRI studies, it is venous CBV (vCBV) which is of interest, and so Grubb's constant, which reflects total CBV/CBF coupling may not be accurate. Recent fMRI studies have shown the

coupling constant, α, to be slightly lower [289, 290], with 0.2 now generally chosen as the assumed value. Using MRI, Chen et al. [289] assessed the effect of hypercapnia on CBF (measured with PASL) and vCBV (measured with VERVE), reporting a smaller coupling constant of 0.18 ± 0.02. In response to moderate hypercapnia (9mmHg), they reported $\Delta CBF/P_{ET}CO_2 = 7.2 \pm 0.5$ %/mmHg and $\Delta vCBV/P_{ET}CO_2 = 5.5 \pm 1.0$ %/mmHg. This supports the findings from PET that the induced changes in blood volume are smaller than those of CBF, suggesting that it is both an increase in vessel diameter and flow velocity which contribute to the observed increase in CBF. The $\Delta CBF/\Delta vCBV$ relationship was shown to be consistent across both hypercapnia and neuronal activation [289].

Hypercapnia is often assumed to be isometabolic, an important assumption for its use in calibrated BOLD [7]. Chen et al. [134] provide evidence to support this assumption, however there is strong support from both animal and human studies which contest this [129-133]. To date, the exact effect of hypercapnia on cerebral metabolism remains controversial [291], as discussed in Chapter 4. The significant global impact of hypercapnia on neuronal oscillations makes it a less ideal stimulus for calibrated BOLD than isocapnic hyperoxia.

Hypercapnia remains a popular investigative tool; it is cost-effective, portable and readily available. It is non-invasive and can be precisely controlled and terminated, making it advantageous over vasoactive stimulants such as acetazolamide [292]. The ability to induce hypercapnia via a simple breath-hold means it can be easily implemented. Whilst the increase in $P_{ET}CO_2$ in response to a breath-hold can be extremely variable across individuals, monitoring $P_{ET}CO_2$ via a nasal cannula allows individual effects to be accounted for, improving the robustness of this technique [151, 293]. Furthermore, combined hyperoxic-hypercapnia techniques have recently been proposed [9, 10], where both CBF and arterial oxygenation are modulated (via hypercapnia and hyperoxia respectively) to yield absolute measurements of $CMRO_2$.

Hypercapnia is also a useful tool for the assessment of cerebrovascular reactivity (CVR). CVR assesses the change in blood flow in response to a vasoactive stimulus and is already a key research tool in disorders such as Alzheimer's disease [294-296], carotid artery disease (see Gupta et al. [297] for a review) and moya moya disease [298-300], with the potential to become a powerful clinical tool [301]. Mandell et al. [302] showed good agreement between ASL and BOLD measurements of CVR in both healthy volunteers and patients with steno-occlusive disease. A significant correlation was also found using simultaneous CBF and BOLD measures of CVR in ischemic cerebrovascular disease [303]. While BOLD reactivity offers increased SNR over ASL measures, the BOLD response is influenced by physiological parameters other than CBF, such as CBV and $CMRO_2$, and so simultaneous BOLD/CBF measurements are ideal for investigating the compromised haemodynamics which underlie altered CVR in disease.

In order for the use of hypercapnia to become a recognised reliable clinical tool, robust measurements of CBF are required [304]. As introduced in Chapter 3, MR methods, in particular ASL, have proven ideal to provide measures of non-ionising, repeatable perfusion quantification. However, ASL is sensitive to changes in transit time and ASL has inherently low SNR and so can struggle to detect small signal changes in response to hypercapnia, as opposed to the larger response to neuronal activation. The remainder of this chapter will assess the optimal method of arterial spin labelling (ASL) for simultaneous measurement of hypercapnia induced perfusion and BOLD changes.

6.3 <u>Perfusion measurements with arterial spin labelling</u>

An increase in CBF is typically associated with a reduction in transit time of arterial blood from its labelled location to the imaging plane (Figure 6-1), faster flowing blood will arrive at the tissue sooner than slower flowing blood. Further, transit time is known to be heterogeneous across the cortex, with shorter transit time closer to large arterial branches [305]. This can lead to potential confounds in CBF quantification based on single phase ASL (one post-label delay (TI)) which

assume a single transit time. As hypercapnia is a known vasodilator (thought to increase both vessel diameter and flow velocity), it follows that hypercapnia will also cause a significant reduction in transit time [306-308] and so it is unlikely that a technique which lacks temporal information, such as single phase ASL, can accurately quantify these perfusion changes. QUIPSSII (Quantitative Imaging of Perfusion using a Single Subtraction) [309] minimises the sensitivity to transit time by applying a saturation pulse after the labelling scheme so as to create a finite bolus of labelled blood. However, in cases of high global flow such as hypercapnia, the labelled blood may have left the saturation plane before saturation is applied and so QUIPSSII may be ineffective [310]. Therefore for accurate CBF quantification, where transit time sensitivity remains a significant confound, a multiphase ASL scheme (where multiple readout pulses are collected following each label pulse) is ideal, as has been recognised by the recent White Paper on ASL which aims to reflect the opinions of the ASL research community as a whole [311].
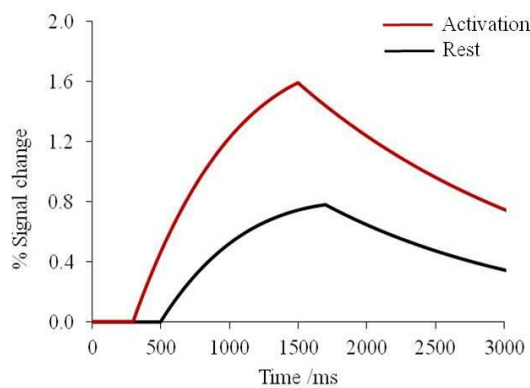
Figure 6-1) Schematic representation of the perfusion-weighted percentage signal change at rest and in response to a task. An increase in perfusion is characterised by an increase in peak signal change with an accompanying reduction in transit time.

An advantage of single phase ASL is the ability to obtain simultaneous measures of CBF and BOLD [85]. Concurrent ASL and BOLD acquisition has a number of key advantages for many studies of cerebral haemodynamics. With the ability to distinguish between neural deactivation and altered neurovascular coupling [312,

313], it also offers the potential to dissociate the physiology underlying changes in the BOLD response in ageing and disease [314]. Perfusion maps are likely to be better localised to the site of neuronal activation, as the BOLD response can be dominated by draining veins [315, 316]. At a spatial resolution of 2x2x3 mm^3, Pfeuffer et al. [317] showed that only 50 % of voxels showing significant activation were common to both perfusion and BOLD weighted signals in response to a visual stimulus. Furthermore, simultaneous acquisition is advantageous for the estimation of $CMRO_2$ via calibrated BOLD, as the temporal variations in the two signals are minimised [318]. The need to assume a constant physiological response across repeated acquisitions is also removed (important for stimuli where habituation may occur which limits sequential ASL and BOLD measures).

Secondary advantages are also obtained. ASL data are notoriously difficult to motion correct, especially if background suppression pulses have been used to reduce physiological noise, owing to the suppression of static tissue signal which removes key spatial information required by motion correcting algorithms [86]. BOLD data acquired from the same imaging volume can be more easily motion corrected, with the resulting transformation matrix later applied to the ASL images.

An inherent problem with combined acquisitions is that the optimal echo time (TE) for ASL and BOLD are not equal. While ASL requires a short TE for high SNR [98], an echo time close to the tissue T_2^* is optimal for BOLD contrast [27]. Interleaved methods acquire CBF and BOLD data with separate excitations (pseudo-simultaneous), so that the TE is optimised for both acquisitions [8, 138, 287], however temporal SNR is compromised. Other research groups have used single shot acquisitions and have selected an intermediate TE which provides some sensitivity to both perfusion (difference between label and control images) and BOLD (sum of label and control images) [183, 290, 319], this increases tSNR but reduces the signal contrast for both modalities.

The Double Acquisition Background Suppressed (DABS) scheme [320] provides a solution to the enforced trade-off between tSNR and TE, whilst overcoming challenges of increased physiological noise faced when using ASL at ultra-high field [321]. Both ASL and BOLD images are acquired within a single TR, each at an optimal TE, with BOLD images being acquired for both the label and control ASL images. Background suppression is achieved with two global adiabatic inversion pulses applied, prior to image acquisition, to minimise the effects of increased field inhomogeneity and physiological noise experienced at high field. The remainder of this chapter will introduce and evaluate a modified multiphase version of the DABS acquisition, which combines the advantages of multiphase ASL readout schemes with that of the simultaneous measurement of CBF and BOLD using DABS.
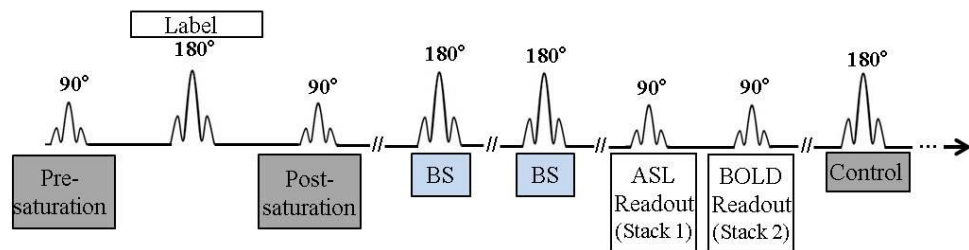
Figure 6-2) Schematic of the standard DABS FAIR pulse sequence. Two EPI readouts are acquired in a single TR to collect both ASL (stack 1) and BOLD (stack 2) at optimal echo times. Background suppression (BS) pulses are applied prior to the ASL readout to minimise physiological noise in the ASL data.

6.4 Look-Locker DABS readout scheme (LL_DABS)

Here a simple modification of the LL-EPI FAIR sequence is presented, termed Look-Locker Double Acquisition with Background Suppression (LL_DABS), which allows for simultaneous acquisition of CBF and BOLD without the need to assume transit time. This has the potential to provide a more accurate quantification of the change in CBF on hypercapnia. As introduced in Chapter 4, BOLD weighting can be obtained from a standard LL-EPI readout scheme by increasing the flip angle of the last readout phase to a 90° pulse. However, the

magnitude of the measured transverse signal is limited by the available signal for recovery, the time between phases (TA). By increasing the time delay prior to the last readout phase, signal recovery is increased resulting in increased BOLD signal contrast as used in standard DABS (Figure 6-3). Due to the continued suppression of the control signal at time TA, the LL_DABS scheme has intrinsic background suppression for all (N-1) readout pulses, reaching a steady state signal as shown in (Figure 6-3B).
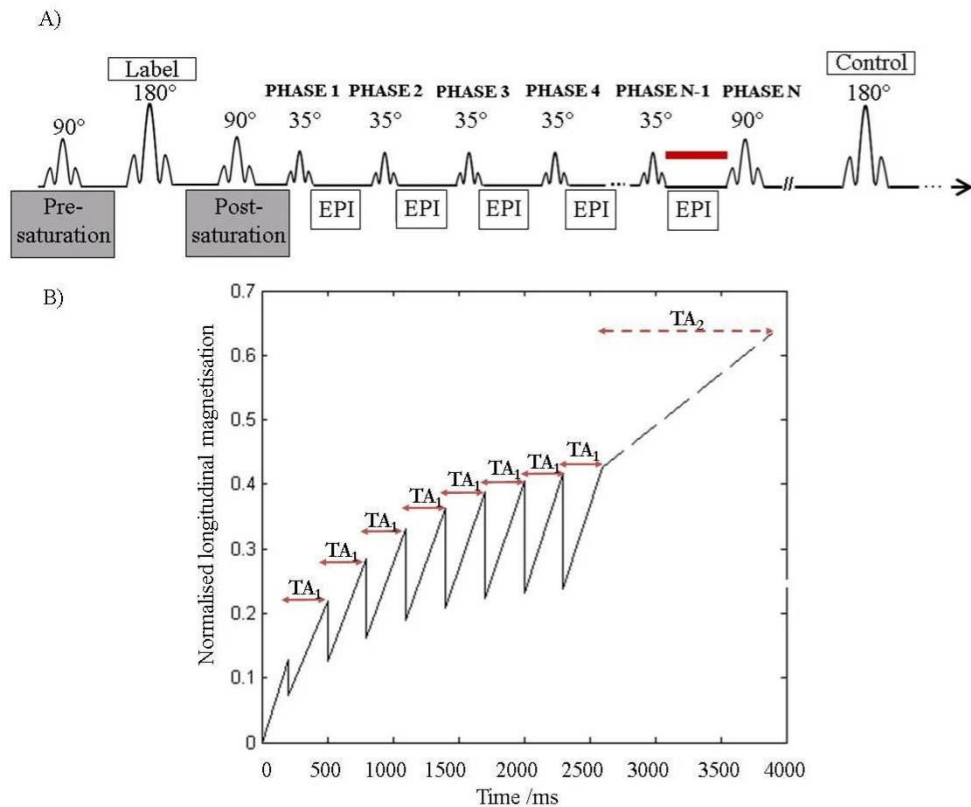
Figure 6-3) A) Schematic of the modified LL-EPI FAIR (LL_DABS) pulse sequence. For N pulses, the time between the (N-1)th and Nth readout is increased to maximise BOLD sensitivity. B) Schematic of the resulting control signal magnetisation (TI/TA/FA = 1400/300/35°), the increased time between the (N-1)th and Nt^{h} readout is labelled as TA$_2$. As TA$_2$ increases, the BOLD sensitivity increases. The echo time can be independently controlled for the Nth readout compared to all (N-1) readout pulses.

The experimental results presented below compare the suitability of standard DABS and LL_DABS for measuring a hypercapnia-induced change in CBF and BOLD. The measured changes in CBF and BOLD are used to calculate the calibration constant (M-value) used in calibration of the BOLD signal. This is used to estimate the change in $CMRO_2$ induced by motor activation for the LL_DABS sequence.

6.4.1 <u>Experimental Protocol</u>

This study was approved by the University of Nottingham Medical School Ethics Committee. Five subjects (aged 24 ± 0.4 years, all male) participated and gave prior, informed, written consent. MR scanning was performed using a Philips Achieva 7 T system with a head volume transmit coil and 32 channel SENSE receive coil, with foam padding used to reduce head motion.

Prior to MRI measurement, the subject sat upright on the scanner bed while baseline metabolic values were estimated and targeted. A trial hypercapnic sequence was then run for the subjects who had not experienced hypercapnia before (n = 2). The trial sequence consisted of 1 minute of subject specific baseline, 1 minute of hypercapnia ($P_{ET}CO_2$ = baseline + 8mmHg), followed by 1 minute of baseline. The 2 subjects who took part in the trial sequence were asked if they were comfortable with the hypercapnic stimulus, with the option to discontinue if they felt they would not be able to tolerate it.

The subject then lay supine in the scanner, with medical air administered until the respiratory challenge commenced. The respiratory challenge consisted of 3 minutes of normocapnic baseline (subject-specific $P_{ET}O_2$ and $P_{ET}CO_2$), followed by 6 minutes of iso-oxic hypercapnia at the subject's resting $P_{ET}O_2$, ($P_{ET}CO_2$ = baseline + 8mmHg), and then 3 minutes of normocapnic baseline (Figure 6-4). The total duration of the respiratory challenge was 12 minutes, including transitions (square-wave). All subjects performed this challenge twice, using the standard DABS and LL_DABS acquisitions. The sequences were pseudo-randomised such that DABS data were acquired first in three subjects and

LL_DABS data first in the remaining two subjects. Subjects received medical air when not on a respiratory sequence.
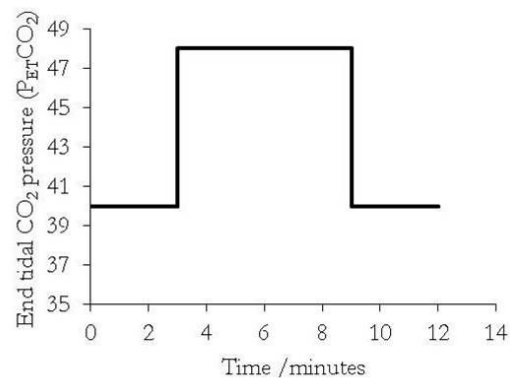
Figure 6-4) Targeted respiratory paradigm: 3 minutes of subject-specific baseline was followed by 6 minutes of hypercapnia (baseline $P_{ET}CO_2$ +8 mmHg) and another 3 minutes of baseline. $P_{ET}O_2$ targeted at subject-specific baseline throughout.

An initial functional localiser scan (GE-EPI, SENSE factor 2, TE/TR=25/3000 ms, 2x2x3 mm^3 resolution, FOV=192x1992x45 mm^3) was acquired to obtain real-time visualisation of the motor cortex via IViewBOLD (Philips, Best, Netherlands). During the localiser, subjects were required to perform a 5 minute bilateral finger-tap task (30 s tap, 30 s rest). At rest, a small white fixation cross on a black background was projected on a screen at the end of the magnet bore, with the active condition cued by a large red "TAP" on a black background. Subjects wore prism glasses throughout in order to see the screen.

The hypercapnic challenge was then performed and data acquired using either DABS or the LL_DABS scheme. A spatial resolution of 2 x 2 x 3 mm^3, FOV of 192 x 192 x 15 mm and SENSE acceleration factor 2 was used for both the DABS and LL_DABS sequences using a GE-EPI readout with 5 contiguous slices per TR. For both schemes pre- and post-saturation pulses were applied to the imaging plane around the labelling, and vascular crushing applied. The DABS FAIR sequence had the following imaging parameters: TR = 4000 ms, 5 contiguous slices, selective and non-selective imaging slab widths of 48 mm and 300 mm respectively, with a TE of 16 ms for ASL acquisition and TE of 25 ms

146

for the BOLD acquisition. Due to the interleaved label and control ASL acquisition, the effective TR for ASL was 8 s. Background suppression inversion pulses were applied at T_{BS1} = 402 ms and T_{BS2} = 1034 ms, with a post-label delay (TI) of 1400 ms used to account for a reduced transit time with hypercapnia. The total scan duration was 12 minutes to match the respiratory paradigm. LL_DABS acquisition parameters were $TI/TA_1/TA_2/TR$=200/300/1300/4000 ms, 9 readout times per TR, and scan duration 12 minutes. For phases 1-8, FA = 35°, while for phase 9, FA = 90° and TE = 23 ms.

Four of the five subjects completed an additional motor task; a bilateral fingertap (24 s on, 40 s off) was repeated for seven cycles. During the functional task, data were collected using the LL_DABS acquisition, with identical parameters to those described above. For volunteer comfort, RespirAct studies were limited to one hour. This time constraint prevented data acquisition with the DABS labelling scheme for the motor task.

Base EPI images were acquired across the same imaging volume for the DABS and LL_DABS acquisition to allow estimation of M_0. Inversion recovery (IR) data were acquired across 10 TI's (100-2500ms) for T_1 mapping, from which a GM mask was created using the threshold ($1.7 \leq T_1 \leq 2.3$ s).

6.5   Data Analysis

6.5.2 Respiratory data

Transition periods were discarded and end-tidal values averaged to estimate the mean $P_{ET}CO_2$ and $P_{ET}O_2$ values on normocapnia and hypercapnia. The raw end-tidal $P_{ET}CO_2$ trace was down-sampled in MATLAB to 0.125 Hz to match the effective TR of 8 s. The interpolated timecourses were created for both the DABS and LL_DABS acquisitions and formed the input model for the GLM analysis in FEAT (FSL, Oxford).

The pressure trace taken from the sample line in the face mask was down-sampled; to 1 Hz to assess potential changes in respiratory pressure, and 0.125 Hz to match the effective TR of the BOLD and ASL acquisitions. It is possible that hypercapnia increases respiratory pressure in order to increase the rate of CO_2 clearance from the blood. For this reason, respiratory pressure was estimated from the root mean square (RMS) amplitude of the pressure trace (P) using RMS $= [\sqrt{\Sigma (P)^2}]/n$, where n is the number of measurements taken (e.g. for a 2 minute time period sampled at 1 Hz, n = 120), and P is positive or negative depending on inhalation or exhalation. The down-sampled pressure trace was used as a covariate of no interest in the GLM analysis.

6.5.3   Pre-processing

Double Acquisition with Background Suppressed FAIR (DABS FAIR)

In DABS, the ASL and BOLD data are acquired in two sequential stacks following labelling, images from stack 1 are ASL-weighted, and images in stack 2 are BOLD-weighted. Stack 1 of the label and control images are subtracted to produce a perfusion-weighted difference image at a single post-label delay (TI) with an effective temporal resolution of 8 seconds. Perfusion-weighted images were visually inspected for motion artefacts, as described above, and motion correction applied to the BOLD-weighted images (acquired in stack 2) using MCFLIRT (FSL, FMRIB, Oxford, UK) separately for label and control conditions. The resulting transformation matrix from the label and control correction was applied to the ASL-weighted images using the applyxfm4D command in FSL (FMRIB, Oxford, UK). After motion correction, the transformation parameters were correlated with the end-tidal CO_2 trace to investigate whether there was increased motion under hypercapnia.

DABS FAIR with Look-Locker readout (LL DABS FAIR)

Label and control images were subtracted to produce a perfusion-weighted difference image for the first 8 phases, with an effective temporal resolution of 8 seconds. Perfusion-weighted images were visually inspected for motion artefacts. Motion induced "ringing" was evident in a number of dynamics in all subjects' timecourses (as illustrated in Figure 6-5) and so motion correction was applied in all cases using MCFLIRT (FSL, FMRIB, Oxford, UK). Since the Look-Locker multiphase perfusion label and control data are difficult to motion correct due to the lack of static signal, motion correction was applied to the BOLD-weighted data from the last phase (TI_9) (control and label image corrected separately). The resulting transformation matrix from the label and control correction was applied to phases 1-8 using the applyxfm4D command in FSL (FMRIB, Oxford, UK) – this assumes no movement between phases 1- 8. After motion correction, the transformation parameters were correlated with the end-tidal CO_2 trace to investigate whether there was increased motion during hypercapnia (due to increased breathing frequency or patient discomfort which may be locked to the hypercapnic stimulus). Statistical analysis of the LL_DABS data was performed in the same manner for both data collected during hypercapnia and to the finger tap paradigm. As described in Section 4.5.3.2, the perfusion-weighted difference images from phases 4-6 (1100 – 2000 ms) were averaged to form an average perfusion-weighted timecourse on which GLM analysis was performed.
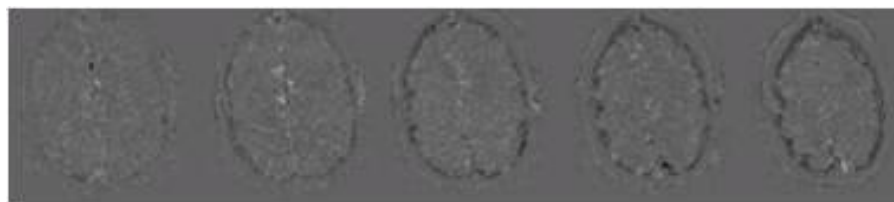
Figure 6-5) Example perfusion-weighted data from a single dynamic at TI = 1400 ms where subject motion has occurred leading to an artefactual ring.

Assessing the response to hypercapnic challenge:

The perfusion-weighted and BOLD data from the hypercapnia challenge were spatially smoothed using a 5 mm FWHM Gaussian kernel. A temporal filter with 720 s cut-off (normocapnic period plus hypercapnic period) was then applied. Maps of statistical significance of the perfusion-weighted data in response to hypercapnia were formed using a GLM analysis in FEAT (FSL, FMRIB). For LL_DABS, the perfusion-weighted image averaged across phases 4-6 (as described above) was used in the GLM analysis. The $P_{ET}CO_2$ trace was used in the GLM analysis as the input model, with the down-sampled pressure trace used as a covariate of no interest. Haemodynamic latency in response to hypercapnia was corrected globally by including a 24 s lag (3 dynamics) in the input model. The delay was determined by aligning the peak change in BOLD/perfusion-weighted signal between dynamics 20-30 (corresponding to step-change in $P_{ET}CO_2$ at the onset of hypercapnia). A binary mask of grey matter (GM) was created by applying a threshold to the T_1 map where GM was identified by $1.7 < T_1 < 2.3$ s. This binary mask was used to identify the 'GM ROI' for subsequent interrogation of global GM changes in CBF.

Assessing the response to the motor task:

As described above, the perfusion-weighted difference images from phases 4-6 (1100 – 2000 ms) of LL_DABS were averaged to form an average perfusion-weighted timecourse on which GLM analysis could be performed. The LL_DABS BOLD and perfusion-weighted data from the motor task were spatially smoothed using a 5 mm FWHM Gaussian kernel. A temporal filter with 128 s cut-off was applied. Maps of statistical significance of the CBF response to the motor task were formed using GLM analysis in FEAT (FSL, FMRIB), using a boxcar model of the times at which subjects were instructed to finger tap convolved with a canonical HRF. The resulting activation maps were converted to binary masks (where $Z > 3$ and $p < 0.05$) in MATLAB from which a 'Motor ROI' could be formed.

6.5.4 CBF Quantification:

The DABS and LL_DABS datasets were separated into active periods (fingertap/hypercapnia conditions) and baseline volumes (rest/normocapnia conditions). The hypercapnia data across the transition periods was discarded.

LL_DABS data were averaged across the voxels forming the 'GM ROI' and 'Motor ROI' to obtain a signal time-course across the 9 readout phases for each condition. The timecourses were normalised by the appropriate M_0 of GM within each ROI estimated from the base EPI images, where M_0 is scaled under hypercapnia to account for a change in T_2^* [67] as described in Section 4.5.3.2. Using the kinetic model of Francis et al. [99], the normalised time courses from the 'GM ROI' and 'Motor ROI' were fit for CBF, transit time (Δa) and exchange time (δ), where tissue arrival time can be estimated from $\Delta a + \delta$. The T_1 of blood at 7 T was assumed to be 2.2 s [186, 187] and the T_1 of tissue assumed to be 2.0 s (in agreement with the T_1 map). Activation induced changes in CBF were then reported as a percentage change for each task.

The perfusion-weighted DABS images were averaged across normocapnia and hypercapnia and then normalised by their respective M_0 of GM (accounting for a change in T_2^* [67]), estimated from the DABS base EPI. The perfusion-weighted signal (ΔM) from the 'GM ROI' was converted to CBF using the general kinetic model of Buxton et al. [98] (Equation 6-1), assuming full inversion efficiency, a capillary transit time (Δt) of 1 s [322], T_1 of blood of 2.2 s [186, 187] and $TI = 1.4$ s.

$$\Delta M = 2\alpha M_{0Blood} CBF (TI - \Delta t) e^{\frac{-TI}{T_{1Blood}}} \qquad \textbf{6-1}$$

6.5.5 BOLD quantification:

As previously described, for LL_DABS, the label and control signal from the last phase (TI_9) provides a BOLD-weighted data set. Stack 2 of the DABS acquisition is BOLD-weighted. Percentage change in BOLD signal was quantified (using MATLAB scripts) for motor and hypercapnia tasks in the 'Motor ROI' and 'GM

151

ROI' respectively. For comparison purposes, BOLD signal was also taken from the control signal at phase 8 (TI = 2300 ms) of the LL_DABS sequence. This is comparable to the standard method of multiphase ASL acquisition (e.g. QUASAR [101]) for which a final 90° readout flip angle is not typically used.

6.5.6 **Calibration of the BOLD signal**

The relative change in CBF and BOLD in response to hypercapnia were used to calculate the *M*-value, the calibration constant, for the 'GM ROI', according to Equation 6-1 derived from Davis et al. [7]. *M* was calculated on an individual subject basis for both the DABS and LL_DABS schemes. Measurements made under hypercapnia are denoted by the subscript 'HC' and normocapnia by the subscript '0'. Here, a value of $\alpha = 0.2$ and $\beta = 1$ are assumed in the calibration (see Chapter 5).

$$M = \frac{\dfrac{\Delta BOLD_{HC}}{BOLD_0}}{1 - \left(\dfrac{CBF_{HC}}{CBF_0}\right)^{\alpha - \beta}} \qquad \textbf{6-2}$$

The DABS and LL_DABS measurements of *M* under hypercapnia were used to estimate the relative change in $CMRO_2$ in the 'Motor ROI' in response to the motor task (Equation 6-2), according to the Davis model [7] as introduced in Chapter 3.

$$\frac{CMRO_2}{CMRO_{2|0}} = \frac{\left(1 - \dfrac{\Delta BOLD}{M.BOLD_0}\right)^{-\beta}}{\left(\dfrac{CBF}{CBF_0}\right)^{\alpha - \beta}} \qquad \textbf{6-3}$$

All statistical analysis was performed using SPSS (SPSS 16, Chicago, IL, USA).

6.5.7 Assessing the optimal scheme (DABS vs. LL_DABS)

To assess the optimal scheme for calibrated BOLD measures, the temporal SNR (tSNR) of the DABS and LL_DABS data was assessed for both the perfusion-weighted and BOLD-weighted data. tSNR of the BOLD-weighted data from phase 8 of the LL_DABS data was also assessed. First, temporal mean and standard deviation images were created by taking the mean and standard deviation across the 4th dimension data set (MATLAB). A tSNR image was then obtained by dividing the temporal mean by temporal standard deviation. For the LL_DABS sequence, the tSNR of the perfusion-weighted image (average across phases 4-6 for LL_DABS) was assessed. tSNR was compared for the respiratory paradigm, motor task and a 2 minute period of medical air whilst the subject was at rest. Contrast-to-noise ratio (CNR) was calculated for both the respiratory challenge and motor task by dividing the mean change in signal in response to hypercapnia/motor task ($S_{HC/task} - S_{Rest}$) by the standard deviation. This was calculated for the whole brain and GM ROI. All statistical analysis was performed using SPSS (SPSS 16, Chicago, IL, USA).

6.6 Results

6.6.8 Respiratory challenge:

Average $P_{ET}O_2$ and $P_{ET}CO_2$ for baseline and hypercapnic stimuli are shown in Table 6-1. There was no significant difference in the hypercapnic step used between each acquisition scheme (Wilcoxon Signed Rank Test). Breathing frequency and inspiratory/expiratory pressure were constant across stimulus blocks (medical air, normocapnia and hypercapnia) as shown in Table **6-2**, (Friedman's one-way ANOVA).

	Normocapnia		Hypercapnia	
	$P_{ET}O_2$	$P_{ET}CO_2$	$P_{ET}O_2$	$P_{ET}CO_2$
DABS	112.6 ± 0.9	39.6 ± 0.4	114.7 ± 0.9	45.1 ± 0.4
LL_DABS	112.3 ± 0.8	39.8 ± 0.4	114.8 ± 1.4	45.2 ± 0.6

Table 6-1) End tidal pressures (mean $\pm$ SE) of O_2 ($P_{ET}O_2$) and CO_2 ($P_{ET}CO_2$) for baseline and hypercapnic periods of the respiratory challenge for the DABS and LL_DABS sequences.

		Breathing Frequency (breaths per minute)	Inspiratory/Expiratory amplitude (mmHg)
DABS	Normocapnia	11.6 ± 2.0	7.7 ± 2.5
	Hypercapnia	12.5 ± 1.7	7.9 ± 2.6
	Medical Air	11.9 ± 2.2	7.4 ± 2.6
LL_DABS	Normocapnia	12.8 ± 2.1	5.7 ± 1.1
	Hypercapnia	11.8 ± 1.8	6.8 ± 1.5
	Medical Air	12.9 ± 2.1	5.2 ± 0.7

Table 6-2) Breathing frequency and inspiratory/expiratory amplitude across medical air, normocapnia and hypercapnia for the DABS and LL_DABS sequences.

6.6.9 Motion correction:

There was no significant difference between the absolute and relative displacement as measured by MCFLIRT (Friedman's one-way ANOVA) for the hypercapnia challenges and motor task. Furthermore, there was no significant correlation between the motor paradigm and the motion parameters (Friedman's one-way ANOVA). However, all subjects showed significant correlation between at least one rotational/translational direction and the hypercapnic stimulus for both DABS ($-0.50 < r^2 < 0.56$) and LL_DABS ($-0.61 < r^2 < 0.56$) sequences.

Figure 6-6 shows an example trace from a representative subject taken from the final BOLD-weighted readout of the LL_DABS sequence during the hypercapnia challenge. Motion correction cropped regions from the top and/or bottom slice in some subjects and so for consistency these slices were removed in all cases.
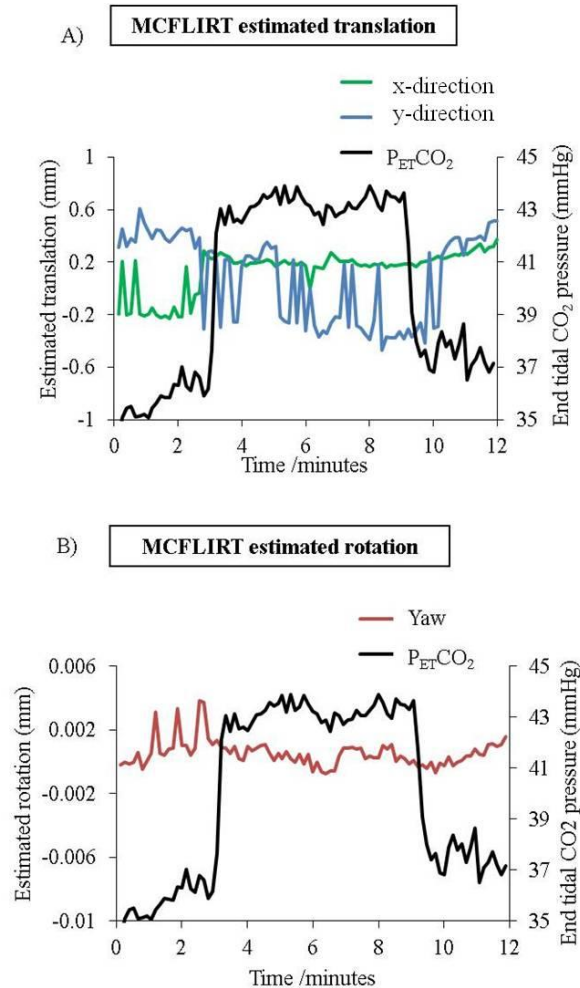
Figure 6-6) Estimated translation (A) and rotation (B) transformations using MCFLIRT (FSL, FMRIB, Oxford, UK) for a representative subject receiving hypercapnia (black solid line) during the LL_DABS sequence. For this subject, translation was significantly correlated in both the x (R^2 = 0.25, p < 0.01) and y direction (R^2 = -0.43, p < 0.01).

6.6.10 <u>Haemodynamic response to hypercapnia</u>

The statistical CBF activation maps in response to hypercapnia showed significant grey matter activation in all subjects (Figure 6-7). However, given the known potent effect of hypercapnia on CBF, the maps for both DABS and LL_DABS do not appear to be as robust as expected for the given Z-statistic of 2.3. Nonetheless, the CBF activation appears to be more closely localised to GM for LL_DABS in comparison to DABS. Activation maps in response to hypercapnia were robust across all subjects for BOLD-weighted data from both DABS and LL_DABS.
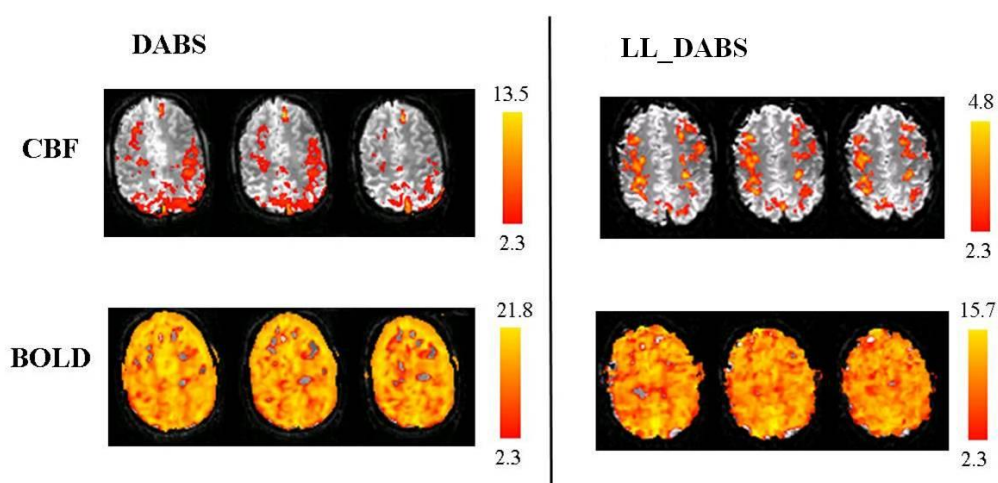
Figure 6-7) Statistical activation maps shown for a single representative subject created using GLM analysis in FEAT (FSL, FMRIB, Oxford, UK). Maps shown for CBF and BOLD as measured with DABS and LL_DABS. Colour bars represent minimum and maximum Z-statistic, where Z > 2.3 and p <0.05.

LL_DABS perfusion-weighted timecourses across the readout phases for normocapnia, hypercapnia and the fingertap task are shown in Figure 6-8 for individual subjects. The variability in shape between individual subjects is clearly evident, highlighting the potential error induced from a single post-label delay of 1400 ms used in DABS. Results from the fitted kinetic model averaged across subjects are provided in Table 6-3.

		CBF (ml/min/100g)	Tissue Arrival Time (ms)
DABS	**Normocapnia**	42 ± 5	--
	Hypercapnia	47 ± 6	--
LL_DABS	**Normocapnia**	49 ± 12	520 ± 67
	Hypercapnia	61 ± 9	442 ± 52

Table 6-3) Absolute CBF (ml/min/100g), tissue arrival time (Δ_{tissue}, in ms) for normocapnia and hypercapnia as measured with LL_DABS and absolute CBF as measured with DABS. Results are averaged across subjects (mean ± SEM).
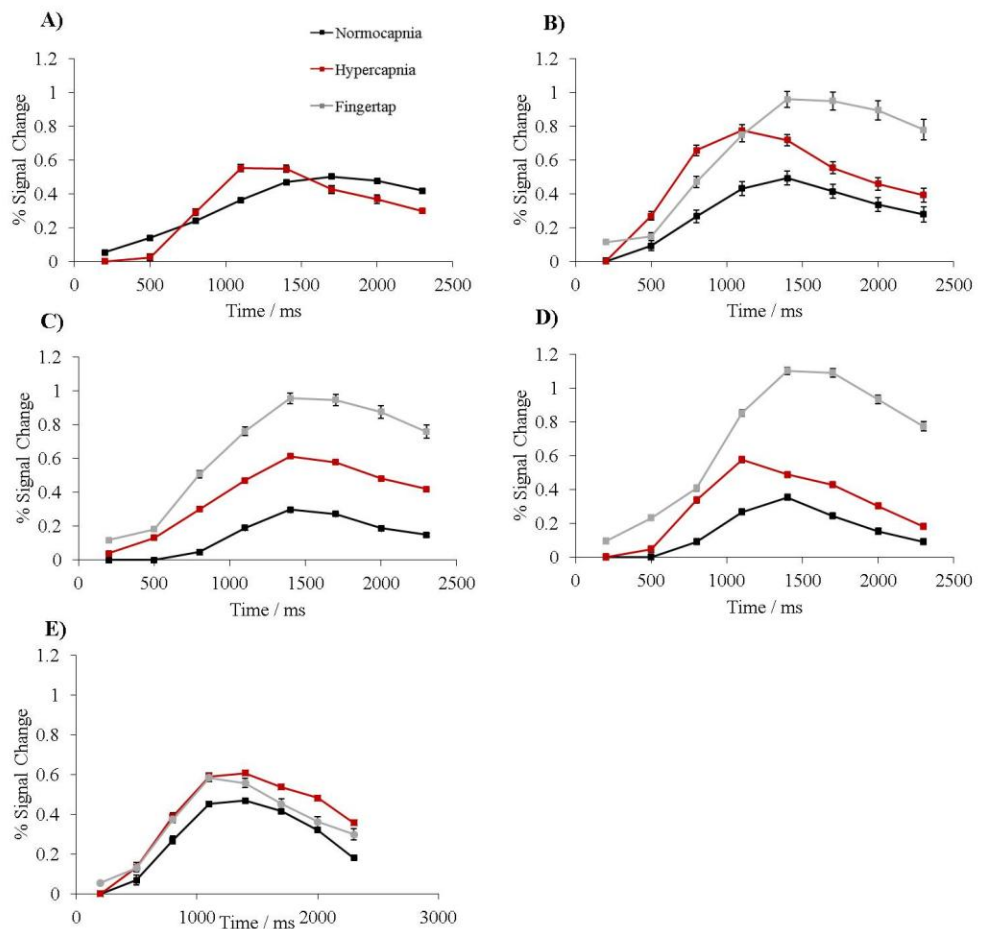
Figure 6-8) LL_DABS timecourses across the first 8 phases for normocapnia (black), hypercapnia (red) and the fingertap task (grey). Data shown for individual subjects (A-E). Subject A did not perform a motor task.

A 7.7 ± 4.1 % increase in CBF per mmHg of CO_2 was measured using LL_DABS. This is in contrast to a 2.9 ± 1.5 % increase in CBF per mmHg of CO_2 measured with DABS. This difference in CBF per mmHg of CO_2 between the two sequences (Figure 6-9) was significant (p = 0.043, Wilcoxon Signed Rank Test).
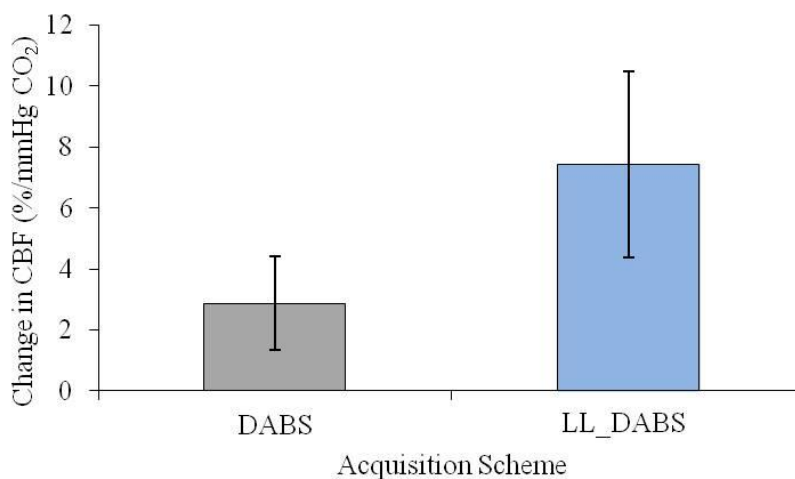
Figure 6-9) Comparison of the measured change in CBF expressed as %/mmHg CO_2 in response to hypercapnia as measured with DABS and LL_DABS. Data areaveraged across all subjects (± SEM). A significant increase is found for LL_DABS.

There was no significant difference between DABS and LL_DABS in the hypercapnia induced BOLD signal change (Wilcoxon Signed Rank Test) (Figure 6-10). The BOLD increase in response to hypercapnia was 0.55 ± 0.11 %/mmHg for DABS and 0.45 ± 0.14 %/mmHg for LL_DABS. The BOLD increase in response to hypercapnia as measured from phase 8 of the LL_DABS sequence (equivalent to QUASAR) was significantly less (-22 ± 8 %) than the measurement from phase 9 given above (p = 0.043, Wilcoxon Signed Rank Test) (Figure 6-10) . This can be explained by the significant reduction in both CNR (64.4 ± 9.0 %, p = 0.043, Wilcoxon Signed Rank Test) and tSNR (53.8 ± 1.3 %, p = 0.043, Wilcoxon Signed Rank Test) between phase 8 and 9 of the LL_DABS sequence.
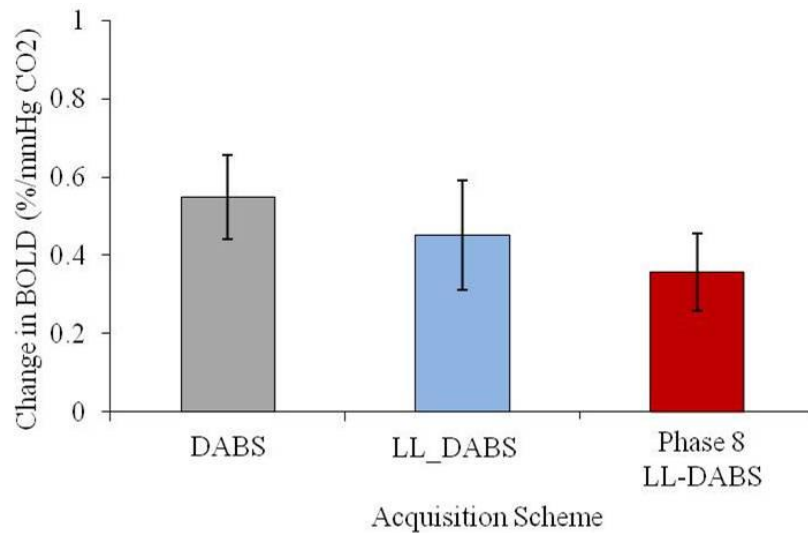
Figure 6-10) Comparison of the measured change (%/mmHg CO$_2$) in BOLD in response to hypercapnia as measured with LL_DABS , DABS and phase 8 (TI = 2300 ms) of the LL_DABS sequence (equivalent to BOLD-weighting from a standard LL-EPI sequence without a final 90° readout). Data are averaged across all subjects (± SEM).

6.6.11 Haemodynamic response to motor activation

CBF and BOLD was simultaneously measured in response to a fingertap task using the LL_DABS sequence. Statistical activation maps from GLM analysis showed a robust CBF response in the primary motor cortex (Figure 6-11). Resting-state CBF increased from 40 ± 3 ml/min/100g to 61 ± 6 ml/min/100g in the 'motor ROI' (threshold at Z > 3), an average increase of 51 ± 7 %, averaged across subjects. This was supported by a decrease in tissue arrival time from 650 ± 89 ms to 346 ± 13 ms. A robust BOLD response was observed in the primary and supplementary motor cortex (Figure 6-11) with a measured increase of 2.6 ± 0.2 % averaged across the 'Motor ROI'.
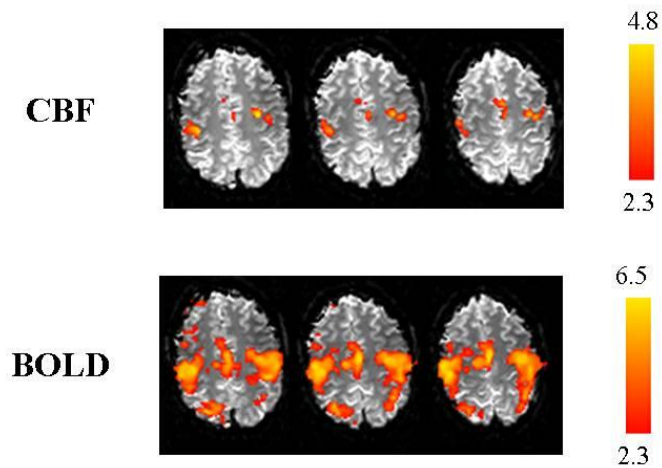
Figure 6-11) Statistical activation maps from a fingertap measured with the LL_DABS scheme shown for a single representative subject created using GLM analysis in FEAT (FSL, FMRIB, Oxford, UK). Colour bars represent minimum and maximum Z-statistic, where Z > 2.3 and p <0.05.

6.6.12 Calibration of the BOLD signal

The hypercapnia induced changes in BOLD and CBF as measured with DABS resulted in an average M-value value of 88 ± 46 %. This was significantly higher and had a considerably larger variance than the M-value calculated using the LL_DABS scheme of 15 ± 7 % (p = 0.043, Wilcoxon Signed Rank Test). Using the measurement of the M-value from the LL_DABS scheme, the relative change in $CMRO_2$ in response to the motor task was 14 ± 4 %. This was significantly lower than the relative change in $CMRO_2$ using the M-value from the DABS sequence (36 ± 11 %), (p = 0.029, Wilcoxon Signed Rank Test).
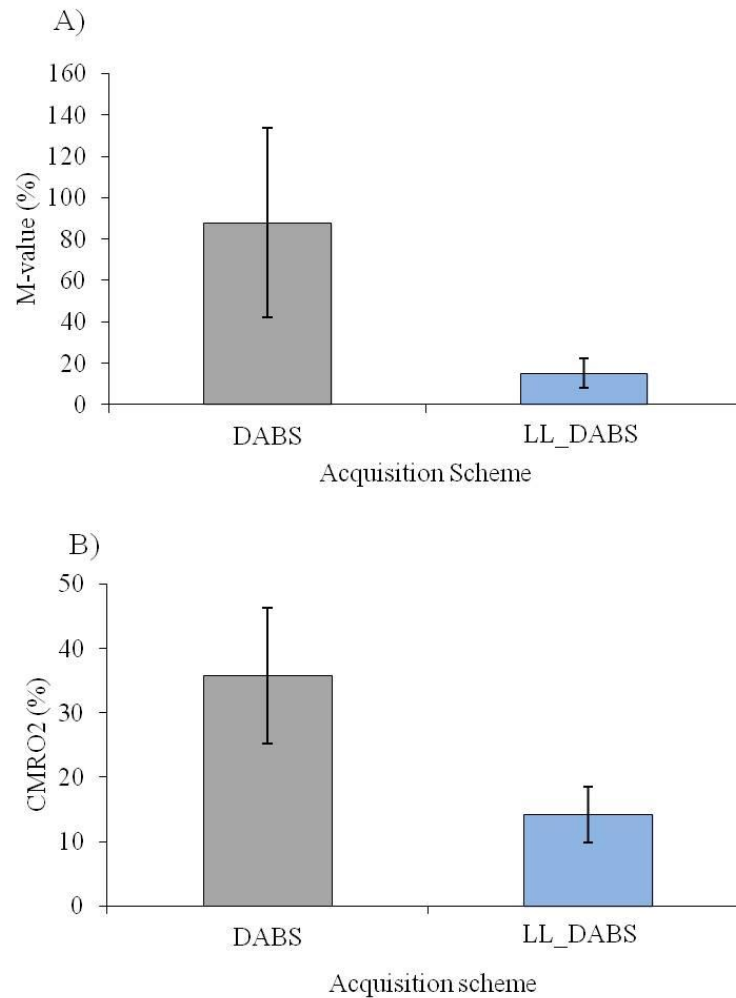
Figure 6-12) Comparison of the measured calibration parameter *M*-value as measured with DABS and LL_DABS. Data are averaged across all subjects (± SEM).

6.6.13 Assessing the optimal scheme (DABS vs. LL_DABS)

The CNR of the perfusion-weighted data for the LL_DABS scheme was significantly increased compared to DABS by 167 ± 41 % , averaged across subjects (p = 0.043, Wilcoxon Signed Rank Test). Whole-brain temporal SNR (tSNR) was compared across the first three minutes of LL_DABS acquisition for the respiratory challenge and motor task, in order to compare medical air with normocapnia. Three out of four showed an increase in whole-brain tSNR with

161

medical air in comparison to normocapnia, 30 ± 38 %, however this change was not significant (Wilcoxon Signed Rank Test).

tSNR in the 'GM ROI' was compared across the first three minutes of the respiratory challenge for the DABS and LL_DABS sequence. tSNR in the 'GM ROI' was significantly increased in the ASL acquisition from the DABS sequence in comparison to LL_DABS (41.2 ± 8.7 %, $p = 0.043$, Wilcoxon Signed Rank Test). There was no significant difference in CNR or tSNR in the 'GM ROI' of the BOLD acquisition between DABS and LL_DABS (Wilcoxon Signed Rank Test).

6.7 <u>Discussion</u>

Hypercapnia is a widely used tool when studying cerebral haemodynamics. As a known vasodilator, it is used to study cerebrovascular reactivity (CVR) and calibrate the BOLD response. The effect of hypercapnia on perfusion is most commonly measured using a single post-label delay time (TI) ASL scheme, due to the relative ease of perfusion quantification and ability to simultaneously acquire CBF and BOLD measurements. However, single phase ASL cannot provide a measurement of transit time (Δ_{tissue}), where transit time refers to the time taken for labelled blood to travel from the arterioles to the capillaries in the tissue bed. Furthermore, under high-flow conditions (such as hypercapnia), it is possible that methods such as QUIPSSII [309] may be unfeasible, and a significant proportion of labelled blood will have left the imaging plane before a readout pulse at a later TI, such that a simple activation-rest subtraction will be erroneous. Here a reasonably short TI of 1400 ms was used for the single phase acquisition, in order to minimise this error. However, from inspecting individual LL_DABS timecourses (as illustrated in Figure 6-8), it can be seen that the difference in the perfusion-weighted signal between normoxia and hypercapnia peaked at 1100 ms in three out of five subjects. This highlights the individual variability in transit time in response to hypercapnia, making it difficult to accurately quantify the perfusion change with a single TI measure.

This chapter presented a modified LL-EPI FAIR sequence termed LL_DABS. The standard LL-EPI FAIR sequence was altered to include a 90° RF pulse applied at the final TI (TI_9). The time between TI_8 and TI_9 was increased from 300ms to 1300ms (maximum available time, given the chosen TA /TR/TE) to increase the time available for signal recovery to maximise the BOLD signal. There was no significant difference between LL_DABS and DABS in either BOLD tSNR or CNR, but a significant improvement in the tSNR and CNR of the BOLD signal was found for LL_DABS compared to the final readout pulse of the standard LL-EPI-FAIR scheme. CNR provides an indication of how easily task induced responses can be detected [323].

Due to the multiple measurements taken in multiphase ASL, it is more sensitive than single phase methods to changes in perfusion, in particular to allow changes in transit time to be quantified. Whilst single phase ASL can be repeated across a range of TI's to form a multiphase data set, this is time-consuming. This study compared single phase and multiphase ASL sequences, using otherwise equivalent scan parameters. Both sequences (DABS and LL_DABS) measured a significant increase in CBF response to hypercapnia, which was further supported by a significant reduction in transit time as measured with LL_DABS. However, the measured change in CBF in response to hypercapnia was significantly greater for LL_DABS, than the DABS method, and CNR in the GM ROI of the perfusion-weighted image was increased.

These findings have important implications for hypercapnia calibrated BOLD. If the hypercapnia-induced perfusion change is underestimated relative to the BOLD change, it will lead to an over-estimation in the calibration constant M-value, and likely lead to an over-estimation of the change in relative $CMRO_2$ in response to a task. The LL_DABS measurements of M-value and change in relative $CMRO_2$ are in close agreement with a recent 7 T study where an increase in relative $CMRO_2$ of 13 % was reported in response to a fingertap, based on an M-value estimate of 15.5 % using hypercapnia calibration with multiphase ASL [308]. The results suggest that if single phase ASL is to be used to measure perfusion in calibrated BOLD, it would be beneficial to consider alternatives to

hypercapnia calibration such as hyperoxia [8] which does not cause a change in CBF.

It can be assumed that the majority of grey matter will show a significant increase in CBF in response to hypercapnia. The GM activation was shown to be more robust for the LL_DABS acquisition, although for both acquisitions, the statistical activation maps of CBF response to hypercapnia were far less robust than for the BOLD maps. The CBF and BOLD activation maps were consistent for the motor task, suggesting that the problem is stimulus amplitude specific. Furthermore, the onset of the hypercapnic stimulus had a significant effect on subject motion, with significant correlation between the $P_{ET}CO_2$ trace and motion correction transformations observed.

Using the DABS scheme it is possible to assess motion during the task. Hypercapnia was found to be associated with increased motion, and there are two plausible explanations for why. It could firstly be explained by subject discomfort. Hypercapnia is characterised by an acidic taste and has previously been shown that a 10mmHg step in $P_{ET}CO_2$ could be detected with an 80 % success rate [324]. However, this study aimed to control for this factor in advance by using a slightly lower step of 8 mmHg (in comparison to previous studies carried out in this research group [130]). Furthermore, for subjects who had not experienced hypercapnia before, a trial sequence was carried out prior to going into the scanner. However, it remains likely that the onset of hypercapnia would still be detected by subjects in this study. Secondly, hypercapnia modulates the ventilatory response, as described in Section 6.2. Should hypercapnia increase the inspiratory/expiratory pressure, it may introduce increased head motion. Both breathing frequency and pressure were assessed between medical air, normocapnia and hypercapnia. No significant change was found in breathing frequency, and although paced breathing was not employed, subjects were asked to breathe regularly throughout. There was also no change in respiratory pressure across the three conditions. However, including the pressure trace as a confound in the GLM analysis increased the number of grey matter voxels showing statistically significant activation. Pressure was measured from the pressure trace via RespirAct^{TM}, which was primarily designed for end-tidal targeting rather than

physiological assessment. A secondary measure of respiratory pressure from respiratory bellows would be beneficial in future experiments.

The findings from this study provide guidance for future research using a hypercapnic stimulus. Here, the potential to underestimate a change in perfusion with single phase ASL in response to hypercapnia have been highlighted. Variability in individual responses to hypercapnia have been observed, therefore it is difficult to simply correct for a change in transit time by reducing the post-label delay and using a single TI. It is important to characterise the shape of the ASL signal curve. The effect of hypercapnia on subject motion must not be underestimated. Motion artefacts could be potentially minimised in future work by modifying the respiratory paradigm to include a ramped transition, to allow the subject to acclimatise to the stimulus and minimise discomfort. Furthermore, paced breathing will prevent any potential changes in breathing frequency.

6.8   Conclusion

Using the LL_DABS sequence, it is possible to quantify both CBF and transit time in response to a task, whilst maintaining high BOLD sensitivity. This study demonstrates the importance of using multiphase ASL for perfusion quantification in high-flow environments, where single phase ASL may lead to a over-estimation of relative $CMRO_2$. By removing the need to assume transit time in simultaneous CBF/BOLD acquisition, the quantitative nature of such acquisitions are improved and sensitivity to perfusion changes are increased. Simultaneous measurement of CBF and BOLD is important for calibration of the BOLD signal and investigating cerebrovascular reactivity. Furthermore, the high temporal SNR of the LL_DABS labelling scheme would enable further modulation of the BOLD signal, allowing simultaneous CBF, BOLD and CBV acquisition [135] in a combined hypercapnia and hyperoxia paradigm.

7 <u>Conclusions</u>

This thesis has used respiratory challenges to investigate the BOLD response, with a view to gaining a more quantitative understanding of this phenomenon. Whilst years of research have been dedicated to understanding this endogenous fMRI signal contrast, a clear understanding remains to be found of how neuronal and vascular mechanisms contribute. This chapter summarises the findings presented in this thesis and looks to how they may help guide future work, with particular emphasis on calibration of the BOLD response.

7.1 <u>The effect of isocapnic hyperoxia on neurophysiology</u>

Calibration of the BOLD response provides the potential for BOLD to become a quantitative fMRI technique, which will be beneficial for the study of cerebral metabolism in ageing and disease. As introduced in Chapter 4, calibration of the BOLD signal using hyperoxia is becoming increasingly popular. This work assessed some of the fundamental assumptions made in hyperoxia calibrated BOLD to determine the validity of the hyperoxia model [8]. An isocapnic hyperoxic stimulus was used throughout removing potential confounds caused by changes in CO_2. Using Phase Contrast MRA (PC-MRA), a T_1-independent method of assessing mean blood flow, it was shown that isocapnic hyperoxia had no significant effect on blood flow in the internal carotid arteries. Using a Look-Locker sampling scheme with FAIR ASL, the effect of isocapnic hyperoxia on arterial cerebral blood volume was assessed. No significant change was found, together with the PC-MRA findings this suggests that isocapnic hyperoxia does not induce vasoconstriction. It is important to note that the assumption of constant cerebral blood flow and volume under hyperoxia is unlikely to hold if constant CO_2 is not maintained (with a stimulus of 100% O_2).

The effect of isocapnic hyperoxia on resting-state neuronal oscillations as measured with MEG was investigated. A small reduction was observed in the occipital lobe, however the response was significantly smaller than the global

response to hypercapnia [130]. It is likely that the change in neuronal oscillations are coupled to a metabolic change, and so these findings suggest that hyperoxia is an ideal alternative to hypercapnia in calibrated BOLD fMRI. Nonetheless, further research into the role of hyperoxia on neuronal oscillations is needed. It would be very interesting to investigate the potential role which hyperoxia may play on attention and cognitive function.

The final part of Chapter 4 assessed the impact of isocapnic hyperoxia on functional hyperaemia; the change in cerebral blood flow evoked by a task. Having shown that isocapnic hyperoxia has no significant effect on cerebral vasculature, any measured changes in the evoked response between normoxic and hyperoxic conditions could be attributed to an increase in O_2. The change in CBF and BOLD were simultaneously assessed and the change in response to a motor task did not significantly differ between normoxic and hyperoxic conditions. Furthermore, there was no significant difference in baseline CBF between normoxia and hyperoxia, in agreement with the PC-MRA results. The findings are contrary to previous literature results which have reported a counter-intuitive increase in the functional hyperaemic response under non-isocapnic hyperoxia [228-230, 241]. However, it is likely that maintaining a constant CO_2 across conditions may explain this difference. Future research is required into the mechanisms which regulate task evoked CBF.

7.2 The dependence of ΔR_2^* on oxygenation across field strength

The power law which relates the change in transverse signal relaxation (ΔR_2^*) to a fractional change in blood oxygenation (1-Y) forms an integral part of calibrated BOLD fMRI. To date, the assumed values are generally taken from analytical and numerical simulations [139, 248, 249], although a small number of experimental measures have been made [9, 250-252]. Here, using an isocapnic hyperoxic stimulus, blood oxygenation was modulated whilst vascular responses were held constant. This allowed the relationship between ΔR_2^* and (1-Y) to be assessed in a quantitative manner. A sub-linear relationship was found across cortical grey matter, across all field strengths (1.5, 3 and 7 T), which could be well

approximated to a linear dependence at all field strengths. This is contrary to prior results, which suggest that the relationship is supralinear at 1.5 T and tend towards a linear dependence at 7 T. These differences can probably be explained by the contribution of both intravascular and extravascular signal to the measured grey matter signal in the present study, despite the removal of large vessels. Experimental measures were combined with in-vitro blood data [20], in order to assess the relative signal contributions across oxygenation and field strength. A rapid decrease in the intravascular signal with increased oxygenation, relative to extravascular signal, may explain the observed sub-linear dependence. In-vivo assessment of pure intra- and extravascular signal would help clarify this. Furthermore, the dynamic range of oxygenation was somewhat limited in this study (0.3-0.4) in comparison to the full theoretical range of 0-1. Including hypoxic data in future studies would increase the dynamic range and provide a better test replication of previous simulations [139, 248, 249].

7.3 The effect of hypercapnia on cerebral haemodynamics

Due to its low cost and wide availability, hypercapnia remains a popular investigative tool in calibrated BOLD fMRI and cerebrovascular reactivity, despite its potential impact on $CMRO_2$. In such studies, it is useful to make simultaneous measurements of CBF and BOLD, and this is generally done in combination with a single phase ASL sequence. Chapter 6 assessed the suitability of using a single phase sequence to measure CBF changes in a high-flow environment, such as under hypercapnia. A modified LL-EPI FAIR ASL sequence was presented (LLDABS), which increased the time before the final RF pulse to allow an increase in signal recovery time such that BOLD sensitivity was maximised for the chosen TR. The measured change in CBF was found to be significantly smaller when measured with single phase ASL using the DABS scheme as opposed to multiphase ASL. This can be explained by the observation that the transit time significantly decreased with hypercapnia. In addition, transit time was found to significantly decrease with hypercapnia, further supporting the use of multiphase ASL (LL_DABS) which does not rely on an assumed transit time. These findings

highlight the importance in choosing a suitable combined BOLD/ASL sequence for simultaneously measuring the BOLD and CBF response to hypercapnia. It is possible that single phase sequences may underestimate the perfusion change, which would lead to an underestimation of a relative change in $CMRO_2$ in the hypercapnia calibrated BOLD model. Furthermore, the improved BOLD sensitivity of the LLDABS sequence means it can be used to acquire simultaneous vCBV [135] in addition to BOLD and CBF, this will provide a useful method to assess cerebral haemodynamics in health and disease.

7.4 <u>Conclusion</u>

The ability to independently modulate O_2 and CO_2 provides a unique perturbation for investigating the mechanisms which underlie the BOLD response. Understanding these mechanisms is crucial to fMRI, which despite its popularity within the field of psychology and neuroscience, currently lacks the quantitative capability required in order for it to be a gold standard clinical imaging technique. The findings presented in this thesis aim to guide future research into the BOLD response, particularly calibrated BOLD fMRI, where the simultaneous acquisition of haemodynamic measurements will prove to be invaluable.

8 <u>References</u>

1.   Ogawa, S., et al., *Brain magnetic resonance imaging with contrast dependent on blood oxygenation.* Proceedings of the National Academy of Sciences, 1990. **87**(24): p. 9868-9872.

2.   Thulborn, K.R., et al., *Oxygenation dependence of the transverse relaxation time of water protons in whole blood at high field.* Biochimica et Biophysica Acta (BBA)-General Subjects, 1982. **714**(2): p. 265-270.

3.   Ogawa, S., et al., *Oxygenation-sensitive contrast in magnetic resonance image of rodent brain at high magnetic fields.* Magnetic Resonance in Medicine, 1990. **14**(1): p. 68-78.

4.   Turner, R., et al., *Echo-planar time course MRI of cat brain oxygenation changes.* Magnetic Resonance in Medicine, 1991. **22**(1): p. 159-166.

5.   Jezzard, P., et al., *Comparison of EPI gradient-echo contrast changes in cat brain caused by respiratory challenges with direct simultaneous evaluation of cerebral oxygenation via a cranial window.* NMR in Biomedicine, 1994. **7**(1-2): p. 35-44.

6.   Kim, S.-G. and S. Ogawa, *Biophysical and physiological origins of blood oxygenation level-dependent fMRI signals.* Journal of Cerebral Blood Flow & Metabolism, 2012. **32**(7): p. 1188-1206.

7.   Davis, T.L., et al., *Calibrated functional MRI: mapping the dynamics of oxidative metabolism.* Proceedings of the National Academy of Sciences of the United States of America, 1998. **95**(4): p. 1834-1839.

8.   Chiarelli, P.A., et al., *A calibration method for quantitative BOLD fMRI based on hyperoxia.* Neuroimage, 2007. **37**(3): p. 808-820.

9.   Wise, R.G., et al., *Measurement of OEF and absolute CMRO2: MRI-based methods using interleaved and combined hypercapnia and hyperoxia.* Neuroimage, 2013. **83**: p. 135-147.

10.   Gauthier, C.J. and R.D. Hoge, *A generalized procedure for calibrated MRI incorporating hyperoxia and hypercapnia.* Human Brain Mapping, 2012. **60**(2): p. 1212-1225.

11.   Levitt, M.H., *Spin dynamics: basics of nuclear magnetic resonance.* 2008: Wiley, Chichester, UK.

12.   Gadian, D.G., *NMR and its application to living systems.* 1995: Oxford Science Publications, Oxford, UK.

13.   Wright, P., et al., *Water proton T 1 measurements in brain tissue at 7, 3, and 1.5 T using IR-EPI, IR-TSE, and MPRAGE: results and optimization.* Magnetic Resonance Materials in Physics, Biology and Medicine, 2008. **21**(1-2): p. 121-130.

14.   Peters, A.M., et al., *T2* measurements in human brain at 1.5, 3 and 7 T.* Magnetic resonance imaging, 2007. **25**(6): p. 748-753.

15.   Hahn, E.L., *Spin echoes.* Physical review, 1950. **80**(4): p. 580-594.

16.   Carr, H.Y. and E.M. Purcell, *Effects of diffusion on free precession in nuclear magnetic resonance experiments.* Physical review, 1954. **94**(3): p. 630-638.

17.   Meiboom, S. and D. Gill, *Modified spin-echo method for measuring nuclear relaxation times.* Review of Scientific Instruments, 1958. **29**(8): p. 688-691.

18.   Cox, E., *Quanitative Whole Body Imaging at High Field*, in *School of Physics and Astronomy.* 2009, University of Nottingham: Nottingham.

19. Golay, X., et al., *Measurement of tissue oxygen extraction ratios from venous blood T2: increased precision and validation of principle.* Magnetic Resonance in Medicine, 2001. **46**(2): p. 282-291.

20. Blockley, N., et al., *Field strength dependence of R1 and R 2* relaxivities of human whole blood to prohance, vasovist, and deoxyhemoglobin.* Magnetic Resonance in Medicine, 2008. **60**(6): p. 1313-1320.

21. Zhao, J.M., et al., *Oxygenation and hematocrit dependence of transverse relaxation rates of blood at 3T.* Magnetic Resonance in Medicine, 2007. **58**(3): p. 592-597.

22. Yacoub, E., et al., *Imaging brain function in humans at 7 Tesla.* Magnetic Resonance in Medicine, 2001. **45**(4): p. 588-594.

23. Lauterbur, P.C., *Image formation by induced local interactions: examples employing nuclear magnetic resonance.* Nature, 1973. **242**(5394): p. 190-191.

24. Pruessmann, K.P., et al., *SENSE: sensitivity encoding for fast MRI.* Magnetic Resonance in Medicine, 1999. **42**(5): p. 952-962.

25. Mansfield, P., *Multi-planar image formation using NMR spin echoes.* Journal of Physics C: Solid State Physics, 1977. **10**(3): p. L55-L58.

26. Bornert, P. and D. Jensen, *Single-shot-double-echo EPI.* Magnetic resonance imaging, 1994. **12**(7): p. 1033-1038.

27. Posse, S., et al., *Enhancement of BOLD-contrast sensitivity by single-shot multi-echo functional MR imaging.* Magnetic Resonance in Medicine, 1999. **42**(1): p. 87-97.

28. Brown, M.A. and R.C. Semelka, *MRI: basic principles and applications*. 2010: Wiley-Blackwell, Cambridge, UK.

29. Park, H., D. Kim, and Z. Cho, *Gradient reversal technique and its applications to chemical-shift related NMR imaging.* Magnetic Resonance in Medicine, 1987. **4**(6): p. 526-536.

30. Takahara, T., J. Zwanenburg, and F. Visser. *Fat suppression with slice-selection gradient reversal (SSGR) revisited.* in *ISMRM 17th Scientific Meeting & Exhibition, Honolulu, Hawaii, USA.* 2009.

31. McGinley, J.V.M., V.C. Srivastava, and D. G.D, *Passive shimming technique for MRI magnets.* Mag. Res. Im, 1997. **15**(3): p. XIX.

32. Gruetter, R., *Automatic, localized in Vivo adjustment of all first-and second-order shim coils.* Magnetic Resonance in Medicine, 1993. **29**(6): p. 804-811.

33. Poole, M. and R. Bowtell, *Volume parcellation for improved dynamic shimming.* Magnetic Resonance Materials in Physics, Biology and Medicine, 2008. **21**(1-2): p. 31-40.

34. Bear, M.F., B.W. Connors, and M.A. Paradiso, *Neuroscience*. Vol. 2. 2007, Baltimore, USA: Lippincott Williams & Wilkins.

35. Ballabh, P., A. Braun, and M. Nedergaard, *The blood-brain barrier: an overview: structure, regulation, and clinical implications.* Neurobiology of disease, 2004. **16**(1): p. 1-13.

36. Grieb, P., et al., *O2 exchange between blood and brain tissues studied with 18O2 indicator-dilution technique.* Journal of Applied Physiology, 1985. **58**(6): p. 1929-1941.

37. Gray, H., *Anatomy of the human body*. 1918: Lea & Febiger.

38. Roy, C.S. and C. Sherrington, *On the regulation of the blood-supply of the brain.* The Journal of Physiology, 1890. **11**(1-2): p. 85.

39.   Ter-Pogossian, M.M., et al., *The determination of regional cerebral blood flow by means of water labeled with radioactive oxygen 15.* Radiology, 1969. **93**(1): p. 31.

40.   Ter-Pogossian, M.M., et al., *The measure in vivo of regional cerebral oxygen utilization by means of oxyhemoglobin labeled with radioactive oxygen-15.* Journal of Clinical Investigation, 1970. **49**(2): p. 381.

41.   Ordidge, R., et al., *Snapshot head imaging at 0.5 T using the echo planar technique.* Magnetic Resonance in Medicine, 1988. **8**(1): p. 110-115.

42.   Ogawa, S. and T.M. Lee, *Magnetic resonance imaging of blood vessels at high fields: in vivo and in vitro measurements and image simulation.* Magnetic Resonance in Medicine, 1990. **16**(1): p. 9-18.

43.   Girouard, H. and C. Iadecola, *Neurovascular coupling in the normal brain and in hypertension, stroke, and Alzheimer disease.* Journal of Applied Physiology, 2006. **100**(1): p. 328-335.

44.   Kwong, K.K., et al., *Dynamic magnetic resonance imaging of human brain activity during primary sensory stimulation.* Proceedings of the National Academy of Sciences, 1992. **89**(12): p. 5675-5679.

45.   Ogawa, S., et al., *Intrinsic signal changes accompanying sensory stimulation: functional brain mapping with magnetic resonance imaging.* Proceedings of the National Academy of Sciences, 1992. **89**(13): p. 5951-5955.

46.   Frahm, J., et al., *Dynamic MR imaging of human brain oxygenation during rest and photic stimulation.* Journal of Magnetic Resonance Imaging, 1992. **2**(5): p. 501-505.

47.   Bandettini, P.A., et al., *Time course EPI of human brain function during task activation.* Magnetic Resonance in Medicine, 1992. **25**(2): p. 390-397.

48.   Weisskoff, R.M. and S. Kiihne, *MRI susceptometry: Image based measurement of absolute susceptibility of MR contrast agents and human blood.* Magnetic Resonance in Medicine, 1992. **24**(2): p. 375-383.

49.   Zhu, X.H., et al., *New Opportunities for High-Field In Vivo MRS in Studying Brain Bioenergetics and Function.* Brain Imaging and Behavior, 2008. **2**(4): p. 232-241.

50.   Gjedde, A., *In: Cerebrovascular Disease. Bajter H, Caplan L, editors.* 1997, Philadelphia: Lippincott-Raven.

51.   Lin, A.L., et al., *Functional neuroimaging: a physiological perspective.* Frontiers in Neuroenergetics, 2010. **2**: p. 1-4.

52.   Du, F., et al., *Tightly coupled brain activity and cerebral ATP metabolic rate.* Proceedings of the National Academy of Sciences, 2008. **105**(17): p. 6409-6414.

53.   Fox, P.T. and M.E. Raichle, *Focal physiological uncoupling of cerebral blood flow and oxidative metabolism during somatosensory stimulation in human subjects.* Proceedings of the National Academy of Sciences, 1986. **83**(4): p. 1140-1144.

54.   Hoge, R.D., et al., *Linear coupling between cerebral blood flow and oxygen consumption in activated human cortex.* Proceedings of the National Academy of Sciences, 1999. **96**(16): p. 9403.

55.   Buxton, R.B. and L.R. Frank, *A model for the coupling between cerebral blood flow and oxygen metabolism during neural stimulation.* Journal of Cerebral Blood Flow & Metabolism, 1997. **17**(1): p. 64-72.

56.   Buxton, R.B., *Introduction to functional magnetic resonance imaging: principles and techniques.* 2002: Cambridge Univ Pr.

57. Zheng, Y., et al., *A model of the hemodynamic response and oxygen delivery to brain.* Neuroimage, 2002. **16**(3): p. 617-637.

58. Drew, P.J., A.Y. Shih, and D. Kleinfeld, *Fluctuating and sensory-induced vasodynamics in rodent cortex extend arteriole capacity.* Proceedings of the National Academy of Sciences, 2011. **108**(20): p. 8473-8478.

59. Kim, T., et al., *Arterial versus total blood volume changes during neural activity-induced cerebral blood flow change: implication for BOLD fMRI.* Journal of Cerebral Blood Flow & Metabolism, 2007. **27**(6): p. 1235-1247.

60. Fernandez-Klett, F., et al., *Pericytes in capillaries are contractile in vivo, but arterioles mediate functional hyperemia in the mouse brain.* Proceedings of the National Academy of Sciences, 2010. **107**(51): p. 22290-22295.

61. Buxton, R.B., E.C. Wong, and L.R. Frank, *Dynamics of blood flow and oxygenation changes during brain activation: the balloon model.* Magnetic Resonance in Medicine, 1998. **39**(6): p. 855-864.

62. Mandeville, J.B., et al., *Evidence of a cerebrovascular postarteriole windkessel with delayed compliance.* Journal of Cerebral Blood Flow & Metabolism, 1999. **19**(6): p. 679-689.

63. Frahm, J., et al., *Dynamic uncoupling and recoupling of perfusion and oxidative metabolism during focal brain activation in man.* Magnetic Resonance in Medicine, 1996. **35**(2): p. 143-148.

64. Sadaghiani, S., K. Ugurbil, and K. Uludag, *Neural activity-induced modulation of BOLD poststimulus undershoot independent of the positive signal.* Magnetic resonance imaging, 2009. **27**(8): p. 1030-1038.

65. Chen, J.J. and G.B. Pike, *Origins of the BOLD post-stimulus undershoot.* NeuroImage, 2009. **46**(3): p. 559-568.

66. Uludag, K., et al., *Coupling of cerebral blood flow and oxygen consumption during physiological activation and deactivation measured with fMRI.* Neuroimage, 2004. **23**(1): p. 148-155.

67. Lu, H., M.J. Donahue, and P. van Zijl, *Detrimental effects of BOLD signal in arterial spin labeling fMRI at high field strength.* Magnetic Resonance in Medicine, 2006. **56**(3): p. 546-552.

68. Malonek, D. and A. Grinvald, *Interactions between electrical activity and cortical microcirculation revealed by imaging spectroscopy: implications for functional brain mapping.* Science, 1996. **272**: p. 551-554.

69. Hu, X., T.H. Le, and K. Ugurbil, *Evaluation of the early response in fMRI in individual subjects using short stimulus duration.* Magnetic Resonance in Medicine, 1997. **37**(6): p. 877-884.

70. Buxton, R.B., *The elusive initial dip.* Neuroimage, 2001. **13**(6): p. 953-958.

71. Kim, D.-S., T.Q. Duong, and S.-G. Kim, *Reply to "Can current fMRI techniques reveal the micro-architecture of cortex?".* Nature neuroscience, 2000. **3**(5): p. 414-414.

72. Logothetis, N., *Can current fMRI techniques reveal the micro-architecture of cortex?* Nature neuroscience, 2000. **3**(5): p. 413-413.

73. Frostig, R.D., et al., *Cortical functional architecture and local coupling between neuronal activity and the microcirculation revealed by in vivo high-resolution optical imaging of intrinsic signals.* Proceedings of the National Academy of Sciences, 1990. **87**(16): p. 6082-6086.

74. Jasdzewski, G., et al., *Differences in the hemodynamic response to event-related motor and visual paradigms as measured by near-infrared spectroscopy.* Neuroimage, 2003. **20**(1): p. 479-488.

75. Jenkinson, M., et al., *Improved optimization for the robust and accurate linear registration and motion correction of brain images.* Neuroimage, 2002. **17**(2): p. 825-841.

76. Glover, G.H., T.Q. Li, and D. Ress, *Image-based method for retrospective correction of physiological motion effects in fMRI: RETROICOR.* Magnetic Resonance in Medicine, 2000. **44**(1): p. 162-167.

77. Worsley, K.J., et al., *A three-dimensional statistical analysis for CBF activation studies in human brain.* Journal of Cerebral Blood Flow and Metabolism, 1992. **12**: p. 900-900.

78. Gruner, J.M., et al., *Brain perfusion CT compared with15O-H2O-PET in healthy subjects.* EJNMMI research. **1**(1): p. 1-10.

79. Orrison, W.W., et al., *Functional brain imaging.* 1995: Mosby St. Louis, MO.

80. Catafau, A.M., *Brain SPECT in Clinical Practice. Part I: Perfusion*.* Journal of Nuclear Medicine, 2001. **42**(2): p. 259-271.

81. Rosen, B.R., et al., *Contrast agents and cerebral hemodynamics.* Magnetic Resonance in Medicine, 1991. **19**(2): p. 285-292.

82. Villringer, A., et al., *Dynamic imaging with lanthanide chelates in normal brain: contrast due to magnetic susceptibility effects.* Magnetic Resonance in Medicine, 1988. **6**(2): p. 164-174.

83. Barker, P., X. Golay, and G. Zaharchuk, *Clinical Perfusion MRI: Techniques and Applications*: Cambridge University Press.

84. Williams, D.S., et al., *Magnetic resonance imaging of perfusion using spin inversion of arterial water.* Proceedings of the National Academy of Sciences, 1992. **89**(1): p. 212-216.

85. Wong, E.C., R.B. Buxton, and L.R. Frank, *Implementation of quantitative perfusion imaging techniques for functional brain mapping using pulsed arterial spin labeling.* NMR in Biomedicine, 1997. **10**(45): p. 237-249.

86. Ye, F.Q., et al., *Noise reduction in 3D perfusion imaging by attenuating the static signal in arterial spin tagging (ASSIST).* Magnetic Resonance in Medicine, 2000. **44**(1): p. 92-100.

87. Garcia, D.M., G. Duhamel, and D.C. Alsop, *Efficiency of inversion pulses for background suppressed arterial spin labeling.* Magnetic Resonance in Medicine, 2005. **54**(2): p. 366-372.

88. St Lawrence, K. and J. Wang, *Effects of the apparent transverse relaxation time on cerebral blood flow measurements obtained by arterial spin labeling.* Magnetic Resonance in Medicine, 2005. **53**(2): p. 425-433.

89. Edelman, R.R., D.G. Darby, and S. Warach, *Qualitative Mapping of Cerebral Blood Flow and Functional Localization with Echo-planar MR Imaging and Signal Targeting with Alternating Radio Frequency™.* Radiology, 1994. **192**: p. 513-520.

90. Detre, J.A., et al., *Tissue specific perfusion imaging using arterial spin labeling.* NMR in Biomedicine, 1994. **7**(1-2): p. 75-82.

91. Dai, W., et al., *Continuous flow-driven inversion for arterial spin labeling using pulsed radio frequency and gradient fields.* Magnetic Resonance in Medicine, 2008. **60**(6): p. 1488-1497.

92. Kwong, K.K., et al., *Mr perfusion studies with t1-weighted echo planar imaging.* Magnetic Resonance in Medicine, 1995. **34**(6): p. 878-887.

93.   Kim, S.G., *Quantification of relative cerebral blood flow change by flow-sensitive alternating inversion recovery (FAIR) technique: Application to functional mapping.* Magnetic Resonance in Medicine, 1995. **34**(3): p. 293-301.

94.   Bernstein, M.A., K.F. King, and X.J. Zhou, *Handbook of MRI pulse sequences.* 2004: Academic Press.

95.   Aslan, S., et al., *Estimation of labeling efficiency in pseudocontinuous arterial spin labeling.* Magnetic Resonance in Medicine, 2010. **63**(3): p. 765-771.

96.   Nezamzadeh, M., et al., *Improved pseudo-continuous arterial spin labeling for mapping brain perfusion.* Journal of Magnetic Resonance Imaging, 2010. **31**(6): p. 1419-1427.

97.   Herscovitch, P. and M.E. Raichle, *What is the correct value for the brain-blood partition coefficient for water?* Journal of Cerebral Blood Flow & Metabolism, 1985. **5**(1): p. 65-69.

98.   Buxton, R.B., et al., *A general kinetic model for quantitative perfusion imaging with arterial spin labeling.* Magnetic Resonance in Medicine, 1998. **40**(3): p. 383-396.

99.   Francis, S.T., R. Bowtell, and P.A. Gowland, *Modeling and Optimization of Look-Locker Spin Labeling for Measuring Perfusion and Transit Time Changes in Activation Studies Taking into Account Arterial Blood Volume.* Mag. Res. Med., 2008. **59**: p. 316-325.

100.   Hendrikse, J., et al., *Measurements of cerebral perfusion and arterial hemodynamics during visual stimulation using TURBO-TILT.* Magnetic Resonance in Medicine, 2003. **50**(2): p. 429-433.

101.   Petersen, E.T., T. Lim, and X. Golay, *Model-Free Arterial Spin Labeling Quantification Approach for Perfusion MRI.* Mag. Res. Med., 2006. **55**: p. 219-232.

102.   Brookes, M.J., et al., *Noninvasive Measurement of Arterial Cerebral Blood Volume Using Look-Locker EPI and Arterial Spin Labeling.* Mag. Res. Med., 2007. **58**: p. 41-54.

103.   Rashid, W., et al., *Abnormalities of cerebral perfusion in multiple sclerosis.* Journal of Neurology, Neurosurgery & Psychiatry, 2004. **75**(9): p. 1288-1293.

104.   Oguz, K.K., et al., *Sickle Cell Disease: Continuous Arterial Spin-labeling Perfusion MR Imaging in Children 1.* Radiology, 2003. **227**(2): p. 567-574.

105.   Lui, S., et al., *Depressive disorders: focally altered cerebral perfusion measured with arterial spin-labeling MR imaging.* Radiology, 2009. **251**(2): p. 476.

106.   Du, A., et al., *Hypoperfusion in frontotemporal dementia and Alzheimer disease by arterial spin labeling MRI.* Neurology, 2006. **67**(7): p. 1215-1220.

107.   Mills, C., et al., *Nuclear magnetic resonance: principles of blood flow imaging.* American Journal of Roentgenology, 1984. **142**(1): p. 165-170.

108.   Schneider, G., et al., *Magnetic resonance angiography: techniques, indications, and practical applications.* 2005: Springer.

109.   Westbrook, C., C.K. Roth, and J. Talbot, *MRI in Practice.* 2005: Wiley-Blackwell.

110.   Lotz, J., et al., *Cardiovascular Flow Measurement with Phase-Contrast MR Imaging: Basic Facts and Implementation1.* Radiographics, 2002. **22**(3): p. 651-671.

111.   Spritzer, C.E., et al., *Rapid MR imaging of blood flow with a phase-sensitive, limited-flip-angle, gradient recalled pulse sequence: preliminary experience.* Radiology, 1990. **176**(1): p. 255-262.

112.   O'Donnell, M., *NMR blood flow imaging using multiecho, phase contrast sequences.* Medical physics, 1985. **12**: p. 59-64.

113.   McRobbie, D.W., *MRI from Picture to Proton.* 2007: Cambridge University Press.

114.   Reimer, P. and M. Boos, *Phase-contrast MR angiography of peripheral arteries: technique and clinical application.* European radiology, 1999. **9**(1): p. 122-127.

115.   Pernicone, J., et al., *Three-dimensional phase-contrast MR angiography in the head and neck: preliminary report.* American Journal of Roentgenology, 1990. **155**(1): p. 167-176.

116.   Graves, M., *Magnetic resonance angiography.* British journal of radiology, 1997. **70**(829): p. 6-28.

117.   Hubel, D.H. and T.N. Wiesel, *Receptive fields, binocular interaction and functional architecture in the cat's visual cortex.* The Journal of Physiology, 1962. **160**(1): p. 106.

118.   Nunez, P.L., *Electric fields of the brain: the neurophysics of EEG.* 2006: Oxford University Press.

119.   Scheuer, M.L., *Continuous EEG monitoring in the intensive care unit.* Epilepsia, 2002. **43**(s3): p. 114-127.

120.   Facco, E., *The role of EEG in brain injury.* Intensive care medicine, 1999. **25**(8): p. 872-877.

121.   Hughes, J. and E. John, *Conventional and Quantitative Electroencephalography in Psychiatry.* The Journal of Neuropsychiatry and Clinical Neurosciences, 1999. **11**(2): p. 190-208.

122.   Brookes, M.J., *A multi-modal approach to functional neuroimaging.* 2005, University of Nottingham.

123.   Hamalainen, M., et al., *Magnetoencephalography-theory, instrumentation, and applications to noninvasive studies of the working human brain.* Reviews of modern Physics, 1993. **65**(2): p. 413.

124.   Brookes, M.J., et al., *GLM-beamformer method demonstrates stationary field, alpha ERD and gamma ERS co-localisation with fMRI BOLD response in visual cortex.* Neuroimage, 2005. **26**(1): p. 302-308.

125.   Kastrup, A., et al., *Changes of cerebral blood flow, oxygenation, and oxidative metabolism during graded motor activation.* Neuroimage, 2002. **15**(1): p. 74-82.

126.   Stefanovic, B., et al., *Hemodynamic and metabolic responses to activation, deactivation and epileptic discharges.* Neuroimage, 2005. **28**(1): p. 205-215.

127.   Mohtasib, R.S., et al., *Calibrated fMRI during a cognitive Stroop task reveals reduced metabolic response with increasing age.* Neuroimage, 2012. **59**(2): p. 1143-1151.

128.   Chiarelli, P.A., et al., *Flow-metabolism coupling in human visual, motor, and supplementary motor areas assessed by magnetic resonance imaging.* Magnetic Resonance in Medicine, 2007. **57**(3): p. 538-547.

129.   Jones, M., et al., *The effect of hypercapnia on the neural and hemodynamic responses to somatosensory stimulation.* Neuroimage, 2005. **27**(3): p. 609-623.

130.   Hall, E.L., et al., *The effect of hypercapnia on resting and stimulus induced MEG signals.* NeuroImage, 2011. **58**(4): p. 1034-1043.

131.   Xu, F., et al., *The influence of carbon dioxide on brain activity and metabolism in conscious humans.* Journal of Cerebral Blood Flow & Metabolism, 2011. **31**: p. 58-67.

132.   Zappe, A., et al., *The influence of moderate hypercapnia on neural activity in the anesthetized nonhuman primate.* Cerebral Cortex, 2008. **18**(11): p. 2666-2673.

133.   Thesen, T., et al., *Depression of cortical activity in humans by mild hypercapnia.* Human Brain Mapping, 2012. **33**(3): p. 715-726.

134.   Chen, J.J. and G.B. Pike, *Global cerebral oxidative metabolism during hypercapnia and hypocapnia in humans: implications for BOLD fMRI.* Journal of Cerebral Blood Flow & Metabolism, 2010. **30**(6): p. 1094-1099.

135.   Driver, I.D., et al., *Calibrated BOLD using direct measurement of changes in venous oxygenation.* Neuroimage, 2012. **63**: p. 1178-1187.

136.   Rostrup, E., et al., *Signal changes in gradient echo images of human brain induced by hypo- and hyperoxia.* NMR in Biomedicine, 1995. **8**(1): p. 41-47.

137.   Losert, C., et al., *Oxygen enhanced MRI of the brain.* Magnetic Resonance in Medicine, 2002. **48**(2): p. 271-277.

138.   Hoge, R.D., et al., *Investigation of BOLD signal dependence on cerebral blood flow and oxygen consumption: the deoxyhemoglobin dilution model.* Magnetic Resonance in Medicine, 1999. **42**(5): p. 849-863.

139.   Boxerman, J.L., et al., *MR contrast due to intravascular magnetic susceptibility perturbations.* Magnetic Resonance in Medicine, 1995. **34**(4): p. 555-566.

140.   Grubb, R.L., et al., *The effects of changes in PaCO2 cerebral blood volume, blood flow, and vascular mean transit time.* Stroke, 1974. **5**(5): p. 630-639.

141.   Bulte, D., et al., *Quantitative measurement of cerebral physiology using respiratory-calibrated MRI.* Neuroimage, 2012. **60**(1): p. 582-591.

142.   Richardson, D.W., et al., *Role of hypocapnia in the circulatory responses to acute hypoxia in man.* Journal of Applied Physiology, 1966. **21**(1): p. 22-26

143.   Moore, L.G., et al., *Variable inhibition by falling CO2 of hypoxic ventilatory response in humans.* Journal of Applied Physiology, 1984. **56**(1): p. 207-210.

144.   Ellingsen, I., et al., *Changes in human cerebral blood flow due to step changes in PAO2 and PACO2.* Acta Physiologica Scandinavica, 1987. **129**(2): p. 157-163.

145.   Slessarev, M., et al., *Prospective targeting and control of end-tidal CO2 and O2 concentrations.* The Journal of Physiology, 2007. **581**(3): p. 1207-1219.

146.   Vesely, A., et al., *MRI mapping of cerebrovascular reactivity using square wave changes in end tidal PCO2.* Magnetic Resonance in Medicine, 2001. **45**(6): p. 1011-1013.

147.   Xie, A., et al., *Cerebrovascular response to carbon dioxide in patients with congestive heart failure.* American journal of respiratory and critical care medicine, 2005. **172**(3): p. 371-378

148.   Stillman, A., X. Hu, and M. Jerosch-Herold, *Functional MRI of brain during breath holding at 4 T.* Magnetic resonance imaging, 1995. **13**(6): p. 893-897.

149.   Kastrup, A., et al., *Regional variability of cerebral blood oxygenation response to hypercapnia.* Neuroimage, 1999. **10**(6): p. 675-681.

150.   Li, T.Q., et al., *Functional MRI of human brain during breath holding by BOLD and FAIR techniques.* Neuroimage, 1999. **9**(2): p. 243-249.

151.   Bright, M.G. and K. Murphy, *Reliable quantification of BOLD fMRI cerebrovascular reactivity despite poor breath-hold performance.* Neuroimage, 2013. **83**: p. 559-568.

152. Kolbitsch, C., et al., *The influence of hyperoxia on regional cerebral blood flow (rCBF), regional cerebral blood volume (rCBV) and cerebral blood flow velocity in the middle cerebral artery (CBFVMCA) in human volunteers.* Magnetic resonance imaging, 2002. **20**(7): p. 535-541.

153. Somogyi, R., et al., *Precise control of end-tidal carbon dioxide levels using sequential rebreathing circuits.* Anaesthesia and intensive care, 2005. **33**(6): p. 726-732.

154. Wenzel, U., et al., *Utility of deadspace and capnometry measurements in determination of surfactant efficacy in surfactant-depleted lungs.* Critical care medicine, 1999. **27**(5): p. 946-952.

155. Verschuren, F., et al., *Volumetric capnography as a bedside monitoring of thrombolysis in major pulmonary embolism.* Intensive care medicine, 2004. **30**(11): p. 2129-2132.

156. Tang, Y., M. Turner, and A. Baker, *Effects of alveolar dead-space, shunt and V/Q distribution on respiratory dead-space measurements.* British journal of anaesthesia, 2005. **95**(4): p. 538-548.

157. Blockley, N.P., et al., *An improved method for acquiring cerebrovascular reactivity maps.* Magnetic Resonance in Medicine, 2011. **65**(5): p. 1278-1286.

158. Henninger, N., et al., *Normobaric hyperoxia delays perfusion/diffusion mismatch evolution, reduces infarct volume, and differentially affects neuronal cell death pathways after suture middle cerebral artery occlusion in rats.* Journal of Cerebral Blood Flow & Metabolism, 2007. **27**(9): p. 1632-1642.

159. Shin, H.K., et al., *Normobaric hyperoxia improves cerebral blood flow and oxygenation, and inhibits peri-infarct depolarizations in experimental focal ischaemia.* Brain, 2007. **130**(6): p. 1631-1642.

160. Hadjiev, D.I. and P.P. Mineva, *Transient ischemic attack may present a target for normobaric hyperoxia treatment.* Medical hypotheses, 2010. **75**(1): p. 128-130.

161. Menzel, M., et al., *Increased inspired oxygen concentration as a factor in improved brain tissue oxygenation and tissue lactate levels after severe human head injury.* Journal of neurosurgery, 1999. **91**(1): p. 1-10.

162. Tolias, C.M., et al., *Normobaric hyperoxia-induced improvement in cerebral metabolism and reduction in intracranial pressure in patients with severe head injury: a prospective historical cohort-matched study.* Journal of neurosurgery, 2004. **101**(3): p. 435-444.

163. Tisdall, M.M., et al., *Increase in cerebral aerobic metabolism by normobaric hyperoxia after traumatic brain injury.* Journal of Neurosurgery: Pediatrics, 2008. **109**(3).

164. NICE, *Diagnosis and management of headaches in young people and adults, CG150.* 2012, National Insitute for Health and Care Excellence: London.

165. Bulte, D.P., et al., *Cerebral perfusion response to hyperoxia.* Journal of Cerebral Blood Flow & Metabolism, 2007. **27**(1): p. 69-75.

166. Kwong, K.K., et al., *EPI Imaging of Global Increase of Brain MR Signal with Breath-hold Preceded by Breathing O2.* Magnetic Resonance in Medicine, 1995. **33**(3): p. 448-452.

167. Driver, I., et al., *Global intravascular and local hyperoxia contrast phase-based blood oxygenation measurements.* Proc. Intl. Soc. Mag. Reson. Med., Salt Lake City, 21, 2013: p. 3251.

168. Bulte, D., et al., *Measurement of cerebral blood volume in humans using hyperoxic MRI contrast.* Journal of Magnetic Resonance Imaging, 2007. **26**(4): p. 894-899.

169. Blockley, N., et al., *Measuring venous blood volume changes during activation using hyperoxia.* Neuroimage, 2012. **59**(4): p. 3266-3274.

170. Kety, S.S. and C.F. Schmidt, *The nitrous oxide method for the quantitative determination of cerebral blood flow in man: theory, procedure and normal values.* Journal of Clinical Investigation, 1948. **27**(4): p. 476-483.

171. Traystman, R.J., *The paper that completely altered our thinking about cerebral blood flow measurement.* Journal of Applied Physiology, 2004. **97**(5): p. 1601-1602.

172. Watson, N., et al., *The effect of hyperoxia on cerebral blood flow: a study in healthy volunteers using magnetic resonance phase contrast angiography.* European journal of anaesthesiology, 2000. **17**(3): p. 152-159.

173. Becker, H.F., et al., *Effect of different levels of hyperoxia on breathing in healthy subjects.* Journal of Applied Physiology, 1996. **81**(4): p. 1683-1690.

174. Loeppky, J.A., U.C. Luft, and E.R. Fletcher, *Quantitative description of whole blood CO2 dissociation curve and Haldane effect.* Respiration Physiology, 1983. **51**(2): p. 167-181.

175. Bray, J.J., *Lecture notes on human physiology.* 1999: Wiley-Blackwell.

176. Noseworthy, M.D., et al., *Tracking Oxygen Effects on MR Signal in Blood and Skeletal Muscle During Hyperoxia Exposure.* Journal of Magnetic Resonance Imaging, 1999. **9**: p. 814-820.

177. Tadamura, E., et al., *Effect of Oxygen Inhalation on Relaxation Times in Various Tissues.* JMRI, 1997. **7**: p. 220-225.

178. O'Connor, J.P.B., et al., *Organ-Specific Effects of Oxygen and Carbogen Gas Inhalation on Tissue Longitudinal Relaxation Times.* Magnetic Resonance in Medicine, 2007. **58**: p. 490-496.

179. Hedegard, W. *Derived copy of Anatomy and Physiology 3*. 2014 25 March 2014.

180. Boyajian, R.A., et al., *Measurement of anterior and posterior circulation flow contributions to cerebral blood flow. An ultrasound-derived volumetric flow analysis.* Journal of neuroimaging: official journal of the American Society of Neuroimaging, 1995. **5**(1): p. 1-3.

181. Zhao, M., et al., *Regional cerebral blood flow using quantitative MR angiography.* American Journal of Neuroradiology, 2007. **28**(8): p. 1470-1473.

182. Field, A.S., et al., *Dietary caffeine consumption and withdrawal: confounding variables in quantitative cerebral perfusion studies? 1.* Radiology, 2003. **227**(1): p. 129-135.

183. Mark, C.I., J.A. Fisher, and B. Pike, *Improved fMRI calibration: Precisely controlled hyperoxic versus hypercapnic stimuli.* Neuroimage, 2011. **54**: p. 1102-1111.

184. Floyd, T.F., et al., *Independent cerebral vasoconstrictive effects of hyperoxia and accompanying arterial hypocapnia at 1 ATA.* Journal of Applied Physiology, 2003. **95**(6): p. 2453-2461

185. Rostrup, E., et al., *The relationship between cerebral blood flow and volume in humans.* Neuroimage, 2005. **24**(1): p. 1-11.

186. Rane, S.D. and J.C. Gore, *Measurement of T1 of human arterial and venous blood at 7T.* Magnetic resonance imaging, 2013. **31**(3): p. 477-479.

187. Grgac, K., P. Zijl, and Q. Qin, *Hematocrit and oxygenation dependence of blood 1H2O T1 at 7 tesla.* Magnetic Resonance in Medicine, 2013. **70**(4): p. 1153-1159.

188. Rooney, W.D., et al., *Magnetic Field and Tissue Dependencies of Human Brain Longitudinal ^1H_2O Relaxation in Vivo.* Magnetic Resonance in Medicine, 2007. **57**: p. 308-318.

189. Lee, S.-P., et al., *Relative changes of cerebral arterial and venous blood volumes during increased cerebral blood flow: implications for BOLD fMRI.* Magnetic Resonance in Medicine, 2001. **45**(5): p. 791-800.

190. Maleki, N., et al., *The Effect of Hypercarbia and Hyperoxia on the Total Blood Flow to the Retina as Assessed by Magnetic Resonance Imaging.* Investigative Ophthalmology & Visual Science, 2011. **52**(9): p. 6867-6874.

191. Zaharchuk, G., A. Martin, and W. Dillon, *Noninvasive imaging of quantitative cerebral blood flow changes during 100% oxygen inhalation using arterial spin-labeling MR imaging.* American Journal of Neuroradiology, 2008. **29**(4): p. 663-667.

192. Goodwin, J.A., et al., *Quantitative fMRI using hyperoxia calibration: reproducibility during a cognitive Stroop task.* Neuroimage, 2009. **47**(2): p. 573-580.

193. Shen, Y., et al., *Magnetic resonance imaging of the mean venous vessel size in the human brain using transient hyperoxia.* Neuroimage, 2011. **55**(3): p. 1063-1067.

194. Seo, J.-G., et al., *Comparison of cognitive effects of lamotrigine and oxcarbazepine in epilepsy patients.* Journal of Clinical Neurology, 2007. **3**(1): p. 31-37.

195. Lindauer, U., et al., *Neuronal activity-induced changes of local cerebral microvascular blood oxygenation in the rat: effect of systemic hyperoxia or hypoxia.* Brain Research, 2003. **975**: p. 135-140.

196. Smith, D.B.D. and P.J. Strawbridge, *Auditory and Visual Evoked Potentials During Hyperoxia.* Electroencephalography and Clinical Neurophysiology, 1974. **37**: p. 393-398.

197. Kaskinoro, K., et al., *Normobaric hyperoxia does not induce significant electroencephalogram changes in healthy male subjects: 7AP4-5.* European Journal of Anaesthesiology (EJA), 2010. **27**(47): p. 121-122.

198. Gross, J., et al., *Dynamic imaging of coherent sources: Studying neural interactions in the human brain.* Proceedings of the National Academy of Science USA, 2001. **98**: p. 694-699.

199. Robinson, S. and J. Vrba, *Functional Neuroimaging by synthetic aperture magnetometry.* 1998, Sendai: Tohoku University Press.

200. Sekihara, K., et al., *Reconstructing Spatio-Temporal Activities of Neural Sources Using an MEG Vector Beamformer Technique.* IEEE Transactions on Biomedical Engineering, 2001. **48**: p. 760-771.

201. Van Drongelen, W., et al., *A Spatial Filtering Technique to Detect and Localize Multiple Sources in the Brain.* Brain Topography, 1996. **9**: p. 39-49.

202. Van Veen, B.D., et al., *Localisation of brain electrical activity via linearly constrained minimum variance spatial filtering.* IEEE Transactions on biomedical engineering, 1997. **44**: p. 867-880.

203. Brookes, M.J., et al., *A general linear model for MEG beamformer imaging.* Neuroimage, 2004. **23**(3): p. 936-946.

204. Brookes, M.J., et al., *Optimising experimental design for MEG beamformer imaging.* Neuroimage, 2008. **39**(4): p. 1788-1802.

205. Cheyne, D., et al., *Neuromagnetic imaging of cortical oscillations accompanying tactile stimulation.* Cognitive brain research, 2003. **17**(3): p. 599-611.

206. Nichols, T. and A. Holmes, *Nonparametric permutation tests for functional neuroimaging: a primer with examples.* Human Brain Mapping, 2002. **15**(1): p. 1-25.

207. Brookes, M.J., et al., *Changes in brain network activity during working memory tasks: a magnetoencephalography study.* Neuroimage, 2010. **55**(4): p. 1804-1815.

208. Attwell, D. and S.B. Laughlin, *An energy budget for signaling in the grey matter of the brain.* Journal of Cerebral Blood Flow & Metabolism, 2001. **21**(10): p. 1133-1145.

209. Logothetis, N.K., et al., *Neurophysiological investigation of the basis of the fMRI signal.* Nature, 2001. **412**(6843): p. 150-157.

210. Mukamel, R., et al., *Coupling between neuronal firing, field potentials, and FMRI in human auditory cortex.* Science, 2005. **309**(5736): p. 951-954.

211. Ossandon, T., et al., *Efficient "pop-out" visual search elicits sustained broadband gamma activity in the dorsal attention network.* The Journal of Neuroscience, 2011. **32**(10): p. 3414-3421.

212. Singh, M., S.G. Kim, and T.S. Kim, *Correlation between BOLD-fMRI and EEG signal changes in response to visual stimulus frequency in humans.* Magnetic Resonance in Medicine, 2003. **49**(1): p. 108-114.

213. Zumer, J.M., et al., *Relating BOLD fMRI and neural oscillations through convolution and optimal linear weighting.* Neuroimage, 2010. **49**(2): p. 1479-1489.

214. Stevenson, C.M., M.J. Brookes, and P.G. Morris, *Beta Band correlates of the fMRI BOLD response.* Human Brain Mapping, 2011. **32**(2): p. 182-197.

215. Winterer, G., et al., *Complex relationship between BOLD signal and synchronization/desynchronization of human brain MEG oscillations.* Human Brain Mapping, 2007. **28**(9): p. 805-816.

216. Murphy, K., A. Harris, and R. Wise, *Measuring the influence of hypercapnia on absolute CMRO2 in humans.* Proc. Intl. Soc. Mag. Reson. Med., Salt Lake City, 21, 2013: p. 3343.

217. Moss, M.C., A.B. Scholey, and K. Wesnes, *Oxygen administration selectively enhances cognitive performance in healthy young adults: a placebo-controlled double-blind crossover study.* Psychopharmacology, 1998. **138**(1): p. 27-33.

218. Ozkurt, B., et al., *Efficacy of high-flow oxygen therapy in all types of headache: a prospective, randomized, placebo-controlled trial.* The American journal of emergency medicine, 2012. **30**(9): p. 1760-1764.

219. Cohen, A.S., B. Burns, and P.J. Goadsby, *High-flow oxygen for treatment of cluster headache.* JAMA: the journal of the American Medical Association, 2009. **302**(22): p. 2451-2457.

220. Siesjo, B.K., *Brain energy metabolism.* 1978, New York: Wiley.

221. Fox, P.T., et al., *Nonoxidative glucose consumption during focal physiologic neural activity.* Science, 1988. **241**(4864): p. 462-464.

222. Vovenko, E., *Distribution of oxygen tension on the surface of arterioles, capillaries and venules of brain cortex and in tissue in normoxia: an experimental study on rats.* Pflugers Archiv, 1999. **437**(4): p. 617-623.

223. Ances, B.M., et al., *Dynamic changes in cerebral blood flow, O2 tension, and calculated cerebral metabolic rate of O2 during functional activation using oxygen phosphorescence quenching.* Journal of Cerebral Blood Flow & Metabolism, 2001. **21**(5): p. 511-516.

224. Masamoto, K., et al., *Trial-by-trial relationship between neural activity, oxygen consumption, and blood flow responses.* Neuroimage, 2008. **40**(2): p. 442-450.

225. Devor, A., et al., *'Overshoot' of O2 is required to maintain baseline tissue oxygenation at locations distal to blood vessels.* The Journal of Neuroscience, 2011. **31**(38): p. 13676-13681.

226. Offenhauser, N., et al., *Activity-induced tissue oxygenation changes in rat cerebellar cortex: interplay of postsynaptic activation and blood flow.* The Journal of Physiology, 2005. **565**(1): p. 279-294.

227. Mintun, M.A., et al., *Blood flow and oxygen delivery to human brain during functional activity: theoretial modeling and experimental data.* Proceedings of the National Academy of Sciences, 2001. **98**(12): p. 6859-6864.

228. Matsuura, T., K. Kashikura, and I. Kanno, *Hemodynamics of local cerebral blood flow induced by somatosensory stimulation under normoxia and hyperoxia in rats.* Comparative Biochemistry and Physiology Part A: Molecular & Integrative Physiology, 2001. **129**(2): p. 363-372.

229. Matsuura, T., et al., *Modulation of evoked cerebral blood flow under excessive blood supply and hyperoxic conditions.* The Japanese journal of physiology, 2000. **50**(1): p. 115-123.

230. Kashikura, K., et al., *Hyperoxia modified activation-induced blood oxygenation level-dependent response of human visual cortex (V1): an event-related functional magnetic resonance imaging study.* Neuroscience letters, 2001. **299**(1): p. 53-56.

231. Rubio, R., et al., *Relationship between adenosine concentration and oxygen supply in rat brain.* Am J Physiol, 1975. **228**(6): p. 1896-1902.

232. Phillis, J.W., *Adenosine and Adenine Nucleotides as Regulators of Cerebral Blood Flow: Roles of Acidosis, Cell Swelling, and KATP Channels.* Critical Reviewsâ„¢ in Neurobiology, 2004. **16**(4).

233. Iadecola, C. and K. Niwa, *Nitric oxide.* Cerebral Blood Flow and Metabolism, 2nd edR Lippincott Williams and Wilkins, Philadelphia, 2002: p. 295-310.

234. Wang, H., et al., *Synaptic and vascular associations of neurons containing cyclooxygenase-2 and nitric oxide synthase in rat somatosensory cortex.* Cerebral Cortex, 2005. **15**(8): p. 1250-1260.

235. Koehler, R.C., D. Gebremedhin, and D.R. Harder, *Role of astrocytes in cerebrovascular regulation.* Journal of Applied Physiology, 2006. **100**(1): p. 307-317.

236. Niwa, K., et al., *Cyclooxygenase-1 participates in selected vasodilator responses of the cerebral circulation.* Circulation research, 2001. **88**(6): p. 600-608.

237. Moreno, A., et al., *Neurophysiological, metabolic and cellular compartments that drive neurovascular coupling and neuroimaging signals.* Frontiers in Neuroenergetics, 2013. **5**.

238. Attwell, D., et al., *Glial and neuronal control of brain blood flow.* Nature, 2010. **468**(7321): p. 232-243.

239. Petzold, G.C. and V.N. Murthy, *Role of astrocytes in neurovascular coupling.* Neuron, 2011. **71**(5): p. 782-797.

240. Iadecola, C. and M. Nedergaard, *Glial regulation of the cerebral microvasculature.* Nature neuroscience, 2007. **10**(11): p. 1369-1376.

241. Tajima, Y., et al., *Cerebral hemodynamic response to acute hyperoxia in awake mice*, in *Brain Research*. 2014.

242. Hyder, F., R.G. Shulman, and D.L. Rothman, *A model for the regulation of cerebral oxygen delivery.* Journal of Applied Physiology, 1998. **85**(2): p. 554-564.

243. Buxton, R.B., *Dynamic models of BOLD contrast.* Neuroimage, 2012. **62**(2): p. 953-961.

244. Driver, I., *The vascular properties of the BOLD signal*, in *Department of Physics and Astronomy.* 2011, University of Nottingham.

245. Sicard, K.M. and T.Q. Duong, *Effects of hypoxia, hyperoxia, and hypercapnia on baseline and stimulus-evoked BOLD, CBF, and CMRO2 in spontaneously breathing animals.* Neuroimage, 2005. **25**(3): p. 850-858.

246. Foucher, J.R., et al., *Correcting for the echo-time effect after measuring the cerebral blood flow by arterial spin labeling.* Journal of Magnetic Resonance Imaging, 2011. **34**(4): p. 785-790.

247. Cavusoglu, M., et al., *Comparison of pulsed arterial spin labeling encoding schemes and absolute perfusion quantification.* Magnetic resonance imaging, 2009. **27**(8): p. 1039-1045.

248. Ogawa, S., et al., *Functional brain mapping by blood oxygenation level-dependent contrast magnetic resonance imaging. A comparison of signal characteristics with a biophysical model.* Biophysical Journal, 1993. **64**(3): p. 803-812.

249. Yablonskiy, D.A. and E.M. Haacke, *Theory of NMR signal behavior in magnetically inhomogeneous tissues: the static dephasing regime.* Magnetic Resonance in Medicine, 1994. **32**(6): p. 749-763.

250. van der Zwaag, W., et al., *fMRI at 1.5, 3 and 7 T: characterising BOLD signal changes.* Neuroimage, 2009. **47**(4): p. 1425-1434.

251. Driver, I., et al., *The change in cerebrovascular reactivity between 3 T and 7 T measured using graded hypercapnia.* Neuroimage, 2010. **51**(1): p. 274-279.

252. Rossi, C., et al., *Manipulation of cortical gray matter oxygenation by hyperoxic respiratory challenge: field dependence of R2* and MR signal response.* NMR in Biomedicine, 2012. **25**(8): p. 1007-1014.

253. Li, D., D.J. Waight, and Y. Wang, *In vivo correlation between blood T2 and oxygen saturation.* Journal of Magnetic Resonance Imaging, 1998. **8**(6): p. 1236-1239.

254. Kennan, R.P., J. Zhong, and J.C. Gore, *Intravascular susceptibility contrast mechanisms in tissues.* Magnetic Resonance in Medicine, 1994. **31**(1): p. 9-21.

255. Weisskoff, R., et al., *Endogenous susceptibility contrast: principles of relationship between blood oxygenation and MR signal change.* Functional MRI of the brain. Berkeley: SMRM, California, 1993: p. 143-151.

256. Weisskoff, R., et al., *Microscopic susceptibility variation and transverse relaxation: theory and experiment.* Magnetic Resonance in Medicine, 1994. **31**(6): p. 601-610.

257. Ugurbil, K., et al., *Functional MRI at high fields: Practice and utility.* 2000, Chichester, UK: John Wiley & Sons.

258. Clingman, C., et al. *Intravascular BOLD transverse relaxation: exchange vs. diffusion through field gradients.* in *Proceedings of the 11th Scientific Meeting and Exhibition of the International Society for Magnetic Resonance in Medicine, Toronto, Ontario, Canada.* 2003.

259. Li, D., Y. Wang, and D. Waight, *Blood oxygen saturation assessment in vivo using T2* estimation.* Magnetic Resonance in Medicine, 1998. **39**(5): p. 685-690.

260. Lu, H. and Y. Ge, *Quantitative evaluation of oxygenation in venous vessels using T2-relaxation-under-spin-tagging MRI.* Magnetic resonance in medicine: official journal of the Society of Magnetic Resonance in Medicine/Society of Magnetic Resonance in Medicine, 2008. **60**(2): p. 357-363.

261.   Thulborn, K., et al., *Oxygenation dependence of the transverse relaxation time of water protons in whole blood at high field.* Biochimica et Biophysica Acta (BBA)-General Subjects, 1982. **714**(2): p. 265-270.

262.   Donahue, M.J., et al., *Blood oxygenation level dependent (BOLD) total and extravascular signal changes and delta R2* in human visual cortex at 1.5, 3.0 and 7.0 T.* NMR in Biomedicine, 2011. **24**(1): p. 25-34.

263.   Song, A.W., et al., *Functional activation using apparent diffusion coefficient-dependent contrast allows better spatial localization to the neuronal activity: evidence using diffusion tensor imaging and fiber tracking.* Neuroimage, 2003. **20**(2): p. 955-961.

264.   Lu, H. and P. van Zijl, *Experimental measurement of extravascular parenchymal BOLD effects and tissue oxygen extraction fractions using multi-echo VASO fMRI at 1.5 and 3.0 T.* Magnetic Resonance in Medicine, 2005. **53**(4): p. 808-816.

265.   Duong, T.Q., et al., *Microvascular BOLD contribution at 4 and 7 T in the human brain: Gradient-echo and spin-echo fMRI with suppression of blood effects.* Magnetic Resonance in Medicine, 2003. **49**(6): p. 1019-1027.

266.   Bizzi, A., et al., *MR of diffusion slowing in global cerebral ischemia.* American Journal of Neuroradiology, 1993. **14**(6): p. 1347-1354.

267.   Chien, D., et al., *MR diffusion imaging of the human brain.* Journal of Computer Assisted Tomography, 1990. **14**(4): p. 514-520.

268.   Boxerman, J.L., et al., *The intravascular contribution to fmri signal change: monte carlo modeling and diffusion-weighted studies in vivo.* Magnetic Resonance in Medicine, 1995. **34**(1): p. 4-10.

269.   Severinghaus, J.W., *Simple, accurate equations for human blood O2 dissociation computations.* Journal of Applied Physiology, 1979. **46**(3): p. 599-602.

270.   Blockley, N.P., V.E. Griffeth, and R.B. Buxton, *A general analysis of calibrated BOLD methodology for measuring CMRO2 responses: Comparison of a new approach with existing methods.* Neuroimage, 2012. **60**(1): p. 279-289.

271.   Griffeth, V.E., et al., *A New Functional MRI Approach for Investigating Modulations of Brain Oxygen Metabolism.* PloS one, 2013. **8**(6): p. e68122.

272.   Griffeth, V.E. and R.B. Buxton, *A theoretical framework for estimating cerebral oxygen metabolism changes using the calibrated-BOLD method: modeling the effects of blood volume distribution, hematocrit, oxygen extraction fraction, and tissue signal properties on the BOLD signal.* Neuroimage, 2011. **58**(1): p. 198-212.

273.   Martindale, J., et al., *Theory and generalization of Monte Carlo models of the BOLD signal source.* Magnetic Resonance in Medicine, 2008. **59**(3): p. 607-618.

274.   Eichling, J.O., et al., *Evidence of the limitations of water as a freely diffusible tracer in brain of the rhesus monkey.* Circulation research, 1974. **35**(3): p. 358-364.

275.   Helenius, J., et al., *Cerebral hemodynamics in a healthy population measured by dynamic susceptibility contrast MR imaging.* Acta radiologica, 2003. **44**(5): p. 538-546.

276.   Fujita, N., *Extravascular contribution of blood oxygenation level-dependent signal changes: A numerical analysis based on a vascular network model.* Magnetic Resonance in Medicine, 2001. **46**(4): p. 723-734.

277.   Kastrup, A., et al., *Assessment of cerebral oxidative metabolism with breath holding and fMRI.* Magnetic Resonance in Medicine, 1999. **42**(3): p. 608-611.

278.   Kress, J.P. and J.J. Marini. *Acute respiratory distress syndrome: adjuncts to lung-protective ventilation.* in *Seminars in respiratory and critical care medicine.* 2001: New York: Thieme Medical Publishers, c1994-.

279.   Kety, S.S. and C.F. Schmidt, *The effects of altered arterial tensions of carbon dioxide and oxygen on cerebral blood flow and cerebral oxygen consumption of normal young men.* Journal of Clinical Investigation, 1948. **27**(4): p. 484.

280.   Reivich, M., *Arterial PCO2 and cerebral hemodynamics.* Survey of Anesthesiology, 1964. **9**(3): p. 212-220.

281.   Ito, H., et al., *Changes in human cerebral blood flow and cerebral blood volume during hyperapnia and hypocapnia measured by positron emission tomography.* Journal of Cerebral Blood Flow & Metabolism, 2003. **23**(6): p. 665-670.

282.   Mason, R.J., et al., *Murray and Nadel's Textbook of Respiratory Medicine: 2-Volume Set.* 2010: Elsevier Health Sciences.

283.   Heistad, D.D. and H.A. Kontos, *Cerebral circulation.* Comprehensive Physiology, 1983.

284.   Duffin, J., *Measuring the respiratory chemoreflexes in humans.* Respiratory physiology & neurobiology, 2011. **177**(2): p. 71-79.

285.   Mark, C.I., J.A. Fisher, and G.B. Pike, *Improved fMRI calibration: precisely controlled hyperoxic versus hypercapnic stimuli.* Neuroimage, 2011. **54**(2): p. 1102-1111.

286.   Rostrup, E., et al., *Regional differences in the CBF and BOLD responses to hypercapnia: a combined PET and fMRI study.* Neuroimage, 2000. **11**(2): p. 87-97.

287.   Bulte, D.P., K. Drescher, and P. Jezzard, *Comparison of hypercapnia based calibration techniques for measurement of cerebral oxygen metabolism with MRI.* Magnetic Resonance in Medicine, 2009. **61**(2): p. 391-398.

288.   Noth, U., et al., *Cerebral vascular response to hypercapnia: determination with perfusion MRI at 1.5 and 3.0 Tesla using a pulsed arterial spin labeling technique.* Journal of Magnetic Resonance Imaging, 2006. **24**(6): p. 1229-1235.

289.   Chen, J.J. and G.B. Pike, *MRI measurement of the BOLD-specific flow-volume relationship during hypercapnia and hypocapnia in humans.* Neuroimage, 2010. **53**(2): p. 383-391.

290.   Chen, J.J. and G.B. Pike, *BOLD-specific cerebral blood volume and blood flow changes during neuronal activation in humans.* NMR in Biomedicine, 2009. **22**(10): p. 1054-1062.

291.   Yablonskiy, D.A., *Cerebral metabolic rate in hypercapnia: controversy continues.* Journal of Cerebral Blood Flow & Metabolism, 2011.

292.   Fierstra, J., et al., *Measuring cerebrovascular reactivity: what stimulus to use?* The Journal of Physiology, 2013. **591**(23): p. 5809-5821.

293.   Murphy, K., A.D. Harris, and R.G. Wise, *Robustly measuring vascular reactivity differences with breath-hold: normalising stimulus-evoked and resting state BOLD fMRI data.* Neuroimage, 2011. **54**(1): p. 369-379.

294.   Gao, Y.-Z., et al., *Regional Cerebral Blood Flow and Cerebrovascular Reactivity in Alzheimer's Disease and Vascular Dementia Assessed by Arterial Spinlabeling Magnetic Resonance Imaging.* Current neurovascular research, 2013. **10**(1): p. 49-53.

295.   Yezhuvath, U.S., et al., *Forebrain-dominant deficit in cerebrovascular reactivity in Alzheimer's disease.* Neurobiology of aging, 2012. **33**(1): p. 75-82.

296. Glodzik, L., et al., *Cerebrovascular Reactivity to Carbon Dioxide in Alzheimer's Disease*. Journal of Alzheimer's Disease, 2013. **35**(3): p. 427-440.

297. Gupta, A., et al., *Cerebrovascular Reserve and Stroke Risk in Patients With Carotid Stenosis or Occlusion A Systematic Review and Meta-Analysis*. Stroke, 2012. **43**(11): p. 2884-2891.

298. Conklin, J., et al., *Impaired cerebrovascular reactivity with steal phenomenon is associated with increased diffusion in white matter of patients with Moyamoya disease*. Stroke, 2010. **41**(8): p. 1610-1616.

299. Heyn, C., et al., *Quantification of Cerebrovascular Reactivity by Blood Oxygen Level-Dependent MR Imaging and Correlation with Conventional Angiography in Patients with Moyamoya Disease*. American Journal of Neuroradiology, 2010. **31**(5): p. 862-867.

300. Kuwabara, Y., et al., *Response to Hypercapnia in Moyamoya Disease Cerebrovascular Response to Hypercapnia in Pediatric and Adult Patients With Moyamoya Disease*. Stroke, 1997. **28**(4): p. 701-707.

301. Spano, V.R., et al., *CO2 Blood Oxygen Level-dependent MR Mapping of Cerebrovascular Reserve in a Clinial Population: Safety, Tolerability, and Technical Feasibility*. Radiology, 2013. **266**(2): p. 592-598.

302. Mandell, D.M., et al., *Mapping cerebrovascular reactivity using blood oxygen level-dependent MRI in patients with arterial steno-occlusive disease comparison with arterial spin labeling MRI*. Stroke, 2008. **39**(7): p. 2021-2028.

303. Faraco, C.C., et al., *Dual echo vessel-encoded ASL for simultaneous BOLD and CBF reactivity assessment in patients with ischemic cerebrovascular disease*. Magnetic Resonance in Medicine, 2014.

304. Liu, T.T., et al., *An introduction to normalization and calibration methods in functional MRI*. Psychometrika, 2013. **78**(2): p. 308-321.

305. Gallichan, D. and P. Jezzard, *Variation in the shape of pulsed arterial spin labeling kinetic curves across the healthy human brain and its implications for CBF quantification*. Magnetic Resonance in Medicine, 2009. **61**(3): p. 686-695.

306. MacIntosh, B.J., et al., *Measuring the effects of remifentanil on cerebral blood flow and arterial arrival time using 3D GRASE MRI with pulsed arterial spin labelling*. J Cereb Blood Flow Metab, 2008. **28**(8): p. 1514-1522.

307. Ho, Y.-C.L., E.T. Petersen, and X. Golay, *Measuring arterial and tissue responses to functional challenges using arterial spin labeling*. Neuroimage, 2010. **49**(1): p. 478-487.

308. Hall, E.L., *Quantitative Methods to Assess Cerebral Haemodynamics*, in *School of Physics and Astronomy*. 2012, University of Nottingham: Nottingham.

309. Wong, E.C., R.B. Buxton, and L.R. Frank, *Quantitative imaging of perfusion using a single subtraction (QUIPSS and QUIPSS II)*. Magnetic Resonance in Medicine, 1998. **39**(5): p. 702-708.

310. Tancredi, F.B., et al., *Comparison of pulsed and pseudocontinuous arterial spin-labeling for measuring CO2-induced cerebrovascular reactivity*. Journal of Magnetic Resonance Imaging, 2012. **36**(2): p. 312-321.

311. Alsop, D.C., et al., *Recommended Implementation of Arterial Spin Labeled Perfusion MRI for Clinical Applications: A consensus of the ISMRM Perfusion Study Group and the European Consortium for ASL in Dementia* In Press.

312. Mullinger, K.J., et al., *Poststimulus undershoots in cerebral blood flow and BOLD fMRI responses are modulated by poststimulus neuronal activity*. Proceedings of the National Academy of Sciences, 2013. **110**(33): p. 13636-13641.

313. Mullinger, K., et al., *Evidence that the negative BOLD response is neuronal in origin: A simultaneous EEG–BOLD–CBF study in humans.* Neuroimage, 2014. **94**: p. 263-274.

314. Jezzard, P. and R.B. Buxton, *The clinical potential of functional magnetic resonance imaging.* Journal of Magnetic Resonance Imaging, 2006. **23**(6): p. 787-793.

315. Lai, S., et al., *Identification of vascular structures as a major source of signal contrast in high resolution 2D and 3D functional activation imaging of the motor cortex at 1. 5T preliminary results.* Magnetic Resonance in Medicine, 1993. **30**(3): p. 387-392.

316. Turner, R., *How much cortex can a vein drain? Downstream dilution of activation-related cerebral blood oxygenation changes.* Neuroimage, 2002. **16**(4): p. 1062-7.

317. Pfeuffer, J., et al., *Perfusion-based high-resolution functional imaging in the human brain at 7 Tesla.* Magnetic Resonance in Medicine, 2002. **47**(5): p. 903-911.

318. Blockley, N.P., et al., *A review of calibrated blood oxygenation level-dependent (BOLD) methods for the measurement of task-induced changes in brain oxygen metabolism.* NMR in Biomedicine, 2013. **26**(8): p. 987-1003.

319. Leontiev, O. and R.B. Buxton, *Reproducibility of BOLD, perfusion, and CMRO2 measurements with calibrated-BOLD fMRI.* Neuroimage, 2007. **35**(1): p. 175-184.

320. Wesolowski, R., P. Gowland, and S. Francis. *Double Acquistion with Background Suppressed (DABS) FAIR at 3T and 7T: advantages for simultaneous BOLD and CBF acquisition.* in *Proceedings of ISMRM.* 2009.

321. Triantafyllou, C., et al., *Comparison of physiological noise at 1.5 T, 3 T and 7 T and optimization of fMRI acquisition parameters.* Neuroimage, 2005. **26**(1): p. 243-250.

322. Gardener, A.G., P.A. Gowland, and S.T. Francis, *Implementation of Quantitative Perfusion Imaging Using Pulsed Arterial Spin Labeling at Ultra-High Field.* Mag. Res. Med., 2009. **61**: p. 874-882.

323. Hyde, J.S., B.B. Biswal, and A. Jesmanowicz, *High-resolution fMRI using multislice partial k-space GR-EPI with cubic voxels.* Magnetic Resonance in Medicine, 2001. **46**(1): p. 114-125.

324. Schwartzstein, R., et al., *Detection of hypercapnia by normal subjects.* Clinical Science, 1987. **73**(Pt 3): p. 333-335.